The Initial Oxidation of Al-Mg alloys

Emila Panda

The Initial Oxidation of Al-Mg alloys

Von der Fakultät Chemie der Universität Stuttgart
zur Erlangung der Würde eines Doktors der Naturwissenschaften (Dr. rer. nat.)
genehmigte Abhandlung

vorgelegt von

Emila Panda

aus Bhubaneswar/Indien

Hauptberichter:	Prof. Dr. Ir. E. J. Mittemeijer
Mitberichter:	Priv.-Doz. Dr. J. Bill
Prüfungsvorsitzender:	Prof. Dr. E. Roduner

Tag der Einreichung:	28.09.2009
Tag der mündlichen Prüfung:	14.12.2009

MAX-PLANCK-INSTITUT FÜR METALLFORSCHUNG STUTTGART
INSTITUT FÜR MATERIALWISSENSCHAFT DER UNIVERSITÄT STUTTGART

Stuttgart, 2009

Contents

1.   General Introduction

1.1.   The initial oxidation of metals and alloys

Thermal oxidation is defined as the chemical reaction between a metal or alloy surface and oxygen molecules from the gas phase to form an oxide phase. The process of thermal oxidation involves a series of concurrent steps, such as, oxygen impingement, physisorption, dissociative chemisorption and subsequent oxide nucleation and growth. A schematic representation of an oxide film grown on a bare metal or alloy substrate by exposure to oxygen gas, along with an indication of some of the concurrent steps in the oxidation process, is shown in Fig. 1.1.

The *initial* rate of oxide formation on a *bare* metallic surface (i.e. without a native oxide or another foreign surface layer) is typically very high. However, as soon as a laterally-closed oxide film is formed on the metallic surface, the oxide film provides a diffusion barrier between the two reactants (i.e., the parent metallic substrate and the oxygen gas) and, consequently, the oxide-film growth rate is drastically reduced (see Fig. 1.2). Continued oxide-film growth can then only proceed if (charged) reacting species (i.e., cations, anions, electrons, holes and vacancies) are transported through the developing oxide film towards the reacting oxide/gas or substrate/oxide interfaces.

The oxide-film growth kinetics will strongly depend on the structure and chemical constitution of the developing oxide phase. For example, the initial oxide-film growth rate is generally lower for an amorphous state of the oxide overgrowth than for a polycrystalline oxide overgrowth due to the absence of grain boundaries in the amorphous oxide film, which can act as fast diffusion paths for the reactant species. This implies that not only kinetics, but also thermodynamics, play a crucial role for the oxidation behavior of metal and alloy surfaces [1]. A thermodynamic description of the oxidation process of metallic substrates comprises the prediction of the energetically-preferred phase constitution of the developing oxide overgrowth on the parent metallic surface as a function of the growth conditions (e.g. temperature, time, partial oxygen pressure, the oxide-film thickness, as well as of the chemical composition and crystallographic orientation of the parent substrate) [1].
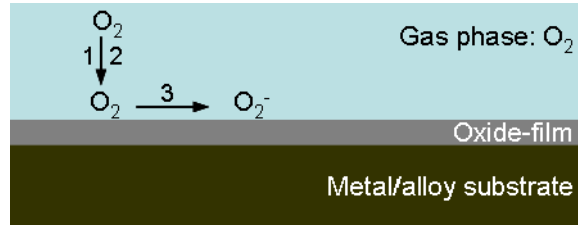
Fig. 1.1: Schematic representation of a growing oxide film on a bare metal or alloy substrate upon thermal oxidation. Some concurrent steps in the oxidation process are indicated: i.e. 1. oxygen impingement; 2. oxygen physisorption and 3. molecular and/or dissociative oxygen chemisorption.
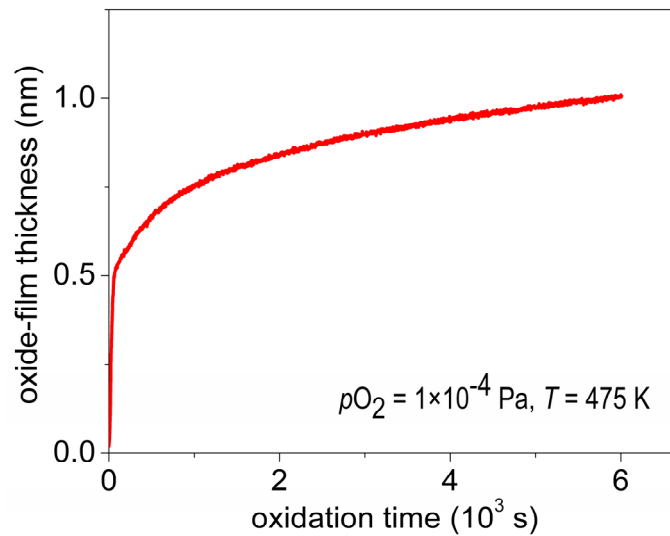
Fig. 1.2: The oxide-film growth curve for the oxidation of the sputter-cleaned Al - 0.8 at.% Mg substrate for 6×10^3 s at $T = 475$ K and at $pO_2 = 1\times10^{-4}$ Pa.

1.1.1   Technological background

The microstructure of the ultra-thin (thickness < 3 nm) oxide film present on the surface of a metal or an alloy decides many of its physical and chemical properties, such as corrosion resistance, adhesion, friction, electrical and thermal conductivity, dielectric capacity and optical appearance [2-10]. Therefore, optimization and control of the structure - property relationships of such oxide films and their associated metal/oxide interfaces are required in a vast array of technological applications, such as novel structural materials based on metal/ceramic composites, metal/oxide seals in medical implant construction, metal/oxide contacts in microelectronics and photovoltaic devices, corrosion-resistant coatings, gas-sensors and oxide-supported transition metal catalysts [11-23].

Functionalization and optimization of ultrathin-oxide-film-based technologies (see above) demand fundamental investigations of the microstructural evolution of ultra-thin oxide films as a function of their growth conditions and the type of metallic substrate. To this end, detailed knowledge of the effect of different pre-treatments of the parent metallic surface (prior to oxidation) on the developing oxide-film microstructure can be of crucial importance.

1.1.2   Scientific background

In recent years, the delicate interrelationships between the oxidation conditions, the oxide-film morphology, the oxide-film growth kinetics and the depth-resolved chemical state of the ions in oxide films, have been revealed for ultra-thin (< 3 nm), *single-metal* oxide overgrowths on surfaces of the same metal (e.g. Al, Zr, Fe, Ni, Cu and Mg) by using combinatorial experimental approaches of several (mostly surface-sensitive) analytical techniques, such as angle-resolved X-ray photoelectron spectroscopy (AR-XPS), real-time in-situ spectroscopic ellipsometry (RISE), low energy electron diffraction (LEED), Scanning Tunneling Microscopy (STM) and/or high-resolution transmission electron microscopy (HR-TEM) [3,24-31].

Such detailed combinatorial experimental studies on the microstructural evolution of *ultra-thin*, *multiple-metal* oxide films on *alloy* substrates have not been conducted up to date. Until now, investigations on the thermal oxidation of metallic alloys have been performed mainly at *high* temperatures (i.e. $T > 800$ K) and *high* pressures (i.e. $0.1 < p < 10^5$ Pa), where, relatively thick (in the micrometer range) oxide scales, composed of multiple, *crystalline* oxide phases, develop on the alloy surface by sequential, preferential oxidation of the alloy constituents [32-40]. The thermal oxidation of metallic alloys at *low* temperatures (say, at $T < 600$ K), has been investigated only scarcely up to date. At these temperatures, thermally activated diffusion of reactants through the developing oxide-film is negligibly small, which typically results in the formation of a thin oxide film of near-limiting thickness (< 10 nm) that is constituted of a metastable, multiple-metal oxide phase. The detailed *microstructure* (i.e. oxide phase constitution, chemical composition, morphology) and the *thickness* of such ultrathin, multiple-metal oxide films are still unknown. For example, for many alloy systems, it is still undetermined if the initial multiple-metal oxide film grown on its alloy surface is single-phase amorphous, single-phase crystalline (e.g. a spinel phase or a crystalline solid solution) or constituted

of several mixed crystalline and/or amorphous oxide phases. Evidently, the detailed microstructural characterization of multiple-metal oxide films is much more challenging than the analysis of single-metal oxide films, because more than one substrate constituent can be incorporated into the developing oxide film (e.g. a multiple-element (e.g. spinel) or multi-phase oxide film can be formed), which is associated with compositional changes occurring in the alloy subsurface during oxide growth. However, up to date, also no comprehensive knowledge exists on the combined effects of chemical segregation and preferential oxidation on the induced compositional changes in the alloy subsurface during the initial stages of oxide-film grown on alloy surfaces at low temperatures.

In particular, if more than one of the alloy constituents has a strong affinity towards oxygen, like in the Al-Mg system (in contrast to binary alloy systems such as Au-Cu, Ag-Cu or Pt-Al, where one constituent is nobler than the other), the interrelationships between the microstructural evolution of the growing oxide film, the oxidation-induced compositional changes in the parent alloy substrate and the oxidation conditions can be highly complicated [4]. Detailed fundamental investigations of the oxide growth kinetics and the developing oxide-film microstructure in such alloy systems therefore present a great scientific challenge. For example, according to bulk thermodynamics, exposure of a bare AlMg alloy surface to 1 mole of oxygen gas can result in one or a combination of the following oxide products:

$$Mg(s) + \tfrac{1}{2} \cdot O_2(g) \rightarrow \{MgO\} \tag{1.1a}$$

$$\tfrac{2}{3} \cdot Al(s) + \tfrac{1}{2} \cdot O_2(g) \rightarrow \tfrac{1}{3} \cdot \{Al_2O_3\} \tag{1.1b}$$

$$\tfrac{1}{4} \cdot Mg(s) + \tfrac{1}{2} \cdot Al(s) + \tfrac{1}{2} \cdot O_2(g) \rightarrow \tfrac{1}{4} \cdot \{MgAl_2O_4\} \tag{1.1c}$$
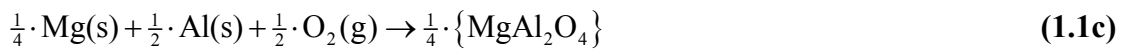
The very low mutual solubility of the competing crystalline MgO and Al_2O_3 oxide phases, as well as the small compositional range of $MgAl_2O_4$, is evidenced from the MgO - Al_2O_3 phase diagram in Fig. 1.3. If the crucial role of surface and interfacial energies on the microstructural evolution of ultra-thin oxide films is also accounted for in the thermodynamic description of the oxidation process [1], it becomes even more difficult to know beforehand which oxide phase represents the most stable (i.e. the thermodynamically preferred) initial oxide overgrowth on the AlMg alloy surface under particular oxidizing conditions.
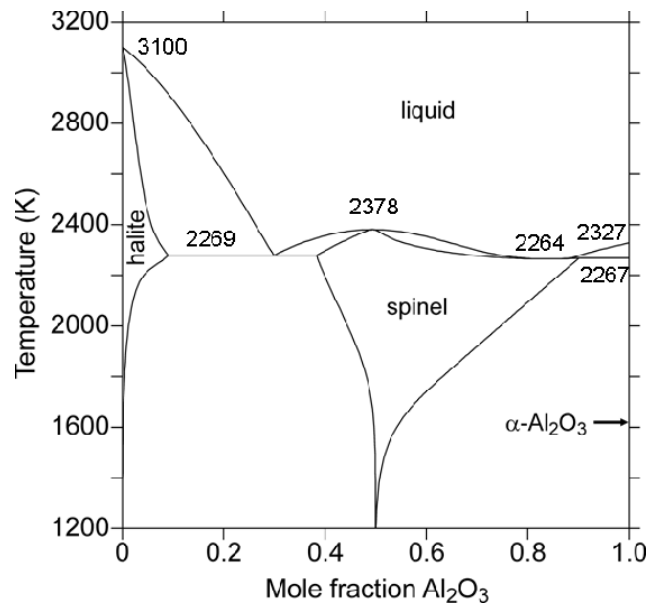
Fig. 1.3: The MgO (halite)-Al_2O_3 phase diagram as taken from Ref. [41].

1.2. Focus of this thesis

This PhD thesis addresses the initial stages of dry, thermal oxidation of bare Al-based Al-Mg alloys as a function of the growth conditions (e.g. oxidation temperature, time, partial oxygen pressure) for different in-vacuo pre-treatments of the alloy surface prior to oxidation. To this end, polycrystalline Al-Mg surfaces with nominal Mg alloying contents of 0.8 and 1.1 at. % were thermally oxidized in a dedicated UHV system (base pressure < 3.0×10^{-8} Pa) for specimen cleaning, annealing, oxidation and in-situ analysis. Two types of in-vacuo surface pre-treatments of the Al – 1.1 at. % Mg alloy surfaces were performed prior to a controlled oxidation step. As a first surface pre-treatment prior to oxidation, the native oxide and other contaminants on the alloy surface were removed by sputter-cleaning (SC) the entire alloy surface with 1 kV Ar^+ ions. As an alternative surface pre-treatment, the sputter-cleaned alloy surface was subjected to a short in-vacuo annealing step at 460 K prior to oxidation. Next, the thus obtained bare SC and pre-annealed alloy surfaces were exposed to $O_2(g)$ in the pressure range of $pO_2 = 1 \times 10^{-4}$ - 1×10^{-2} Pa for durations varying from 15 s up to 6 hrs and for various temperatures in the range of $T = 300 - 610$ K.

Real-time in-situ spectroscopic ellipsometry (RISE) was applied to investigate the initial oxide-film growth kinetics in dependence of the surface pre-treatment and the

oxidation temperature. The depth-resolved chemical constitution of the grown oxide films, as well as the local chemical states of the alloy constitutents (i.e., Al and Mg) in the oxide film and in the alloy subsurface, were established by in-situ AR-XPS. Furthermore, the microstructures of some of the grown oxide films were analyzed on an atomic scale by cross-sectional HR-TEM. Pronounced differences in the oxide-film growth kinetics and the developing oxide-film microstructure as a function of the oxidation temperature for the two pre-treated alloy surfaces are revealed and discussed.

Also thermodynamic model calculations were performed to predict which type of amorphous oxide overgrowth (i.e., am-Al_2O_3, am-MgO and am-$MgAl_2O_4$) is most stable on the bare AlMg alloy surfaces as a function of the alloying content at the alloy/oxide interface, the growth temperature and the oxide-film thickness. In these model calculations, the crucial role of surface and interfacial energies on the microstructural evolution of the ultra-thin oxide films has been accounted for. On the basis of the macroscopic atom approach, expressions have been derived for the estimation of the energies of the interfaces between the AlMg substrate and the competing am-Al_2O_3, am-MgO and am-$MgAl_2O_4$ overgrowths. The thus obtained model predictions on the thermodynamically preferred microstructural evolution of the initial oxide overgrowth on bare AlMg alloy substrate are compared with corresponding experimental data obtained by AR-XPS and HR-TEM.

1.3. The initial oxidation of Al-Mg alloys

Al and Mg both fall in the category of lights metals and therefore find numerous technological applications in areas where weight reduction is a major concern (i.e., in automotive and aerospace industries). The solubility of Mg in Al metal at 100°C is only about 1 at.% (see Fig. 1.4). Commercially-applied Al-based Al-Mg alloys typically have a nominal Mg alloying content in the range of 0.5 to 12 at.%. A lower Mg alloying content enhances the alloy's formability, which is important for use in e.g. exterior and interior trim parts of the automobiles, refrigerators, automobile gas and oil lines. Higher Mg alloying contents generally lead to an improvement of the castability, strength and wet-corrosion resistance, thereby finding applications in dairy and food handling, cooking utensils, fittings for chemical and sewage use, pressure vessels and marine uses [43-46].
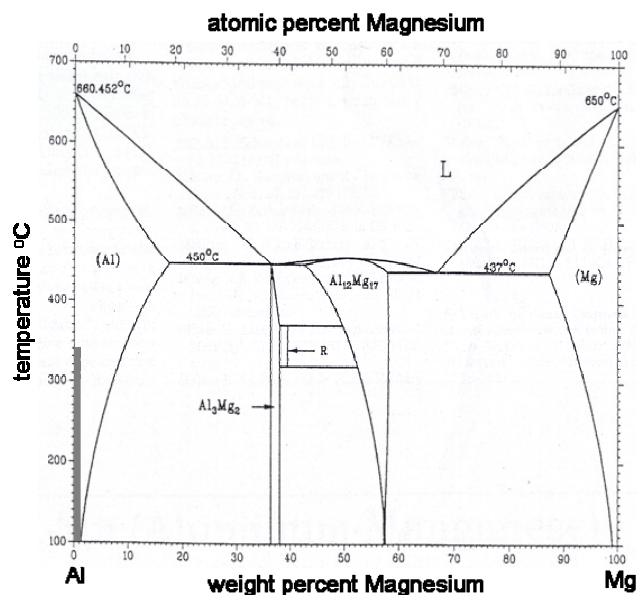
Fig. 1.4: The Al-Mg phase diagram [42]. The compositional range of Al-based AlMg alloys, as well as the oxidation temperature range, considered in the present study is indicated by the grey area. In the present work, oxidation has been carried out in the temperature (T) range of 300 – 610 K on Al-0.8 at.% Mg and Al-1.1 at.% Mg alloy surfaces.

In recent years, many important thermodynamic and kinetic aspects of ultra-thin single-metal oxide overgrowths on their pure metal substrates, such as e.g. the amorphous-to-crystalline transition beyond a critical oxide-film thickness and the governing mechanism(s) and driving forces for the oxide-film growth, have been revealed in great detail by using a combinatorial experimental approach of RISE, AR-XPS, LEED and/or HR-TEM [24-26]. On the contrary, the microstructural evolution of ultra-thin, multiple-metal oxide films on bare alloy substrates has only scarcely been investigated up to date [4,47-49]. Earlier works on the oxidation of AlMg alloy surfaces were mostly conducted towards higher temperatures under atmospheric conditions with a native Al-oxide film on the alloy surface at the onset of oxidation [32-38]. In only a few investigations, the oxide films were grown under controlled conditions at room temperature in an ultra high vacuum environment (as studied by e.g. Auger electron spectroscopy [50,51]), but without providing a detailed, quantitative analysis of the depth-dependent oxide-film microstructure as a function of growth conditions.

The pre-treatment of the surface of an alloy component is a commonly employed processing step in industry to optimize the parent substrate properties in terms of its e.g. wettability, friction, adhesion and/or corrosion resistance [52-55]. Such surface pre-

treatments can be classified into three distinct categories, i.e., mechanical, chemical and electrochemical surface pre-treatments. Processing steps, such as sandblasting, mechanical abrasion, machining the solid surface, liquid and vapour degreasing, corona discharge treatment and plasma spray coating, fall in the category of mechanical surface pre-treatments. Similarly, pre-oxidation and etches with chromic acid, hydrochloric acid, hydrofluoric acid, sodium hydroxide and alkaline hydrogen peroxide are typical examples of chemical surface pre-treatments. Further, chromic acid based anodize, sodium hydroxide anodize, sulfuric acid anodize and alkaline hydrogen peroxide anodize fall in the category of electrochemical surface pre-treatments [54,55].

Various surface pre-treatments of metals and alloys and the thereby modified physico-chemical surface characteristics have been reviewed in the literature [54,55]. However, the effect of *in-vacuo* surface pre-treatment of alloy surfaces on the microstructure of the initial oxide overgrowth has only very scarcely studied up to date [56]. A pronounced effect of the type of in-vacuo surface pre-treatments of AlMg alloy surfaces on the microstructure of the initial oxide overgrowth is reported in Chapter 4 of this thesis.

Although many experimental and theoretical investigations of solid-solid metallic/ceramic interfaces have been reported in the literature, most of these studies have focused on epitaxial interfaces between pure *metals* and their *crystalline* oxides (cf. Refs. [11-14,57-59] and the references therein). Investigations on epitaxial interfaces between *alloys* and their *crystalline* oxides have been reported only very scarcely up to date [see Refs. [4,14,60] and references therein]. Indeed, due to the preferential oxidation of one of the alloy constituents and the competing segregation of one of the bulk alloying constituents (and/or bulk impurities) from the interior of the alloy towards the alloy/oxide interface [4,60], the local chemistries and microstructures of alloy/oxide interfaces are much more complex than those of the corresponding metal/oxide interfaces. No literature studies have been found to be reported yet on the energetics and microstructures of the interfaces between *alloys* and *amorphous* oxides, although it has been recently demonstrated that ultra-thin (< 3 nm) amorphous oxide films on metallic substrates can be thermodynamically stable (as compared to their corresponding crystalline oxide films on the same metallic substrate) by their relatively low surface and interface energies [1,61].

Fig. 1.5: Interface energies $\gamma_{\langle AlMg\rangle-\{MgO\}}$, $\gamma_{\langle AlMg\rangle-\{Al_2O_3\}}$ and $\gamma_{\langle AlMg\rangle-\{MgAl_2O_4\}}$ for the amorphous oxide overgrowths $\{MgO\}$, $\{Al_2O_3\}$ and $\{MgAl_2O_4\}$ on the most densely packed surface of the $\langle AlMg\rangle$ substrate (i.e. $\langle AlMg\{111\}\rangle$ for $0 \le x^i_{Mg} \le 0.5$ and $\langle AlMg\{0001\}\rangle$ for $0.5 \le x^i_{Mg} \le 1.0$; see Chapter 2) as function of the Mg alloying content of the substrate at the alloy/oxide interface (x^i_{Mg}) at growth temperature of $T = 300$ K.

As evidenced by thermodynamic calculations (see Chapter 2) and experimental observations by AR-XPS and HR-TEM (see Chapters 3-6), for the growth of ultrathin oxide-films on Al-Mg alloy surfaces at low temperatures (of, say, $T \le 425$ K), *amorphous* Al_2O_3 is the most stable amorphous oxide overgrowth. The relatively high stability of ultrathin am-Al_2O_3 films on the Al-Mg substrates is due to the relatively low energy of the interface between am-Al_2O_3 and the Al-Mg alloy (see Fig. 1.5). As a result, for the formation of a multi-component, amorphous oxide film on Al-Mg substrates, interface thermodynamics favors phase separation of Al_2O_3 and MgO such that Al_2O_3 occurs at the interface and MgO occurs at the surface. This is in accordance with the experimental observations (see Chapters 2 and 4). The model predictions and experimental observations also reveal a strong driving force for the Gibbsian segregation of Mg from the interior of the alloy to the concerned alloy/oxide interface. With increasing oxide-film thickness and increasing Mg content of the oxide-film, crystalline MgO becomes thermodynamically preferred. The gradual development of long range order in the

initially amorphous (Al,Mg)-oxide overgrowths sets in for thickening oxide films grown at $T \geq 475$ K (see Chapter 6).

1.4.   Experimental approach

A comprehensive characterization of the growth kinetics and microstructural evolution of ultra-thin oxide overgrowths on bare AlMg alloy substrates requires a combinatorial experimental approach of various *in-situ*, surface-sensitive, preferably non-destructive analytical techniques. In the present work, a combinatorial experimental approach of in-situ RISE, in-situ AR-XPS and ex-situ HR-TEM have been used to characterize the ultrathin oxide films (with thickness of, typically, < 3 nm) as grown on the pre-treated Al-Mg alloy surfaces by thermal oxidation. A photograph of the dedicated, custom-designed ultra high vacuum (UHV) system for specimen cleaning, annealing, oxidation, and in-situ RISE and AR-XPS analysis, as applied in this work, is shown in Fig. 1.6. The UHV system is also equipped with a UHV side-chamber for in-vacuo thin-film deposition by Molecular beam Epitaxy (MBE), as applied in this study to deposit an Al capping layer on the oxidized alloy surfaces before their exposure to the ambient for subsequent *ex-situ* HR-TEM analysis. An optical micrograph of the surface of an as-prepared AlMg alloy specimen (prior to its introduction into the UHV system) is shown in Fig. 1.7.
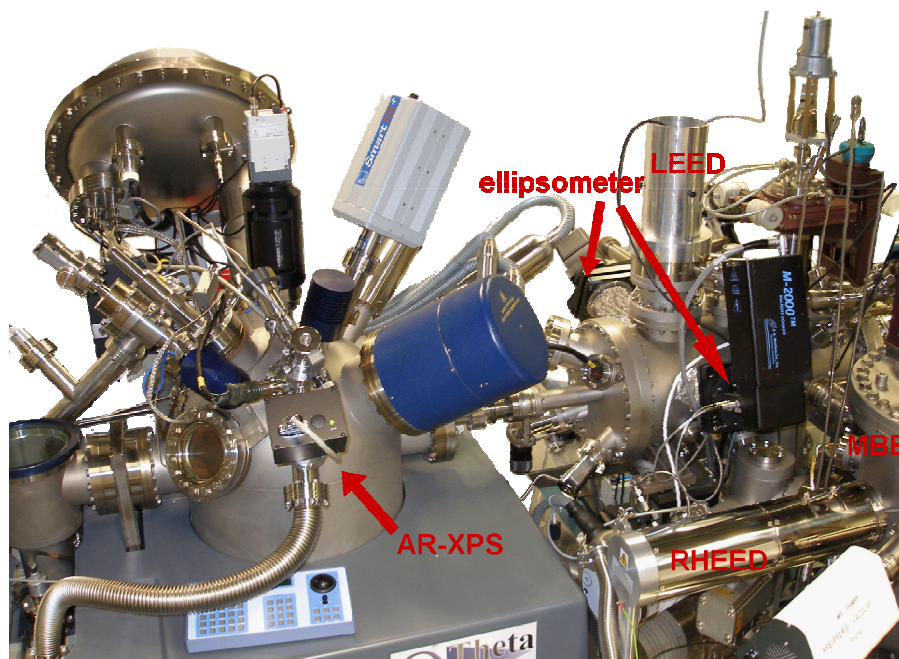
Fig. 1.6: Overview of the dedicated, custom-designed UHV system for specimen cleaning, annealing, oxidation and in-situ analysis by AR-XPS and RISE. The UHV side-chamber for thin-film deposition by MBE is partially visible in the lower-right corner.
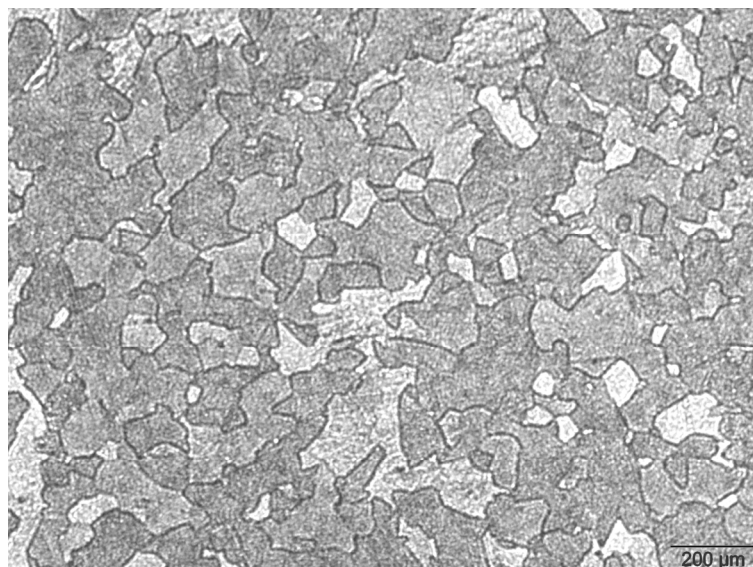
Fig. 1.7: Light optical micrograph of an etched (50ml of distilled water, 30 ml of HCL, 10 ml of HNO_3 and 10 ml of HF) surface of an as-prepared polycrystalline Al – 1.1 at.% Mg after mechanical preparation (casting, annealing and polishing; see Chapter 3. The alloy specimen has an average grain size in the range of 50-100 μm.

1.4.1   Angle-resolved X-ray Photoelectron Spectroscopy (AR-XPS)

XPS measures the kinetic energy of photoelectrons emitted from a solid upon its irradiation with photons (i.e., employing the photoelectric effect). The basic equation of XPS is expressed as:

$$E_k = h\nu - E_B \qquad\qquad\qquad (1.2)$$

where, E_k is the kinetic energy of the detected photoelectrons, $h\nu$ is the incident photon energy and E_B is the electron binding energy.

The measured energy spectra (i.e., electron intensity versus binding energy; BE) provide information on the chemical environment of the detected elements in the surface region, as well as on the overall surface composition of the investigated material. The information depth of the AR-XPS analysis equals $3\lambda \times \cos\alpha$, where λ denotes the effective attenuation length (EAL) of the detected Al 2p or Mg 2p photoelectrons in the solid (α is the photoelectron detection angle with respect to the surface normal). Employing incident Al Kα X-ray irradiation (as in the present study), the EAL of Al 2p or Mg 2p photoelectrons emitted from the Al-Mg substrate is about $\lambda \approx 3$ nm, which results in an information depth of the AR-XPS analysis in the range of 2.4 - 8.4 nm for photoelectron detection angles in the range of 83º - 23º (as employed in this study, where $\alpha = 23°$ and $\alpha = 83°$ correspond to more near-normal and more grazing detection angles, respectively). Thus, chemical information from the subsurface region (i.e., ~ 7 nm) and the outer-surface (i.e., ~ 1 nm) of a solid are obtained through a variation of the photoelectron detection angle in the AR-XPS analysis [62].

The state-of-the-art AR-XPS equipment as employed in the present investigation employs a so-called parallel-detection mode by simultaneous recording of the emitted photoelectrons over the angular detection range of $(\alpha, \phi) = (23°, 43°)$ to $(\alpha, \phi) = (83°, 94°)$ in six ranges of 10° each (for details, see Ref. [63]). The interdependent angles α and ϕ are defined as the angles between the directions of the detected photoelectrons and the sample surface normal and the directions of the detected photoelectrons and the incident photon beam, respectively.

Figs. 1.8(a-d) show a spectral reconstruction of Al 2p and Mg 2p XPS spectra, as recorded at a detection angle set of $(\alpha, \psi) = (38°, 54.75°)$ from an oxidized Al-Mg alloy

surface (oxidations for 130 s and 6000 s at $T = 560$ K and $pO_2 = 1 \times 10^{-2}$ Pa). It follows that both Al and Mg are incorporated in the grown oxide film. Furthermore, a different chemical state is detected for the Mg cations at the alloy/oxide interface as compared to their chemical state in the interior of the oxide film (Fig. 1.8b).

The accurate quantification of the recorded AR-XPS spectra in terms of e.g. the thickness and the depth-resolved chemical constitution of the grown oxide films, requires practically and generally applicable quantitative procedures, which account for the dependencies of the resolved photoelectron intensities and their associated inelastic background on the angular detection angle. To this end, pre-existing knowledge and/or reasonable estimates of e.g. the intrinsic plasmon excitation probabilities in the alloy, the oxide-film density and/or the effective attenuation lengths of the corresponding detected photoelectrons in the oxide film are required [47]. The details on the developed procedures for spectral reconstruction and quantification are provided in Chapter 3.
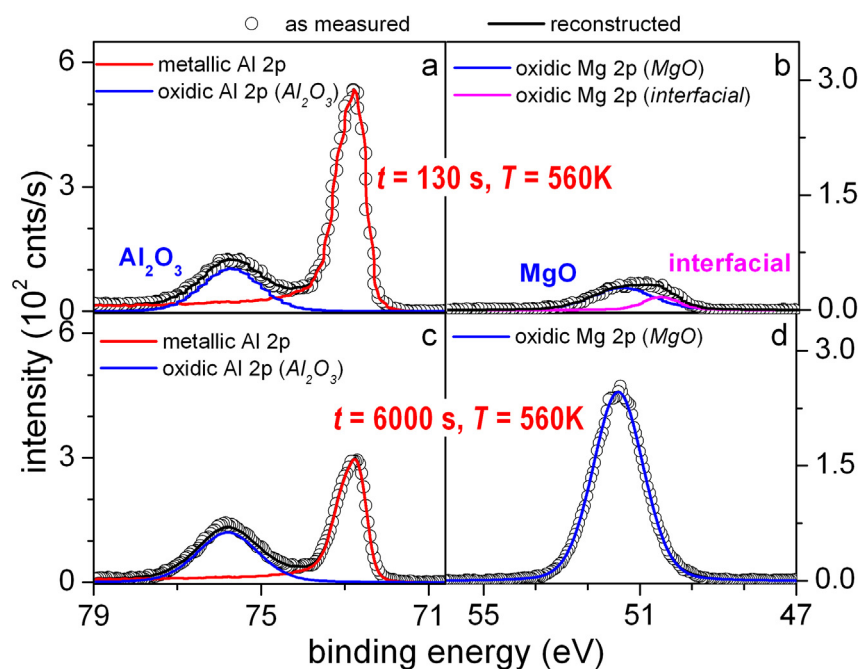
Fig. 1.8: Reconstruction of the as-measured Al 2p and Mg 2p spectra, as recorded from Al-0.8 at.% Mg substrate oxidized at $T = 560$ K and at $pO_2 = 1 \times 10^{-2}$ Pa for (a,b) $t = 130$ s and (c,d) $t = 6000$ s. The spectra were recorded at a detection angle set of $(\alpha, \psi) = (38^{\circ}, 54.75^{\circ})$.

1.4.2   *Real-time in-situ Spectroscopic Ellipsometry (RISE)*

Ellipsometry is a non-destructive, optical technique, which is based on the measurement of the variations in the polarization state of light reflected from a surface upon its interaction with a solid surface. The amount of ellipticity induced in the reflected polarized light depends on the optical properties of the substrate and the overlying film and the film thickness [48,64].
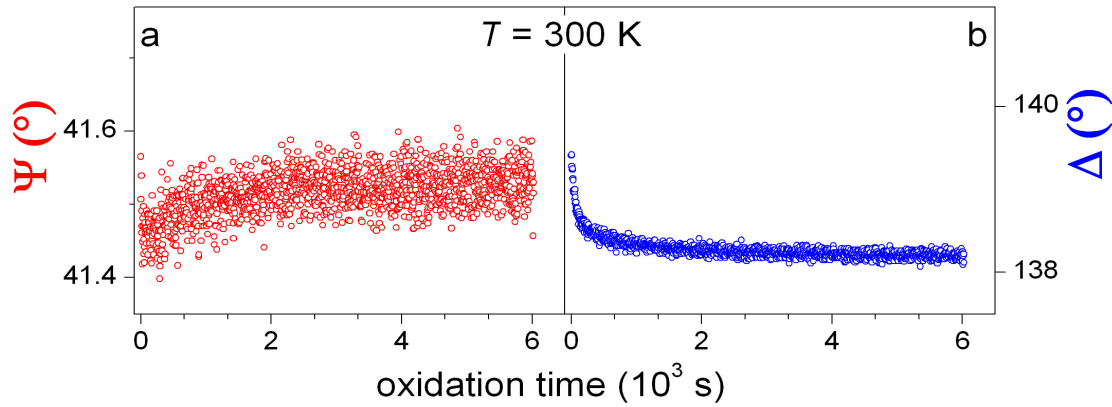
Fig. 1.9: As-measured (by RISE) values of (a) ψ and (b) Δ at a wavelength of $\lambda = 589$ nm as function of oxidation time for the oxidation of a bare (i.e. sputter-cleaned) Al-1.1 at.% Mg substrate for 6×10^3 s at *T* = 300 K and at $pO_2 = 1 \times 10^{-4}$ Pa. The wavelength of $\lambda = 589$ nm is at about the centre of the wavelength range from 350 nm to 800 nm. See Chapter 3 for details.

In the present study the changes in the ellipsometric phase shift and amplitude ratio dependent parameters Δ and ψ were recorded simultaneously over the wavelength range from $\lambda = 350 - 850$ nm (in intervals of ~ 0.8 nm) during oxidation of the bare Al-based AlMg alloy substrates in the combined UHV system with a time step of about 1.4 s. The elliptically-shaped analysis area of the real-time *in-situ* spectroscopic ellipsometric (RISE) measurements equals 2×8 mm^2 area. Typical as-measured courses of ψ and Δ as a function of oxidation time (*t*, up to 6000 s) at an exemplary wavelength of $\lambda = 589$ nm for the oxidation of the bare Al - 1.1 at.% Mg substrate at *T* = 300 K and at $pO_2 = 1 \times 10^{-4}$ Pa are given in Fig. 1.9. As evidenced from the quantification of the recorded RISE data (see Chapter 3), a total decrease in Δ (i.e., $\delta\Delta$) of 1° upon oxidation of the *bare* AlMg substrate corresponds to an oxide-film thickness increase of about 0.56 nm [48,64]. On the other hand, ψ provides valuable information on the concurrent processes of oxygen

incorporation and chemisorption during the initial stages of interaction of the oxygen gas with the bare alloy surface [26,48]: more details are provided in Chapter 3.

1.4.3   High-resolution Transmission Electron Microscopy (HR-TEM)

The principle of HR-TEM relies on two consecutive processes occurring upon irradiation of a thin-foil (electron-transparent) specimen with a high-energetic electron beam. In the first process, the incident electrons are scattered by the specimen (the so called dynamical diffraction), while in the second process, the scattered electrons are refracted by an electron lens to form an image [65]. The quality of the image depends on the imaging conditions. For example, thicker (> 100 nm) specimens induce larger contrast-losses of electrons due to inelastic scattering. Similarly, due to the effect of lens aberration, as well as a degradation of interference among electrons in the second process, the image contrast may contain some optical artifacts. A careful consideration in these imaging conditions may provide an accurate picture of the 'true' atomic arrangement in the specimen. Along with the atomic arrangement of the specimen, many kinds of lattice defects present in the investigated region of the real crystal (e.g., vacancies, dislocations, stacking faults, twins, grain boundaries etc.) can be accurately analyzed using HR-TEM.

In the present study, cross-sectional HR-TEM analysis of several oxidized alloy surfaces has been performed to determine the microstructures of the oxide film and its interface with the parent alloy substrate. For the overgrowth of crystalline oxide films at high temperatures and towards higher thicknesses, the type of crystalline oxide overgrowth (i.e., either a γ-Al_2O_3 or a MgO) along with its orientation-relationship with respect to that of the substrate have been revealed (see Chapter 6 for details). For the *ex-situ* analysis of the oxide overgrowths by HR-TEM, the *in-situ* grown oxide films were sealed with ~ 150 nm Al capping layer in molecular beam epitaxy (MBE) before taking them out of the UHV system. Subsequently, a very thin cross-sectional TEM lamella (thickness: 80 – 100 nm; size 3 μm × 4 μm) was cut using a dual focused ion beam (FIB). Subsequent HR-TEM analysis was carried out with a JEOL JEM-ARM1250 electron microscope (acceleration voltage of 1250 kV) at (one of the grains of the) substrate|oxide-film|Al-seal TEM cross-section. During the HR-TEM analysis, the TEM lamella (holder) was cooled with liquid nitrogen to prevent the occurrence of any microstructural modifications in the irradiated area of the specimen due to the high-energy electron beam

[25]. A thus-obtained cross-sectional HR-TEM image of an oxide film grown on an Al -

0.8 at.% Mg substrate by thermal oxidation for 6×10^3 s at $T = 600$ K is shown in Fig. 1.10.
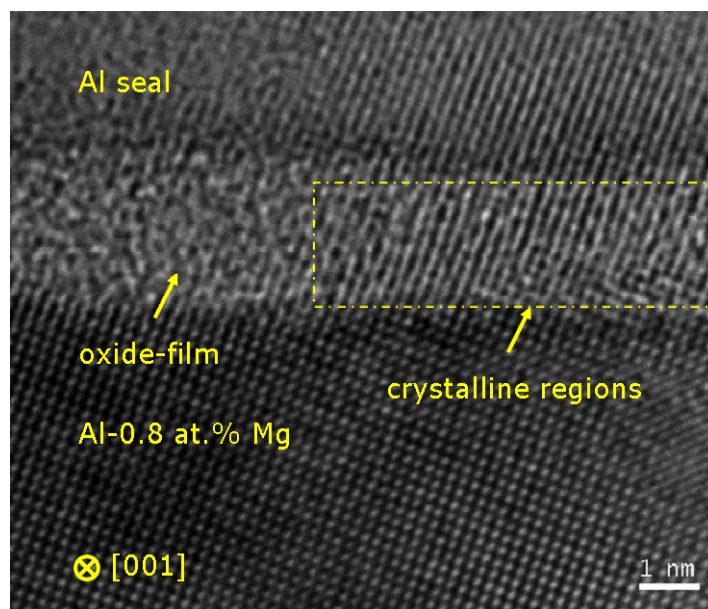
Fig. 1.10. Cross-sectional high resolution transmission electron micrograph of the oxide film (in the local chemical environments of Al_2O_3 and MgO; as detected by AR-XPS) formed on the sputter-cleaned surface of an Al - 0.8 at.% Mg substrate by thermal oxidation for $t = 6 \times 10^3$ s at $T = 600$ K and $pO_2 = 1 \times 10^{-2}$ Pa (and subsequent in-situ deposition of a MBE-grown Al seal). The direction of the primary electron beam was along the zone axis [001] of the Al-0.8 at.% Mg substrate.

1.5.   Outline of the thesis

In Chapter 2, a thermodynamic model is presented to predict the type of initial, amorphous oxide overgrowth (i.e., *am*-Al_2O_3, *am*-MgO or *am*-$MgAl_2O_4$) on a bare AlMg substrate as a function of the Mg alloying element content at the substrate/oxide interface, the growth temperature and the oxide-film thickness (up to 5 nm). To this end, expressions for the estimation of the energies of the interfaces between the AlMg substrate and the competing *am*-Al_2O_3, *am*-MgO and *am*-$MgAl_2O_4$ overgrowths have been derived on the basis of the macroscopic atom approach. The thus-obtained model predictions were compared with experimental results.

Chapter 3 presents the procedures for evaluation and quantification of the measured AR-XPS and RISE data, as recorded from the oxidized AlMg alloy substrates. As a result, the relationships between the relative depth distributions of Al and Mg in the

developing oxide films, the oxide-film growth kinetics and the oxidation-induced compositional changes in the AlMg alloy substrate could be established as function of the oxidation conditions.

In Chapter 4, the effect of substrate surface pre-treatment and oxidation temperature on the growth kinetics and chemical constitution of ultra-thin (< 3 nm) oxide films grown on bare Al − 1.1 at.% Mg alloy surfaces was studied by a combined experimental approach of real-time in situ spectroscopic ellipsometry (RISE) and angle-resolved X-ray photoelectron spectroscopy (AR-XPS). It follows that, as long as the chemical segregation of Mg from the alloy's interior to the alloy/oxide interface is kinetically hindered, the oxide-film growth kinetics, the developing oxide-film microstructure, as well as the local chemical states of the Al and Mg cations in the oxide, exhibit a strong dependence on the alloy surface pre-treatment.

In Chapter 5, the interrelationships between the oxidation temperature, the oxide-film growth kinetics and the developing oxide-film microstructure are revealed and discussed for the thermal oxidation of the sputter-cleaned Al-Mg alloy substrates in the temperature range of T = 300 - 610 K. It follows that, depending on the oxide growth conditions, a single or a combination of different chemical states occurs for the Al and Mg cations incorporated in the grown oxide films.

Finally, the gradual amorphous-to-crystalline transition in the grown (Al,Mg)-oxide films with increasing thickness was investigated by HR-TEM in Chapter 6. It is shown that the amorphous-to-crystalline transition proceeds by a phase separation: still predominantly amorphous oxide regions next to crystallized oxide regions constituted of an MgO-type of oxide phase with a fcc oxygen sublattice.

References

[1]   F. Reichel, L. P. H Jeurgens and E. J. Mittemeijer, Acta Mat. **56** (2008) 659.

[2]   P. Nolte, A. Stierle, N. Y. Jin-Phillipp, N. Kasper, T. U. Schulli and H. Dosch, Science **321** (2008) 1654.

[3]   A. Lyapin, L.P.H. Jeurgens, P.C.J. Graat and E.J. Mittemeijer, J. Appl. Phys. **96** (2004) 7126.

[4]   L. P. H. Jeurgens, M. S. Vinodh and E. J. Mittemeijer, Acta Mat. **56** (2008) 4621.

[5]   A. Pasquarello and A. M. Stoneham, J. Physics: Condensed Matter **17** (2005) V1.

[6]   H.-J. Freund, Surf. Sci. **601** (2007) 1438.

[7]   M. Koyama, Y. Kamimuta, M. Koike, M. Suzuki and A. Nishiyama, Jap. J. Appl. Phys. **43** (2004) 1788.

[8]   Z. R. Dai, Z. W. Pan and Z. L. Wang, Adv. Funct. Mater. **13** (2003) 9.

[9]   E. Comini, G. Faglia, G. Sberveglieri, Z. Pan and Z. L. Wang, Appl. Phys. Lett. **81** (2002) 1869.

[10]   A. Gupta, X. W. Li and G. Xiao, Appl. Phys. Lett. **78** (2001) 1894.

[11]   J. G. Li, Mater. Chem. Phys. **47** (1997) 126.

[12]   C. T. Campbell, Surf. Sci. Rep. **27** (1997) 1.

[13]   F. S. Ohuchi and M. Kohyama, J. Am. Ceram. Soc. **74** (1991) 1163.

[14]   S. B. Sinnott and E. C. Dickey, Mater. Sci. Eng. R **43** (2003) 1.

[15]   E. Pagounis, M. Talvitie and V. K. Lindroos, Comp. Sci. and Tech. **56** (1996) 1329.

[16]   V. Da Costa, C. Tiusan, T. Dimopoulos and K. Ounadjela, Phy. Rev. Lett. **85** (2000) 876.

[17]   G. Hu and Y. Suzuki, Phy. Rev. Lett. **89** (2002) 4.

[18]   A. Atkinson, Rev. Mod. Phys. **57** (1985) 437.

[19]   L. P. H. Jeurgens, W. G. Sloof, F. D. Tichelaar and E. J. Mittemeijer, J. Appl. Phys. **92** (2002) 1649.

[20]   E. Comini, G. Faglia, G. Sberveglieri, Z. W. Pan and Z. L. Wang, Appl. Phys. Lett. **81** (2002) 1869.

[21]   Z. R. Dai, Z. W. Pan and Z. L. Wang, Adv. Funct. Mat. **13** (2003) 9.

[22]   J. Gustafson, R. Westerstroem, A. Mikkelsen, X. Torrelles, O. Balmes, N. Bovet, J. N. Andersen, C. J. Baddeley and E. Lundgren, Phys. Rev. B **78** (2008) 6.

[23]   C. R. Henry, Surf. Sci. Rep. **31** (1998) 235.

[24] F. Reichel, L. P. H Jeurgens, G. Richter and E. J. Mittemeijer, J. Appl. Phys. **103** (2008) 093515.

[25] F. Reichel, L. P. H Jeurgens, G. Richter, P. A. van Aken and E. J. Mittemeijer, Acta Mater. **55** (2007) 6027.

[26] F. Reichel, L. P. H. Jeurgens and E. J. Mittemeijer, Acta Mat. **56** (2008) 2897.

[27] A. Lyapin, L. P. H. Jeurgens and E.J. Mittemeijer, Acta Mat. **53** (2005) 2925.

[28] M. Kurth, P. C. J. Graat and E.J. Mittemeijer, Thin Solid Films **500** (2006) 61.

[29] F. Wiame, V. Maurice and P. Marcus, Surf. Sci. **601** (2007) 1193.

[30] P. C. J. Graat, M. A. J. Somers and E. J. Mittemeijer, Thin Solid Films **340** (1999) 87.

[31] P. C. J. Graat, M. A. J. Somers, Surf. Interface Anal. **26** (1998) 773.

[32] G. R. Wakefield and R. M. Sharp, Appl. Surf. Sci. **51** (1991) 95.

[33] D. H. Kim, E. P. Yoon and J. S. Kim, J. Mat. Sc. Lett. **15** (1996) 1429.

[34] K. Shimizu, G. M. Brown, K. Kobayashi, P. Skeldon, G. E. Thompson and G. C. Wood, Corr. Sci. **40** (1998) 557.

[35] K. J. Holub and L. J. Matienzo, Appl. Surf. Sci. **9** (1981) 22.

[36] W. W. Smeltzer, J. Electrochem. Soc. **105** (1958) 67.

[37] C. Lea and J. Ball, Appl. Surf. Sci. **17** (1984) 344.

[38] I. M. Ritchie, J. V. Sanders and P. L. Weickhardt, Oxidation of Metals **3** (1971) 91.

[39] N. Hussain, K. A. Shahid, I. H. Khan and S. Rahman, Oxidation of Metals **43** (1995) 363.

[40] R. Wang, M. J. Straszheim and R. A. Rapp, **21** (1984) 71.

[41] B. Hallstedt, J. Am. Ceram. Soc. **75** (1992) 1497.

[42] J. L. Murray, Bull. Alloy Phase Diag. **3** (1982) 60.

[43] L. F. Mondolfo, Aluminum Alloys: Structure and Properties, Butterworths, London (1976).

[44] E. Brillas, P. L. Cabot, F. Centellas, J. A. Garrido, E. Perez and R. M. Rodriguez, *Electrochimica Acta*; **43** (1998) 799.

[45] Metals Handbook. Properties and Selection of Metals, 8th edn., Americal Society for Metals, Ohio (1961) 1.

[46] G.L. Song and A. Atrens, Adv. Eng. Mat. **1** (1999) 11.

[47] L. P. H. Jeurgens, M. S. Vinodh, and E. J. Mittemeijer, Appl. Surf. Sci. **253** (2006) 627.

[48] M. S. Vinodh, L. P. H. Jeurgens, and E. J. Mittemeijer, J. Appl. Phys. **100** (2006) 044903.

[49] G. −W. Zhou, J. A. Eastman, R. C. Birtcher, P. M. Baldo, J. E. Pearson, L. J. Thompson, L. Wang and J. C. Yang, J. Appl. Phys. **101** (2007) 033521.

[50] F. J. Esposto, C. S. Zhang, P. R. Norton and R. S. Timsit, Surf. Sci. **302** (1994) 109.

[51] J. Bloch, D.J. Bottomley, J.G. Mihaychuk, H. M. van Driel and R.S. Timsit, Surf. Sci. **322** (1995) 168.

[52] J. Kim, M. Teo, P. C. Wong, K. C. Wong and K. A. R. Mitchell, Appl. Surf. Sci. **252** (2005) 1305.

[53] V. V. Belloncle, M. Rousseau and N. Terrien, NDT&E Int. **40** (2007) 419.

[54] G. W. Critchlow and D. M. Brewis, Int. J. Adhesion and Adhesives. **16** (1996) 255.

[55] G. W. Critchlow and D. M. Brewis, Int. J. Adhesion and Adhesives. **15** (1995) 161.

[56] T. Nijdam, L. P. H. Jeurgens, J. Chen and W. G. Sloof, Oxidation of Metals **64** (2005) 355.

[57] F. Reichel, L.P.H Jeurgens and E.J. Mittemeijer, Phys. Rev. B **74** (2006) 144103.

[58] M. W. Finnis, J Phys Cond Mat **8** (1996) 5811.

[59] M. Rühle, J Europ Ceram Soc **16** (1996) 353.

[60] I. J. Bennett, J. M. Kranenburg and W. G. Sloof, J. Am. Ceram. Soc. **88** (2005) 2209.

[61] L. P. H. Jeurgens, W. G. Sloof, F. D. Tichelaar and E. J. Mittemeijer, Phys. Rev. B **62** (2000) 4707.

[62] D. Briggs and M.P. Seah (ed.), Practical Surface Analysis by Auger and X-ray Photoelectron Spectroscopy (John Wiley & Sons, Volume 1, 1983).

[63] M. S. Vinodh and L. P. H. Jeurgens, Surf. Interface Anal. **36** (2004) 1629.

[64] R. M. A. Azzam and N. M. Bashara, Ellipsometry and Polarized Light (North-Holland, Amsterdam, 1987).

[65] S. Horiuchi, Fundamentals of High-Resolution Transmission Electron Microscopy (North-Holland, Amsterdam, 1994).

2. Interface thermodynamics of ultrathin, amorphous oxide overgrowths on AlMg alloys

E. Panda, L. P. H. Jeurgens and E. J. Mittemeijer

Abstract

A thermodynamic model has been presented for the prediction of the type of initial, amorphous oxide overgrowth (i.e., *am*-Al$_2$O$_3$, *am*-MgO or *am*-MgAl$_2$O$_4$) on bare AlMg substrates as function of the Mg alloying element content at the substrate/oxide interface, the growth temperature and the oxide-film thickness (up to 5 nm). On the basis of the macroscopic atom approach, expressions have been derived for the estimation of the energies of the interfaces between the AlMg substrate and the competing *am*-Al$_2$O$_3$, *am*-MgO and *am*-MgAl$_2$O$_4$ overgrowths. For all cases a strong driving force has been revealed for the interfacial (chemical) segregation of Mg. It has been found that *am*-Al$_2$O$_3$ is the most stable amorphous oxide phase on the AlMg substrate for $T < 610$ K; its relatively high stability is governed by a relatively low interface energy. The model predictions are in good agreement with corresponding experimental results on the chemical constitution of ultrathin amorphous oxide films grown on Al- and Mg-based alloy substrates in the temperature range of $300 - 400$ K.

2.1. Introduction

The interface (energy) of a metal or metallic alloy substrate and its ultrathin (< 5 nm) oxide overgrowth controls properties such as its wettability, adhesion of the oxide film and friction, electrical conductivity and optical appearance of the metal/oxide assembly. Therefore, fundamental knowledge and optimization of the structure - property relationships of such metal/oxide interfaces is of paramount importance for a vast array of technological applications, such as metal/oxide contacts in microelectronics and photovoltaic devices, corrosion-resistant coatings, gas-sensors and oxide-supported transition metal catalysts, and for the development of novel structural materials based on metal/ceramic composites, and metal/oxide seals in medical implant construction [1-4].

Substantial experimental and theoretical investigation of solid-solid metallic/ceramic interfaces has been reported in the literature, but most of these studies have focused on epitaxial interfaces between single-element *metals* and their *crystalline* oxides (cf. Refs. [1-7] and the references therein). Investigations on epitaxial interfaces between metallic *alloys* and their *crystalline* oxides have been scarce up to date [see Refs. [4,8,9] and references therein]. Indeed, the local chemistries and microstructures of alloy/oxide interfaces are much more complex than those of the corresponding single metal/oxide interfaces. For example, chemical and/or stress-induced segregation of one of the bulk alloying constituents (or bulk impurities) may occur from the interior of the alloy substrate towards the alloy/oxide interface, thereby drastically affecting the interface properties [8,9]. Compositional changes in the alloy subsurface region can also be induced by the preferential oxidation of one of the alloy constituents during oxidation [9,10]. Consequently the resulting oxide film is not necessarily composed of a single-metal oxide phase, but can contain a mixture of several single-metal oxide phases or be comprised of a multi-metal oxide phase (e.g., a spinel phase) [9,10].

To our knowledge, no studies have been reported yet on the energetics and microstructures of the interfaces between metallic *alloys* and their *amorphous* oxides. Such work is the more relevant because it has been demonstrated recently that ultra-thin (< 3 nm) *amorphous* oxide films on metallic substrates can be thermodynamically stable (as compared to their corresponding *crystalline* oxide films on the same metallic substrate) because of their relatively low surface and interface energies [11,12]. Only beyond a certain critical oxide-film thickness, (e.g. about 0.7 ± 0.1 nm, 0.8 ± 0.1 nm and 4.0 ± 0.5 nm for oxide overgrowths on Al{111}, Al{100} and Al{110}, respectively [13]), bulk thermodynamics favour the occurrence of the corresponding crystalline oxide phase (i.e. γ-Al_2O_3 versus *am*-Al_2O_3 for oxidation of Al).

The initial oxide films grown on bare (i.e. without a native oxide) AlMg substrates at $T < 450$ K have been shown recently to be amorphous as well and to contain both Al and Mg in an oxidized chemical state by high-resolution transmission electron microscopy (HR-TEM) analysis [14] and angle-resolved X-ray Photoelectron Spectroscopy (AR-XPS) [9,14,15]. For thicker oxide films grown at more elevated temperatures (i.e. $T > 450$ K), these amorphous oxide films gradually transform into bulk-thermodynamically-preferred *crystalline*-MgO [9,14].

The present work addresses, in particular, the energetics of the interface between AlMg alloy substrates and their competing, initial, ultrathin ($\leq$ 5 nm), *amorphous* oxide overgrowths of *am*-Al$_2$O$_3$, *am*-MgO and *am*-MgAl$_2$O$_4$ as function of the growth temperature (T), the substrate orientation and the (segregated) Mg alloying element fraction at the alloy/oxide interface (x_{Mg}^i). To this end, a macroscopic atom approach (see e.g. Refs. [11,12,16,17]) is followed to arrive at expressions for the interface energies of the AlMg alloy substrate and the *am*-Al$_2$O$_3$, *am*-MgO and *am*-MgAl$_2$O$_4$ overgrowths as function of T and x_{Mg}^i (see Sec. 2.3). The thus calculated energies of the crystalline-*amorphous* interfaces between the alloy and the amorphous oxide phases are compared with corresponding literature values of similar types of crystalline-*crystalline* metal-oxide interfaces, as obtained by density function theory (DFT) calculations (see Sec. 2.5.1). Next, to predict which of these amorphous oxide overgrowths is thermodynamically preferred (i.e. most stable) on the bare AlMg alloy substrates as a function of T and x_{Mg}^i, the bulk, interface and surface energy contributions to the total Gibbs energies of the various oxide overgrowths on the alloy substrate (for cells of unit volume; see Sec. 2.2) are compared in Sec. 2.5.2. Finally, the thus obtained model predictions on the thermodynamically preferred constitution of the initial amorphous oxide overgrowth on bare AlMg alloy substrate are compared with corresponding experimental data obtained in this work.

2.2. Set-up of the model

Results obtained in the present research project [14] demonstrate that, ultra-thin (< 3 nm) oxide films grown on AlMg alloy surfaces by thermal oxidation at T < 450 K are amorphous and of uniform thickness. Therefore, in the following treatment, the focus is on the growth of a homogeneous amorphous oxide film, $\{\text{oxide}\}$, of uniform thickness, $h_{\{\text{oxide}\}}$, on a single-crystalline AlMg alloy substrate, $\langle\text{AlMg}\rangle$, by e.g. thermal oxidation at relatively low growth temperatures, T < 500 K. The braces $\{\ \}$ and the brackets $\langle\ \rangle$ refer to the amorphous and the crystalline solid state, respectively. The Al and/or Mg atoms incorporated in these ultrathin amorphous oxide films exhibit Al$_2$O$_3$-like and MgO-like local chemical states as in the corresponding 'bulk' oxide phases, respectively [9].

Accordingly, the competing oxide phases considered are 'bulk' amorphous {MgO} and {Al$_2$O$_3$}, as well as {MgAl$_2$O$_4$}[1] [9,14].

(a) amorphous {MgO}   (b) amorphous {Al$_2$O$_3$}   (c) amorphous {MgAl$_2$O$_4$}
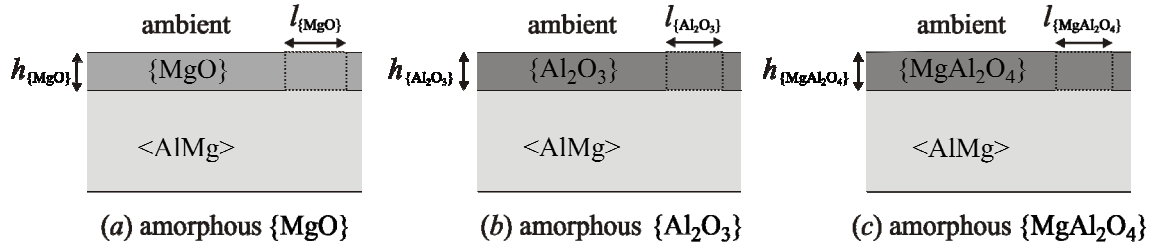
Fig. 2.1: Schematic drawings of amorphous (**a**) {MgO}, (**b**) {Al$_2$O$_3$} and (**c**) {MgAl$_2$O$_4$} overgrowths with uniform film thicknesses, $h_{\{MgO\}}$, $h_{\{Al_2O_3\}}$ and $h_{\{MgAl_2O_4\}}$, on top of identical single-crystalline Al-Mg alloy substrates, $\langle AlMg \rangle$, in contact with the ambient (e.g., vacuum, a gas atmosphere or an adsorbed layer). The indicated "unit cells" of the competing {MgO}, {Al$_2$O$_3$} and {MgAl$_2$O$_4$} overgrowths with respective volumes of $h_{\{MgO\}} \times l^2_{\{MgO\}}$, $h_{\{Al_2O_3\}} \times l^2_{\{Al_2O_3\}}$ and $h_{\{MgAl_2O_4\}} \times l^2_{\{MgAl_2O_4\}}$ contain the same molar quantity of oxygen.

To predict which of the pure single-phase amorphous oxide overgrowths is thermodynamically preferred on the $\langle AlMg \rangle$ substrate, the energetics of the {MgO}, {Al$_2$O$_3$} and/or {MgAl$_2$O$_4$} films grown on the same alloy substrate, $\langle AlMg \rangle$, must be compared. Consider "unit cells" of {MgO}, {Al$_2$O$_3$} and {MgAl$_2$O$_4$} of volume $h_{\{MgO\}} \times l^2_{\{MgO\}}$, $h_{\{Al_2O_3\}} \times l^2_{\{Al_2O_3\}}$ and $h_{\{MgAl_2O_4\}} \times l^2_{\{MgAl_2O_4\}}$, respectively (see Fig. 2.1 and Ref. [11]), containing the same molar quantity of oxygen. The corresponding oxidations are described by the following reactions (as defined per mole O reactant):

$$\text{Mg(s)} + \tfrac{1}{2} \cdot \text{O}_2\text{(g)} \rightarrow \{\text{MgO}\} \tag{2.1a}$$

$$\tfrac{2}{3} \cdot \text{Al(s)} + \tfrac{1}{2} \cdot \text{O}_2\text{(g)} \rightarrow \tfrac{1}{3} \cdot \{\text{Al}_2\text{O}_3\} \tag{2.1b}$$

$$\tfrac{1}{4} \cdot \text{Mg(s)} + \tfrac{1}{2} \cdot \text{Al(s)} + \tfrac{1}{2} \cdot \text{O}_2\text{(g)} \rightarrow \tfrac{1}{4} \cdot \{\text{MgAl}_2\text{O}_4\} \tag{2.1c}$$

---
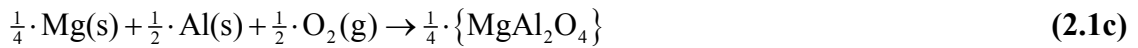
[1] Note that, according to bulk thermodynamics of the corresponding *crystalline* oxide phases [41], the mutual solid solubility of $\langle \alpha\text{-Al}_2\text{O}_3 \rangle$ and $\langle \text{MgO} \rangle$ is negligibly small at $T < 1200$ K, and the pure crystalline spinel phase $\langle \text{MgAl}_2\text{O}_4 \rangle$ is only stable in a very narrow compositional range at relatively high temperatures (i.e., $T > 1200$ K).

Because the considered {MgO}, {Al$_2$O$_3$} and {MgAl$_2$O$_4$} "unit cells" (Fig. 2.1) contain the same molar quantity of oxygen, the molar quantities of oxide phase contained in the different "unit cells" differ [due to the different metal-to-oxygen atomic ratios of the concerned oxide phases; see Eqs. 2.1(a)-(c)]. Under the constraint that no growth strain is present in the amorphous oxide films at the growth temperature [5,11], it holds that

$$\frac{l^2_{\{MgO\}} \cdot h_{\{MgO\}}}{V_{\{MgO\}}} = \frac{l^2_{\{Al_2O_3\}} \cdot h_{\{Al_2O_3\}}}{V_{\{Al_2O_3\}}} = \frac{l^2_{\{MgAl_2O_4\}} \cdot h_{\{MgAl_2O_4\}}}{V_{\{MgAl_2O_4\}}},$$ (2.2)

where $l^2_{\{MgO\}}$, $l^2_{\{Al_2O_3\}}$ and $l^2_{\{MgAl_2O_4\}}$ represent the surface areas; $h_{\{MgO\}}$, $h_{\{Al_2O_3\}}$ and $h_{\{MgAl_2O_4\}}$ are the heights (corresponding to the film thicknesses); and $V_{\{MgO\}}$, $V_{\{Al_2O_3\}}$ and $V_{\{MgAl_2O_4\}}$ denote the molar volumes per mol O (i.e., [m^3/mol O]) of the unstrained {MgO}, {Al$_2$O$_3$} and {MgAl$_2$O$_4$} oxide "unit cells", respectively. The interface area of an "unit cell" is proportional with $V^{2/3}_{\{oxide\}}$, where, $V_{\{oxide\}}$ is the molar volume per mol O of the unstrained oxide "unit cell". Therefore, the ratios of the interface areas of the {Al$_2$O$_3$} and {MgAl$_2$O$_4$} "unit cells" with respect to that of the corresponding {MgO} "unit cell" are given by,

$$\frac{l^2_{\{Al_2O_3\}}}{l^2_{\{MgO\}}} = \frac{V^{2/3}_{\{Al_2O_3\}}}{V^{2/3}_{\{MgO\}}} \text{ and } \frac{l^2_{\{MgAl_2O_4\}}}{l^2_{\{MgO\}}} = \frac{V^{2/3}_{\{MgAl_2O_4\}}}{V^{2/3}_{\{MgO\}}}$$ (2.3)

respectively.

Now to predict which of the amorphous oxide overgrowths on the $\langle AlMg \rangle$ substrate is thermodynamically preferred, the oxidation energetics for a unit area of substrate surface (interface) have to be considered. In terms of the above "model set-up", then the total Gibbs energies, $G^{cell}_{\{oxide\}}$, of the {MgO}, {Al$_2$O$_3$} and/or {MgAl$_2$O$_4$} cells must be compared **per unit area of the {MgO} unit cell** (i.e., the {MgO} unit cell is, arbitrarily, chosen as the reference state). This leads to the following expressions for $G^{cell}_{\{MgO\}}$, $G^{cell}_{\{Al_2O_3\}}$ and $G^{cell}_{\{MgAl_2O_4\}}$:

$$G^{cell}_{\{MgO\}} = h_{\{MgO\}} \cdot \frac{\Delta G^f_{\{MgO\}}}{V_{\{MgO\}}} + \gamma_{\langle AlMg \rangle - \{MgO\}} + \gamma_{\{MgO\} - ambient}$$ (2.4a)

$$G^{cell}_{\{Al_2O_3\}} = \frac{l^2_{\{Al_2O_3\}}}{l^2_{\{MgO\}}} \cdot \left(h_{\{Al_2O_3\}} \cdot \frac{\Delta G^f_{\{Al_2O_3\}}}{V_{\{Al_2O_3\}}} + \gamma_{\langle AlMg \rangle - \{Al_2O_3\}} + \gamma_{\{Al_2O_3\} - ambient} \right)$$ (2.4b)

$$G_{\{MgAl_2O_4\}}^{cell} = \frac{l_{\{MgAl_2O_4\}}^2}{l_{\{MgO\}}^2} \cdot \left(h_{\{MgAl_2O_4\}} \cdot \frac{\Delta G_{\{MgAl_2O_4\}}^f}{V_{\{MgAl_2O_4\}}} + \gamma_{\langle AlMg\rangle-\{MgAl_2O_4\}} + \gamma_{\{MgAl_2O_4\}-ambient} \right) \quad \textbf{(2.4c)}$$

where $\Delta G_{\{MgO\}}^f$, $\Delta G_{\{Al_2O_3\}}^f$ and $\Delta G_{\{MgAl_2O_4\}}^f$ are the bulk (chemical) Gibbs energies of oxide

formation *per mole oxygen* (i.e. in J·mole^{-1} O); $\gamma_{\langle AlMg\rangle-\{MgO\}}$, $\gamma_{\langle AlMg\rangle-\{Al_2O_3\}}$ and

$\gamma_{\langle AlMg\rangle-\{MgAl_2O_4\}}$ represent the energies of the interfaces (in J·m^{-2}) between the alloy

substrate and the respective amorphous oxide phase; $\gamma_{\{MgO\}-ambient}$, $\gamma_{\{Al_2O_3\}-ambient}$ and

$\gamma_{\{MgAl_2O_4\}-ambient}$ are the surface energies (in J·m^{-2}) of the respective amorphous oxides in

contact with the ambient (e.g., vacuum, a gas atmosphere or an adsorbed layer). Using

Eqs. (2.2) and (2.3), Eqs. (2.4b) and (2.4c) can be rewritten as

$$G_{\{Al_2O_3\}}^{cell} = h_{\{MgO\}} \cdot \frac{\Delta G_{\{Al_2O_3\}}^f}{V_{\{MgO\}}} + \frac{\left(V_{\{Al_2O_3\}}\right)^{2/3}}{\left(V_{\{MgO\}}\right)^{2/3}} \cdot \gamma_{\langle AlMg\rangle-\{Al_2O_3\}} + \frac{\left(V_{\{Al_2O_3\}}\right)^{2/3}}{\left(V_{\{MgO\}}\right)^{2/3}} \cdot \gamma_{\{Al_2O_3\}-ambient} \quad \textbf{(2.5a)}$$

$$G_{\{MgAl_2O_4\}}^{cell} = h_{\{MgO\}} \cdot \frac{\Delta G_{\{MgAl_2O_4\}}^f}{V_{\{MgO\}}} + \frac{\left(V_{\{MgAl_2O_4\}}\right)^{2/3}}{\left(V_{\{MgO\}}\right)^{2/3}} \cdot \gamma_{\langle AlMg\rangle-\{MgAl_2O_4\}} +$$
$$\frac{\left(V_{\{MgAl_2O_4\}}\right)^{2/3}}{\left(V_{\{MgO\}}\right)^{2/3}} \cdot \gamma_{\{MgAl_2O_4\}-ambient} \quad \textbf{(2.5b)}$$

2.3.   Alloy/oxide interface energies

Experimental values for the solid-solid interface energies between alloy substrates and

their amorphous overgrowths [i.e. values for $\gamma_{\langle AlMg\rangle-\{MgO\}}$, $\gamma_{\langle AlMg\rangle-\{Al_2O_3\}}$ and $\gamma_{\langle AlMg\rangle-\{MgAl_2O_4\}}$;

see Eqs. (2.4a), (2.5a) and (2.5b)] are not available as function of the alloy composition

and the oxide growth temperature (*T*). Expressions allowing theoretical estimation of such

interface energies have been derived here (see what follows) on the basis of the

macroscopic atom approach (see Refs. [11,12,16,17] and references therein).

The energy of the interface between the $\langle AlMg\rangle$ substrate and its amorphous oxide

overgrowth can be described as the resultant of three additive energy contributions [11],

i.e.

$$\gamma_{\langle AlMg\rangle-\{oxide\}} = \gamma_{\langle AlMg\rangle-\{oxide\}}^{interaction} + \gamma_{\langle AlMg\rangle-\{oxide\}}^{entropy} + \gamma_{\langle AlMg\rangle-\{oxide\}}^{enthalpy}, \quad \textbf{(2.6)}$$

where $\gamma_{\langle\text{AlMg}\rangle-\{\text{oxide}\}}^{\text{interaction}}$ is the (negative; i.e., oxidation promoting) interaction contribution resulting from the chemical interaction of the amorphous oxide and the $\langle\text{AlMg}\rangle$ alloy substrate across the interface, $\gamma_{\langle\text{AlMg}\rangle-\{\text{oxide}\}}^{\text{entropy}}$ is the positive entropy related contribution resulting from the ordering (i.e., decrease in configurational entropy) of the amorphous oxide near the interface with the crystalline AlMg alloy substrate, and $\gamma_{\langle\text{AlMg}\rangle-\{\text{oxide}\}}^{\text{enthalpy}}$ is the relatively small positive enthalpy contribution arising from the relative increase in enthalpy of the AlMg alloy substrate atoms at the interface (as compared to the bulk) due to the liquid-type of bonding with the amorphous oxide at the interface. For a more detailed description of the various energy contributions to solid-solid interface energies, see Refs. [11,12,17]; in the following only the resulting expressions for the cases considered are given.

2.3.1   *Energy of the* $\langle\text{AlMg}\rangle-\{\text{MgO}\}$ *interface*

The interface energy contribution, $\gamma_{\langle\text{AlMg}\rangle-\{\text{MgO}\}}^{\text{interaction}}$ [see Eq. (2.6)], can be given as a function of the growth temperature, T, and the molar fraction x_{Mg}^{i} of Mg in the alloy *at* the $\langle\text{AlMg}\rangle-\{\text{MgO}\}$ interface (see footnote [2]) according to [11] :

$$\gamma_{\langle\text{AlMg}\rangle-\{\text{MgO}\}}^{\text{interaction}}(T,x_{\text{Mg}}^{\text{i}}) = \frac{1}{3}\cdot\left(x_{\text{Mg}}^{\text{i}}\cdot\frac{\Delta H_{\text{O in}\langle\text{Mg}\rangle}^{\infty}}{A_{\{\text{O}\}}} + \left(1-x_{\text{Mg}}^{\text{i}}\right)\cdot\left[\frac{\Delta H_{\text{O in}\langle\text{Al}\rangle}^{\infty}}{A_{\{\text{O}\}}} + \frac{\Delta H_{\text{Mg in}\langle\text{Al}\rangle}^{\infty}}{A_{\{\text{Mg}\}}} \right] \right), \quad \textbf{(2.7a)}$$

where $\Delta H_{\text{O in}\langle\text{Mg}\rangle}^{\infty}$ and $\Delta H_{\text{O in}\langle\text{Al}\rangle}^{\infty}$ are the enthalpies of mixing 1 mol O atoms at infinite dilution in $\langle\text{Mg}\rangle$ and $\langle\text{Al}\rangle$, respectively (as estimates for the chemical interactions of O and the alloy constituents across the interface); $\Delta H_{\text{Mg in}\langle\text{Al}\rangle}^{\infty}$ is the enthalpy of mixing 1 mol of Mg at infinite dilution in $\langle\text{Al}\rangle$ metal (as estimate for the chemical interaction of the dissimilar metallic atoms Al and Mg across the $\langle\text{AlMg}\rangle-\{\text{MgO}\}$ interface). The geometrical factor 1/3 in Eq. (2.7a) represents the fractional contact area of the Wigner-

---

[2] The molar fraction, x_{Mg}^{i}, of Mg in the AlMg alloy *at* the alloy/oxide interface ($0 \leq x_{\text{Mg}}^{\text{i}} \leq 1$) at the growth temperature is governed by the Gibbsian segregation of Mg from the interior of the alloy to the alloy/oxide interface before and during the oxide-film growth process [9,14]. See also Sec. 2.5.1.

Seitz cells of the oxygen in the oxide *at* the $\langle \text{AlMg} \rangle - \{\text{MgO}\}$ interface (as projected on the interface plane, while assuming the shape of the Wigner-Seitz cell to be intermediate between a cube and a sphere; see Refs. [11,16]). A dense packing of oxygen at the alloy/oxide interface will be thermodynamically preferred [11] (as experimentally observed; see Ref. [18]). Therefore, the molar interface area, $A_{\{\text{O}\}}$, of O in the oxide at the $\langle \text{AlMg} \rangle - \{\text{MgO}\}$ interface can be approximated by the interface area containing one mole of O ions, taking the most densely-packed plane of the corresponding (unstrained) crystalline oxide phase parallel to the alloy/oxide interface. The corresponding estimate for the molar interface area, $A_{\{\text{Mg}\}}$, follows from the value of $A_{\{\text{O}\}}$ by employing the metal-to-oxygen ratio of the bulk oxide phase: i.e. $A_{\{\text{Mg}\}} \approx A_{\{\text{O}\}}$ for $\{\text{MgO}\}$ (see Table 2.3).

Analogously, the entropy-related and enthalpy contributions to the resultant $\langle \text{AlMg} \rangle - \{\text{MgO}\}$ interface energy can be estimated by

$$\gamma_{\langle \text{AlMg} \rangle - \{\text{MgO}\}}^{\text{entropy}}(T) = \frac{-T \cdot \Delta S_{\{\text{MgO}\}}^{\text{deficient}}}{A_{\{\text{O}\}}} \tag{2.7b}$$

and

$$\gamma_{\langle \text{AlMg} \rangle - \{\text{MgO}\}}^{\text{enthalpy}}(T, x_{\text{Mg}}^{\text{i}}) = \frac{1}{3} \cdot \left[\frac{x_{\text{Mg}}^{\text{i}} \cdot H_{\langle \text{Mg} \rangle}^{\text{fuse}} + \left(1 - x_{\text{Mg}}^{\text{i}}\right) \cdot H_{\langle \text{Al} \rangle}^{\text{fuse}}}{A_{\langle \text{AlMg} \rangle}(x_{\text{Mg}}^{\text{i}})} \right] \tag{2.7c}$$

respectively. An (over)estimate for $\Delta S_{\{\text{MgO}\}}^{\text{deficient}}$ is given by the entropy difference of crystalline and amorphous MgO per mole O [i.e., J·K^{-1}·mol^{-1} O] (see discussion in Ref. [11]); $H_{\langle \text{Al} \rangle}^{\text{fuse}}$ and $H_{\langle \text{Mg} \rangle}^{\text{fuse}}$ denote the molar enthalpies of fusion of $\langle \text{Al} \rangle$ and $\langle \text{Mg} \rangle$, respectively; and $A_{\langle \text{AlMg} \rangle}(x_{\text{Mg}}^{\text{i}})$ is the interface area of the alloy substrate containing one mole of atoms of the alloy, with a molar fraction, x_{Mg}^{i}, of Mg in the substrate *at* the $\langle \text{AlMg} \rangle - \{\text{MgO}\}$ interface (see footnote 2, Table 2.3 and Sec. 2.4). Substitution of Eqs. 2.7(a)-(c) in Eq. (6) then leads to the following expression for the energy of the $\langle \text{AlMg} \rangle - \{\text{MgO}\}$ interface as a function of T and x_{Mg}^{i}:

$$\gamma_{\langle \text{AlMg} \rangle - \{ \text{MgO} \}}(T, x_{\text{Mg}}^{\text{i}}) = \frac{-T \cdot \Delta S_{\{ \text{MgO} \}}^{\text{deficient}}}{A_{\{ \text{O} \}}} + \frac{1}{3} \cdot \left\{ x_{\text{Mg}}^{\text{i}} \cdot \left[\frac{\Delta H_{\text{O in} \langle \text{Mg} \rangle}^{\infty}}{A_{\{ \text{O} \}}} + \frac{H_{\langle \text{Mg} \rangle}^{\text{fuse}}}{A_{\langle \text{AlMg} \rangle}(x_{\text{Mg}}^{\text{i}})} \right] + \right.$$

$$\left. \left(1 - x_{\text{Mg}}^{\text{i}}\right) \cdot \left[\frac{\Delta H_{\text{O in} \langle \text{Al} \rangle}^{\infty}}{A_{\{ \text{O} \}}} + \frac{H_{\langle \text{Al} \rangle}^{\text{fuse}}}{A_{\langle \text{AlMg} \rangle}(x_{\text{Mg}}^{\text{i}})} + \frac{\Delta H_{\text{Mg in} \langle \text{Al} \rangle}^{\infty}}{A_{\{ \text{Mg} \}}} \right] \right\} \qquad \textbf{(2.8)}$$

2.3.2   Energy of the $\langle \text{AlMg} \rangle - \{ \text{Al}_2\text{O}_3 \}$ interface

Analogous to the treatment in Sec. 2.3.1, the expression for the energy of the $\langle \text{AlMg} \rangle - \{ \text{Al}_2\text{O}_3 \}$ interface as a function of T and x_{Mg}^{i} can be given by:

$$\gamma_{\langle \text{AlMg} \rangle - \{ \text{Al}_2\text{O}_3 \}}(T, x_{\text{Mg}}^{\text{i}}) = \frac{-T \cdot \Delta S_{\{ \text{Al}_2\text{O}_3 \}}^{\text{deficient}}}{A_{\{ \text{O} \}}} + \frac{1}{3} \cdot \left\{ x_{\text{Mg}}^{\text{i}} \cdot \left[\frac{\Delta H_{\text{O in} \langle \text{Mg} \rangle}^{\infty}}{A_{\{ \text{O} \}}} + \frac{H_{\langle \text{Mg} \rangle}^{\text{fuse}}}{A_{\langle \text{AlMg} \rangle}(x_{\text{Mg}}^{\text{i}})} + \frac{\Delta H_{\text{Al in} \langle \text{Mg} \rangle}^{\infty}}{A_{\{ \text{Al} \}}} \right] + \right.$$

$$\left. \left(1 - x_{\text{Mg}}^{\text{i}}\right) \cdot \left[\frac{\Delta H_{\text{O in} \langle \text{Al} \rangle}^{\infty}}{A_{\{ \text{O} \}}} + \frac{H_{\langle \text{Al} \rangle}^{\text{fuse}}}{A_{\langle \text{AlMg} \rangle}(x_{\text{Mg}}^{\text{i}})} \right] \right\} \qquad \textbf{,(2.9)}$$

where $\Delta H_{\text{Al in} \langle \text{Mg} \rangle}^{\infty}$ is the enthalpy of mixing 1 mol of Al at infinite dilution in $\langle \text{Mg} \rangle$ and the molar interface area of Al in the oxide at the $\langle \text{AlMg} \rangle - \{ \text{Al}_2\text{O}_3 \}$ interface is approximated by $A_{\{ \text{Al} \}} = \frac{3}{2} \cdot A_{\{ \text{O} \}}$ (see Table 2.3).

2.3.3   Energy of the $\langle \text{AlMg} \rangle - \{ \text{MgAl}_2\text{O}_4 \}$ interface

Analogous to the treatment in Sec. 2.3.1, the expression for the energy of the $\langle \text{AlMg} \rangle - \{ \text{MgAl}_2\text{O}_4 \}$ interface as a function of T and x_{Mg}^{i} can be given by:

$$\gamma_{\langle \text{AlMg} \rangle - \{ \text{MgAl}_2\text{O}_4 \}}(T, x_{\text{Mg}}^{\text{i}}) = \frac{-T \cdot \Delta S_{\{ \text{MgAl}_2\text{O}_4 \}}^{\text{deficient}}}{A_{\{ \text{O} \}}} + \frac{1}{3} \cdot \left\{ x_{\text{Mg}}^{\text{i}} \cdot \left[\frac{\Delta H_{\text{O in} \langle \text{Mg} \rangle}^{\infty}}{A_{\{ \text{O} \}}} + \frac{H_{\langle \text{Mg} \rangle}^{\text{fuse}}}{A_{\langle \text{AlMg} \rangle}(x_{\text{Mg}}^{\text{i}})} + \frac{\Delta H_{\text{Al in} \langle \text{Mg} \rangle}^{\infty}}{A_{\{ \text{Al} \}}} \right] \right.$$

$$\left. + \left(1 - x_{\text{Mg}}^{\text{i}}\right) \cdot \left[\frac{\Delta H_{\text{O in} \langle \text{Al} \rangle}^{\infty}}{A_{\{ \text{O} \}}} + \frac{H_{\langle \text{Al} \rangle}^{\text{fuse}}}{A_{\langle \text{AlMg} \rangle}(x_{\text{Mg}}^{\text{i}})} + \frac{\Delta H_{\text{Mg in} \langle \text{Al} \rangle}^{\infty}}{A_{\{ \text{Mg} \}}} \right] \right\}$$

$$\textbf{, (2.10)}$$

where the molar interface areas of Al and Mg in the oxide at the $\langle \text{AlMg} \rangle - \{ \text{MgAl}_2\text{O}_4 \}$ interface are approximated by $A_{\{ \text{Al} \}} = 2 \cdot A_{\{ \text{O} \}}$ and $A_{\{ \text{Mg} \}} = 4 \cdot A_{\{ \text{O} \}}$, respectively (See Table 3).

Table 2.1. Physical constants employed in the model calculations ($T_0 = 298.15$ K); see Sec. 2.4.

constant	value		unit	ref.
molar volume at T_0	$V^0_{\{Al_2O_3\}} = 3.190 \times 10^{-5}$		$m^3 \cdot mole^{-1}$	[11]
	$V^0_{\{MgO\}} = 1.311 \times 10^{-5}$		$m^3 \cdot mole^{-1}$	[12]
	$V^0_{\{MgAl_2O_4\}} = 4.535 \times 10^{-5}$		$m^3 \cdot mole^{-1}$	[12]
enthalpy of mixing	$\Delta H^\infty_{Mg\ in\ \langle Al\rangle} = -7$		$kJ \cdot mole^{-1}$	[16]
	$\Delta H^\infty_{Al\ in\ \langle Mg\rangle} = -8$		$kJ \cdot mole^{-1}$	[16]
enthalpy of fusion	$H^{fuse}_{\langle Al\rangle} = 10.711$		$kJ \cdot mole^{-1}$	[19]
	$H^{fuse}_{\langle Mg\rangle} = 8.477$		$kJ \cdot mole^{-1}$	[19]

Table 2.2. Coefficients of linear thermal expansion, $\alpha(T) = A + B \cdot \Delta T + C \cdot \Delta T^2$, for various metal and oxide phases, as employed in the calculations (see Sec. 2.4). For $\langle Al \rangle$, $\langle MgO \rangle$ and $\langle MgAl_2O_4 \rangle$ the tabulated values of $\alpha(T)$, as reported in Refs. [20,21], were used.

phase	coefficient	value	ref.	Temperature range
$\langle Mg \rangle$, a-axis	A	2.465×10^{-5} K^{-1}	[20]	for $T_0 \leq T \leq 900$ K
	B	1.7812×10^{-8} K^{-2}		with $T_0 = 293$ K
	C	6.354×10^{-12} K^{-3}		
$\langle Mg \rangle$, c-axis	A	2.564×10^{-5} K^{-1}	[20]	for $T_0 \leq T \leq 900$K
	B	1.8622×10^{-8} K^{-2}		with $T_0 = 293$ K
	C	9.810×10^{-13} K^{-3}		
$\langle \gamma - Al_2O_3 \rangle$	A	2.6068×10^{-6} K^{-1}	[21]	for $T_0 \leq T \leq 900$ K
	B	1.1499×10^{-8} K^{-2}		with $T_0 = 298.15$ K

2.4.   Data used in the calculations

The total Gibbs energies, $G_{\{\text{oxide}\}}^{\text{cell}}$, of the {MgO}, {Al$_2O_3$} and/or {MgAl$_2O_4$} cells (per unit area of the {MgO} unit cell; see Sec. 2.2) were calculated from Eqs. (2.4a), (2.5a) and (2.5b) for the various low-index crystallographic surfaces of a parent $\langle\text{AlMg}\rangle$ substrate with $0 \leq x_{\text{Mg}}^{\text{i}} \leq 1$ in the growth temperature and thickness ranges of $T = 298.15$ – 900 K and $0 \leq h_{\{\text{MgO}\}} \leq 5$ nm, respectively. For the thermodynamic assessment of $\Delta G_{\{\text{oxide}\}}^{\text{f}}$, $\Delta S_{\{\text{oxide}\}}^{\text{deficient}}$, $\Delta H_{\text{O in}\langle\text{Mg}\rangle}^{\infty}$, $\Delta H_{\text{O in}\langle\text{Al}\rangle}^{\infty}$, the 'bulk' amorphous oxide phases were considered as undercooled liquids below the glass transition temperature [11,12] (with corresponding data taken from Ref. [19]). The molar volumes, $V_{\{\text{oxide}\}}$, of the concerned amorphous oxide phases as a function of T were either taken from Ref. [11] or estimated from the empirical expressions provided in Ref. [12], while employing the linear thermal expansion coefficients of the corresponding crystalline oxide phases (as approximates for those of the amorphous ones); see Tables 2.1 and 2.2.

     The interface energies $\gamma_{\langle\text{AlMg}\rangle-\{\text{MgO}\}}$, $\gamma_{\langle\text{AlMg}\rangle-\{\text{Al}_2\text{O}_3\}}$ and $\gamma_{\langle\text{AlMg}\rangle-\{\text{MgAl}_2\text{O}_4\}}$ were calculated as a function of T and x_{Mg}^{i} using Eqs.(2.8), (2.9) and (2.10), respectively. For the calculation of the area of the *alloy substrate* at the $\langle\text{AlMg}\rangle-\{\text{oxide}\}$ interface containing one mole of atoms of the alloy, as function of T and x_{Mg}^{i}, (i.e. for the assessment of $A_{\langle\text{AlMg}\rangle}(T, x_{\text{Mg}}^{\text{i}})$; see Sec. 2.3), the structure of the parent $\langle\text{AlMg}\rangle$ substrate adjacent to the interface with its oxide overgrowth was taken to be face centered cubic (fcc) for $0 \leq x_{\text{Mg}}^{\text{i}} \leq 0.5$ and hexagonal close packed (hcp) for $0.5 \leq x_{\text{Mg}}^{\text{i}} \leq 1.0$ (see Tables 2.3 and 2.4; i.e. two corresponding values of $A_{\langle\text{AlMg}\rangle}$ were determined for $x_{\text{Mg}}^{\text{i}} = 0.5$). The unstrained lattice parameter of the $\langle\text{AlMg}\rangle$ substrate at $T_0 = 298.15$ K as a function of the nominal Mg content, x_{Mg}^{b}, was obtained from the corresponding empirical relationships given in Table 2.4 (as obtained using data from Refs. [22-24] and X-ray diffraction data obtained in this work). The linear thermal expansion coefficient of the $\langle\text{AlMg}\rangle$ phase was taken equal to that of fcc $\langle\text{Al}\rangle$ for $0 \leq x_{\text{Mg}}^{\text{i}} \leq 0.5$ and equal to hcp $\langle\text{Mg}\rangle$ for $0.5 \leq x_{\text{Mg}}^{\text{i}} \leq 1.0$ [20] (see Table 2.2). The molar interface areas of the *oxide ions* at the

$\langle \text{AlMg} \rangle - \{\text{oxide}\}$ interfaces as a function of T (i.e. values of $A_{\{O\}}$, $A_{\{Mg\}}$ and $A_{\{Al\}}$; see Sec. 2.3) were approximated by the area containing one mole of O ions in the most densely-packed plane of the corresponding (unstrained) crystalline oxide phase (see Sec. 2.3.1 and Refs. [11,12]): the resulting expressions for $A_{\{O\}}$, $A_{\{Mg\}}$ and $A_{\{Al\}}$ have been gathered in Table 2.3. All other physical constants (e.g., $\Delta H^{\infty}_{\text{Mg in} \langle \text{Al} \rangle}$ and $\Delta H^{\infty}_{\text{Al in} \langle \text{Mg} \rangle}$) used in the interface-energy calculations have been reported in Table 2.1.

Table 2.3. Expressions for the molar interface areas of the alloy constituents and the oxide ions *at* the $\langle \text{AlMg} \rangle - \{\text{MgO}\}$, $\langle \text{AlMg} \rangle - \{\text{Al}_2\text{O}_3\}$ and $\langle \text{AlMg} \rangle - \{\text{MgAl}_2\text{O}_4\}$ interfaces, as employed in the calculations of the interface energies $\gamma_{\langle \text{AlMg} \rangle - \{\text{MgO}\}}$, $\gamma_{\langle \text{AlMg} \rangle - \{\text{Al}_2\text{O}_3\}}$ and $\gamma_{\langle \text{AlMg} \rangle - \{\text{MgAl}_2\text{O}_4\}}$ (cf. Eqs. (2.8), (2.9) and (2.10)); see Sec. 2.4.

phase	molar interface area [m$^2 \cdot$mole^{-1}]
$\langle \text{AlMg} \rangle$-fcc ($0 \leq x^i_{\text{Mg}} \leq 0.5$)	$\{111\}: \quad A^{\text{fcc}}_{\langle \text{AlMg} \rangle} = \frac{\sqrt{3}}{4} \cdot N \cdot \left(a^{\text{fcc}}_{\langle \text{AlMg} \rangle} \right)^2$
	$\{110\}: \quad A^{\text{fcc}}_{\langle \text{AlMg} \rangle} = \frac{\sqrt{2}}{2} \cdot N \cdot \left(a^{\text{fcc}}_{\langle \text{AlMg} \rangle} \right)^2$
	$\{100\}: \quad A^{\text{fcc}}_{\langle \text{AlMg} \rangle} = \frac{1}{2} \cdot N \cdot \left(a^{\text{fcc}}_{\langle \text{AlMg} \rangle} \right)^2$
$\langle \text{AlMg} \rangle$-hcp ($0.5 \leq x^i_{\text{Mg}} \leq 1$)	$\{0001\}: \quad A^{\text{hcp}}_{\langle \text{AlMg} \rangle} = \frac{\sqrt{3}}{2} \cdot N \cdot \left(a^{\text{hcp}}_{\langle \text{AlMg} \rangle} \right)^2$
	$\{1100\}: \quad A^{\text{hcp}}_{\langle \text{AlMg} \rangle} = a^{\text{hcp}}_{\langle \text{AlMg} \rangle} \cdot c^{\text{hcp}}_{\langle \text{AlMg} \rangle} \cdot N$
	$\{1\bar{1}01\}: \quad A^{\text{hcp}}_{\langle \text{AlMg} \rangle} = a^{\text{hcp}}_{\langle \text{AlMg} \rangle} \cdot N \cdot \sqrt{\left(c^{\text{hcp}}_{\langle \text{AlMg} \rangle} \right)^2 + \frac{3}{4} \cdot \left(a^{\text{hcp}}_{\langle \text{AlMg} \rangle} \right)^2}$
$\{\text{Al}_2\text{O}_3\}$	$A_{\{O\}} \cong \frac{\sqrt{3}}{4} \cdot N \cdot \left(\frac{1}{2} \cdot a_{\langle \gamma - \text{Al}_2\text{O}_3 \rangle} \right)^2$; $A_{\{Al\}} = \frac{3}{2} \cdot A_{\{O\}}$
$\{\text{MgO}\}$	$A_{\{O\}} \cong \frac{\sqrt{3}}{4} \cdot N \cdot \left(a_{\langle \text{MgO} \rangle} \right)^2$; $A_{\{Mg\}} = A_{\{O\}}$
$\{\text{MgAl}_2\text{O}_4\}$	$A_{\{O\}} = \frac{\sqrt{3}}{4} \cdot N \cdot \left(\frac{1}{2} \cdot a_{\langle \text{MgAl}_2\text{O}_4 \rangle} \right)^2$; $A_{\{Al\}} = \frac{1}{2} \cdot A_{\{Mg\}} = 2 \cdot A_{\{O\}}$

Table 2.4. Unstrained lattice parameters at T_0 = 298.15 K of the "unit cells" of various metal, alloy and oxide phases, as employed in the calculations; see Sec. 2.4. The symbol $x_{\mathrm{Mg}}^{\mathrm{b}}$ denotes the bulk Mg alloying fraction.

phase	lattice parameter (Å)	ref.
$\langle \mathrm{Al} \rangle$-fcc	$a = 4.0494$	[22]
$\langle \mathrm{Mg} \rangle$-hcp	$a = 3.2088,\ c = 5.2099$	[23]
$\langle \mathrm{AlMg} \rangle$-fcc $(0 \le x_{\mathrm{Mg}}^{\mathrm{b}} \le 0.5)$	$a_{\langle \mathrm{AlMg} \rangle}^{\mathrm{fcc}}(T_0) = 0.5108 \cdot x_{\mathrm{Mg}}^{\mathrm{b}} + 4.0477$	[24], this study
$\langle \mathrm{AlMg} \rangle$-hcp $(0.5 \le x_{\mathrm{Mg}}^{\mathrm{b}} \le 1)$	$a_{\langle \mathrm{AlMg} \rangle}^{\mathrm{hcp}}(T_0) = \text{-}0.0034 \cdot x_{\mathrm{Al}}^{\mathrm{b}} + 3.209$	[24], this study
	$c_{\langle \mathrm{AlMg} \rangle}^{\mathrm{hcp}}(T_0) = \text{-}0.0039 \cdot x_{\mathrm{Al}}^{\mathrm{b}} + 5.2077$	[24], this study
$\langle \gamma\text{-}\mathrm{Al_2O_3} \rangle$	$a = 7.924$	[25]
$\langle \mathrm{MgO} \rangle$	$a = 4.2112$	[26]
$\langle \mathrm{MgAl_2O_4} \rangle$	$a = 8.0831$	[27]

Table 2.5. Surface energies $\gamma_{\{\mathrm{Al_2O_3}\}\text{-vacuum}}$, $\gamma_{\{\mathrm{MgO}\}\text{-vacuum}}$ and $\gamma_{\{\mathrm{MgAl_2O_4}\}\text{-vacuum}}$ of amorphous $\{\mathrm{MgO}\}$, $\{\mathrm{Al_2O_3}\}$ and $\{\mathrm{MgAl_2O_4}\}$ in contact with vacuum at T_0 (= 298.15 K) and their corresponding temperature coefficients, $\partial \gamma_{\{\mathrm{oxide}\}\text{-vacuum}} / \partial T$. The surface energies (and their temperature dependencies) of the most densely packed Al{111} and Mg{0001} metal surfaces have been included as well. For details, see Sec. 2.4 and Refs. [12,28].

phase	$\gamma\,(T_0)$ (J·m^{-2})	$\partial\gamma/\partial T$ (J·m^{-2}·K^{-1})	ref.
$\{\mathrm{Al_2O_3}\}$	0.88	-0.187×10^{-3}	[11]
$\{\mathrm{MgO}\}$	0.92	-0.925×10^{-4}	[12,29]
$\{\mathrm{MgAl_2O_4}\}$	0.85	-0.925×10^{-4}	[12,15,30]
$\langle \mathrm{Al}\{111\} \rangle$	0.92	-0.8×10^{-4}	[31]
$\langle \mathrm{Mg}\{0001\} \rangle$	0.62	-1.2×10^{-4}	[31]

The values employed for the surface energies of the amorphous oxides in contact with vacuum (i.e. values for $\gamma_{\{MgO\}\text{-vacuum}}$, $\gamma_{\{Al_2O_3\}\text{-vacuum}}$ and $\gamma_{\{MgAl_2O_4\}\text{-vacuum}}$; including their relatively weak temperature dependencies) are provided by Table 2.5 (as estimated according to the procedures outlined in Refs. [12,28]).

2.5. Model predictions

2.5.1 *Interface and surface energies*

The interface energies $\gamma_{\langle AlMg\rangle-\{MgO\}}$, $\gamma_{\langle AlMg\rangle-\{Al_2O_3\}}$ and $\gamma_{\langle AlMg\rangle-\{MgAl_2O_4\}}$ for the amorphous oxide overgrowths, $\{MgO\}$, $\{Al_2O_3\}$ and $\{MgAl_2O_4\}$, on the most densely packed $\langle AlMg\rangle$ substrate surface at $T = 300$ K and $T = 600$ K (as calculated using Eqs.(2.8), (2.9) and (2.10), respectively), are shown as function of the Mg alloying content at the alloy/oxide interface, x_{Mg}^i, in Fig. 2.2. It follows that, within the studied temperature range and for $0 \leq x_{Mg}^i \leq 1$: $\gamma_{\langle AlMg\rangle-\{Al_2O_3\}} < \gamma_{\langle AlMg\rangle-\{MgAl_2O_4\}} < \gamma_{\langle AlMg\rangle-\{MgO\}}$. Thus, the $\langle AlMg\rangle-\{Al_2O_3\}$ interface is thermodynamically preferred with respect to the corresponding $\langle AlMg\rangle-\{MgAl_2O_4\}$ and $\langle AlMg\rangle-\{MgO\}$ interfaces.

The relatively low energy of the $\langle AlMg\rangle-\{Al_2O_3\}$ interface is predominantly due to a relatively high density of oxygen-metal bonds across the interface [as expressed by the relatively low value of the molar interface area of O, $A_{\{O\}}$, in Eq. (2.9)] and hence a more negative chemical interaction contribution to the interface energy, $\gamma_{\langle AlMg\rangle-\{Al_2O_3\}}$. Due to the relatively strong Mg-O chemical bond strength (as compared to the Al-O bond strength [12]), the (negative, i.e., favourable) interaction contribution to the interface energies (see Sec. 2.3) becomes more negative with increasing Mg alloying content, x_{Mg}^i, at the $\langle AlMg\rangle-\{oxide\}$ interface. This leads to the observed decrease of the considered interface energies with increasing x_{Mg}^i. This implies the existence of a strong driving force for the chemical (Gibbsian) segregation of Mg from the interior of the $\langle AlMg\rangle$ substrate to the $\langle AlMg\rangle-\{oxide\}$ interface (in agreement with experimental observations reported in Refs. [9,14]; see also discussion in Sec. 2.6). All interface energies slightly

increase (become less negative, i.e. the interfaces become less stable) with increasing temperature due to correspondingly small increases of the (negative) interaction and (positive) entropy contributions to the interface energies (see also Refs. [11,12]).

Similar values and relative trends (as function of T and x_{Mg}^i) were obtained by the calculations for the interface energies of the amorphous oxide overgrowths on the other low index crystallographic surfaces of the parent $\langle AlMg \rangle$ substrate (see Table 2.3). This implies that the energy of the interface between an amorphous oxide and its parent metal substrate is more or less independent of the crystallographic orientation of the parent metal substrate (in contrast with the energy of the interface between a (semi-) coherent crystalline oxide film and the same substrate, e.g., see Ref. [5]), which is in accordance with similar findings in Refs. [11,12].
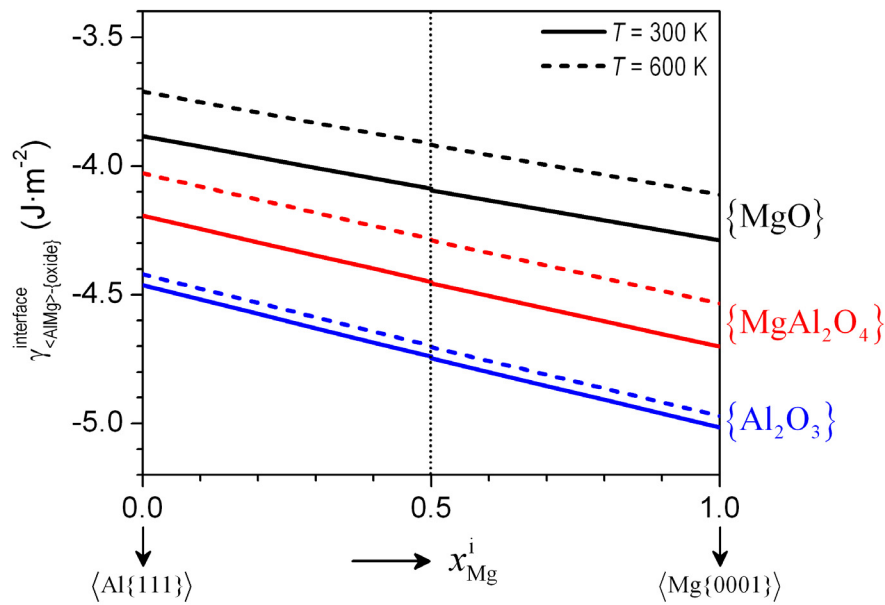
Fig. 2.2: Interface energies $\gamma_{\langle AlMg \rangle - \{MgO\}}$, $\gamma_{\langle AlMg \rangle - \{Al_2O_3\}}$ and $\gamma_{\langle AlMg \rangle - \{MgAl_2O_4\}}$ for the amorphous oxide overgrowths $\{MgO\}$, $\{Al_2O_3\}$ and $\{MgAl_2O_4\}$ on the most densely packed surface of the $\langle AlMg \rangle$ substrate (i.e. $\langle AlMg\{111\} \rangle$ for $0 \leq x_{Mg}^i \leq 0.5$ and $\langle AlMg\{0001\} \rangle$ for $0.5 \leq x_{Mg}^i \leq 1.0$; see Sec. 2.4) as function of the Mg alloying content of the substrate at the alloy/oxide interface (x_{Mg}^i) at growth temperatures of $T = 300$ K and 600 K. The interface energies were calculated applying Eqs.(2.8), (2.9) and (2.10), respectively (employing the data given in Tables 2.1 to 2.4). The very small kink in the curves at $x_{Mg}^i = 0.5$ results from the fcc $\rightarrow$ hcp transition of the $\langle AlMg \rangle$ substrate, as adopted in the calculations. For further details, see Sec. 2.4.

The present theoretical estimates for the interface energies cannot be compared with experimental data, because these do not exist. However, theoretical values for the work of adhesion at 0 K have been obtained for a number of systems mainly by application of density functional theory (DFT) [6, 33-40]. The here obtained estimates for the interface energies can be used to determine corresponding estimates for the work of adhesion and these can then be compared with the mentioned DFT predictions. To this end we proceed as follows.

Table 2.6. Work of separation ($W^{sep}_{\langle M \rangle \text{-} \langle M_x O_y \rangle}$) or work of adhesion ($W^{ad}_{\langle M \rangle \text{-} \langle M_x O_y \rangle}$) at 0 K, of the crystalline-*crystalline* interfaces between the densely-packed metal surfaces and the most-densely-packed O-terminated crystallographic planes of crystalline $\langle Al_2O_3 \rangle$, $\langle MgAl_2O_4 \rangle$ and $\langle MgO \rangle$.

$W^{ad}_{\langle M \rangle \text{-} \langle M_x O_y \rangle} / W^{sep}_{\langle M \rangle \text{-} \langle M_x O_y \rangle}$ $(J \cdot m^2)$	ref.
$W^{sep}_{\langle Al(111) \rangle - \langle \alpha\text{-}Al_2O_3(0001) \rangle} \sim 10.1$	[34]
$W^{sep}_{\langle Nb(111) \rangle - \langle \alpha\text{-}Al_2O_3(0001) \rangle} \sim 10.0^{\pm 0.1}$	[33]
$W^{sep}_{\langle Cu(111) \rangle - \langle \alpha\text{-}Al_2O_3(0001) \rangle} \sim 7.7^{\pm 0.1}$	[37]
$W^{sep}_{\langle Ni(111) \rangle - \langle \alpha\text{-}Al_2O_3(0001) \rangle} \sim 6.7^{\pm 0.1}$	[36]
$W^{sep}_{\langle Cu(111) \rangle - \langle \alpha\text{-}Al_2O_3(0001) \rangle} \sim 5.7^{\pm 0.3}$	[36]
$W^{ad}_{\langle Ni(111) \rangle - \langle MgO(001) \rangle} \sim (1.93+2.33+1.18=) \ 5.4$	[12,24,38]
$W^{ad}_{\langle Al(001) \rangle - \langle MgAl_2O_4(001) \rangle} \sim (2.4+0.9+0.9) = 4.2$	[31,35][3]
$W^{ad}_{\langle Cu(111) \rangle - \langle MgO(001) \rangle} \sim (0.86+1.29+1.18=) \ 3.3$	[12,31,38]
$W^{ad}_{\langle Cu(111) \rangle - \langle MgO(001) \rangle} \sim 2.9$	[39]
$W^{ad}_{\langle Al(111) \rangle - \langle MgO(001) \rangle} \sim (0.438+0.94+1.18=) \ 2.6$	[12,31,40]

[3] This result does not represent the most densely packed $\langle Al \rangle - \langle MgAl_2O_4 \rangle$ interface.

The interface-energy values as obtained in this work for the most densely packed substrate surface, after extrapolating to $T = 0$ K and averaging over $0 \leq x_{Mg}^i \leq 1$, are: $\gamma_{\langle AlMg \rangle - \{Al_2O_3\}} = -4.8^{\pm 0.3}$ J·m^2, $\gamma_{\langle AlMg \rangle - \{MgAl_2O_4\}} = -4.6^{\pm 0.3}$ J·m^2 and $\gamma_{\langle AlMg \rangle - \{MgO\}} = -4.3^{\pm 0.2}$, respectively. The interface-energy values at 0 K can be converted into values for the work of adhesion at 0 K. The work of adhesion, $W_{\langle AlMg \rangle - \{oxide\}}^{ad}$, is defined as the Gibbs energy change for creating free surfaces from the concerned interface, which free surfaces are in thermodynamic equilibrium with the ambient (*here*: vacuum) [6]. Hence

$$W_{\langle AlMg \rangle - \{oxide\}}^{ad} = \gamma_{\{oxide\}\text{-vacuum}} + \gamma_{\langle AlMg \rangle \text{-vacuum}} - \gamma_{\langle AlMg \rangle - \{oxide\}} , \qquad \textbf{(2.11a)}$$

where $\gamma_{\{oxide\}\text{-vacuum}}$ and $\gamma_{\langle AlMg \rangle \text{-vacuum}}$ are the surface energies of the concerned amorphous oxide phase and the $\langle AlMg \rangle$ alloy (in equilibrium with the ambient), respectively. Substitution of the corresponding interface energies (as derived in this work) and reported surface energies (all at 0 K) into Eq. (2.11a) gives: $W_{\langle AlMg \rangle - \{Al_2O_3\}}^{ad} = 6.5^{\pm 0.2}$ J·m^2, $W_{\langle AlMg \rangle - \{MgAl_2O_4\}}^{ad} = 6.3^{\pm 0.2}$ J·m^2 and $W_{\langle AlMg \rangle - \{MgO\}}^{ad} = 6.0^{\pm 0.1}$, all at 0 K. These values of $W_{\langle AlMg \rangle - \{oxide\}}^{ad}$ can now be compared to DFT data for the work of adhesion ($W_{\langle M \rangle - \langle M_xO_y \rangle}^{ad}$) and for the work of separation ($W_{\langle M \rangle - \langle M_xO_y \rangle}^{sep}$; see footnote [4]), at 0 K, of crystalline-*crystalline* interfaces between similar types of densely-packed metal surfaces and the most-densely-

---

[4] In most DFT calculations of crystalline-crystalline metal-oxide interfaces, the work of separation, $W_{\langle M \rangle - \langle M_xO_y \rangle}^{sep}$, is determined, instead of the work of adhesion as defined above (see Eq. (2.11a)). The work of separation is defined as the difference between the total energy of the relaxed ensemble of metal slab, oxide slab and its interface and the sum of the total energies of the 'unrelaxed' slabs at large interface separation (i.e. with the separated slabs subjected to the same strain at the same volume as in the interface ensemble) [35,36]. This implies that strain-energy contributions due to the lattice mismatch at the crystalline-crystalline metal-oxide interfaces, as well as the equilibration of the created surfaces with the ambient, are generally not accounted for in $W_{\langle M \rangle - \langle M_xO_y \rangle}^{sep}$ [6,37]. Since the crystalline-*amorphous* metal-oxide interface energies are (taken to be) strain-free (see Sec. 2.2 and [5]), it may be assumed for further comparison that: $W_{\langle M \rangle - \{M_xO_y\}}^{ad} \approx W_{\langle M \rangle - \langle M_xO_y \rangle}^{sep}$; i.e., ignoring a possible effect of equilibration of the created surfaces with the ambient.

packed O-terminated crystallographic planes of crystalline $\langle Al_2O_3 \rangle$, $\langle MgAl_2O_4 \rangle$ and $\langle MgO \rangle$; see Table 2.6.

It can be concluded that the values of $W^{ad}_{\langle AlMg \rangle - \{oxide\}}$ for the crystalline-*amorphous* interfaces, as calculated on the basis of the macroscopic atom approach in this work, (see above and Fig. 2.2) fall well within the range of corresponding values of $W^{ad}_{\langle M \rangle - \langle M_xO_y \rangle}$ and $W^{sep}_{\langle M \rangle - \langle M_xO_y \rangle}$ for similar types of crystalline-*crystalline* interfaces, as obtained by calculations on the basis of mainly density functional theory. Further, the reported DFT values of $W^{ad}_{\langle M \rangle - \langle M_xO_y \rangle}$ and $W^{sep}_{\langle M \rangle - \langle M_xO_y \rangle}$ for the interfaces between O-terminated α-Al$_2$O$_3$(0001) and e.g. Al(111), Cu(111) and Ni(111) are substantially higher (i.e. their corresponding interface energies are lower) than the interfaces of O-terminated MgO(100) with the corresponding metals, in accordance with the present calculations (see above and Fig. 2.2).

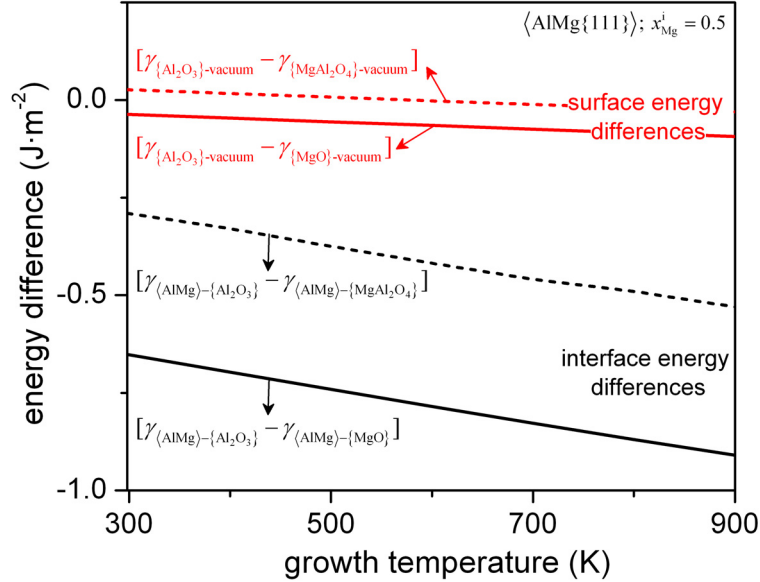**Fig. 2.3:** Interface- and surface-energy differences of the $\{MgO\}$ and $\{MgAl_2O_4\}$ overgrowths with respect to the interface and surface energies of the $\{Al_2O_3\}$ overgrowth, on the most densely packed surface of the $\langle AlMg \rangle$ substrate (with $x^i_{Mg} = 0.5$) versus the growth temperature. For details, see Sec. 2.5.1.

The surface energies of the amorphous oxide overgrowths increase in the order: $\gamma_{\{MgAl_2O_4\}\text{-vacuum}} < \gamma_{\{Al_2O_3\}\text{-vacuum}} << \gamma_{\{MgO\}\text{-vacuum}}$ with corresponding values (in J·m^2) of $\gamma_{\{MgAl_2O_4\}\text{-vacuum}} = 0.85 - 0.925 \cdot 10^{-4}\cdot(T-T_0)$, $\gamma_{\{Al_2O_3\}\text{-vacuum}} = 0.88 - 0.187 \cdot 10^{-3}\cdot(T-T_0)$ and $\gamma_{\{MgO\}\text{-vacuum}} = 0.92 - 0.925 \cdot 10^{-4}\cdot(T-T_0)$ (with $T_0 = 298.15$ K; see Table 2.5).

It follows that the $\{Al_2O_3\}$ overgrowth on the $\langle AlMg \rangle$ substrate not only has the lowest interface energy (as compared to both $\{MgO\}$ and $\{MgAl_2O_4\}$; see above), but also has a relatively low surface energy (as compared to that of $\{MgO\}$). The relative interface- and surface-energy differences of the $\{MgO\}$ and $\{MgAl_2O_4\}$ overgrowths with respect to the $\{Al_2O_3\}$ overgrowth are plotted as a function of the growth temperature in Fig. 2.3 (for $x_{Mg}^i = 0.5$). Clearly, the surface-energy differences, $[\gamma_{\{Al_2O_3\}\text{-vacuum}} - \gamma_{\{MgAl_2O_4\}\text{-vacuum}}]$ and $[\gamma_{\{Al_2O_3\}\text{-vacuum}} - \gamma_{\{MgO\}\text{-vacuum}}]$, between the amorphous oxide phases are negligibly small as compared to their corresponding interface-energy differences, $[\gamma_{\langle AlMg \rangle - \{Al_2O_3\}} - \gamma_{\langle AlMg \rangle - \{MgAl_2O_4\}}]$ and $[\gamma_{\langle AlMg \rangle - \{Al_2O_3\}} - \gamma_{\langle AlMg \rangle - \{MgO\}}]$, i.e., the interface-energy differences dominate over the surface-energy differences. These results indicate that, for the formation of an amorphous oxide film on the $\langle AlMg \rangle$ substrate, which contains both Al and Mg (see Secs. 2.2 and 2.6), interface thermodynamics favours phase separation of $\{Al_2O_3\}$ and $\{MgO\}$ such that $\{Al_2O_3\}$ occurs at the interface and $\{MgO\}$ at the surface.[5]

2.5.2 Total Gibbs energies

To predict which of the amorphous oxide overgrowths is thermodynamically preferred (i.e. most stable) on the most densely packed $\langle AlMg \rangle$ substrate, the total Gibbs energies $G_{\{MgO\}}^{cell}$, $G_{\{Al_2O_3\}}^{cell}$ and $G_{\{MgAl_2O_4\}}^{cell}$ of the defined $\{MgO\}$, $\{Al_2O_3\}$ and/or $\{MgAl_2O_4\}$ "unit cells" (per unit area of the $\{MgO\}$ "unit cell"; see Fig. 2.1 and Sec. 2.2) have been plotted

---

[5] Note that the interface (and surface) energies of $\{MgAl_2O_4\}$ fall in between those of $\{Al_2O_3\}$ and $\{MgO\}$; see Figs. 2.2 and 2.3. Thus, a hypothetical, pure $\{MgAl_2O_4\}$ overgrowth (see Sec. 2.2) will have a stability in between those of the corresponding pure $\{Al_2O_3\}$ and pure $\{MgO\}$ overgrowths.

in Figs. 2.4(a) and 2.4(b) as function of x_{Mg}^i for $\{MgO\}$ unit cell thicknesses of $h_{\{MgO\}} = 1$ nm and $h_{\{MgO\}} = 5$ nm, respectively (at $T = 300$ K, 600 K and 900 K). The corresponding bulk, interface and surface energy contributions *per unit area of the* $\{MgO\}$ *unit cell* (i.e. the terms $h_{\{MgO\}} \cdot \Delta G_{\{oxide\}}^f / V_{\{MgO\}}$, $\gamma_{\langle AlMg \rangle - \{oxide\}} \cdot l_{\{oxide\}}^2 / l_{\{MgO\}}^2$ and $\gamma_{\{oxide\}\text{-vacuum}} \cdot l_{\{oxide\}}^2 / l_{\{MgO\}}^2$ in Eqs. (2.4a), (2.5a) and (2.5b), respectively) are shown in Figs. 2.5, 2.6 and 2.7, respectively, as function of the growth temperature.
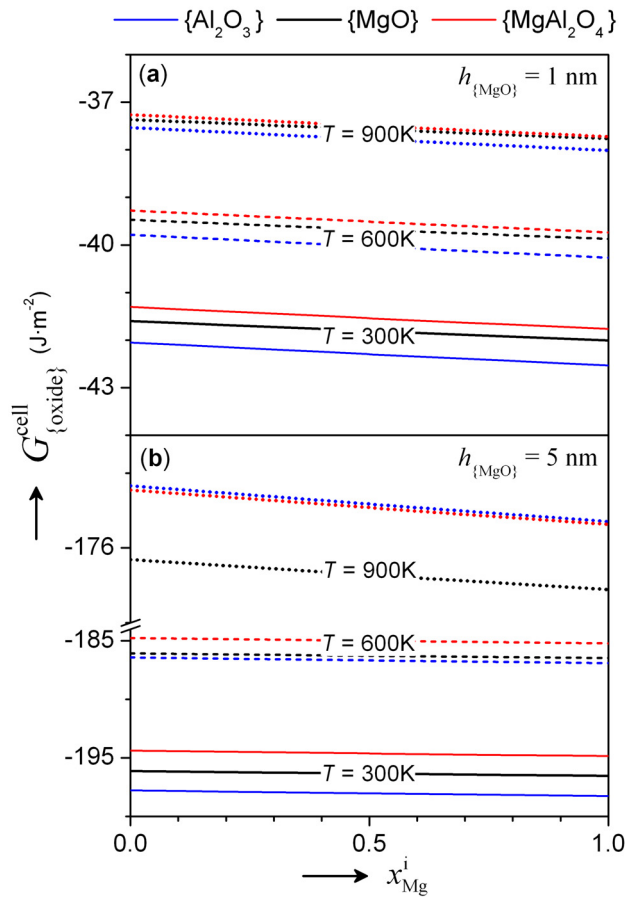
Fig. 2.4: Total Gibbs energies, $G_{\{MgO\}}^{cell}$, $G_{\{Al_2O_3\}}^{cell}$ and $G_{\{MgAl_2O_4\}}^{cell}$, of the defined "unit cells" of the $\{MgO\}$, $\{Al_2O_3\}$ and $\{MgAl_2O_4\}$ overgrowths on the most densely packed surface of the $\langle AlMg \rangle$ substrate (*per unit area of the* $\{MgO\}$ *"unit cell"*; See Sec. 2.2) versus the Mg alloying content at the alloy/oxide interface, x_{Mg}^i . The total Gibbs energies $G_{\{MgO\}}^{cell}$, $G_{\{Al_2O_3\}}^{cell}$ and $G_{\{MgAl_2O_4\}}^{cell}$ were calculated applying Eqs. (2.4a), (2.5a) and (2.5b), respectively, for growth temperatures of $T = 300$ K, 600 K and 900 K and $\{MgO\}$ unit cell thicknesses of (**a**) $h_{\{MgO\}} = 1$ nm and (**b**) $h_{\{MgO\}} = 5$ nm (using the data reported in Tables 2.1 to 2.5).
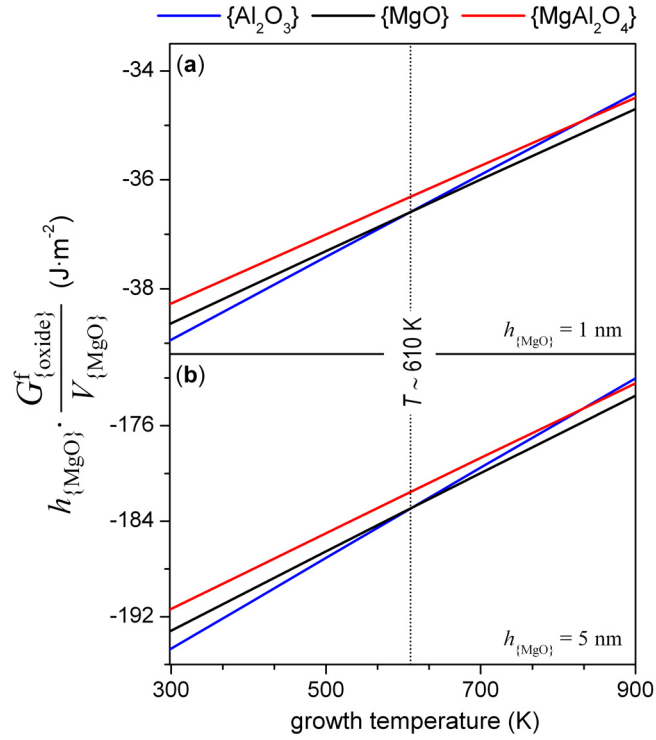
Fig. 2.5: *Bulk* (chemical) energy contributions $h_{\{MgO\}} \cdot \Delta G^f_{\{MgO\}} / V_{\{MgO\}}$, $h_{\{MgO\}} \cdot \Delta G^f_{\{Al_2O_3\}} / V_{\{MgO\}}$ and $h_{\{MgO\}} \cdot \Delta G^f_{\{MgAl_2O_4\}} / V_{\{MgO\}}$ (*per unit area of the* $\{MgO\}$ *unit cell*; See Sec. 2.2) to the corresponding total Gibbs energies $G^{cell}_{\{MgO\}}$, $G^{cell}_{\{Al_2O_3\}}$ and $G^{cell}_{\{MgAl_2O_4\}}$ of the "unit cells" of the $\{MgO\}$, $\{Al_2O_3\}$ and/or $\{MgAl_2O_4\}$ overgrowths as a function of the growth temperature for $\{MgO\}$ "unit cell" thicknesses of (**a**) $h_{\{MgO\}}$ = 1 nm and (**b**) $h_{\{MgO\}}$ = 5 nm. The bulk energy contributions are independent of the type and orientation of the alloy substrate (and thus of the Mg alloying content at the alloy/oxide interface, x^i_{Mg}). It follows that $\Delta G^f_{\{MgO\}} > \Delta G^f_{\{Al_2O_3\}}$ at T < 610 K, whereas $\Delta G^f_{\{MgO\}} < \Delta G^f_{\{Al_2O_3\}}$ at $T \geq$ 610 K (see dotted vertical line and Sec. 2.5.2). The corresponding *total* Gibbs energies $G^{cell}_{\{MgO\}}$, $G^{cell}_{\{Al_2O_3\}}$ and $G^{cell}_{\{MgAl_2O_4\}}$ of the concerned oxide cells are presented in Fig. 2.4.

The total energies, $G^{cell}_{\{oxide\}}$, *decrease* (i.e. become more negative and thus the corresponding oxides become more stable) with *decreasing* growth temperature (*T*), and *increasing* Mg alloying fraction at the oxide/alloy interface (x^i_{Mg}; see Fig. 2.4). The observed decreases of $G^{cell}_{\{oxide\}}$ with decreasing *T* (and increasing $h_{\{MgO\}}$) are dominated by the corresponding changes in the *bulk* energy contribution $h_{\{MgO\}} \cdot \Delta G^f_{\{oxide\}} / V_{\{MgO\}}$ (compare Figs. 2.4 and 2.5), whereas the slight decrease of $G^{cell}_{\{oxide\}}$ with increasing x^i_{Mg} is

governed by the decrease of the interface-energy contribution, $\gamma_{\langle AlMg \rangle - \{oxide\}} \cdot l^2_{\{oxide\}} / l^2_{\{MgO\}}$

with increasing x^i_{Mg} (see discussion in Sec. 2.5.1). The interface- and surface-energy

contributions to $G^{cell}_{\{oxide\}}$ exhibit only weak temperature dependencies (as compared to the

bulk energy contribution; compare Figs. 2.4, 2.6 and 2.7).

At growth temperatures $T < 610$ K, it holds for the bulk Gibbs energies of oxide

formation: $\Delta G^f_{\{Al_2O_3\}} < \Delta G^f_{\{MgO\}} < \Delta G^f_{\{MgAl_2O_4\}}$ (independent of x^i_{Mg}; cf. Fig. 2.5). Hence,

recognizing also its relatively low interface and surface energies (see Sec. 2.5.1), $\{Al_2O_3\}$

is always the most stable amorphous oxide overgrowth on the $\langle AlMg \rangle$ substrate at $T <$

610 K (independent of x^i_{Mg} and $h_{\{MgO\}}$: i.e. $G^{cell}_{\{Al_2O_3\}} < G^{cell}_{\{MgO\}} < G^{cell}_{\{MgAl_2O_4\}}$ at $T < 610$ K (see

Fig. 2.4; not regarding the possible formation of corresponding crystalline oxide phases

for thicker films formed at elevated temperatures $T > 500$ K [5,11,12,18], see further

below). According to the present calculations, the $\{MgAl_2O_4\}$ overgrowth is never a

thermodynamically preferred oxide overgrowth on the $\langle AlMg \rangle$ substrate.

At growth temperatures $T \geq 610$ K, $\Delta G^f_{\{MgO\}} < \Delta G^f_{\{Al_2O_3\}}$ (Fig. 2.5). Hence, in

particular for increasing oxide-film thicknesses at $T > 610$ K, the relatively low interface

and surface energies of the $\{Al_2O_3\}$ overgrowths (cf. Fig. 2.2) can be overcompensated

by the lower bulk Gibbs energy contribution of the $\{MgO\}$ overgrowth, thereby $\{MgO\}$

becomes the most stable amorphous oxide overgrowth on the $\langle AlMg \rangle$ substrate (compare

Figs. 2.4, 2.6 and 2.7). The thickness, $h^{crit}_{\{MgO\}}$, beyond which the $\{MgO\}$ overgrowth on

the $\langle AlMg \rangle$ substrate becomes thermodynamically more stable than the corresponding

$\{Al_2O_3\}$ overgrowth on the same substrate, *decreases* with increasing growth temperature

above 610 K (due to the bulk energy contribution to $G^{cell}_{\{MgO\}}$ increasing more with

increasing temperature than the bulk energy contribution to $G^{cell}_{\{Al_2O_3\}}$). At $h^{crit}_{\{MgO\}}$ it holds

that $G^{cell}_{\{Al_2O_3\}} = G^{cell}_{\{MgO\}}$, whereas for $h_{\{MgO\}} > h^{crit}_{\{MgO\}}$ it follows that $G^{cell}_{\{MgO\}} < G^{cell}_{\{Al_2O_3\}}$. The

critical thickness, $h^{crit}_{\{MgO\}}$, beyond which the $\{MgO\}$ overgrowth becomes

thermodynamically preferred (with respect to the $\{Al_2O_3\}$ overgrowth) on the most

densely packed $\langle\text{AlMg}\rangle$ substrate (for $x_{\text{Mg}}^{\text{i}} = 0.5$) is shown versus the growth temperature in Fig. 2.8. It follows that $h_{\{\text{MgO}\}}^{\text{crit}}$ decreases from about 5 nm at $T \sim 690$ K to about 2 nm at $T \sim 900$ K. However, at temperatures $T > 700$ K and thicknesses > 1 nm, the crystalline modification of the oxide overgrowth is preferred [9,12,14], which is not considered here.
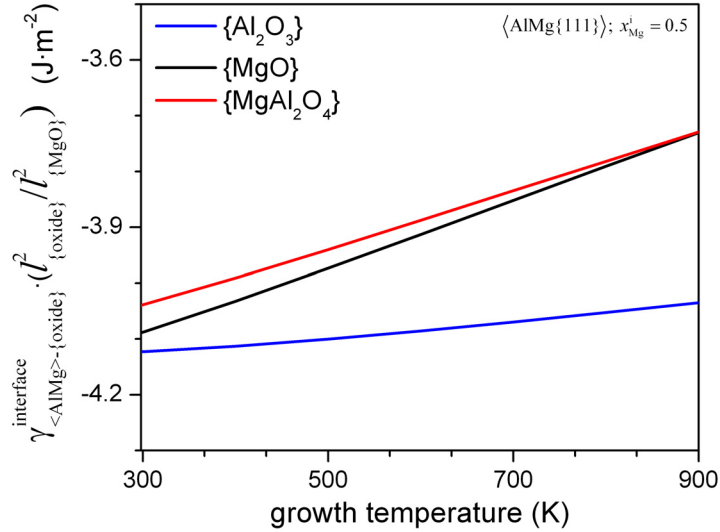
Fig. 2.6: *Interface*-energy contributions $\gamma_{\langle\text{AlMg}\rangle-\{\text{MgO}\}}$, $\gamma_{\langle\text{AlMg}\rangle-\{\text{Al}_2\text{O}_3\}} \cdot l_{\{\text{Al}_2\text{O}_3\}}^2 \big/ l_{\{\text{MgO}\}}^2$ and $\gamma_{\langle\text{AlMg}\rangle-\{\text{MgAl}_2\text{O}_4\}} \cdot l_{\{\text{MgAl}_2\text{O}_4\}}^2 \big/ l_{\{\text{MgO}\}}^2$ (*per unit area of the* $\{\text{MgO}\}$ *"unit cell"*; See Sec. 2.2) to the corresponding total Gibbs energies $G_{\{\text{MgO}\}}^{\text{cell}}$, $G_{\{\text{Al}_2\text{O}_3\}}^{\text{cell}}$ and $G_{\{\text{MgAl}_2\text{O}_4\}}^{\text{cell}}$ of the "unit cells" of the $\{\text{MgO}\}$, $\{\text{Al}_2\text{O}_3\}$ and/or $\{\text{MgAl}_2\text{O}_4\}$ overgrowths on the most densely packed surface of the $\langle\text{AlMg}\rangle$ substrate versus the growth temperature. The interface-energy contributions were calculated for $x_{\text{Mg}}^{\text{i}} = 0.5$ by substitution of Eqs.(2.8), (2.9) and (2.10) in the appropriate terms of Eqs. (2.4a), (2.5a) and (2.5b), respectively (data used taken from Tables 2.1 to 2.4). The area ratios $l_{\{\text{Al}_2\text{O}_3\}}^2 \big/ l_{\{\text{MgO}\}}^2$ and $l_{\{\text{MgAl}_2\text{O}_4\}}^2 \big/ l_{\{\text{MgO}\}}^2$ of the $\{\text{Al}_2\text{O}_3\}$ and $\{\text{MgAl}_2\text{O}_4\}$ "unit cells" with respect to that of the $\{\text{MgO}\}$ "unit cell" are $\left(V_{\{\text{Al}_2\text{O}_3\}}\right)^{2/3} \big/ \left(V_{\{\text{MgO}\}}\right)^{2/3}$ and $\left(V_{\{\text{MgAl}_2\text{O}_4\}}\right)^{2/3} \big/ \left(V_{\{\text{MgO}\}}\right)^{2/3}$, respectively [see Eqs. (2.3a) and (2.3b) in Sec. 2.2]. The corresponding *total* Gibbs energies $G_{\{\text{MgO}\}}^{\text{cell}}$, $G_{\{\text{Al}_2\text{O}_3\}}^{\text{cell}}$ and $G_{\{\text{MgAl}_2\text{O}_4\}}^{\text{cell}}$ of the oxide "unit cells" are presented in Fig. 2.4.
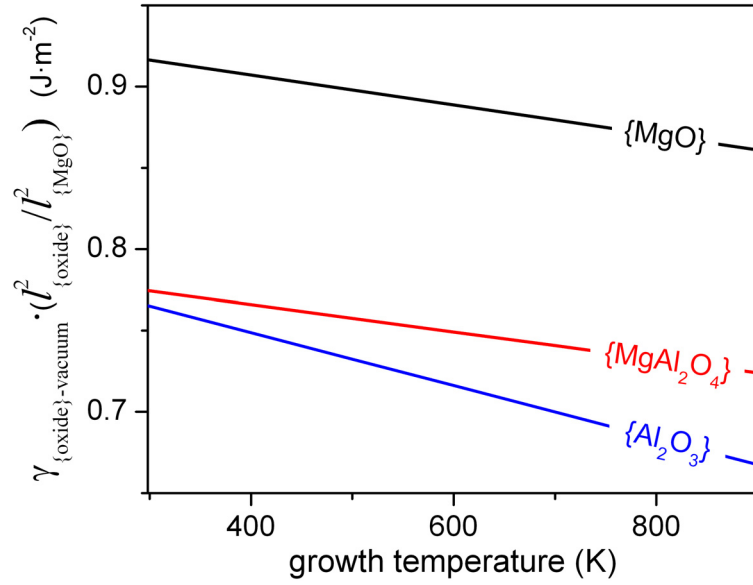
Fig. 2.7: *Surface*-energy contributions $\gamma_{\{MgO\}\text{-vacuum}}$, $\gamma_{\{Al_2O_3\}\text{-vacuum}} \cdot l^2_{\{Al_2O_3\}} / l^2_{\{MgO\}}$ and $\gamma_{\{MgAl_2O_4\}\text{-vacuum}} \cdot l^2_{\{MgAl_2O_4\}} / l^2_{\{MgO\}}$ (*per unit area of the* $\{MgO\}$ *unit cell*; See Sec. 2.2) to the total Gibbs energies $G^{\text{cell}}_{\{MgO\}}$, $G^{\text{cell}}_{\{Al_2O_3\}}$ and $G^{\text{cell}}_{\{MgAl_2O_4\}}$ of the "unit cells" of the $\{MgO\}$, $\{Al_2O_3\}$ and/or $\{MgAl_2O_4\}$ overgrowths versus the growth temperature. The surface-energy contributions were calculated using the appropriate terms in Eqs. (2.4a), (2.5a) and (2.5b), (data used taken from Tables 2.1 and 2.5). The area ratios $l^2_{\{Al_2O_3\}} / l^2_{\{MgO\}}$ and $l^2_{\{MgAl_2O_4\}} / l^2_{\{MgO\}}$ of the $\{Al_2O_3\}$ and $\{MgAl_2O_4\}$ "unit cells" with respect to the $\{MgO\}$ "unit cell" correspond to $\left(V_{\{Al_2O_3\}}\right)^{2/3} \Big/ \left(V_{\{MgO\}}\right)^{2/3}$ and $\left(V_{\{MgAl_2O_4\}}\right)^{2/3} \Big/ \left(V_{\{MgO\}}\right)^{2/3}$, respectively [see Eqs. (2.3a) and (2.3b) in Sec. 2.2]. The corresponding *total* Gibbs energies $G^{\text{cell}}_{\{MgO\}}$, $G^{\text{cell}}_{\{Al_2O_3\}}$ and $G^{\text{cell}}_{\{MgAl_2O_4\}}$ of the oxide "unit cells" are presented in Fig. 2.4.

2.6. Model predictions versus experiment

The thermodynamic model predictions obtained in this work for thin amorphous $\{Al_2O_3\}$, $\{MgO\}$ and $\{MgAl_2O_4\}$ overgrowths on $\langle AlMg \rangle$ substrates (Sec. 2.5) can be compared with experimental observations by our group on the developing microstructure of the initial oxide overgrowth on bare Al-based and Mg-based alloy surfaces by dry, thermal oxidation [9,14,15]; other data are unknown to us.

The amorphous oxide film grown on an Al-0.8 at% Mg alloy upon aging at room temperature for about 1 week under atmospheric conditions (oxide-film thickness: 2.49 ± 0.18 nm), was found to be composed of Al₂O₃ only (AR-XPS analysis), i.e., without the

incorporation of Mg in the native oxide; see Fig. 2.9. Furthermore, ultrathin oxide films grown in a UHV system by thermal oxidation of bare *Al-based* AlMg substrates at $T <$ 425 K also resulted in amorphous oxide films consisting of only Al_2O_3. These results are in full agreement with the present model prediction (see Sec. 2.5.2 and Figs. 2.4 and 2.8). The depth distribution of the Al and Mg cations in the ultra-thin (i.e. 0.8 to 1.6 nm thick) oxide films grown upon oxidation of bare *Mg-based* AlMg substrates at 304 K [9] (as determined by AR-XPS [9,15]), are shown in Fig. 2.10 as function of the pO_2 employed during oxidation. The incorporated Al and Mg cations exhibit Al_2O_3-like and MgO-like local chemical states (cf. Ref. [9]), which are concentrated at the alloy/oxide interface and near the surface, respectively. This depth distribution agrees with the theoretical prediction (see Sec. 2.5.1).
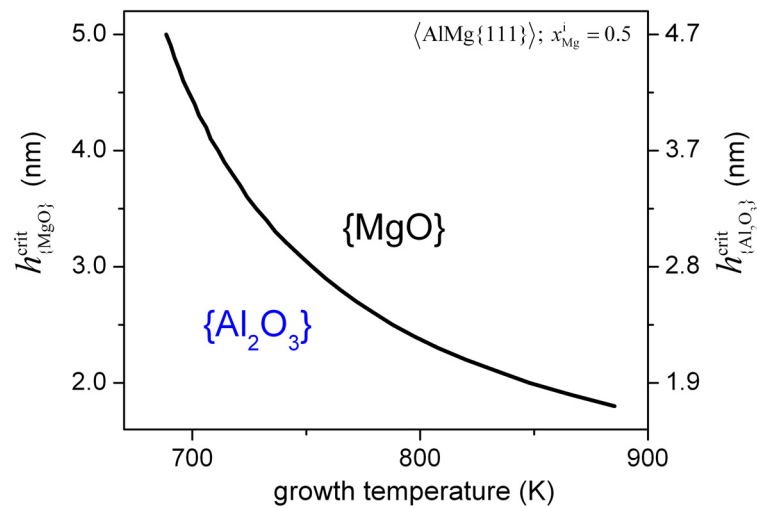
Fig. 2.8: Critical oxide-film thickness, $h_{\{MgO\}}^{crit}$, beyond which the amorphous $\{MgO\}$ overgrowth on the most densely packed surface of the $\langle AlMg \rangle$ substrate (with $x_{Mg}^{i} = 0.5$) becomes thermodynamically more stable than the corresponding amorphous $\{Al_2O_3\}$ overgrowth on the same alloy substrate, as function of the growth temperature. Only for increasing oxide-film thicknesses (at $T > 610$ K), the relatively low interface and surface energies of the $\{Al_2O_3\}$ overgrowth (cf. Fig. 2.2) can be overcompensated by the lower bulk Gibbs energy contribution of the $\{MgO\}$ overgrowth (cf. Fig. 2.5), thereby stabilizing the amorphous $\{MgO\}$ overgrowth (as compared to the $\{Al_2O_3\}$ overgrowth); see Sec. 2.5.2. The thickness, $h_{\{MgO\}}$, of the $\{MgO\}$ overgrowth is related to the corresponding thickness, $h_{\{Al_2O_3\}}$, of the $\{Al_2O_3\}$ overgrowth by Eq. (2.2) in Sec. 2.2.
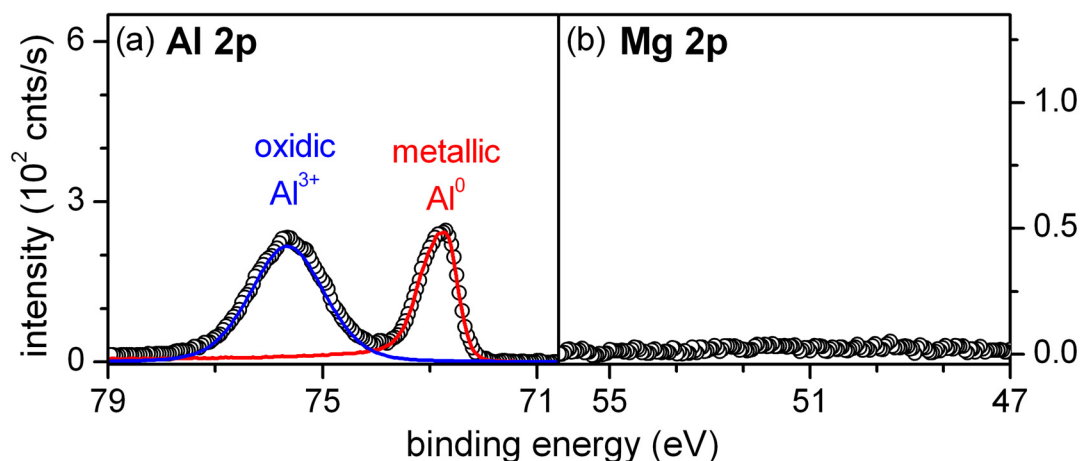
Fig 2.9: (**a**) As-measured and reconstructed Al 2p and (**b**) as-measured Mg 2p XPS spectra [15] of an Al-based Al - 0.8 at% Mg substrate with native oxide (native oxide thickness of 2.49±0.18 nm), as formed after ageing at room temperature under atmospheric conditions, as recorded by AR-XPS. Note that no Mg (i.e. only Al) has been incorporated into the native oxide.
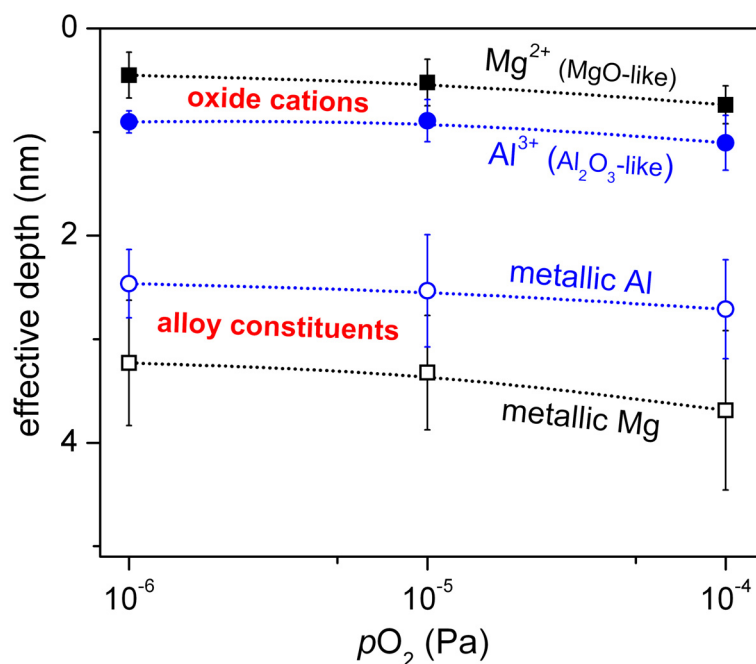
Fig. 2.10: Effective depths of Mg and Al cations in ultra-thin (i.e. 0.8 to 1.6 nm thick), amorphous oxide films grown on *Mg-based* Mg – 2.63% Al substrates by dry, thermal oxidation for 1 hour at $T = 304$ K at various pO_2 (as determined by AR-XPS) [9,15].

At more elevated temperatures $T \geq 400$ K, thermally activated segregation of Mg from the interior of the Al-based AlMg substrates towards the reacting alloy/oxide interface is observed, as evidenced by the appearance of an additional local chemical state of $Mg^{\delta+}$ *at* the reacting alloy/oxide interface; see Fig. 2.11 (for details, see Ref. [14]).

This finding provides the experimental evidence for the predicted driving force (interface-energy reduction) for chemical segregation of Mg from the interior of the $\langle AlMg \rangle$ substrate to the $\langle AlMg \rangle - \{oxide\}$ interface (see Sec. 2.5.1 and Fig. 2.2).
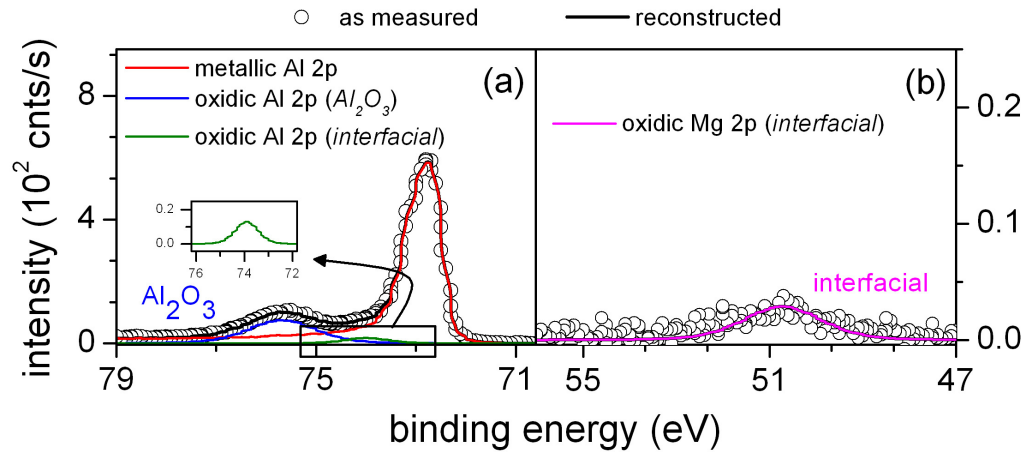
Fig. 2.11: As measured and reconstructed (**a**) Al 2p and (**b**) Mg 2p XPS spectra [15] of an Al-based sputter cleaned Al - 1.1% Mg alloy substrate after exposure for 6×10^3 s to pure oxygen gas at 400 K and $pO_2 = 1 \times 10^{-4}$ Pa. The thickness of this amorphous (HR-TEM analysis) oxide film is 0.62±0.07 nm. For the oxidations at $T \geq 400$ K, thermally activated segregation of Mg from the interior of the alloy substrate to the alloy/oxide interface is evidenced from the appearance of an interfacial Mg-oxide Mg2p peak at 50.60 eV (see Ref. [43] for details). Note that, a 'bulk' MgO local chemical state would give rise to an oxidic Mg2p peak in the range of 51.60 – 51.26 eV [43] (a metallic Mg2p would occur at 49.6 eV [14]).

2.7. Conclusions

For the first time a thermodynamic model to predict the type of initial (amorphous) oxide overgrowth on an *alloy* substrate has been presented that incorporates contributions of bulk, interface and surface energies. The model has been applied to the oxidation of AlMg substrates over the entire composition range. The main results are:

-   At growth temperatures $T < 610$ K, $\{Al_2O_3\}$ is predicted to be the most stable amorphous oxide overgrowth on $\langle AlMg \rangle$ substrates (i.e. independent of the substrate orientation, the Mg alloying content at the alloy/oxide interface and the oxide-film thickness), in agreement with experiment.

- At growth temperatures $T > 610$ K and for increasing oxide-film thicknesses, the relatively low interface and surface energies of the $\{Al_2O_3\}$ overgrowth can be overcompensated by the lower bulk Gibbs energy contribution of the $\{MgO\}$ overgrowth, thereby stabilizing the amorphous $\{MgO\}$ overgrowth (as compared to the $\{Al_2O_3\}$ overgrowth) on the $\langle AlMg \rangle$ substrate.

- The pure $\{MgAl_2O_4\}$ overgrowth, is only stable within a very narrow compositional range and has a stability in between those of the corresponding $\{Al_2O_3\}$ and $\{MgO\}$ overgrowths.

- The interface of the amorphous Al_2O_3 overgrowth with the parent alloy substrate is considerably more stable than the corresponding interfaces of the $\{MgAl_2O_4\}$ and $\{MgO\}$ overgrowths, whereas the differences between the surface energies are much smaller. As a result, for the formation of a multi-component, amorphous oxide film on the $\langle AlMg \rangle$ substrate, interface thermodynamics favours phase separation of $\{Al_2O_3\}$ and $\{MgO\}$ such that $\{Al_2O_3\}$ occurs at the interface and $\{MgO\}$ occurs at the surface. This is in accordance with the experimental observations.

- The model predicted decrease of the interface energies with increasing Mg alloying content *at* the alloy/oxide interface provides a driving force for the Gibbsian segregation of Mg from the interior of the alloy to the concerned alloy/oxide interface. Experimental results support this finding.

- The values of the energies of the crystalline-*amorphous* alloy/oxide interfaces between the alloy substrate and *am*-Al_2O_3, *am*-MgO or *am*-$MgAl_2O_4$, as estimated on the basis of the current model based on the macroscopic atom approach, are consistent with literature values for the energies of corresponding crystalline-*crystalline* metal/oxide interfaces, assessed on the basis of mainly density functional theory.

References

[1] J. G. Li, Mater Chem Phys **47** (1997) 126.

[2] C. T. Campbell, Surf Sci Rep **27** (1997) 1.

[3] F. S. Ohuchi and M. J. Kohyama, Am Ceram Soc **74** (1991) 1163.

[4] S. B. Sinnott and E. C. Dickey, Mater Sci Eng R **43** (2003) 1.

[5] F. Reichel, L. P. H. Jeurgens and E. J. Mittemeijer, Phys Rev B **74** (2006) 144103.

[6] M. W. Finnis, J Phys Cond Mat **8** (1996) 5811.

[7] M. Rühle, J Europ Ceram Soc **16** (1996) 353.

[8] I. J. Bennett, J. M. Kranenburg and W. G. Sloof, J Am Ceram Soc **88** (2005) 2209.

[9] L. P. H. Jeurgens, M. S. Vinodh and E. J. Mittemeijer, Acta Mat **56** (2008) 4621.

[10] T. J. Nijdam, L. P. H. Jeurgens and W. G. Sloof, Acta Mat **51** (2003) 5295.

[11] L. P. H. Jeurgens, W. G. Sloof, F. D. Tichelaar and E. J. Mittemeijer, Phys Rev B (2000) 4707.

[12] F. Reichel, L. P. H. Jeurgens and E. J. Mittemeijer, Acta Mat **56** (2008) 659.

[13] F. Reichel, L. P. H. Jeurgens and E. J. Mittemeijer, J Appl Phys **103** (2008) 093515.

[14] E. Panda, L. P. H. Jeurgens and E. J. Mittemeijer, Submitted (2009).

[15] L. P. H. Jeurgens, M. S. Vinodh and E. J. Mittemeijer, Appl Surf Sci **62** (2000) 4707.

[16] F. R. de Boer, R. Boom, W. C. M. Mattens, A. R. Miedema and A. K. Niessen, Cohesion in metals: transition metal alloys. Amsterdam: North-Holland; 1989 [chapters 2 and 4].

[17] F. Sommer, R. N. Singh and E. J. Mittemeijer, J Alloys and Compounds **467** (2009) 142.

[18] F. Reichel, L. P. H. Jeurgens, G. Richter, P. A. van Aken and E. J. Mittemeijer, Acta Mat **55** (2007) 6027.

[19] M. W. Chase Jr, J. Phys Chem Ref Data, **9** (1998) 156; JANAF Thermochemical Tables, Part I and II (American Institute of Physics, New, York, 1998).

[20] Y. S. Touloukian, R. K. Kirby, R. E. Taylor and T. Y. R. Lee, Thermophysical Properties of Matter: Thermal Expansion, Metallic Elements and Alloys, vol. 12, p. 61. New York: IFI/Plenum; 1975.

[21] Y. S. Touloukian, R. K. Kirby, R. E. Taylor and T. Y. R. Lee, Thermophysical Properties of Matter: Thermal Expansion; Non-metallic Solids, vol. 13, p. 288, 479. New York: IFI/Plenum; 1977.

[22] Powder Diffraction file, 04-0787 from International Center for Diffraction Data (ICDD).

[23] Powder Diffraction file, 00-035-0821 from International Center for Diffraction Data (ICDD).

[24] E. A. Brandes and G. B. Brook, Smithells Metals Reference Book 7th Ed. p. 14-14. Oxford: Butterworth-Heinemann; 1992.

[25] Powder Diffraction file, 29-0063 from International Center for Diffraction Data (ICDD).

[26] Powder Diffraction file, 00-045-0946 from International Center for Diffraction Data (ICDD).

[27] Powder Diffraction file, 00-021-1152 from International Center for Diffraction Data (ICDD).

[28] F. Reichel, L. P. H. Jeurgens and E. J. Mittemeijer, Acta Mat **56** (2008) 5894.

[29] N. Ikemiya, J. Umemoto, S. Hara and K. Ogino, ISIJ Int **33** (1993) 156.

[30] L. R. Ping, A-M Azad and T. W. Dung, Mater Res Bull **36** (2001) 1417.

[31] S. H. Overbury, P. A. Bertrand and G. A. Somorjai, Chem Rev **75** (1975) 547.

[32] F. Reichel, L. P. H. Jeurgens and E. J. Mittemeijer, Acta Mat **58** (2007) 6027.

[33] I. Batyrev, A. Alavi and M. W. Finnis, Phys Rev B **62** (2000) 4698.

[34] W. Zhang and J. R. Smith, Phys Rev Lett **85** (2000) 3225.

[35] R. Schweinfest, S. Köstlmeier, F. Ernst, C. Elsässer, T. Wagner and M. W. Finnis, Philosoph Mag A **81** (2001) 927.

[36] W. Zhang, J. R. Smith and A. G. Evans, Acta Mater **50** (2002) 3803.

[37] A. Hashibon, C. Elsässer and M. Rühle Acta Mater **53** (2005) 5323.

[38] D. Matsunaka and Y. Shibutani, Phys Rev B **77** (2008) 165435.

[39] R. Benedek, M. Minkoff and L. H. Yang, Phys Rev B **54** (1996) 7697.

[40] Y. Zhang and Y. Yao, Mod Phys Lett **22** (2008) 3135.

[41] B. Hallstedt, J Am Ceram Soc **75** (1992) 1497.

[42] P. C. Snijders, L. P. H. Jeurgens and W. G. Sloof, Surf Sci **589** (2005) 98.

[43] E. Panda, L. P. H. Jeurgens and E. J. Mittemeijer, Submitted (2009).

3. The initial oxidation of Al-Mg alloys:

Depth-resolved quantitative analysis by angle-resolved XPS and real-time in-situ ellipsometry

E. Panda, L. P. H. Jeurgens and E. J. Mittemeijer

Abstract

Real-time in-situ spectroscopic ellipsometry (RISE) and in-situ, angle-resolved X-ray Photoelectron Spectroscopy (AR-XPS) have been applied to establish the relationships between the growth kinetics and the developing microstructure of ultra-thin (< 3 nm) oxide films grown on clean Al - 1.12 at.% Mg alloy surfaces by thermal oxidation in the temperature range of $T = 300 - 485$ K. To this end, procedures for the depth-resolved quantitative AR-XPS analysis of ultra-thin, multiple-element and/or multi-phase oxide overgrowths on binary alloy surfaces were developed. As a result, the relationships between the relative depth distributions of Al and Mg in the developing oxide films, the oxide-film growth kinetics and the oxidation-induced compositional changes in the AlMg alloy substrate could be established as function of the oxidation conditions.

3.1. Introduction

The ever-increasing need to optimize the functionality and stability of ultra-thin (< 3 nm) oxide films, as employed in modern catalytic and microelectronic technologies, demands a comprehensive characterization of their microstructures as function of the growth conditions [1-9]. This necessitates the development of new or improved analytical techniques, combinatorial approaches and quantitative procedures for the accurate determination of, in particular, the oxide-film growth kinetics, morphology and structure, as well as of the elemental depth distributions and the chemical state of the ions within the oxide and at the substrate/oxide interface.

It has been demonstrated only very recently [3,10-13] that many important thermodynamic and kinetic aspects of ultra-thin oxide overgrowth, such as e.g. the

amorphous-to-crystalline transition beyond a critical oxide-film thickness and the governing mechanism(s) and driving forces for oxide-film growth, can be revealed in great detail in particular by using a combinatorial experimental approach of real-time in-situ spectroscopic ellipsometry (RISE), angle-resolved X-ray photoelectron spectroscopy (AR-XPS), low energy electron diffraction (LEED) and/or high-resolution transmission electron microscopy (HR-TEM). To this end, detailed procedures were developed for the quantitative AR-XPS and RISE analysis of the microstructural evolution of *single-phase* oxide overgrowths on bare metals (cf. Refs. [2,10,12,14-16]). However, the quantitative AR-XPS and RISE analysis of ultra-thin, *multiple-element* and/or *multi-phase* oxide films on *alloy* substrates has not received such attention up to date [17,18]. Certainly, the development of such procedures for AR-XPS and RISE analysis of these complex oxide films is much more challenging, because more than one substrate constituent can be incorporated into the developing oxide film (e.g. a multiple-element (e.g. spinel) or multi-phase oxide film can be formed), which is associated with compositional changes occurring in the alloy subsurface during oxide growth. In particular if *more than one* of the alloy constituents has a strong affinity for oxygen, like in the Al-Mg system (in contrast with binary alloy systems such as Au-Cu, Ag-Cu or Pt-Al, where one constituent is much nobler than the other), the interrelationships of the microstructural evolution of the growing oxide film, the oxidation-induced compositional changes in the parent alloy substrate and the oxidation conditions can be complicated [3,19].

The current paper presents advanced procedures for the depth-resolved quantitative AR-XPS and RISE analysis of ultra-thin, multiple-element / multi-phase oxide-films on a metallic substrate (see, in particular, Secs. 3.3 and 3.4). The developed procedures were applied to amorphous (Al,Mg)-oxide films grown on bare (i.e. after removal of the native oxide by sputter cleaning) *Al-based* AlMg alloy surfaces by (dry) thermal oxidation in the temperature range of $T = 300 - 485$ K at a partial oxygen pressure of $pO_2 = 1 \times 10^{-4}$ Pa. The present analyses provided detailed knowledge on the developing oxide-film microstructure and the accompanying compositional changes in the alloy subsurface as function of the oxidation temperature (see Sec. 3.5.2).

The alloying constituents Al and Mg are lights metals and therefore find numerous technological applications in areas where weight reduction is a major concern (i.e., in automotive and aerospace industries). Commercially used Al-based Al-Mg alloys generally have a nominal Mg alloying content in the range of 0.5 to 12 at.% [20-22].

Earlier works on the oxidation of AlMg alloy surfaces were mostly conducted at higher temperatures under atmospheric conditions, in the presence of a native Al-oxide film on the alloy surface at the onset of oxidation (e.g. Refs. [23-25]). In only a few investigations, the oxide films were grown under controlled conditions at room temperature in an ultra high vacuum environment [26,27], but without providing a detailed, quantitative analysis of the depth-dependent oxide-film microstructure.

3.2. Experimental

3.2.1   Material and sample preparation

An Al-based AlMg alloy with a Mg content of 1.12 at.% (henceforth referred to as *Al – 1.1% Mg alloy*) was prepared by melting appropriate weight fractions of high purity Al (> 99.99 wt.%) and Mg (> 99.99 wt.%) at a temperature of 973 K in a graphite crucible in a vacuum–melting furnace (base pressure < 10^{-6} mbar after flushing two times with pure Ar gas) and subsequent casting in a copper mould [3]. Next, the surface of the cast ingot was cleaned by chemical etching (20-30 g of NaOH in 500 ml of distilled water) and subsequently cleaned ultrasonically for 900 s in isopropanol. The thus obtained as-cast rod consisted of an AlMg solid-solution matrix with small Al_3Mg_2 precipitates (designated as β phase). To dissolve this β phase, the as-cast rods were sealed in a quartz tube filled with pure Ar gas (sealed after, successively, evacuating, heating and flushing) and then annealed for 72 hours at 693 K and subsequently quenched in distilled water to obtain a single phase material. The thus obtained rods possessed a non-homogeneous grain-size distribution with pores, also at the centre of the rod. To remove the pores, homogenize the grain-size distribution and decrease the average grain size, the rods were hammered (all-sided) down by 10 mm (from a diameter of $\phi = 20$ mm to $\phi = 10$ mm), then subsequently annealed for 900 s at 573 K in a conventional furnace and finally quenched in distilled water to maintain the single-phase nature of the material (see above). Inductive Coupled Plasma–Optical Emission Spectrometry (ICP–OES) analysis of the thus obtained rod showed a nominal Mg concentration of 1.12 at.% and the following impurity concentrations (in ppm wt %): Zn = 70, Mn = 40, Na = 30, C = 72 ± 8, and [Fe, Ca, Cu, Cr, Ti, Y, O] < 10.

Next, disc-shaped specimens ($\phi = 10$ mm; thickness = 1 mm) were cut from the rod using a SiC cut-off wheel. The specimen surfaces were prepared by grinding (using

SiC grinding paper down to 8 μm) and subsequent one-side polishing (using diamond paste down to 0.25 μm grain size) on soft clothes with a mixture of ethanol, soap and distilled water as lubricant. After each polishing step, the specimens were cleaned ultrasonically in ethanol for 900 s. Then, as a final polishing step, the specimen surface was polished with a suspension of 0.05 μm γ-Al_2O_3 grains for 60 s and subsequent ultrasonically cleaned for 1800 s in distilled water and isopropanol consecutively. The arithmetic mean roughness of the polished specimen surfaces was as low as 1.35 nm (as determined by atomic force microscopy for a scanned area of 1×1 μm^2). X-ray diffraction analysis showed that the thus obtained specimens were single-phased (i.e., an Al-Mg solid solution) with a pronounced {100} texture. The average grain size (as observed by light optical microscopy) was within the range of 50-100 μm. The homogeneity of the Mg alloying content in each alloy specimen employed in this study was confirmed by measuring 3 horizontal and 3 perpendicular line scans (lengths 7 - 9 mm; step size 200 μm) on a specimen cross-section of 10 mm diameter by Electron Probe Microanalysis. Finally, all selected specimens were cleaned again ultrasonically for 1800 s in isopropanol prior to their introduction into the UHV system (see Sec. 3.2.2).

3.2.2 *Oxidation*

Each prepared specimen (Sec. 3.2.1) was introduced into a combined UHV system (base pressure < 3×10^{-8} Pa) for in-vacuo specimen cleaning, controlled oxidation and in-situ analysis by e.g. AR-XPS and RISE. Prior to each oxidation experiment, the (native) oxide and other contaminants (generally only adventitious carbon) on the specimen surface were removed by sputter-cleaning (SC) at room temperature with a 1 kV Ar$^+$ beam (rastering the entire sample surface and employing sample rotation at a speed of about 6 °/s) until no other elements than the pure alloy constituents (i.e. Al and Mg) were detected in a measured XPS survey spectrum recorded over the binding energy (BE) range from 0 to 1200 eV (for instrumental details, see Section 3.2.3). The AlMg specimens as obtained after the described SC treatment are further designated as the *sputter-cleaned (SC)* substrates.

Next, ultra-thin (thickness < 3 nm; see Sec. 3.5.1) oxide films were grown in-situ by exposure of the *SC* substrate for 6×10^3 s to pure oxygen gas (ultra-high purity ≥ 99.99990 vol.% with a specified residual gas content of H_2O ≤ 0.5 vpm, N_2 / Ar ≤ 2.0 vpm, C_nH_m ≤ 0.1 vpm and CO_2 ≤ 0.1 vpm) in the temperature (*T*) range of 300 - 485 K at

a partial oxygen pressure of $pO_2 = 1 \times 10^{-4}$ Pa. Uniform sample heating (i.e. with minimal temperature gradients along the sample surface) was performed by adjusting a focused, halogen light beam on the backside of the specimen [12]. The surface temperature was controlled by a type-K thermocouple wire mechanically pressed onto the sample surface. See Ref. [12] for further experimental details.

3.2.3 AR-XPS analysis

In-situ AR-XPS analysis of the specimen surface before and after oxidation was performed using a Thermo VG Thetaprobe system employing monochromatic Al Kα radiation (hv = 1486.68 eV). XPS survey spectra, covering a binding energy (BE) range from 0 eV to 1200 eV, were recorded with a step size and constant pass energy of 0.2 eV and of 200 eV, respectively. For the bare and oxidized alloy surfaces, AR-XPS spectra of the Al 2p (BE range: 70.59 - 79 eV), Mg 2p (BE range: 47 - 56 eV) and O 1s (BE range: 527 – 538.5 eV; as measured only for the oxidized substrate) regions were recorded with a step size and constant pass energy of 0.1 eV and 50 eV, respectively. The AR-XPS measurements were performed in so-called parallel data acquisition mode by detecting the photoelectrons simultaneously over the angular detection range of $(\alpha, \phi) = (23°, 43°)$ to $(\alpha, \phi) = (83°, 94°)$ in six ranges of 10° each (for details, see Ref. [28]). The interdependent angles α and φ are defined as the angles between the directions of the detected photoelectrons and the sample surface normal and the directions of the detected photoelectrons and the incident photon beam, respectively. To maximize the XPS analysis area on the specimen surface, the AR-XPS spectra of the bare and oxidized substrates were measured at nine defined locations on the surface (incident X-ray spot size: ~400 μm), equally distributed over an entire analysis area of 3×3 mm^2.

3.2.4 RISE analysis

In-situ RISE measurements of the SC substrates during in-vacuo heating up and subsequent oxidation were carried out using a J. A. Woollam Co., Inc. rotating compensator ellipsometer M-2000L, equipped with a Xe light source (800 wavelengths, λ, in the range of λ = 245-900 nm), which is mounted directly on the flanges of the UHV reaction chamber (with angles of incidence and reflection of 70° with respect to the sample surface normal). Spectra of the ellipsometric phase shift and amplitude ratio dependent parameters Δ and ψ versus λ (with a range for λ from 350 nm till 850 nm, in

intervals of ~0.8 nm) were recorded from the bare and oxidizing alloy surface over a 2×8 mm^2 elliptically shaped area with a time step of 1.4 s. The measured Δ and ψ values were corrected for possible in-plane and out-of-plane window effects due to strain-induced birefringence of the fused quartz (BOMCO) windows using a Si/SiO$_2$ reference sample. For more, details see Refs. [2,18].

3.3.   AR-XPS spectra reconstruction

For the quantification of the measured AR-XPS spectra, the recorded spectra were first averaged over all measured positions of the sample surface for each angular range of photoelectron detection employed (see Sec. 3.2.3). Next, the thus obtained spectra were corrected for the electron kinetic energy dependent transmission of the spectrometer analyzer by adopting the corresponding correction factor as provided by the manufacturer.

Then, for each detection angle set employed (with α and ϕ taken equal to their values at the centre of each angular detection range; see Sec. 3.2.3), the total primary zero loss (PZL) intensities [16] of the intrinsic (i.e. background corrected) metallic and oxidic Al 2p main peaks, the intrinsic oxidic Mg 2p main peaks (no metallic Mg 2p main peak is discernable; see Sec. 3.3.1) and/or the intrinsic O 1s main peaks were resolved from the measured AR-XPS spectra of the bare and oxidized alloy substrates according to the procedure described in detail in Refs. [16,17,29]. Some alloy system specific details of the employed procedures for quantitative evaluation of the measured AR-XPS spectra recorded from the SC and oxidized AlMg alloy surfaces are given below. The average BE values (with their corresponding standard deviations) as determined for the resolved metallic and oxidic Al 2p main peaks, the oxidic Mg 2p main peaks, as well as for the resolved O1s main peaks, have been gathered in Table 3.1.

Table 3.1. Average binding energy (BE) (and corresponding standard deviations) pertaining to the metallic Al 2p main peak, the various oxidic Al 2p and Mg 2p main peaks and the O 1s main peaks, as resolved from the AR-XPS of the oxidized SC Al – 1.1% Mg substrates within the oxidation temperature range of T = 300 – 485 K. The oxidation temperature range in which each spectral component is discernable in the measured spectra of the oxidized alloy has also been indicated. Since the 'MgO-like' oxidic Mg 2p main peak shifts to lower BE values with increasing oxidation temperature, a corresponding BE range (instead of the temperature-averaged value) has been given. See Sec. 3.3 and Figs. 3.1 and 3.2 for further details.

Main peak	Designation	BE (eV)	T-range (K)
metallic Al 2p		72.71 ± 0.005	300 – 485
oxidic Mg 2p	MgO-like	(51.60 - 51.26) ± 0.06	410 - 485
	interfacial-Mg-oxide	50.60 ± 0.08	400 - 485
oxidic Al 2p	Al$_2$O$_3$-like	75.60 ± 0.08	300 – 485
	interfacial-Al-oxide	73.94 ± 0.13	300 – 425
O 1s	LBE	531.91 ± 0.22	300 – 485
	MBE	532.95 ± 0.20	300 – 485
	HBE	534.32 ± 0.27	300 – 485

3.3.1 AR-XPS spectra of the sputter-cleaned alloy substrate

The subsurface region of the SC alloy substrate was fully depleted of Mg during the sputter cleaning treatment due to the preferential sputtering (removal) of Mg and the concurrent bombardment-enhanced segregation of Mg towards the ion-bombarded alloy surface (see Ref. [30] for details). Consequently, no Mg 2p signal intensities were detected in the measured AR-XPS spectra of the SC Al - 1.1% Mg substrate (i.e. prior to oxidation but after in-vacuo cleaning). Therefore, for each detection angle set employed, only the *metallic* Al 2p main peak was resolved from the measured Al 2p spectrum of the SC substrate, according to the procedure described in Refs. [17,29]. The subtracted inelastic background of the asymmetrically-shaped metallic Al 2p main peak was

calculated using Tougaard's formalism [31] for a homogeneous substrate and adopting a three-parameter universal cross-section for inelastic-electron scattering with $B = 16.5$ eV^2, $C = 230$ eV^2 and $D = 4.5$ eV^2 [32]. The corresponding *total* metallic Al 2p PZL intensity was obtained from the integrated area of the thus-obtained intrinsic Al 2p main peak (which includes its extrapolated intrinsic tail part towards higher BEs [16,17]) by employing the intrinsic surface plasmon excitation probability and bulk plasmon excitation probabilities for the Al 2p photoelectron emission processes in the alloy of 0.02 and 0.11, respectively [16].
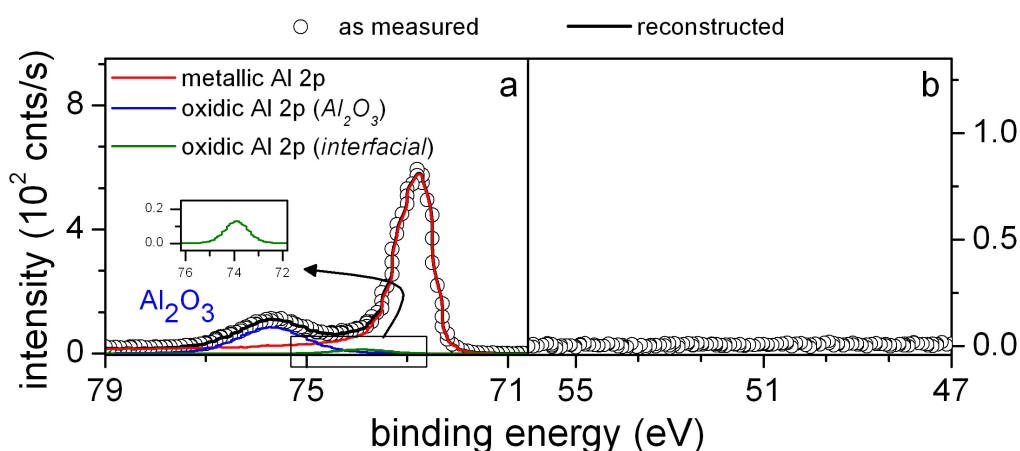
Fig. 3.1: (**a**) As measured and reconstructed Al 2p XPS spectra and (**b**) as-measured Mg 2p XPS spectra of the SC Al - 1.1% Mg alloy substrate after exposure for 6×10^3 s to pure oxygen gas at 300 K and pO$_2$ $= 1 \times 10^{-4}$ Pa for the detection angle set of $(\alpha, \phi) = (38^\circ, 54.75^\circ)$ (see Secs. 3.2.3 and 3.3.2). The 'as-measured' spectra have been corrected for the analyzer transmission function and zero-background offset [16,17]. For details of the procedures used, see Sec. 3.3.

3.3.2   *AR-XPS spectra of the oxidized alloy substrate*

For each detection angle, the metallic and oxidic Al 2p main peaks, the oxidic Mg 2p main peaks as well as the O 1s main peaks, in the measured spectra of the oxidized alloy substrate were resolved, according to the procedures described in Refs. [17,29]. Typical spectral reconstructions of the measured Al 2p and Mg 2p XPS spectra of an oxidized SC Al - 1.1% Mg substrate (oxidized for 6×10^3 s at pO$_2 = 1 \times 10^{-4}$ Pa and at 300 K and 475 K respectively) are presented in Figs. 3.1(a,b) and 3.2(a-d) respectively. Figs. 3.1(a,b) show

typical measured and reconstructed Al 2p and Mg 2p spectra pertaining to an detection angle set of $(\alpha, \phi) = (38°, 54.75°)$, whereas Figs. 2(a-d) show exemplary spectra recorded at near-normal and grazing detection angle sets of $(\alpha, \phi) = (28°, 46.81°)$ and $(\alpha, \phi) = (78°, 89.26°)$, respectively. The corresponding (i.e., corresponding with Figs. 3.2(a-d)) spectral reconstructions of the O 1s spectra are shown in Figs. 3.3(a,b).
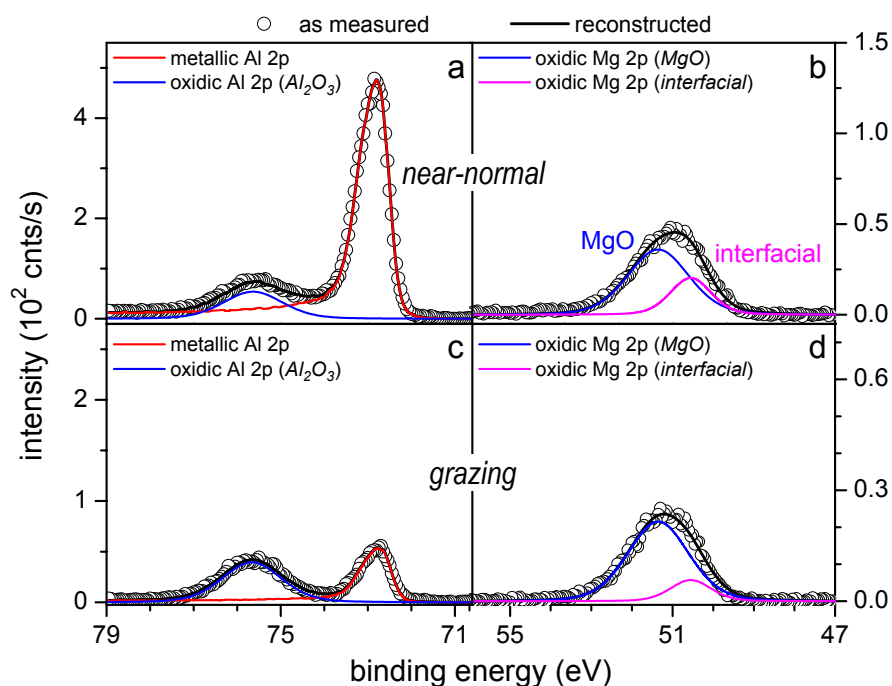
Fig. 3.2: As measured and reconstructed Al 2p and Mg 2p XPS spectra of the SC Al - 1.1% Mg alloy substrate after exposure for 6×10^3 s to pure oxygen gas at 475 K and $p\mathrm{O}_2 = 1 \times 10^{-4}$ Pa for a set of **(a,b)** near-normal and **(c,d)** grazing detecting angle-sets of $(\alpha, \phi) = (28°, 46.81°)$ and $(\alpha, \phi) = (78°, 89.26°)$, respectively (see Secs. 3.2.3 and 3.3.2). See caption of Fig. 3.1 for further details.
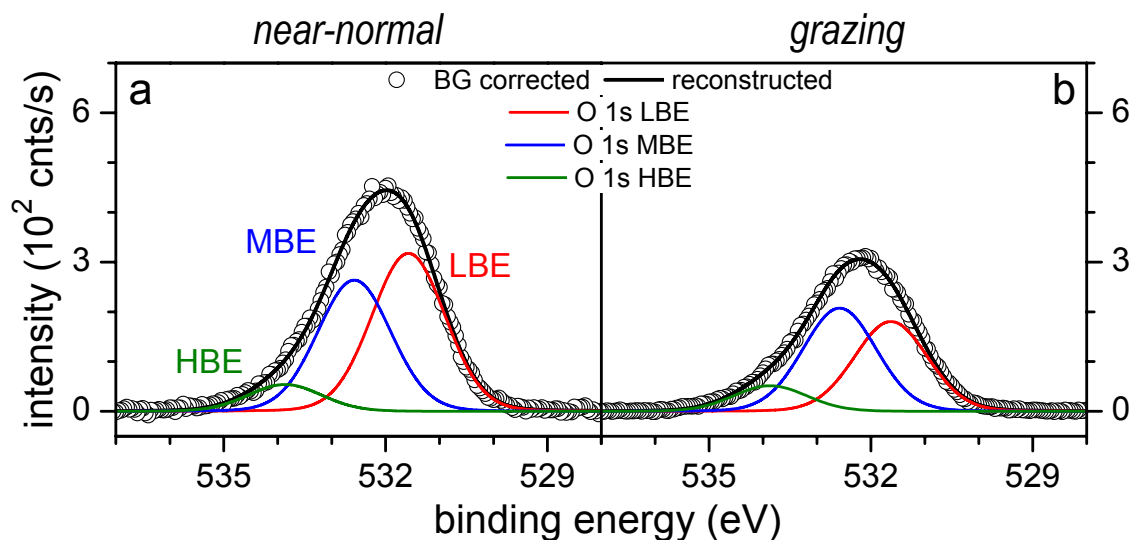
Fig. 3.3: As measured and reconstructed O 1s spectra of the SC Al - 1.1% Mg alloy substrate (oxidized for 6×10^3 s at 475 K and $pO_2 = 1 \times 10^{-4}$ Pa) for a set of (**a**) near-normal and (**b**) grazing detecting angle-sets of $(\alpha, \phi) = (28°, 46.81°)$ and $(\alpha, \phi) = (78°, 89.26°)$, respectively (see Secs. 3.2.3 and 3.3.2.C). See caption of Fig. 3.1 for further details.

A.   Metallic and oxidic Al 2p spectra

The measured Al 2p spectra of the oxidized Al - 1.1% Mg substrates are constituted of one metallic Al 2p main peak and, depending on the oxidation condition (see Sec. 3.5.2), up to two oxidic Al 2p main peaks at the higher-BE side of the resolved Al 2p envelop (further designated as '*Al₂O₃-like*' and '*interfacial-Al-oxide*' component, respectively; see Table 3.1, Figs. 3.1(a), 3.2(a,c) and Sec. 3.5.2).

The *metallic* and *oxidic* Al 2p main peaks (plus their inelastic backgrounds) were simultaneously resolved by least-squares fitting of corresponding reconstructed main peaks plus their backgrounds to the measured Al 2p peak envelope, as described below. The shape of the intrinsic (i.e. the background corrected) *metallic Al 2p* main peak was adopted from the shape of the intrinsic metallic Al 2p main peak, as resolved from the corresponding spectrum of the bare alloy substrate (Sec. 3.3.1). The shape of the intrinsic *oxidic Al 2p* main peaks were described by a symmetric, mixed Gaussian-Lorentzian line-shape functions with identical Gaussian fractions (fG), but with different positions, heights and full-width-at-half-maximums (FWHM). Only the positions and heights were allowed to vary with detection angle (i.e. fG and FWHM were taken the same for all

detection angles) [17]. For each iteration in the fitting procedure (see below), the thickness-dependent backgrounds of the metallic and oxidic main peaks were calculated using Tougaard's formalism [31] for the case of a homogeneous alloy substrate covered with a thin γ-Al$_2$O$_3$ film of uniform thickness, while adopting different three-parameter universal cross sections for inelastic-electron scattering [31] in the alloy (as given in Sec. 3.3.1) and in the oxide (as taken non-zero for energy losses larger than the band gap energy of 5.7 eV for γ-Al$_2$O$_3$ with B = 3.8 eV^2, C = 99 eV^2 and D = 23.5 eV^2). The value of the oxide-film thickness, as required in the aforementioned inelastic background calculations, was determined (in each iteration of the fitting procedure; see below) from the ratio of total PZL intensities of the resolved metallic and oxidic Al 2p main peaks in the Al 2p spectrum (see Secs. 3.4.1.A and 3.4.1.B). For further details, see Refs. [17], [16].

Linear-least-squares (LLS) fitting of the total reconstructed to the measured spectra was performed simultaneously for the entire set of AR-XPS Al 2p spectra recorded at different detection angle sets from a single oxidized alloy substrate. The positions and heights of the metallic and oxidic Al 2p main peaks, as well as the FWHMs of the oxidic Al 2p main peaks (see above), were employed as fit parameters, while allowing only the heights of the metallic and oxidic Al 2p main peaks, as well as the position of the dominant '*Al$_2$O$_3$-like*' oxidic Al 2p main peak, to vary also with detection angle.

B.   Oxidic Mg 2p spectra

As for the measured AR-XPS spectra of the SC Al - 1.1% Mg substrate (see Sec. 3.3.1), no *metallic* Mg signal intensities were detected in the measured AR-XPS spectra of the oxidized Al - 1.1% Mg substrates (see Figs. 3.1(b), 3.2(b,d) and Table 3.1).[1] The measured Mg 2p spectra of the oxidized SC alloy substrates are only constituted of up to two oxidic Mg 2p main peaks at the lower and higher BE side of the Mg 2p envelop (further designated as '*MgO-like*' and '*interfacial-Mg-oxide*' component, respectively; see

---

[1] Since the metallic Mg 2p intensity is absent in the measured spectra of the SC and oxidized Al - 1.1% Mg substrates, a possible overlap of the second bulk plasmon peak associated with the metallic Mg 2p main peak with the metallic and oxidic Al 2p main peaks can be ruled out here. This significantly simplifies the procedure for spectra evaluation of the Al 2p region (see Sec. 3.3.2.A), as compared to that for the *Mg-based* MgAl alloy substrates as described in detail in Ref. [17].

Figs. 2(b,d), Table 3.1 and Sec. 3.5.2). The oxidic Mg 2p main peaks plus their individual inelastic backgrounds were constructed analogously to the treatment applied to the oxidic Al 2p main peaks (see Sec. 3.3.2.A; while using an oxide-film thickness value for the inelastic background calculations as obtained from the previous reconstruction of the corresponding Al 2p spectrum. Only the heights of the oxidic Mg 2p main peaks were allowed to vary also with detection angle.

C.   O 1s spectra

For the oxide films grown in this study, the measured O 1s spectra of the oxidized SC alloy substrates were always constituted of three O 1s main peaks: one at the lower-BE-side, one in the centre and one at the higher-BE side of the O 1s envelop, further designated as lower-BE (LBE), middle-BE (MBE) and higher-BE component (see Figs. 3.3(a,b) and Table 3.1). The PZL intensities of the LBE, MBE and HBE O 1s main peaks were resolved from the as-measured O1s AR-XPS spectra according to the procedure described in Ref. [17]; i.e. by subtraction of a Shirley-type background and subsequent LLS fitting with three Gaussian-Lorentzian line shape functions with equal FWHMs and Gaussian fractions, but with different positions and heights. The fitting was performed simultaneously for the entire set of O 1s spectra recorded at different detection angle sets from a single oxidized alloy substrate, while employing the positions, heights, FWHM and the Gaussian fraction of the O 1s main peaks as fit parameters (and allowing only the heights of the three O 1s main peaks to vary also with detection angle).

3.4.   Quantification; oxide-film constitution, composition and growth kinetics

3.4.1   AR-XPS

A.   Primary Zero Loss Photoelectron intensities

AR-XPS quantification of each of the grown oxide films was performed using the resolved Al 2p, Mg 2p and O 1s main peaks from the corresponding measured AR-XPS spectra of the oxidized alloy substrate (as recorded at the six different detection angle sets; see Sec. 3.2.3). To this end, theoretical Al 2p, Mg 2p and O 1s PZL intensities were

calculated (as indicated below) and fitted to the corresponding experimentally resolved PZL intensities, while adopting the film thickness and the composition of the oxide-film as fit parameters in the calculation of the theoretical PZL intensities (see what follows).

Since no *metallic* Mg 2p signal intensities were detected from the measured AR-XPS spectra of the SC and oxidized Al - 1.1% Mg substrates under study (see Secs. 3.3.1 and 3.3.2.B), the *total metallic* PZL intensity, $I_{(Al,Mg),sub}$, for a given detection angular set (α, ϕ), is given by the total metallic Al 2p PZL intensity [17,28,29]

$$I_{(Al,Mg),sub} = I_{Al,sub} = K \cdot \cos\alpha \cdot C_{Al,sub} \cdot \sigma_{Al} \cdot \lambda_{Al,sub} \cdot W_{Al} \cdot \exp\left(-\frac{L}{\lambda_{Al,ox} \cdot \cos\alpha}\right), \qquad \textbf{(3.1)}$$

where K is an instrumental factor; $C_{Al,sub}$ denotes the total molar density of Al atoms in the Mg-depleted subsurface region of the alloy substrate (as taken equal to that of Al metal); σ_{Al} and W_{Al} are the total Al 2p photoionization cross section and asymmetry factor (describing the intrinsic anisotropy of σ_{Al} [28,33]), respectively; $\lambda_{Al,sub}$ and $\lambda_{Al,ox}$ represent the effective attenuation lengths (EAL) of the detected Al 2p photoelectrons in the alloy substrate and in the oxide film (of uniform thickness L), respectively [28,33].

Similarly, the corresponding *oxidic Al 2p* ($I_{Al,ox}$), *oxidic Mg 2p* ($I_{Mg,ox}$) and *oxygen* ($I_{O,ox}$) total PZL intensities are given by [17,28,29]

$$I_{Al,ox} = K \cdot C_{Al,ox} \cdot \sigma_{Al} \cdot \lambda_{Al,ox} \cdot W_{Al} \cdot \cos\alpha \cdot \left[1 - \exp\left(-\frac{L}{\lambda_{Al,ox} \cdot \cos\alpha}\right)\right], \qquad \textbf{(3.2a)}$$

$$I_{Mg,ox} = K \cdot C_{Mg,ox} \cdot \sigma_{Mg} \cdot \lambda_{Mg,ox} \cdot W_{Mg} \cdot \cos\alpha \cdot \left[1 - \exp\left(-\frac{L}{\lambda_{Mg,ox} \cdot \cos\alpha}\right)\right], \qquad \textbf{(3.2b)}$$

$$I_{O,ox} = K \cdot C_{O,ox} \cdot \sigma_{O} \cdot \lambda_{O,ox} \cdot W_{O} \cdot \cos\alpha \cdot \left[1 - \exp\left(-\frac{L}{\lambda_{O,ox} \cdot \cos\alpha}\right)\right], \qquad \textbf{(3.2c)}$$

respectively. Here $C_{Al,ox}$, $C_{Mg,ox}$ and $C_{O,ox}$ denote the overall molar densities of Al, Mg and O ions in the grown oxide film; σ_{Al}, σ_{Mg} and σ_{O} are the total Al 2p, Mg 2p and O 1s photoionization cross sections; W_{Al}, W_{Mg} and W_{O} are the Al 2p, Mg 2p and O 1s asymmetry factors; $\lambda_{Al,ox}$, $\lambda_{Mg,ox}$ and $\lambda_{O,ox}$ are the EALs of the detected Al 2p, Mg 2p and O 1s photoelectrons in the oxide film, respectively.

Further, the *total oxidic* PZL intensity, i.e. $I_{(Al,Mg),ox} = I_{Al,ox} + I_{Mg,ox}$, was approximated by [17]

$$I_{(Al,Mg),ox} = K \cdot C_{(Al,Mg),ox} \cdot \sigma^{av}_{(Al,Mg)} \cdot \lambda^{av}_{(Al,Mg),ox} \cdot W^{av}_{(Al,Mg)} \cdot \cos\alpha \cdot \left[1 - \exp\left(-\frac{L}{\lambda^{av}_{(Al,Mg),ox} \cdot \cos\alpha} \right) \right],$$

(3.3)

where $C_{(Al,Mg),ox} = C_{Al,ox} + C_{Mg,ox}$. The *averaged* Al 2p – Mg 2p total photoionization cross section, asymmetry factor and EAL in Eq. (3.3) are defined in Ref. [17]: i.e.

$$\sigma^{av}_{(Al,Mg)} \equiv \left[(1 - x_{Mg}) \cdot \sigma_{Al} + x_{Mg} \cdot \sigma_{Mg} \right] \quad , \quad W^{av}_{(Al,Mg)} \equiv \left[(1 - x_{Mg}) \cdot W_{Al} + x_{Mg} \cdot W_{Mg} \right] \quad \text{and}$$

$\lambda^{av}_{(Al,Mg),ox} \equiv \left[(1 - x_{Mg}) \cdot \lambda_{Al,ox} + x_{Mg} \cdot \lambda_{Mg,ox} \right]$, respectively (with x_{Mg} as the atom fraction of Mg in the Al-based AlMg alloy).

B.   Oxide-film thickness and composition

For each of the grown oxide films, average values for the oxide-film thickness (L), as well as for the total cation ($C_{(Al,Mg),ox}$; i.e. Al plus Mg) and anion ($C_{O,ox}$) molar densities in the grown oxide film, were calculated by least-squares minimization of the differences of the measured intensity ratios of $I_{Al,sub}/I_{O,ox}$, $I_{Al,sub}/I_{(Al,Mg),ox}$ and $I_{O,ox}/I_{(Al,Mg),ox}$ and calculated values for these intensity ratios (see Eqs. 3.1, 3.2c and 3.3), following iterative calculation procedures as described in Ref. [17]; the fitting was performed to the measured intensity ratios applying 5 different methods of calculation to each of the six detection angle sets and using the physical constants given in Table 3.2. Only intensity ratios were considered in the fitting procedure, because the instrumental factor K in Eqs. 3.1, 3.2c and 3.3 is unknown. The EALs, as required in the calculations (i.e. $\lambda_{Al,ox}$, $\lambda^{av}_{(Al,Mg),ox}$ and $\lambda_{O,ox}$), were determined using procedures as referred to in Sec. 3.4.1.A, while adopting the material properties of either MgO, γ-Al$_2$O$_3$ or MgAl$_2$O$_4$ (see Table 3.2); see what follows.

Table 3.2. Physical constants used for the quantification of the AR-XPS spectra recorded from the oxidized Al-based Al − 1.12% Mg alloys. The symbols ρ, E, σ and β denote the density, band gap, total photoionization cross-sections and asymmetry factors, respectively. See Sec. 3.4 for details.

Material	Constant	Value	Unit	Ref.
Al metal	ρ_{Al}	2.669×10^3	kg/m^3	[29]
Al - 1.1% Mg	$\rho_{Al-1.1\% Mg}$	2.685×10^3	kg/m^3	from XRD in this work
γ-Al$_2$O$_3$	$\rho_{\gamma\text{-Al}_2O_3}$	3.63×10^3	kg/m^3	[29]
	$E_g^{\gamma\text{-Al}_2O_3}$	5.7	eV	[29]
MgAl$_2$O$_4$	$\rho_{MgAl_2O_4}$	3.64×10^3	kg/m^3	[17]
	$E_g^{MgAl_2O_4}$	5.8	eV	[17]
MgO	ρ_{MgO}	3.58×10^3	kg/m^3	[17]
	E_g^{MgO}	7.8	eV	[17]
alloy/oxide	$\sigma_{Al\,2p}$	7.6704×10^{-25}	m^2	[33]
	$\sigma_{Mg\,2p}$	4.7765×10^{-25}	m^2	
	$\sigma_{O\,1s}$	37.9471×10^{-25}	m^2	
	$\beta_{Al\,2p}$	0.9370	-	[33]
	$\beta_{Mg\,2p}$	0.8557	-	
	$\beta_{O\,1s}$	1.9915	-	

The resulting thickness values for the oxidized Al - 1.1% Mg substrates, as determined by adopting the physical properties of either γ-Al$_2$O$_3$ or MgO or MgAl$_2$O$_4$ in the quantification, can be compared in Figs. 3.4(a,b). It follows that similar thickness values with similar standard deviations are obtained, irrespective of the type of oxide phase used in the calculation. The oxide phase adopted in the definitive quantification procedure was selected on the basis of the estimated Mg content in the grown oxide film, as described next.
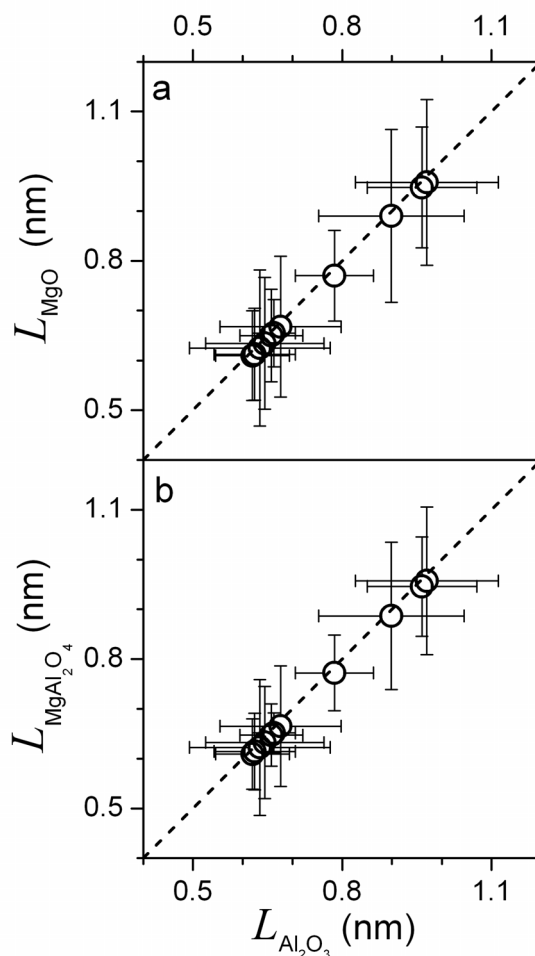
Fig. 3.4: Oxide-film thickness values ($L_{Al_2O_3}$) and corresponding standard deviations, as calculated by adopting the EALs and molar densities for γ-Al$_2$O$_3$, versus the corresponding values as determined by using the EALs and molar densities for **(a)** MgO (thickness: L_{MgO}) or **(b)** MgAl$_2$O$_4$ (thickness: $L_{MgAl_2O_4}$) (see Sec. 3.4.1.B and Table 3.2). The data pertain to the oxidation of the SC Al − 1.1% Mg substrate for 6×10^3 s in the temperature range of 300 − 485 K at a pO$_2$ of 1×10^{-4} Pa.

If no distinct oxidic Mg 2p main peak was detected by AR-XPS (see Fig. 3.1(b) and Sec. 3.3.2.B), the physical properties of γ-Al$_2$O$_3$ were adopted in the aforementioned quantification (see Table 3.2). On the other hand, if an oxidic Mg 2p signal was distinguishable in the measured AR-XPS of the oxidized alloy, the quantification was performed by adopting the properties of γ-Al$_2$O$_3$, MgAl$_2$O$_4$ and/or MgO, as decided on the basis of the estimated Al/Mg cationic ratio in the grown oxide film (i.e. $C_{Al,ox}/C_{Mg,ox}$), and as described in the next paragraph. This estimate of $C_{Al,ox}/C_{Mg,ox}$ was determined

from Eqs. (3.2a) and (3.2b) using the calculated thickness value, L, as obtained in the first step of the procedure (i.e., employing the material properties of γ-Al_2O_3; see above discussion and Figs. 3.4(a,b) for justification).

If the thus obtained estimate for $C_{Al,ox}/C_{Mg,ox}$ lies in between the corresponding cationic ratios for γ-Al_2O_3 and $MgAl_2O_4$ (i.e. $C_{Al,ox}/C_{Mg,ox} > 2$) then one set of values for L, $C_{(Al,Mg),ox}$ and $C_{O,ox}$ was calculated by adopting the properties of γ-Al_2O_3 (which comprises a total of 30 values; i.e. 5 different methods of calculation applied to each of six different detection angle sets; see above). Next, another set of values for L, $C_{(Al,Mg),ox}$ and $C_{O,ox}$ was calculated by adopting the properties of $MgAl_2O_4$. The final values and errors of L, $C_{(Al,Mg),ox}$ and $C_{O,ox}$ for the grown oxide film were now taken equal to the averages and standard deviations of the thus obtained 60 calculated values for L, $C_{(Al,Mg),ox}$ and $C_{O,ox}$.

Analogously, if the estimate for $C_{Al,ox}/C_{Mg,ox}$ falls in between those for $MgAl_2O_4$ and MgO (i.e. $0 < C_{Al,ox}/C_{Mg,ox} < 2$), two sets of values for L, $C_{(Al,Mg),ox}$ and $C_{O,ox}$ were determined by adopting the physical properties of $MgAl_2O_4$ and MgO (Table 3.2) in separate runs. Final values and errors of L, $C_{(Al,Mg),ox}$ and $C_{O,ox}$ were taken equal to the averages and standard deviations of the thus obtained 60 calculated values for L, $C_{(Al,Mg),ox}$ and $C_{O,ox}$.

C. Oxide-film constitution

The effective depth below the specimen surface, $\langle z_{i,ox} \rangle$, of each of the identified chemical species within the oxide film was calculated from the corresponding PZL intensities, as resolved for a set of near-normal and grazing detection angle sets (α_1, ϕ_1) and (α_2, ϕ_2), respectively, according to [17]

$$\langle z_{i,ox} \rangle = \lambda_{i,ox} \cdot \frac{\cos\alpha_1 \cdot \cos\alpha_2}{\cos\alpha_1 - \cos\alpha_2} \cdot \ln\left[\frac{I_{i,ox}(\alpha_1) \cdot W_i(\alpha_2, \phi_2)}{I_{i,ox}(\alpha_2) \cdot W_i(\alpha_1, \phi_1)}\right], \tag{3.4}$$

where the ith species corresponds with one of the resolved oxidic Al 2p, oxidic Mg 2p or O 1s main peaks (see Figs. 3.1-3.3 and Sec. 3.3.2). By using various combinations of near-normal and grazing detection angle sets (in the ranges of $\alpha_1 = 25\text{-}45°$ and $\alpha_2 = 65\text{-}$

80°, respectively, where ϕ_1 and ϕ_2 follow directly from α_1 and α_2 according to the experimental set-up [17]), four values of $\left\langle z_{i,ox} \right\rangle$ were determined for each identified chemical species. A relatively small spread in the effective depth values for a single chemical species indicates that the species is concentrated at a specific depth below the surface. A relatively large spread of the thus obtained effective depth values for a single chemical species then indicates a relatively large spread of the chemical species concerned around the corresponding averaged value of $\left\langle \overline{z_{i,ox}} \right\rangle$ [17].

3.4.2   RISE data evaluation

The oxide-film growth kinetics and optical parameters (i.e. the complex index of refraction, $N = n - ik$, where n and k denote the index of refraction and the extinction coefficient, respectively) of the developing oxide-film were determined by fitting model descriptions of the ellipsometric spectra $\psi(\lambda)$ and $\Delta(\lambda)$ (for $\lambda = 245 - 900$ nm) as a function of the oxidation time (t) to the corresponding measured data of $\psi(\lambda, t)$ and $\Delta(\lambda, t)$ using the WVASE32 software package [18,34]. To this end, a (physically) realistic model for the optical response of the studied alloy-substrate/oxide-film system was constructed, further designated as the *'alloy|EMA|Cauchy'* model.

First, the optical properties of the parent alloy substrate at the growth temperature [i.e., $n(\lambda, t = 0)$ and $k(\lambda, t = 0)$] were directly determined (for each conducted oxidation experiment) from the measured spectra of $\psi(\lambda)$ and $\Delta(\lambda)$ of the SC alloy substrate at the growth temperature prior to oxidation [2,10]. In this way, the optical model description accounts for the compositional changes in the surface region of the alloy substrate prior to oxidation as induced by:

   (i)   the preferential sputtering of Mg and the concurrent bombardment enhanced Gibbsian segregation of Mg to the free alloy surface during the sputter cleaning step (see Ref. [30] and Secs. 3.3.1 and 3.5.2).

   (ii) the Gibbsian segregation of Mg to the free alloy surface during in-vacuo heating up to the desired oxidation temperature (see Sec. 3.5.2).
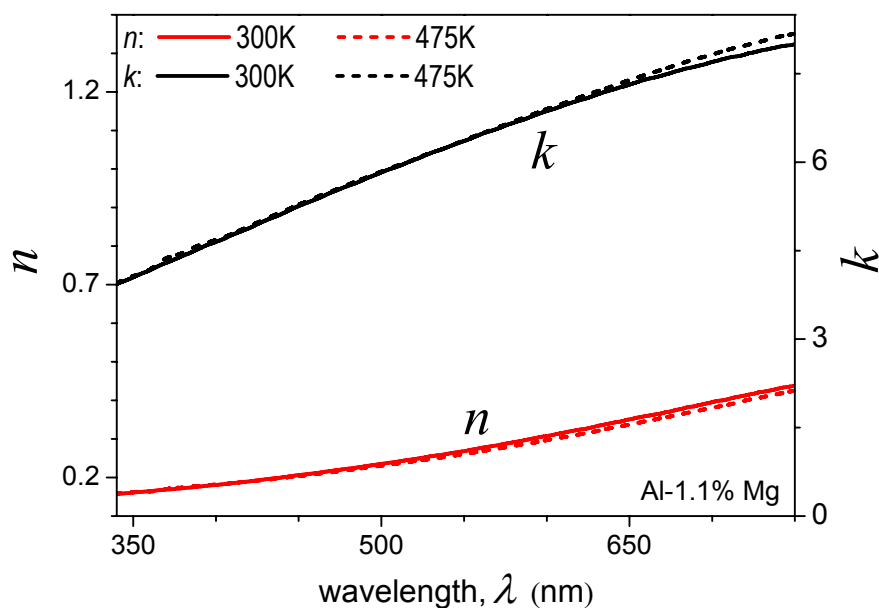
Fig. 3.5: The values of the index of refraction (*n*) and the extinction coefficient (*k*) as function of the wavelength (λ), as determined by RISE for the SC Al – 1.1% Mg substrate after in-situ heating to 300K and 475K (under UHV conditions), but prior to subsequent oxidation (see Sec. 3.4.2).

Typical spectra of $n(\lambda, t = 0)$ and $k(\lambda, t = 0)$ for the SC Al - 1.1% Mg substrate at 300K and 475K (i.e. directly before subsequent oxidation) are shown in Fig. 3.5. It follows that the optical constants of the SC Al – 1.1% Mg substrate have only a very weak temperature dependence in the studied range from T = 300 - 485 K. Furthermore, no apparent changes of $n(\lambda)$ and $k(\lambda)$ occurred after successive cycles of sputter cleaning, annealing and subsequent oxidation (Sec. 3.2.2). This is consistent with our previous findings [12] that sample rotation during sputter cleaning very effectively suppresses roughening of ion-bombarded crystalline solid surfaces (which would lead to a change of, in particular, the refractive index, *n* [18]).

Next, oxide overgrowth was modelled by adopting an oxide layer of variable uniform thickness, $L^{ox}(t)$, on top of the alloy substrate. As revealed by the AR-XPS analysis of the oxidized SC Al - 1.1% Mg alloy, the grown oxide films are constituted of an Al-oxide phase up to oxidation temperatures of $T \leq 385$ K, whereas a mixed (Al,Mg)-oxide phase is formed at more elevated temperatures $T \geq 400$ K (cf. Sec. 3.5.2). The refractive index of the thickening oxide layer as a function of the wavelength can be described by a Cauchy-type dependence: i.e. $n(\lambda) = A + B/\lambda^2 + C/\lambda^4$ (with the constants *A*, *B* and *C* designated as the Cauchy coefficients). The Cauchy parameter *A* for each

grown oxide film was determined in a separate fit parameter study (see below; with an average value of $A = 1.674$ as determined for all the oxide films grown in this study). The Cauchy parameters B and C (which describe the wavelength dependence of n) were taken equal to those of α-Al$_2$O$_3$ (i.e. $B = 7.15 \cdot 10^{-3}$ µm^2 and $C = -2.06 \cdot 10^{-4}$ µm^4 [10]). Furthermore, the extinction coefficient of the transparent oxide layer can be taken zero over the wavelength range considered: i.e. $k(\lambda) \equiv 0$.

To account for the characteristic ellipsometric absorption due to the presence of the metal/oxide interfacial region for the ultra-thin (< 3 nm) oxide overgrowths on metals and alloy surfaces (as required for an accurate model description of $\Delta(\lambda, t)$ and, in particular, $\Psi(\lambda, t)$; for details, see Refs. [2,8,10]), an intermediate layer of submonolayer thickness, $L^{int}(t) \leq {}^1/_4 \cdot$ML (i.e., ≤ 0.05 nm; see below) was adopted in-between the parent alloy substrate and the thickening oxide layer (see also discussion on the 'interfacial-Al-oxide' Al 2p component in Sec. 3.5.2). The optical constants of this intermediate layer were described by an Effective Medium Approximation (EMA) based on the Maxwell-Garnett formulation, while adopting the top oxide layer and the parent alloy substrate with the prevailing surface composition as the matrix and the inclusion (with a corresponding EMA fraction, f^{EMA}), respectively [2,10,18,35]. This implies that, for segregated Mg alloy surfaces (see Sec. 3.5.2), the corresponding EMA layer also partly incorporates the optical constants of Mg.

Since the oxide films grown in this study are very thin (< 1.5 nm), a strong correlation occurs for the fit parameters $L^{ox}(t)$, $L^{int}(t)$, A and f^{EMA} upon the simultaneous fitting of $\Delta(\lambda, t)$ and $\Psi(\lambda, t)$ as a function of t [2,10]. These correlations were avoided by separate determination of values for A and f^{EMA} and using the thus obtained values as constants in the final fitting of $\Delta(\lambda, t)$ and $\Psi(\lambda, t)$ to the measured data to determine values for $L^{ox}(t)$ and $L^{int}(t)$. To this end, two different approaches were adopted, as described below.

In the *first approach*, individual estimates of A were determined at the end of each oxide growth curve (i.e. after $t = 6 \times 10^3$ s) by fitting the calculated to the corresponding measured spectra of $\Delta(\lambda)$ and $\Psi(\lambda)$ for $t = 6 \times 10^3$ s, while taking the thickness, $L^{ox}(t = 6 \times 10^3$ s), of the top layer equal to the corresponding thickness value as determined by AR-XPS at the end of the oxidation (see Sec. 3.5.1), thereby neglecting the much smaller thickness of the EMA layer. This resulted in an averaged value (and corresponding

standard deviation) of $A = 1.674 \pm 0.12$ for all oxide films grown in this study. As determined in a separate fit parameter study (by varying f^{EMA} for all the experiments conducted in this study), the value of f^{EMA} can be taken as a constant of 0.85 for all investigated oxide films. A first set of oxide-film growth curves, $L(t) = L^{\text{ox}}(t) + L^{\text{int}}(t)$, was then obtained by fitting the calculated to the measured data of $\Delta(\lambda, t)$ and $\Psi(\lambda, t)$ for $A = 1.674$ and $f^{\text{EMA}} = 0.85$, while adopting $L^{\text{ox}}(t)$ and $L^{\text{int}}(t)$ as time-dependent fit parameters.

In the *second approach*, the individually optimised values of A (instead of a single averaged value of A; see above) were applied and again f^{EMA} was taken as 0.85. Results according to the second approach of the fitting of $\Delta(\lambda, t)$ and $\Psi(\lambda, t)$ at a typical wavelength of $\lambda = 589$ nm (i.e. at about the centre of the wavelength range from 350 nm to 800 nm) are shown in Figs. 3.6(a-d) for the oxidation of the SC substrates at $T = 300$ K and $T = 475$ K.

It was found that no noticeable and systematic differences exist between the oxide growth curves [i.e. $L(t) = L^{\text{ox}}(t) + L^{\text{int}}(t)$] as obtained from the first approach and the second approach. Therefore a correspondingly averaged growth curve was determined for each oxidation experiment (see Sec. 3.5.1), and these are discussed in the following section. The average of the absolute thickness differences between the two growth curves was taken as an estimate for the error in the thickness determination.
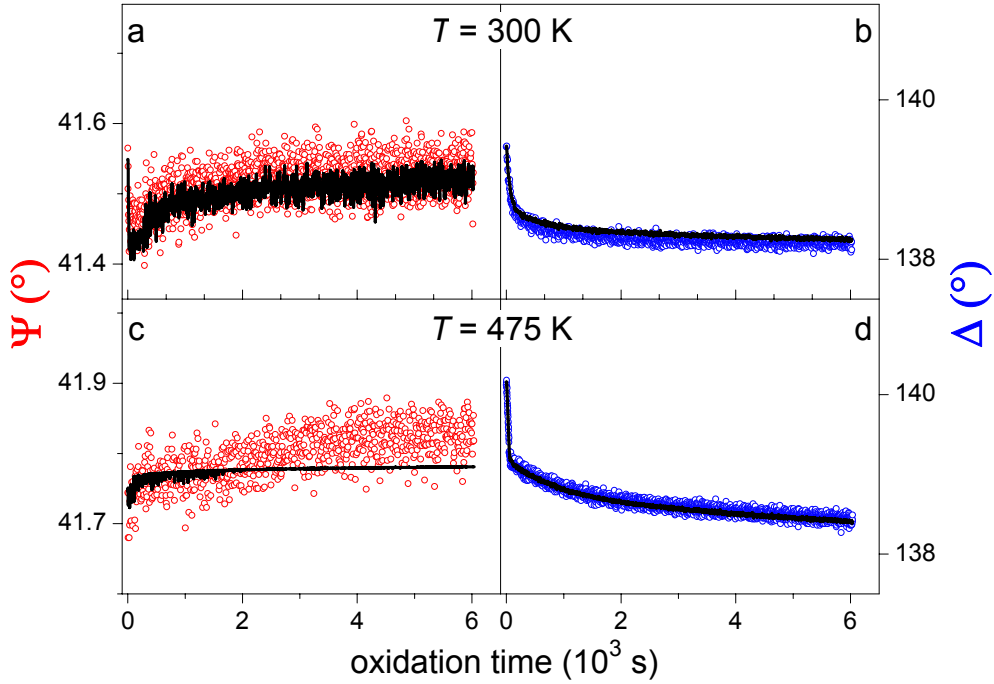
Fig. 3.6: As-measured (by RISE; open markers) and fitted (lines) values of Δ and ψ at a wavelength of λ = 589 nm as function of oxidation time by application of *'alloy|EMA|Cauchy'* model (second approach; see Sec. 3.4.2) for the oxidation of the bare SC Al-1.1% Mg substrate for 6×10^3 s at (a,b) 300 K and (c, d) 475 K ($pO_2 = 1 \times 10^{-4}$ Pa). The wavelength of λ = 589 nm is at about the centre of the wavelength range from 350 nm to 800 nm; the Δ and ψ data recorded in the wavelength range 350 nm to 800 nm have been fitted *simultaneously* (see Secs. 3.2.4 and 3.4.2).

3.5. Results and discussion

3.5.1 Oxide-film growth

Measured and fitted (see Sec. 3.4.2) values of ψ and Δ as a function of oxidation time at the central wavelength of λ = 589 nm are shown in Figs. 3.6(a-d) for the oxidation of the SC Al – 1.1% Mg substrates at T = 300 K and T = 475 K. The measured courses of $\Delta(\lambda, t)$ and $\Psi(\lambda, t)$ are comparable to those reported for the thermal oxidation of other bare metal and alloy surfaces (see Refs. [2,10,13,18]). Clearly, the '*Alloy/EMA/Cauchy*' model accurately describes the dependence of Δ on oxidation time for the temperature range studied (i.e. 300 - 485 K). This also holds for the evolution of $\Psi(\lambda, t)$ for $T \leq 425$ K. However, the observed gradual (approximately linear) increase of Ψ with increasing

oxidation time at more elevated temperatures $T \geq 450$ K (cf. Fig. 3.6c) is not fitted well by the model, which is explained below.

The *ellipsometric parameter* Ψ is insensitive to the thickness of the dielectric oxide film [10,18,35]; it instead provides valuable information on the concurrent processes of oxygen incorporation and chemisorption during the initial stages of interaction of the oxygen gas with the bare alloy surface [10,18]. The observed initial drop in Ψ (i.e., $\delta\Psi$) at the onset of oxidation [see Figs. 3.6(a,c)] is generally attributed to initial oxygen incorporation (associated with a Ψ *decrease*) dominating over oxygen chemisorption (associated with a Ψ *increase*) during the initial stage of interaction of the oxygen gas with the bare alloy surface [10,18,36]. Since oxygen incorporation is suppressed with respect to oxygen chemisorption for more densely packed metallic surfaces [10], the observed decrease of $\delta\Psi$ with increasing T from about 0.1º at 300 K to 0.05º at 475 K [see Figs. 3.6(a,c)] can be attributed to the more pronounced annihilation of excess vacancies in the SC alloy surface region at higher temperatures (these excess vacancies originate from the ion-bombardment of the alloy surface during the sputter cleaning step; see Sec. 3.2.1). As evidenced by the subsequent steep increase of Ψ [see Fig. 3.6(a,c)], oxygen chemisorption already prevails over oxygen incorporation within several seconds of oxidation.

The increase of Ψ saturates within several minutes of oxidation due to the formation of a 'closed' three-dimensional oxide film covering the entire alloy surface [10]. Whereas a (near-limiting) value of Ψ is then attained for the oxidations at $T \leq 425$ K, the value of ψ still gradually increases upon continued oxidation at $T > 425$ K (see Fig. 3.6c). Such a gradual, but distinct, increase of ψ during prolonged oxidation has also been reported for the thermal oxidation of SC Mg-based alloy surfaces (with Al-alloying contents of 2.6 at.% and 7.3 at.%) and has been ascribed to the Gibbsian segregation of Mg from the interior of the alloy to the alloy/oxide interface during the slow oxidation stage [18] (see also Sec. 3.5.2). Such compositional changes in the alloy substrate at the interface *during* oxidation at $T > 425$ K are not accounted for in the *'Alloy/EMA/Cauchy'* model (see Sec. 3.4.2). Fortunately, this does not noticeably affect the determination of the value for the oxide-film thickness by model fitting (as obtained from the simultaneous fitting of both $\Delta(\lambda, t)$ and $\Psi(\lambda, t)$; see Sec. 3.4.2), because the ellipsometric parameter Ψ is insensitive to the oxide-film thickness [see above and Sec. 3.4.2; the thickness values

determined by model fitting are governed by the employed optical parameters and the relative change in Δ; see further below].
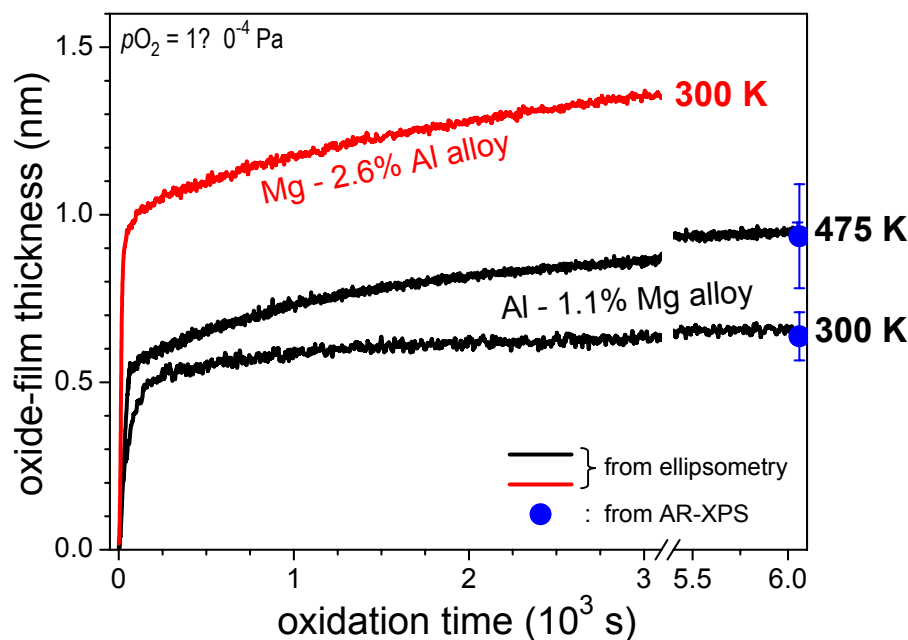
Fig. 3.7: Oxide-film growth curves, as obtained by RISE (see Sec. 3.4.2) for the oxidation of the SC Al-1.1% Mg substrate for 6×10^3 s at 300 K and 475 K ($pO_2 = 1 \times 10^{-4}$ Pa). The corresponding oxide-film thicknesses, as determined by in-situ AR-XPS at the end of the oxidations (see Sec. 3.4.1.B), have also been given. Furthermore, an oxide-film growth curve, as obtained by RISE for the oxidation of a bare SC Mg - 2.63 at.% Al substrate (i.e. corresponding to a *Mg-based* MgAl alloy) for 3.6×10^3 s at 300 K and at $pO_2 = 1 \times 10^{-4}$ Pa (as taken from Ref. [3]) has been included for comparison with the data obtained in this work for *Al-based* AlMg alloys.

Oxide-film growth curves, $L(t) = L^{ox}(t) + L^{int}(t)$, as determined by model fitting to the measured data of $\Delta(\lambda, t)$ and $\Psi(\lambda, t)$ shown in Fig. 3.6, are presented in Fig. 3.7.[2] As generally holds for ultra-thin (i.e. < 3 nm) dielectric films [10,18,35], the observed decrease of the *ellipsometric parameter Δ* is directly proportional to the increase of the oxide-film thickness (compare Figs. 3.6(b,d) and 3.7).

---

[2] In the temperature range of 300 K – 350 K, the individually fitted value of $L^{int}(t)$ typically decreases from about 0.05 nm at the onset of oxidation to approximately 0.02 nm during the slow oxidation stage. At temperatures above 350 K, its initial value is even lower (i.e. $L^{int}(t) < 0.05$ nm) and approaches zero during the slow oxidation stage.

The oxide-film growth kinetics are characterized by an initial regime of very fast film growth, which is succeeded by a second oxidation stage in which the film growth rate continuously decreases and becomes very small: i.e. a near-limiting oxide-film thickness, L_{lim}, is attained. The value of L_{lim} at $t = 6 \times 10^3$ s changes *non-monotonically* with increasing T from about 0.66 ± 0.06 nm at 300 K to about 0.62 ± 0.07 nm at $T = 400$ K to about 0.95 ± 0.1 nm at 485 K (for more details, see Fig. 3.8 and its discussion below). This passivation behavior (i.e., occurrence of L_{lim}) is typical for the oxidation of metals and alloys at low temperatures, where the rate of thermal diffusion of cations and/or anions through the developing oxide film under influence of the chemical potential (i.e. concentration) gradient is negligibly small [10,37].
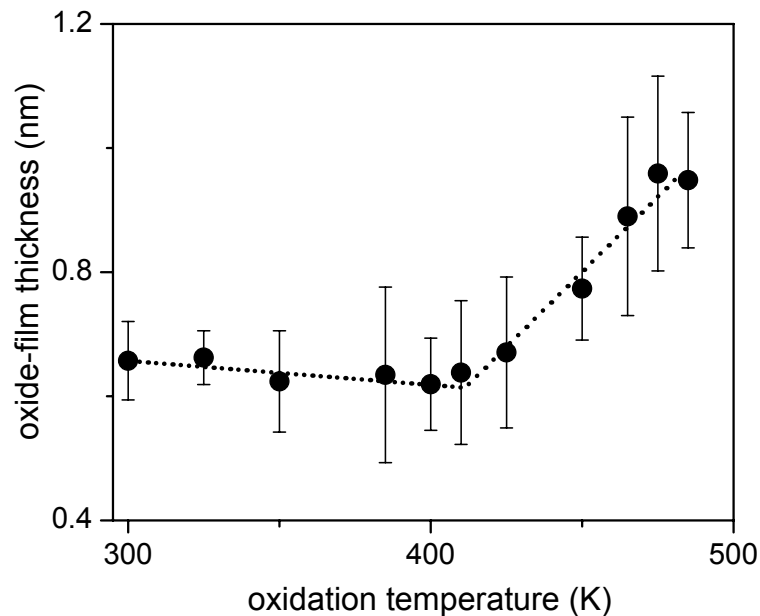
Fig. 3.8: Near-limiting oxide-film thicknesses, as determined by AR-XPS (see Sec. 3.4.1.B), versus oxidation temperature for the oxidation of the SC Al – 1.1% Mg substrates for 6×10^3 s at $pO_2 = 1 \times 10^{-4}$ Pa. The dotted line has been drawn to guide the eye.

An oxide-film growth curve, as obtained by RISE for the thermal oxidation of a SC *Mg-based* Mg – 2.6 at.% Al alloy at 300 K (as taken from Ref. [3]), has also been included in Fig. 3.7, for comparison with the oxide-film growth curve obtained in this work for the *Al-based* alloy. Clearly, the initial oxide film formed at 300 K on the Mg-based alloy is considerably thicker (i.e. about two times) than the corresponding oxide film grown on the Al-based alloy. Evidently, this thickness difference develops during the

formation of a 'closed' oxide film in the initial, very fast oxidation regime (see Fig. 3.7); the subsequent oxide-film growth rate in the second stage of slow oxidation (see above) is only somewhat higher for the Mg-based alloy. Hence it can be suggested that the average thickness at which a 'closed' oxide film is formed, which acts as a diffusion barrier for further oxidation [10,37], is delayed for Al-Mg alloys with a high Mg solute content, which can be due to an island-type of oxide growth mode for high Mg concentrations at the bare alloy surface (see also Ref. [36]).

The (near-)limiting oxide-film thickness values at $t = 6 \times 10^3$ s, as determined by AR-XPS (see Sec. 3.4.1.B), have been plotted as function of the oxidation temperature in Fig. 3.8. A direct comparison of the (near-)limiting thickness values (and corresponding errors), as determined by RISE and AR-XPS after $t = 6 \times 10^3$ s, is given in Fig. 3.9. It follows that (see Fig. 3.8) the limiting oxide-film thickness reached after 6×10^3 s *decreases* marginally from 0.66 ± 0.06 nm at $T = 300$ K to 0.62 ± 0.07 nm at $T = 400$ K, whereas at more elevated temperatures (i.e. $T \geq 410$ K) a distinct increase of the *near*-limiting thickness with increasing temperature is observed (see also Fig. 3.7). Such an unusual *decrease* of the limiting thickness with *increasing* temperature in the range of $T = 300 - 400$ K has also been reported very recently for the thermal oxidation of bare Al(111) single-crystalline surfaces and has been attributed to a slight increase with temperature of the activation energy for cation transport within the amorphous oxide-film regime (i.e. up to $T \leq 450$ K) [10]. Indeed, the oxide films grown on the SC Al – 1.1% Mg substrates at temperatures in the range of $T = 300 - 400$ K are all amorphous as evidenced by high-resolution transmission electron microscopy performed in this project [36]. The subsequent increase of the (near-limiting) thickness at $t = 6 \times 10^3$ s with increasing temperature for $T \geq 410$ K can be attributed to the enhanced thermally-activated diffusion of ions, as well as electrons (by thermionic emission), at $T \geq 410$ K [10,37]. Furthermore, the amorphous-to-crystalline transformation of the thickening oxide film at $T > 400$ K (see Refs. [11,36]) can give rise to an (additional) increase of the limiting thickness (due to an associated change of the surface-charge field strength [10,37]).
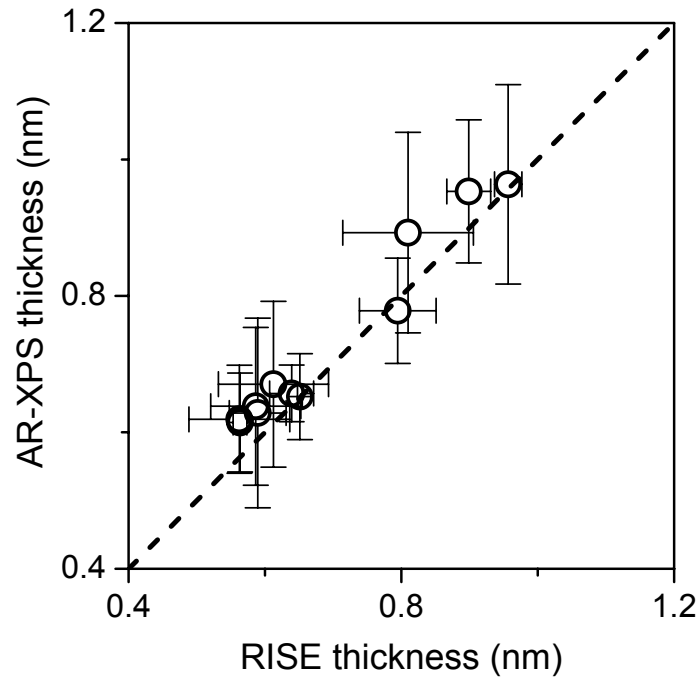
Fig. 3.9: Oxide-film thickness values (L^{XPS}), as determined by AR-XPS analysis (Sec.3.4.1.B), versus the corresponding thickness values (L^{RISE}), as obtained by RISE using the *'alloy|EMA|Cauchy'* model (Sec. 3.4.2). All data pertain to the thermal oxidation of a bare *SC* Al − 1.1% Mg substrate for 6×10^3 s at $pO_2 = 1 \times 10^{-4}$ Pa within the temperature range of 300 − 485 K. The dashed line represents the ideal relationship $L^{XPS} = L^{RISE}$.

3.5.2 Oxide-film constitution

During the in-vacuo sputter treatment performed to clean the Al − 1.1% Mg substrate prior to oxidation (i.e. to remove either the native oxide or previously grown oxide film; see Sec. 3.2.1), the alloy subsurface region becomes fully depleted of Mg due to the concurrent processes of preferential sputtering (removal) of Mg and bombardment-enhanced segregation of Mg towards the ion-bombarded alloy surface (see Ref. [30] for details). Consequently, no Mg 2p signal intensity was detected in the measured AR-XPS spectra of the SC Al - 1.1% Mg substrate (i.e. prior to oxidation but after in-vacuo cleaning) (see Sec. 3.3.1).

The effective depths of the various Al and Mg species corresponding to the various Al 2p and Mg 2p spectral components, as resolved from the AR-XPS spectra of the oxidized Al − 1.1% Mg substrate (see Figs. 3.1, 3.2 and Secs. 3.3.2 and 3.4.1.C), are shown as function of the oxidation temperature in Fig. 3.10. The Al-to-Mg atomic ratio

(see Sec. 3.4.1.B) of the grown oxide films is shown as function of the oxidation temperature in Fig. 3.11.

Al 2p : ● 'Al$_2$O$_3$' ; ○ 'interfacial-Al-oxide' ; ● metallic

Mg 2p : ★ 'MgO' ; ☆ 'interfacial-Mg-oxide'
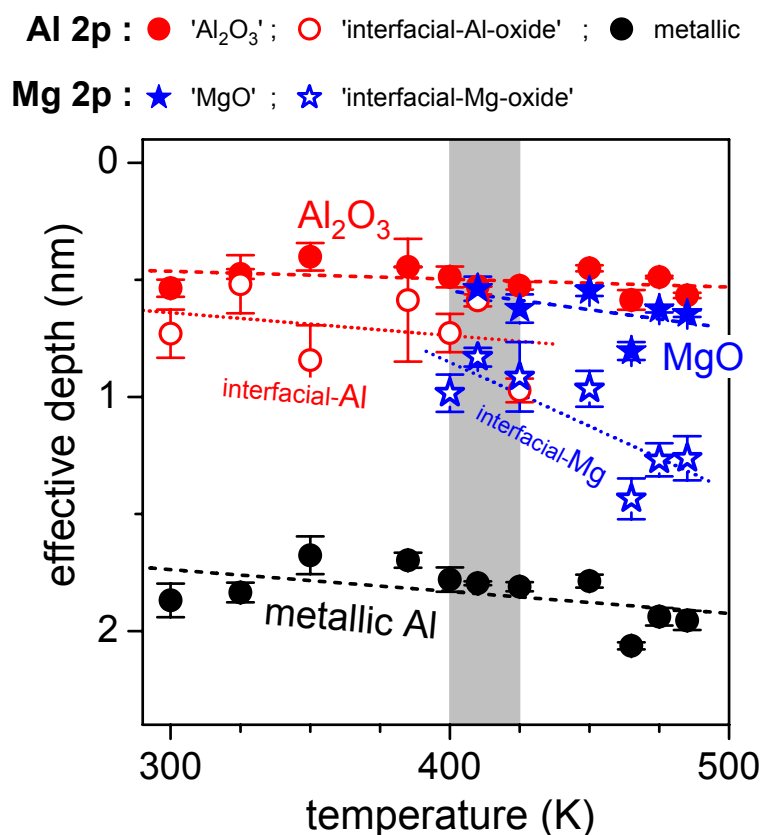
Fig. 3.10: Calculated effective depths below the oxide-film surface (see Sec. 3.4.1.C) as a function of oxidation temperature for the Al and Mg species corresponding to the resolved metallic Al 2p and the oxidic Al 2p and Mg 2p spectral components (see Fig. 3.1). All data pertain to the oxidation of the SC Al – 1.1% Mg substrates for 6×10^3 s at pO$_2$ = 10^{-4} Pa. The (transition) temperature range of T = 400 – 425 K in which the 'MgO-like' and 'interfacial-Mg-oxide' Mg 2p spectral components appear, and the 'interfacial-Al-oxide' Al 2p spectral component disappears, has been indicated in grey. The dotted lines have been drawn to guide the eye.
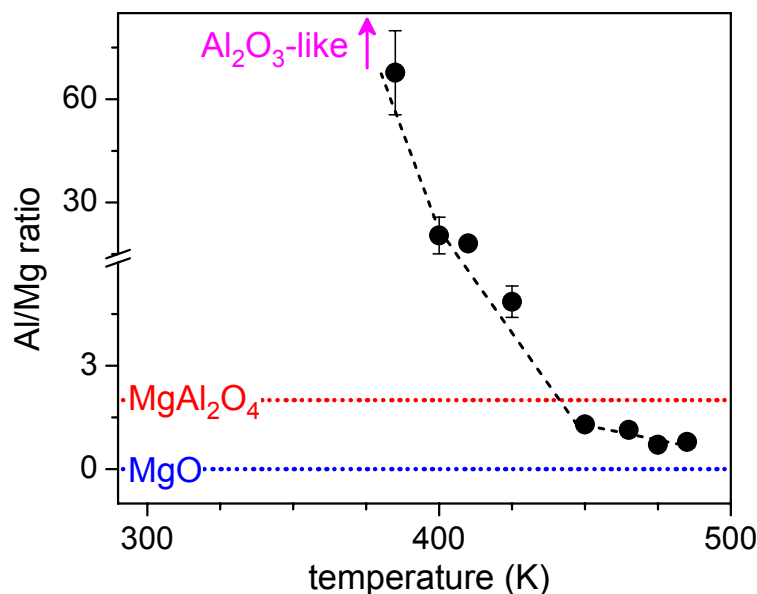
Fig. 3.11: The overall Al-to-Mg cationic ratio of the grown oxide films as a function of oxidation temperature, as obtained from the AR-XPS analysis of the oxidized SC Al – 1.1% Mg substrates (oxidized for 6×10^3 s at $pO_2 = 10^{-4}$ Pa) (see Sec. 3.4.1.B). The corresponding Al/Mg-ratios for stoichiometric MgO and MgAl$_2$O$_4$ have been indicated by the dotted lines. The dashed line through the data points has been drawn to guide the eye. Note that no Mg in the oxide film was detected for oxidation on a *bare* SC substrate at $T \leq 385$ K.

It follows from Figs. 3.10 and 3.11 that, oxidation of the SC Al - 1.1% Mg substrates at low temperatures $T \leq 385$ K results in the formation of an Al-oxide film of limiting thickness (Fig. 3.8 and Sec. 3.5.1), which indicates that the thermally-activated diffusion is too slow to promote the Gibbsian segregation of Mg from the alloy's interior to the Mg-depleted alloy substrate region adjacent to the oxide film during the process of oxidation. Thus, no Mg is incorporated in the oxide films for $T \leq 385$ K (Fig. 3.11). Two different local chemical environments exist for the Al cations in these oxide films grown at $T \leq 385$ K [see Fig. 3.1(a)]. The 'Al$_2$O$_3$-like' Al 2p main peak originates from Al cations in the interior of the oxide film (Fig. 3.10). The 'interfacial-Al-oxide' component can be attributed to a deficient coordination of Al cations by nearest-neighbour O anions *at* the alloy/oxide interface (Fig. 3.10) [11]. The resulting lower valence state of the interfacial-Al cations (i.e., Al$^{\delta+}$ with $\delta < 3$) is compatible with its lower BE position [as compared to that of the 'Al$_2$O$_3$-like' main peak; see Figs. 3.1(a) and 3.2(a,c)]. The interfacial Al-oxide detected by AR-XPS is identified with the interfacial EMA layer (of

submonolayer thickness) as adopted in the ellipsometric *'Alloy/EMA/Cauchy'* model description (see Sec. 3.2.4).

For the oxidations at $T \geq 400$ K for 6×10^3 s, some Mg was incorporated in the oxide films (Fig. 3.11), in association with sequential appearances of an 'interfacial-Mg-oxide' and a 'MgO-like' oxidic Mg species, as suggested by corresponding Mg 2p components in the measured AR-XPS spectra of the oxidized alloy (Figs. 3.2(b,d) and 3.10). Analogous to the discussion of the resolved oxidic Al 2p species (see above and Fig. 3.10), the 'MgO-like' component arises from Mg cations in the interior of the oxide film, whereas the 'interfacial-Mg-oxide' species is due to the presence of Mg cations with a lower valence state (as compared to Mg^{2+}) at the alloy/oxide interface (as a result of the deficient coordination of Mg cations by nearest-neighbour O anions at the alloy/oxide interface [11]). The emergence of the 'interfacial-Mg-oxide' component within the (transition) temperature range between 400 and 425 K (indicated by the grey area in Fig. 3.10) is associated with the disappearance of the 'interfacial-Al-oxide' component (absent beyond $T > 425$ K). These observations indicate that Mg segregates from the interior of the alloy to the reacting alloy/oxide interface for oxidation at $T \geq 400$ K. The segregation of Mg *at* the interface between the Al – Mg alloy substrate and its amorphous Al-oxide overgrowth is driven by a lowering of the interfacial energy [38].

As a next step, the segregated Mg ions *at* the alloy/oxide interface can 'hop' into (interstices of the oxygen-ion arrangement of) the amorphous (Al-rich) oxide film under influence of the surface-charge field setup by chemisorbed oxygen species at the oxide surface, [10,37,40]. As a result the 'MgO-like' oxidic Mg 2p main peak arises in the measured AR-XPS spectra of the oxidized alloy at $T \geq 400$ K [Figs. 3.2(b,d)]. Due to the enhanced uptake of Mg by the growing oxide film at elevated *T*, the overall Al/Mg-ratio of the grown oxide films decreases with increasing temperature for $T \geq 400$ K (Fig. 3.11). The anion-to-cation ratio [i.e. O/(Al+Mg)] of the oxide film decreases with increasing temperature from 1.4(±0.1) at 300 K to 1.25(±0.05) at 485 K, thereby approaching the overall stoichiometry of MgO (as determined by AR-XPS; see Sec. 3.4.1.B).

3.6.   Conclusions

Quantitative analysis of the depth dependent composition and constitution of oxide films and their growth kinetics is possible by combining real-time, in situ spectroscopic ellipsometry (RISE) and angle-resolved X-ray photoelectron spectroscopy (AR-XPS).

Such generally applicable, advanced AR-XPS and RISE methods have been developed for particularly oxidizing alloy substrates, i.e. for multiple element and multiple phase oxide films.

Application of this new combinatorial approach to the initial, thermal oxidation of sputter-cleaned Al - 1.12 at.% Mg alloy surfaces at $T = 300 - 485$ K (at $pO_2 = 1 \times 10^{-4}$) provided the following description of the oxide-film growth kinetics and the accompanying compositional and constitutional changes in the alloy subsurface and the oxide-film:

The in-vacuo sputter-cleaning (SC) treatment prior to oxidation depletes the subsurface region fully of Mg, due to the concurrent processes of preferential sputtering (removal) of Mg and bombardment-enhanced segregation of Mg towards the ion-bombarded alloy surface.

Upon exposure of these SC alloy surfaces to pure oxygen gas at $T \leq 425$ K, oxygen incorporation (into the alloy subsurface) very initially prevails over oxygen chemisorption, but already after several seconds of oxidation oxygen chemisorption prevails over oxygen incorporation. The initial oxygen incorporation is suppressed with respect to oxygen chemisorption at more elevated oxidation temperatures ($T \geq 450$ K) due to the enhanced annihilation of excess vacancies in the SC alloy surface region (at elevated temperature) prior to oxidation. A 'closed' oxide film covering the entire alloy surface, which acts as a diffusion barrier for further oxidation, is formed within a few minutes of oxidation.

At $T \leq 385$ K, no Mg is incorporated in the oxide film due to the kinetically suppressed segregation of Mg to the Mg-depleted alloy substrate region adjacent to the alloy/oxide interface; i.e., the formed oxide-film is Al_2O_3-like; with a substoichiometric 'interfacial-Al-oxide' component at the alloy/oxide interface. At $T \geq 400$ K, Mg can be taken up in the oxide film, due to the enhanced interfacial segregation of Mg in the substrate: an 'interfacial-Mg-oxide' appears under simultaneous disappearance of the 'interfacial-Al-oxide'.

The oxide film at elevated temperature has 'Al_2O_3-like' and 'MgO-like' nature with an overall composition in between those of $MgAl_2O_4$ and MgO. Further growth at these elevated temperatures is governed by the preferential oxidation of Mg at the alloy/oxide interface, which leads to an overall decrease of the Al/Mg-ratio of the grown oxide films for $T \geq 400$ K, thereby approaching the overall stoichiometry of MgO.

References

[1]   P. Nolte, A. Stierle, N. Y. Jin-Phillipp, N. Kasper, T. U. Schulli and H. Dosch, Science **321** (2008) 1654.

[2]   A. Lyapin, L. P. H. Jeurgens, P. C. J. Graat and E. J. Mittemeijer, J. Appl. Phys. **96** (2004) 7126.

[3]   L. P. H. Jeurgens, M. S. Vinodh, and E. J. Mittemeijer, Acta Mat. **56** (2008) 4621.

[4]   A. Pasquarello and A. M. Stoneham, J. Physics: Condensed Matter **17** (2005) V1.

[5]   H.-J. Freund Surf. Sci. **601** (2007) 1438.

[6]   M. Koyama, Y. Kamimuta, M. Koike, M. Suzuki and A. Nishiyama, Jap. J. Appl. Phys. **43** (2004) 1788.

[7]   Z. R. Dai, Z. W. Pan and Z. L. Wang, Adv. Funct. Mater. **13** (2003) 9.

[8]   E. Comini, G. Faglia, G. Sberveglieri, Z. Pan and Z. L. Wang, Appl. Phys. Lett. **81** (2002) 1869.

[9]   A. Gupta, X. W. Li and G. Xiao, Appl. Phys. Lett. **78** (2001) 1894.

[10]   F. Reichel, L. P. H Jeurgens and E. J. Mittemeijer, Acta Mat. **56** (2008) 2897.

[11]   F. Reichel, L. P. H Jeurgens, G. Richter and E. J. Mittemeijer, J. Appl. Phys. **103** (2008) 093515.

[12]   F. Reichel, L. P. H Jeurgens, G. Richter, P. A. van Aken and E. J. Mittemeijer, Acta Mater. **55** (2007) 6027.

[13]   A. Lyapin, L. P. H. Jeurgens and E. J. Mittemeijer, Acta Mat. **53** (2005) 2925.

[14]   M. Kurth, P. C. J. Graat and E. J. Mittemeijer, Thin Solid Films **500** (2006) 61.

[15]   M. Kurth, P. C. J. Graat, H. D. Carstanjen and E. J. Mittemeijer, Surf. Interf Anal. **38** (2006) 931.

[16]   L. P. H. Jeurgens, W. G. Sloof, F. D. Tichelaar, C. G. Borsboom and E. J. Mittemeijer, Appl. Surf. Sci. **161** (2000) 139.

[17]   L. P. H. Jeurgens, M. S. Vinodh and E. J. Mittemeijer, Appl. Surf. Sci. **253** (2006) 627.

[18] M. S. Vinodh, L. P. H. Jeurgens and E.J. Mittemeijer, J. Appl. Phys. **100** (2006) 044903.

[19] T. J. Nijdam, L. P. H. Jeurgens and W. G. Sloof, Acta Mater. **51** (2003) 5295.

[20] L. F. Mondolfo, Aluminum Alloys: Structure and Properties, (Butterworths, London 1976).

[21] E. Brillas, P.L. Cabot, F. Centellas, J. A. Garrido, E. Perez and R. M. Rodriguez, Electrochimica Acta **43** (1998) 799.

[22] Metals Handbook. Properties and Selection of Metals, 8th edn., Americal Society for Metals, Ohio (1961) 1.

[23] G. R.Wakefield and R. M. Sharp, Appl. Surf. Sci. **51** (1991) 95.

[24] D. H. Kim, E. P. Yoon and J. S. Kim, J. Mat. Sc. Lett. **15** (1996) 1429.

[25] K. Shimizu, G. M. Brown, K. Kobayashi, P. Skeldon, G. E. Thompson and G. C. Wood, Corr. Sci. **40** (1998) 557.

[26] F. J. Esposto, C. S. Zhang, P. R. Norton and R. S. Timsit, Surf. Sci. **302** (1994) 109.

[27] J. Bloch, D. J. Bottomley, J. G. Mihaychuk, H. M. van Driel and R. S. Timsit, Surf. Sci. **322** (1995) 168.

[28] M. S. Vinodh and L. P. H. Jeurgens, Surf. Interface Anal. **36** (2004) 1629.

[29] F. Reichel, PhD Thesis, 2007, University of Stuttgart, p. 140.

[30] F. Reichel, L. P. H Jeurgens and E. J. Mittemeijer, Phys. Rev. B **74** (2006) 144103.

[31] S. Tougaard, Solid State Commun. **61** (1987) 547.

[32] S. Tougaard, Surf. Int. Anal. **25** (1997) 137.

[33] M. B. Trzhaskovskaya, V. I. Nefedov and V. G. Yarzhemsky, Atomic Data and Nuclear Data Tables **77** (2001) 97.

[34] Guide to Using WVASE32[TM], J.A. Woolam Co., Inc. (1997).

[35] R. M. A. Azzam and N. M. Bashara, *Ellipsometry and Polarized Light,* (North-Holland, Amsterdam, 1987).

[36] E. Panda, L. P. H Jeurgens and E. J. Mittemeijer, submitted for publication.

[37] L. P. H. Jeurgens, A. Lyapin and E. J. Mittemeijer, Act. Mater. **53** (2005) 4871.

[38]   E. Panda, L. P. H Jeurgens and E. J. Mittemeijer, Submitted for publication.

[39]   A. Jablonski and C. J. Powell Surf Sci Reports **47** (2002) 33.

[40]   P. C. J. Graat, M. A. J. Somers and E. J. Mittemeijer, Z. Metallkd. **93** (2002) 532.

4.   Effect of in-vacuo surface pre-treatment on the growth kinetics and chemical constitution of ultra-thin oxide films on Al-Mg alloy substrates

E. Panda, L. P. H. Jeurgens, E. J. Mittemeijer

Abstract

The effect of in-vacuo substrate surface pre-treatment on the growth kinetics and chemical constitution of ultra-thin (< 3 nm) oxide films grown on bare Al – 1.1 at.% Mg alloy surfaces was studied by a combined experimental approach of real-time *in situ* spectroscopic ellipsometry (RISE) and angle-resolved X-ray photoelectron spectroscopy (AR-XPS). One alloy surface pre-treatment prior to oxidation consisted of the removal of the native oxide and other contaminants on the alloy surface by sputter-cleaning under UHV conditions. A second surface pre-treatment involved exposing such sputter-cleaned surfaces to a short in-vacuo annealing step at 460 K. Next, ultra-thin (< 3 nm) oxide films were grown on these two pre-treated alloy surfaces by exposure to $O_2(g)$ within the temperature range of T = 300 - 485 K (at pO_2 = 1×10^{-4} Pa). It was found that, as long as the chemical segregation of Mg from the alloy's interior to the alloy/oxide interface is kinetically hindered, the oxide-film growth kinetics, the developing oxide-film constitution, as well as the local chemical states of the Al and Mg cations in the oxide layer depend strongly on the alloy surface pre-treatment. At $T \geq 450$ K, the thermally activated interfacial segregation of Mg becomes pronounced and, only then, the developing oxide-film constitution is approximately independent of the surface pre-treatment.

4.1.   Introduction

Pre-treatment of alloy substrate surfaces is a common, initial processing step in the fabrication of high-temperature coating systems (such as those applied to blades and vanes in turbine engines) to prolong lifetime of components during service in oxidizing

and corrosive environments at operation temperatures in the range of 1000 - 1500 K [1]. Such surface pre-treatments typically consist of a laser-surface melting [2] or pre-annealing [3] step to refine the microstructure (reduced grain size) in the (sub)surface region of the alloy substrate, followed by a controlled pre-oxidation step (typically at temperatures > 900 K), to produce a well-defined, protective (i.e. slow growing, adhesive and thermally stable), initial oxide layer on the alloy substrate surface (before the subsequent deposition of a thermal barrier topcoat) [1].

Perhaps surprisingly, up to date, the effect of alloy surface pre-treatments on the developing oxide-film microstructure at low temperatures, $T < 500$ K, has not been investigated rigorously. As demonstrated by the present study, at such low oxidation temperatures, the thermally-activated diffusion of reacting species in the alloy substrate and in the oxide is negligibly small and, consequently, the effect of the surface pre-treatment on the microstructure of the resulting ultrathin (< 5 nm) oxide films can be pronounced. Tailoring the microstructure of such oxide films by well-defined surface pre-treatments of their parent alloy substrates can therefore be a powerful tool in the functionalization of ultrathin (< 3 nm) oxide films as applied in nanotechnologies like tunnel junctions, gas sensors, model catalysts and (thin) diffusion barriers for corrosion-resistance [4-20].

The present study addresses the effect of different *in-vacuo* surface pre-treatments on the growth kinetics and constitutional evolution of ultrathin (< 3 nm) oxide films grown on Al-based Al – 1.1 at.% Mg alloy surfaces by thermal oxidation in the temperature range of $T = 300$ - 485 K (at constant partial oxygen pressure of $pO_2 = 1 \times 10^{-4}$ Pa). Two types of *in-vacuo* surface pre-treatments of the Al – 1.1 at.% Mg alloy surfaces, each followed by a controlled oxidation step, were performed in a dedicated UHV system for specimen processing and analysis. As a first surface pre-treatment prior to oxidation, the native oxide and other contaminants on the alloy surface were removed by sputter-cleaning the entire alloy surface. A second surface pre-treatment involved that, the sputter-cleaned (as described above) alloy surface was subjected to a short in-vacuo annealing step at 460 K prior to oxidation. Real-time in-situ spectroscopic ellipsometry was applied to investigate the initial oxide-film growth kinetics in dependence on the surface pre-treatment and the oxidation temperature in the range of $T = 300$ - 485 K (Sec. 4.2.2). The depth-resolved chemical constitution of the grown oxide films, as well as the local chemical states of the alloy constitutents (i.e. Al and Mg) in the oxide film and in

the alloy subsurface, were determined by in-situ angle-resolved X-ray Photoelectron spectroscopy (Sec. 4.3.1). Pronounced differences in the oxide-film growth kinetics and the developing oxide-film constitution for the two types of pre-treated alloy surfaces were revealed and discussed (Sec. 4.4).

4.2.   Experimental

4.2.1   *Material and sample preparation*

Disc-shaped specimens (10 mm diameter; 1 mm thickness) of a single-phase, polycrystalline Al-based AlMg solid-solution alloy with a homogeneous Mg content of 1.12 at.% and an average grain size in the range of 50 - 100 μm (henceforth referred to as Al − 1.1% Mg alloy) were prepared by successive melting, casting and annealing procedures, as described in Ref. [21]. The prepared alloys have the following impurity concentrations (ppm in mass; as determined by Inductive Coupled Plasma–Optical Emission Spectrometry): Zn = 70, Mn = 40, Na = 30, C = 72 ± 8, and [Fe, Ca, Cu, Cr, Ti, Y, O] < 10.

4.2.2   *Surface pre-treatment and oxidation*

The oxidations were all carried out in an especially-designed UHV system for specimen processing and analysis, which consists of several interconnected UHV side-chambers (all with a base pressure < 3×10^{-8} Pa) that are equipped with various in-situ surface-sensitive analytical techniques, such as AR-XPS and RISE (as described in Secs. 4.3.1 and 4.3.2, respectively).

After introduction of the specimen into the UHV system (as well as prior to each successive oxidation experiment of the same specimen; see what follows), the (native) oxide and other contaminants (generally only adventitious carbon) on the specimen surface were removed by sputter-cleaning (SC) at room temperature with a 1 kV Ar^+ beam (rastering the entire sample surface and employing sample rotation at a speed of about 6 º/s) until no other elements than the pure alloy constituents (i.e. Al and/or Mg) were detected in a measured XPS survey spectrum recorded over the binding energy (BE) range from 0 to 1200 eV (for instrumental details, see Ref. [21]). The AlMg specimens as obtained after this described SC treatment are further designated as the *sputter-cleaned*

(SC) substrates. As an alternative, second surface pre-treatment, some of the sputter-cleaned alloy surfaces were subsequently in-vacuo annealed for 1200 s at $T = 460$ K, and further referred to as *sputter-cleaned/annealed (SC/Ann)* substrates. The annealing temperature of 460 K was chosen, because at this temperature the thermally-activated surface segregation of Mg onto the clean SC alloy surface is sufficiently fast to establish a Mg-rich surface (as verified by AR-XPS; see Sec. 4.2.2), while the temperature is still low enough to prevent surface roughening effects as a consequence of e.g. Mg evaporation and thermal etching, as observed in Ref. [22] for the in-vacuo annealing of pure Mg metal surfaces.

Next, ultra-thin (thicknesses < 3 nm; see Sec. 4.4.2.A) oxide films were grown by in-situ exposure of the SC or SC/Ann alloy surfaces for 6×10^3 s to pure oxygen gas (i.e. $\geq$ 99.99990 vol.% with a specified residual gas content of $H_2O \leq 0.5$ vpm, N_2 / Ar ≤ 2.0 vpm, $C_nH_m \leq 0.1$ vpm and $CO_2 \leq 0.1$ vpm) at a partial oxygen pressure (pO_2) of 1×10^{-4} Pa in the temperature range of $T = 300$ - 485 K. Further experimental details have been provided in Ref. [21].

4.3. In-situ analysis and quantification

4.3.1 AR-XPS analysis and quantification

In-situ AR-XPS analyses of the bare alloy substrates (i.e. either the SC or SC/Ann pre-treated alloy surface) and the oxidized alloy substrates were performed to determine the thickness, the depth-resolved chemical constitution, and the overall chemical composition of the grown oxide films. To verify the cleanness of the alloy surfaces after the sputter treatment (see Sec. 4.2.2), XPS survey spectra, covering a binding energy (BE) range from 0 eV to 1200 eV, were recorded with a step size and constant pass energy of 0.2 eV and of 200 eV, respectively, using a Thermo VG Thetaprobe system employing monochromatic Al Kα radiation ($hv = 1486.68$ eV; spot size 400 μm). For the bare and oxidized alloy surfaces, AR-XPS spectra of the Al 2p (BE range: 70.59 - 79 eV), Mg 2p (BE range: 47 - 56 eV) and O 1s (BE range: 527 – 538.5 eV) regions were recorded with a step size and constant pass energy of 0.1 eV and 50 eV, respectively. The AR-XPS measurements were performed in so-called parallel data acquisition mode by detecting the photoelectrons simultaneously over the angular detection range of $(\alpha, \phi) = (23°, 43°)$

to $(\alpha, \phi) = (83^\circ, 94^\circ)$ in six ranges of 10° each (for details, see Ref. [23]). The interdependent angles α and ϕ are defined as the angles between the directions of the detected photoelectrons and the sample surface normal and the directions of the detected photoelectrons and the incident photon beam, respectively. To maximize the XPS analysis area on the specimen surface, the AR-XPS spectra of the bare and oxidized substrates were measured at nine defined locations on the surface (incident X-ray spot size: ~400 μm), equally distributed over an entire analysis area of 3×3 mm^2. Typical as-measured Al 2p and Mg 2p spectra of the SC and SC/Ann alloy substrate, as recorded at a detection angle set of $(\alpha, \phi) = (38^\circ, 54.75^\circ)$, are shown in Figs. 4.1(a-d).
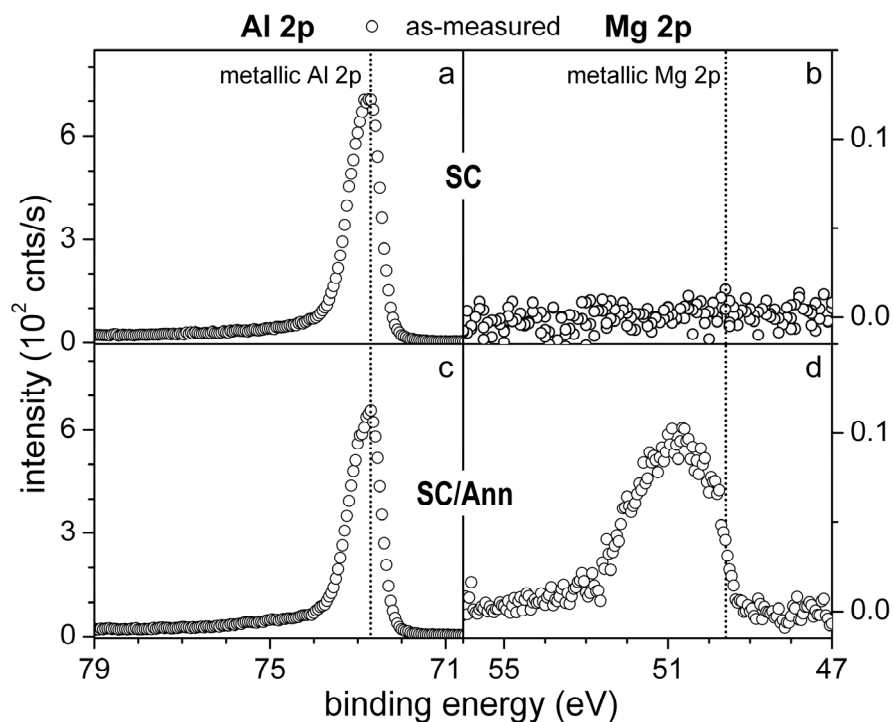
Fig. 4.1: Al 2p and Mg 2p AR-XPS spectra, as-measured at a detection angle set of $(\alpha, \phi) = (38^\circ, 54.75^\circ)$, from (**a,b**) the sputter-cleaned (SC) and from (**c,d**) the sputter-cleaned/annealed (SC/Ann) Al - 1.1 at.% Mg substrates. The 'as-measured' spectra have been corrected for the analyzer transmission function and zero-background offset. Due to the high affinity of Mg for oxygen, the segregated Mg at the SC/Ann alloy surface in (d) has largely oxidized during the in-vacuo annealing step and/or subsequent AR-XPS measurement. The vertical, dashed lines denote the BE positions of the metallic Al 2p and Mg 2p peaks.

Fig. 4.2: Spectral reconstructions of the Al 2p and Mg 2p spectra, as-measured at a detection angle set of $(\alpha, \phi) = (38°, 54.75°)$ from (**a, b**) the SC and from (**c, d**) the SC/Ann Al - 1.1 at.% Mg substrate after oxidation for 6×10^3 s at 300K ($pO_2 = 1 \times 10^{-4}$ Pa). The oxide films, as grown on the oxidized SC and SC/Ann alloy substrates, have thicknesses of $0.66^{\pm 0.06}$ nm and $0.72^{\pm 0.05}$ nm, respectively (as determined by AR-XPS; see Sec. 4.3.1). The vertical, dashed lines denote the BE positions of the Al_2O_3-like and MgO-like oxidic Al 2p and Mg 2p peaks.

Before quantitative AR-XPS analysis was carried out, the measured Al 2p, Mg 2p and O 1s AR-XPS recorded spectra were averaged over all measured positions of the sample surface for each angular range of photoelectron detection employed (see Ref. [21]). Next, the thus obtained spectra were corrected for the electron kinetic energy dependent transmission of the spectrometer analyzer by adopting the corresponding correction factor as provided by the manufacturer. Then, for each detection angle (with α and ϕ taken equal to their values at the centre of each angular detection range; see above), the Al 2p and Mg 2p primary zero loss (PZL) intensities [24] of the corresponding asymmetrically shaped metallic main peaks (i.e. including the tail towards higher BE values, but excluding the intrinsic plasmon intensity [24]), as well as the symmetrically shaped Al 2p and Mg 2p oxidic and O 1s main peaks, were resolved from the measured AR-XPS spectra of the bare and the oxidized substrate according to the procedure

described in detail in Refs. [21,25]. Typical as-measured and reconstructed Al 2p and Mg 2p AR-XPS spectra, as recorded at a detection angle set of $(\alpha, \phi) = (38°, 54.75°)$ from the SC and SC/Ann Al - 1.1% Mg substrates after oxidations for 6×10^3 s at 300 K, 400 K and 475 K, are presented in Figs. 4.2 – 4.4, respectively.

Fig. 4.3: Spectral reconstructions of the Al 2p and Mg 2p spectra, as-measured at a detection angle set of $(\alpha, \phi) = (38°, 54.75°)$ from **(a, b)** the SC and from **(c, d)** the SC/Ann Al - 1.1 at.% Mg substrate after oxidation for 6×10^3 s at 400K ($pO_2 = 1\times10^{-4}$ Pa). The oxide films, as grown on the oxidized SC and SC/Ann alloy substrates, have thicknesses of $0.62^{\pm0.07}$ nm and $0.73^{\pm0.05}$ nm, respectively (as determined by AR-XPS; see Sec. 4.3.1). The vertical, dashed lines denote the BE positions of the Al_2O_3-like, MgO-like and interfacial Mg-oxide oxidic Al 2p and Mg 2p peaks.

The average BE values (and corresponding standard deviations), as determined for the resolved metallic and oxidic Al 2p and Mg 2p main peaks, as well as for the resolved O1s main peaks positioned at the lower-binding-energy (LBE), middle-binding-energy (MBE) and higher-binding-energy (HBE) side of the measured O 1s peak envelop[1], have

---

[1] Spectral reconstructions of the measured O 1s spectra have been presented in Ref. [21].

been gathered in Table 4.1. The temperature range for which each resolved spectral component can be discerned in the measured spectra of the oxidized alloy has also been indicated in Table 4.1.
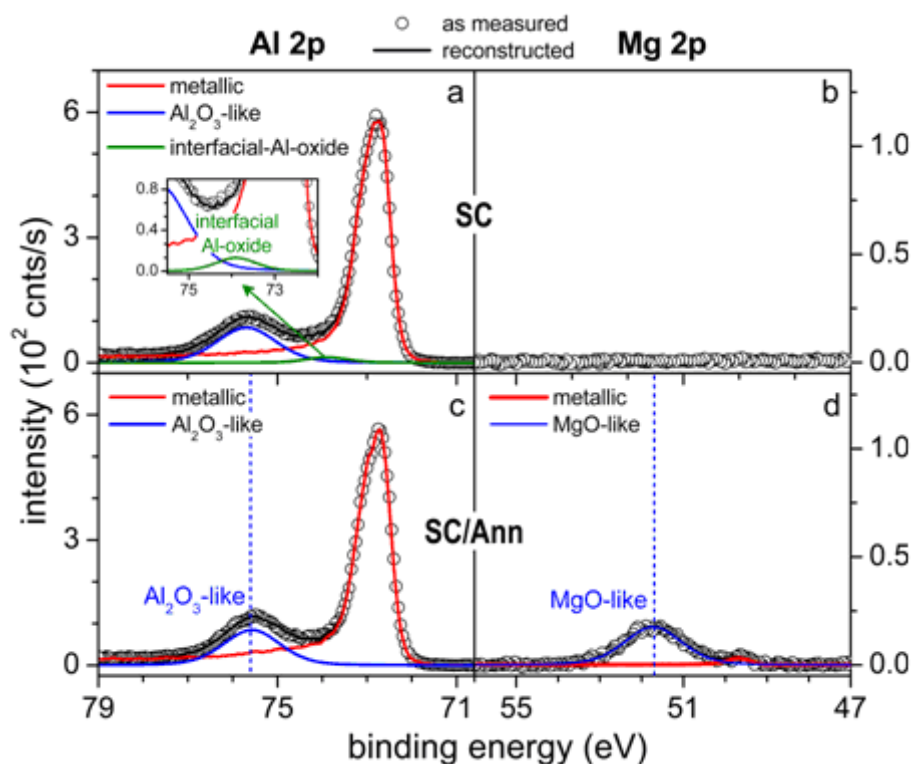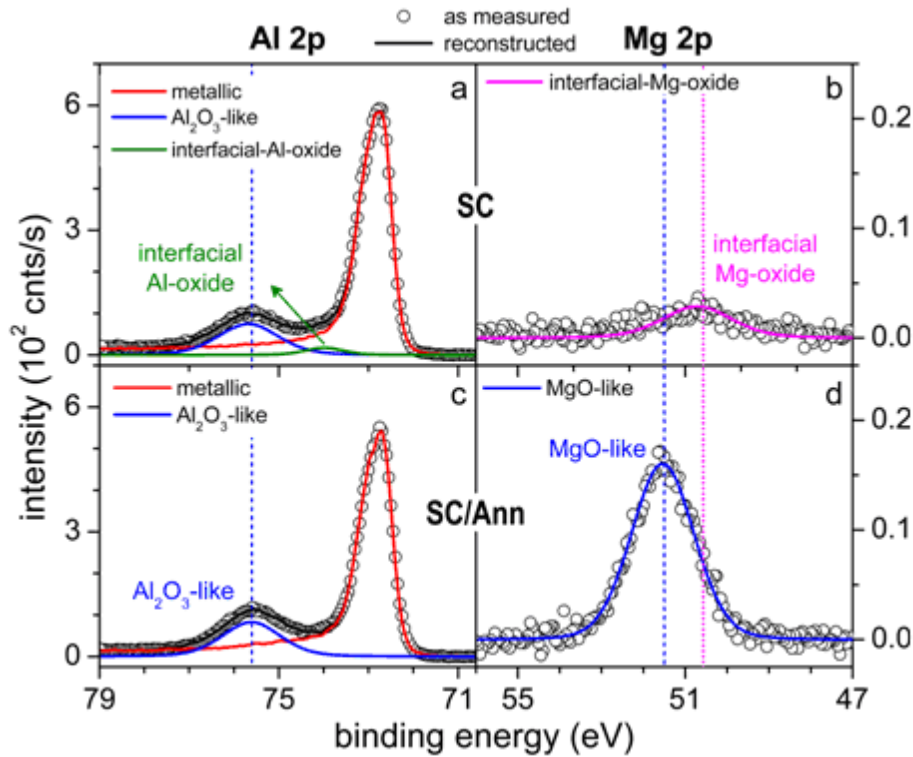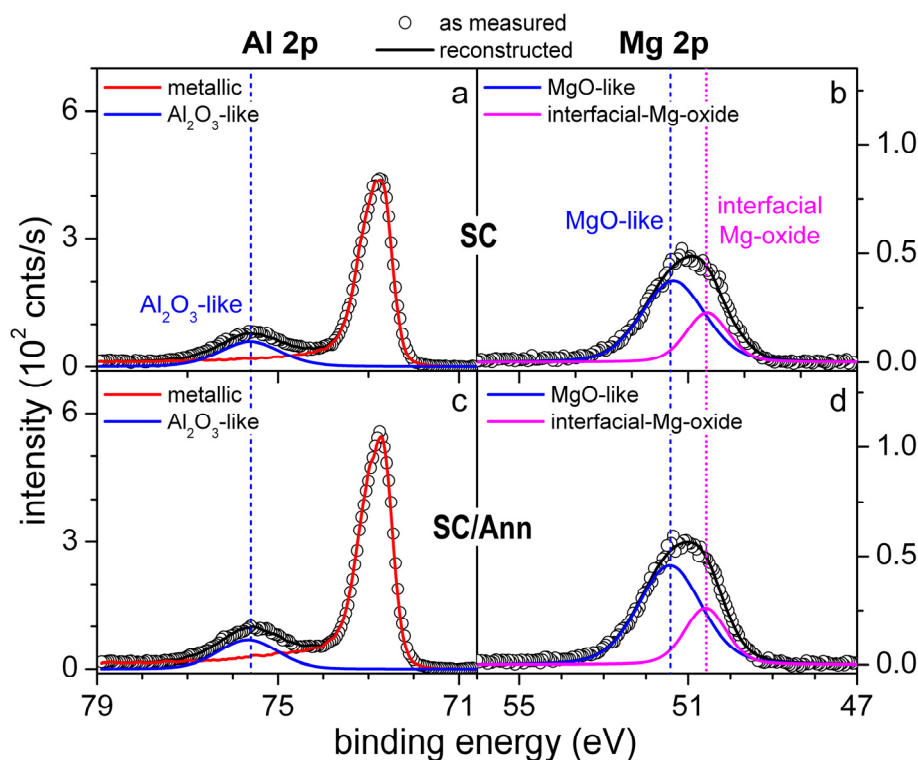

Fig. 4.4: Spectral reconstruction of the Al 2p and Mg 2p spectra, as-measured at a detection angle set of $(\alpha, \phi) = (38^\circ, 54.75^\circ)$ from (**a, b**) the SC and from (**c, d**) the SC/Ann Al - 1.1 at.% Mg substrate after oxidation for 6×10^3 s at 475K ($pO_2 = 1 \times 10^{-4}$ Pa). The oxide films, as grown on the oxidized SC and SC/Ann alloy substrates, have thicknesses of $0.96^{\pm 0.16}$ nm and $0.87^{\pm 0.1}$ nm, respectively (as determined by AR-XPS; see Sec. 4.3.1). The vertical, dashed lines denote the BE positions of the Al$_2$O$_3$-like, MgO-like and interfacial Mg-oxide oxidic Al 2p and Mg 2p peaks.

The average oxide-film thicknesses (L), as well as the cation ($C_{\mathrm{AlMg,ox}}$) and/or anion ($C_{\mathrm{O,ox}}$) molar densities in the grown oxide films, were calculated (by iteration for each detection angle set) from the resolved metallic Al 2p, metallic Mg 2p, oxidic Al 2p, oxidic Mg 2p and O 1s PZL intensities, according to the iterative procedure described in detail in Refs. [21,25].

Furthermore, the effective depths (below the specimen surface) of each of the identified chemical species (Al, Mg and O) within the oxide film were calculated from

their corresponding PZL intensities, as resolved for sets of near-normal and grazing detection angles in the ranges of $\alpha_1 = 25 - 35°$ and $\alpha_2 = 60 - 75°$, respectively (for details, also see Refs. [21,25]).

Table 4.1. Average binding energy (BE) values (and corresponding standard deviations) of the metallic and oxidic Al 2p, Mg 2p main peaks and the O 1s main peaks, as resolved from the AR-XPS spectra recorded from the oxidized SC and SC/Ann Al – 1.1% Mg substrates within the oxidation temperature range of $T = 300 – 485$ K. The temperature range for which each resolved spectral component can be discerned in the measured spectra of the oxidized alloy has been indicated in the last column of the table. The 'MgO-like' oxidic Mg 2p main peak exhibits a shift to lower BE values with increasing oxidation temperature and therefore a corresponding BE range (instead of an average BE value) has been given. See Sec. 4.4.1, 4.4.2.B and Figs. 4.1-4.4(a-d), 4.7(a,b) for further details.

Main peak	Assignment	Binding energy (eV)	Pre-treatment	T (K)
metallic Al 2p	Al metal	$72.71^{\pm0.01}$	both	300 - 485
metallic Mg 2p	Mg metal	$49.59^{\pm0.05}$	SC/Ann	300
oxidic Mg 2p	MgO-like	$(51.72 - 51.26)^{\pm0.08}$	SC	410 - 485
			SC/Ann	300 - 485
	interfacial-Mg-oxide	$50.57^{\pm0.07}$	SC	400 - 485
			SC/Ann	450 - 485
oxidic Al 2p	Al$_2$O$_3$-like	$75.60^{\pm0.06}$	both	300 - 485
	interfacial-Al-oxide	$73.9^{\pm0.1}$	SC	300 - 425
O 1s	LBE	$531.9^{\pm0.2}$	both	300 - 485
	MBE	$532.9^{\pm0.2}$	both	300 - 485
	HBE	$534.2^{\pm0.3}$	both	300 - 485

A detailed description of the employed procedures for quantitative AR-XPS analysis, which includes tabulated values of the physical constants (e.g. metal and oxide densities, effective attenuation lengths, asymmetry factors, band gap energies and total photoionization cross sections) adopted in the calculations, is provided in Ref. [21].

4.3.2   *RISE analysis and quantification*

RISE measurements of the oxidizing SC and SC/Ann substrates were carried out using a J. A. Woollam Co., Inc. rotating compensator ellipsometer M-2000L, equipped with a Xe light source (800 wavelengths, λ, in the range of $\lambda = 245-900$ nm), which is mounted directly on the flanges of the UHV reaction chamber (with angles of incidence and reflection of 70° with respect to the sample surface normal). Spectra of the ellipsometric phase shift and amplitude ratio dependent parameters Δ and ψ versus λ (over $\lambda = 350-850$ nm in intervals of ~0.8 nm) were recorded from the bare and oxidizing alloy surface over a 2×8 mm^2 ellipse-shaped area with a time step of 1.4 s (for details see Ref. [21]).

The oxide-film growth kinetics and optical parameters (i.e. the complex index of refraction, $N = n - ik$, where n and k denote the index of refraction and the extinction coefficient, respectively) of the developing oxide-film were determined by fitting model descriptions of the ellipsometric spectra $\psi(\lambda)$ and $\Delta(\lambda)$ (for $\lambda = 245 - 900$ nm) as a function of the oxidation time (t) to the corresponding measured data of $\psi(\lambda, t)$ and $\Delta(\lambda, t)$ [21]. To this end, a (physically) realistic model for the optical response of the studied alloy-substrate/oxide-film system was constructed, further designated as the *'alloy|EMA|Cauchy'* model, which considers the overgrowth of a transparent oxide film of uniform thickness on top of the bare alloy substrate in combination with an intermediate suboxidic layer of submonolayer thickness (i.e. $\leq$ 0.05 nm; to account for the characteristic ellipsometric absorption at the alloy/oxide interface). For details of the RISE evaluation procedure, see Ref. [21].

4.4.   Results and discussion

4.4.1   *The bare SC and SC/Ann alloy substrates*

As-measured Al 2p and Mg 2p spectra, recorded from the SC and SC/Ann Al - 1.1% Mg substrates prior to oxidation, are shown in Figs. 4.1(a-d). Clearly (compare Figs. 4.1b and

4.1d), no Mg is detected in the (sub)surface region of the SC alloy surface by AR-XPS, whereas a distinct Mg signal is discerned for the SC/Ann surface (i.e., after in-vacuo annealing of the SC alloy surface for 1200 s at $T = 460$ K; see Sec. 4.2.2).

Due to the lower surface binding energy and lower mass of Mg as compared to Al [26,27], the Mg surface atoms are preferentially sputtered during the in-vacuo sputter-cleaning treatment, thereby depleting the alloy (sub)surface region fully of Mg. On the other hand, subsequent in-vacuo annealing of the Mg-depleted SC alloy surface (thermally) activates the segregation of Mg from the interior of the alloy at its surface (as driven by the lower surface energy of Mg as compared to Al [27,28]) (Fig. 4.1d). It is thus concluded that the two different in-vacuo surface pre-treatments, performed in this study, result in either Mg-depleted (*for the SC alloy surfaces*) or Mg-enriched (*for the SC/Ann alloy surfaces*) alloy surfaces prior to oxidation.

For an incident Ar^+ energy of 1 kV (as employed for the SC step in the present study; see Sec. 4.2.2), the depletion of Mg will extend to a depth of about 2 to 3 nm below the ion-bombarded alloy surface (as governed by the concurrent processes of preferential sputtering (removal) of Mg and bombardment-enhanced segregation of Mg towards the alloy surface; see Ref. [27]). The information depth of the AR-XPS analysis equals $3\lambda \times \cos\alpha$, where λ denotes the effective attenuation length (EAL) of the detected Al 2p or Mg 2p photoelectrons (α is the photoelectron detection angle with respect to the surface normal; see Sec. 4.3.1). The EAL for the detected Mg 2p or Al 2p photoelectrons emitted from the AlMg substrate is about 3 nm [21]. Thus the information depth of the AR-XPS analysis is in the range of 2.4 - 8.4 nm (for $23° \leq \alpha \leq 83°$; see Sec. 4.3.1). Hence, at near-normal detection angles, the information depth of the AR-XPS analysis should exceed the estimated depth of Mg-depletion zone of 2 to 3 nm. However, since the probed photoelectron intensity exponentially decays with increasing depth below the surface, the detected Mg 2p signal intensity that originates from depths below the Mg-depleted surface region (i.e. for depths < ~3nm) falls below the detection limit of the AR-XPS analysis (of about 0.1 at.% Mg), and an Mg 2p signal is not observed (Fig. 4.1b).
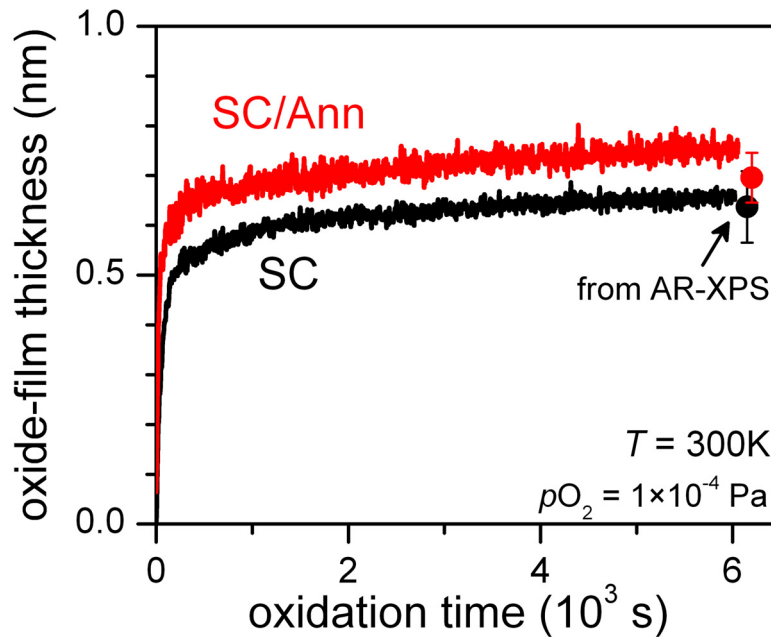
Fig. 4.5: Oxide-film growth curves, as determined by RISE, for the oxidation of the bare SC and SC/Ann Al - 1.1 at.% Mg substrates at 300K ($pO_2 = 1 \times 10^{-4}$ Pa) (see Sec. 4.3.2). The corresponding total oxide-film thicknesses of the oxide films grown after 6×10^3 s, as determined by AR-XPS (see Sec. 4.3.1), have also been plotted.

4.4.2   The oxidized SC and SC/Ann alloy substrates

A.   Oxide-film growth kinetics

Oxide-film growth curves (i.e. total oxide-film thickness, L, versus oxidation time, t), as determined by model fitting to the measured data of $\Delta(\lambda, t)$ and $\Psi(\lambda, t)$ for the oxidations of the bare SC and SC/Ann Al - 1.1 at.% Mg substrates for 6×10^3 s at 300K (see Sec. 4.3.2), are shown in Fig. 4.5. The corresponding oxide-film thicknesses, as determined by AR-XPS at the end of each oxidation (i.e. after 6×10^3 s of oxidation; see Sec. 4.3.1), have been plotted as a function of the oxidation temperature in Fig. 4.6.

The oxidation kinetics are characterized by an initial regime of very fast film growth, which is succeeded by a second oxidation stage in which the film growth rate becomes very small. This passivation behaviour is typical for the oxidation of metals and alloys at low temperatures, where the rate of diffusion of cations and/or anions through the developing oxide film under influence of the (electro)chemical potential (i.e. concentration) gradients, as well as electron transport by thermionic emission, become negligibly small [5,29-31]. Consequently, for the oxidation of the SC and SC/Ann surfaces at $T \leq 425$ K, approximately constant, near-limiting oxide-film thicknesses,

$L_{\text{lim}}^{t=6000s}$, of about $0.64^{\pm 0.09}$ nm and $0.72^{\pm 0.09}$ nm are attained, respectively (Fig. 4.6). The near-limiting oxide-film thicknesses are systematically, on average, about 0.1 nm (i.e. about $^1/_2$ an oxide monolayer [32]) lower for the oxidized SC surfaces than for the corresponding oxidized SC/Ann surfaces. As revealed by RISE analysis (Fig. 4.5), these thickness differences mainly arise during the first-stage growth kinetics (the oxide-film growth rates on the SC and SC/Ann surfaces are approximately equal during the second, slow oxidation stage, as reached after e.g. ~ 387 s and ~ 417 s of oxidation on the SC and SC/Ann surface at 300 K, respectively; cf. Fig. 4.5). The transition from the initial, fast to the second, slow oxidation stage is associated with the formation of a laterally-closed oxide film (i.e. a passivating oxide film) on the oxidizing metal or alloy surface [29]. As discussed in the following, the formation of a closed oxide film is promoted (and thereby a lower thickness is reached at the end of the initial, fast oxidation stage) on the SC surface (as compared to the SC/Ann surface) due to more favourable surface and interface energies and a higher Pilling-Bedworth ratio (P-B ratio; symbol R) of the corresponding oxide overgrowth.
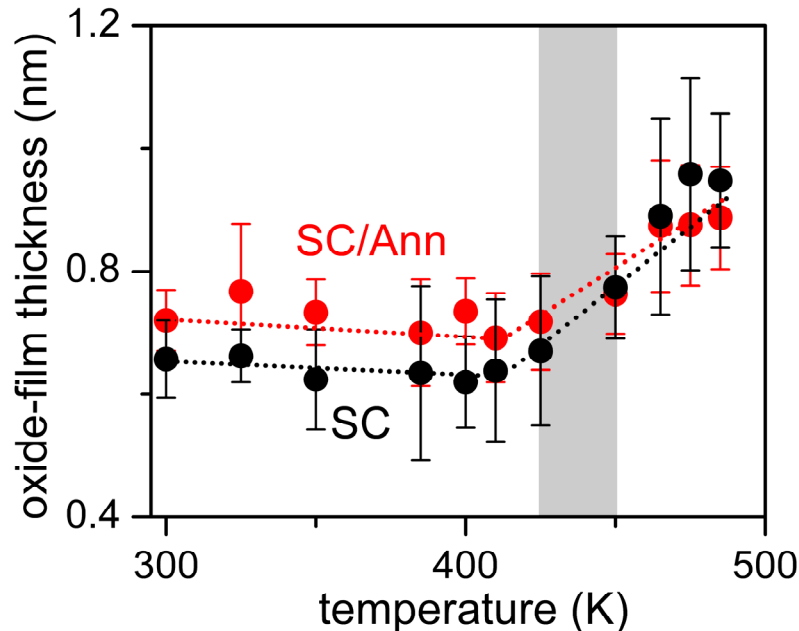
Fig. 4.6: Oxide-film thickness, as determined by AR-XPS (see Sec. 4.3.1), versus oxidation temperature for the oxide films grown on the SC and SC/Ann Al – 1.1 at.% Mg substrates after 6×10^3 s of oxidation (at pO_2 = 1×10^{-4} Pa). The transition temperature range of 425 K $\leq T \leq$ 450 K, beyond which an effect of the surface pre-treatment on the oxide-film growth kinetics is no longer apparent, has been indicated by the grey area. The dotted lines have been drawn to guide the eye.

Table 4.2. Surface (γ^S) and interface energies ($\gamma^S_{M|M_xO_y}$) of am-Al$_2$O$_3$ and am-MgO overgrowths on Al and Mg substrates at $T = 298.15$ K, respectively.

Energy	Solid	Symbol	Value (J/m^2)	ref.
Surface	Al(111)	$\gamma^S_{Al(111)}$	0.91	[35]
	Al(110)	$\gamma^S_{Al(110)}$	1.05	[35]
	Al(100)	$\gamma^S_{Al(100)}$	1.03	[35]
	Mg(0001)	$\gamma^S_{Mg(0001)}$	0.58	[35]
	Mg(1100)	$\gamma^S_{Mg(1100)}$	0.64	[35]
	Mg(1101)	$\gamma^S_{Mg(1101)}$	0.71	[35]
	am-Al$_2$O$_3$	$\gamma^S_{am\text{-}Al_2O_3}$	0.88	[32]
	am-MgO	$\gamma^S_{am\text{-}MgO}$	0.92	[36]
Interface	Al(111)| am-Al$_2$O$_3$	$\gamma_{Al(111)|am\text{-}Al_2O_3}$	-4.463	[36]
	Al(110)| am-Al$_2$O$_3$	$\gamma_{Al(110)|am\text{-}Al_2O_3}$	-4.495	[36]
	Al(100)| am-Al$_2$O$_3$	$\gamma_{Al(100)|am\text{-}Al_2O_3}$	-4.474	[36]
	Mg(0001)| am-MgO	$\gamma_{Mg(0001)|am\text{-}MgO}$	-4.30	[36]
	Mg(1100)| am-MgO	$\gamma_{Mg(1100)|am\text{-}MgO}$	-4.31	[36]
	Mg(1101)| am-MgO	$\gamma_{Mg(1101)|am\text{-}MgO}$	-4.32	[36]

For the initial formation and growth of an *unstrained amorphous* oxide[2] on the SC and SC/Ann alloy surfaces, the oxide growth mode will not only depend on the substrate-temperature-dependent mobility of the oxygen adatom species [31,33], but also on the relative surface and interface energy contributions of the evolving substrate/film system: i.e. the surface energies γ_M^S and $\gamma_{M_xO_y}^S$ of the bare alloy surface and the oxide overgrowth, respectively, as well as the energy, $\gamma_{M|M_xO_y}$, of the interface between the alloy substrate and the oxide. At constant substrate temperature, a layer-by-layer-type of oxide growth mode and thereby a more rapid formation of a closed oxide film will be promoted for a relatively high surface energy of the alloy substrate in combination with relatively low surface and interface energies of the oxide overgrowth on the pre-treated alloy surface: i.e. $\gamma_M^S > \gamma_{M_xO_y}^S + \gamma_{M|M_xO_y}$. As discussed in Sec. B, the amorphous oxide films grown on the *Mg-depleted* (i.e. Al-rich) SC surfaces (see Sec. 4.4.1 and Figs. 4.1(a,b)) at $T < 425$ K are exclusively (or predominantly) constituted of Al-oxide (with no or very little Mg in oxidized state; see Sec.4.4.2.B), whereas the oxide films on the *Mg-enriched* SC/Ann alloy surfaces also contain a considerable amount of Mg in the oxidized state. Therefore, the surface energies of the Mg-depleted SC and Mg-enriched SC/Ann surfaces can be approximated by the surface energies of Al and Mg metal, respectively (see Table 4.2). Similarly, rough estimates for the surface energies of the amorphous Al_2O_3-like and MgO-like overgrowths[3] on the Mg-depleted SC and Mg-enriched SC/Ann surfaces (see Sec. 4.4.1) are obtained from the surface energies of am-Al_2O_3 and am-MgO, respectively (see Table 4.2). Theoretical estimates for the corresponding Al|am-Al_2O_3 and Mg|am-MgO interface energies have also been given in Table 4.2. It follows that the surface energy of Al (as an approximate for the SC surface) is much higher than that of Mg (as an approximate for the SC/Ann surface), whereas the am-Al_2O_3 surface energy and the Al|am-Al_2O_3 interface energies are much lower than the am-MgO surface and Mg|am-MgO interface energies, respectively. Consequently, $\gamma_{Al}^S - \left(\gamma_{am-Al_2O_3}^S + \gamma_{Al|am-Al_2O_3} \right) > \gamma_{Mg}^S - \left(\gamma_{MgO}^S + \gamma_{MgO} \right)$.

---

[2] HR-TEM investigations of the oxidized SC/Ann surfaces in the same project [34] show that the oxide films grown at $T < 475$ K are amorphous and of approximately uniform thickness. Furthermore, the occurrence of growth strain in these ultrathin amorphous oxide films can be neglected [32,35].

[3] Initial interaction of oxygen from the gas phase with the Mg-enriched alloy surface likely proceeds with the preferential oxidation of segregated Mg atoms [6] and thus the formation of an initially Mg-rich oxide phase.

Hence, a layer-by-layer-like oxide growth mode, and thereby the formation of a closed oxide film on the alloy surface, is promoted on the SC surface (as compared to the SC/Ann alloy surface), in accordance with the lower (average) oxide-film thickness reached at the end of the first, initial growth stage on the SC surface (see above and Fig. 4.5). Moreover, the Al_2O_3 overgrowth on the SC surface has a P-B ratio $R_{SC} > 1$, whereas the MgO-like overgrowth on the SC/Ann surface has a P-B ratio $R_{SC/Ann} < 1$ (see Table 4.3),[4] which suggests that a closed oxide layer is earlier realized on the Al-rich SC surface.

Table 4.3. Physical quantities of Al and Mg metal, as well as their corresponding amorphous oxides, at $T = 298.15$ K (the density of the amorphous oxides have been taken from [35]).

Solid	density (g/cm^3)	molar mass (g/mole)	P-B ratio
Al	2.70	26.9815	
			1.61
am-Al$_2$O$_3$	3.17	101.9613	
Mg	1.77	24.3050	
			0.96
am-MgO	3.07	40.3044	

The oxide-film growth rate during the second oxidation stage at $T > 425$ K increases with increasing oxidation temperature due to the enhanced thermally-activated diffusion of ions (i.e. Mg cations, Al cations and/or O anions) in the oxide film and an increased contribution to electron transport by thermionic emission (at $T \geq 410$ K) [5,26-29,37]. For the oxidations at $T > 425$ K, approximately equal oxide-film thicknesses of $\sim0.9^{\pm0.1}$ nm occur for the SC and SC/Ann surfaces after 6×10^3 s of oxidation at 485 K (which is the highest oxidation temperature considered in this study), because at these elevated temperatures the chemical constitution and overall composition of the thickening

---

[4] The P-B ratio of a metal oxide is defined as the ratio of the volume, $V_{M_xO_y}$, of the metal oxide per metal atom, and the volume of the metal substrate per metal atom, V_M.

oxide films then have become independent of the surface pre-treatment (see Sec. 4.4.2.B). The corresponding transition temperature range of $425 \text{ K} \leq T \leq 450 \text{ K}$, beyond which an effect of the surface pre-treatment on the oxide-film growth kinetics is no longer apparent, has been indicated by the grey area in Fig. 4.6.
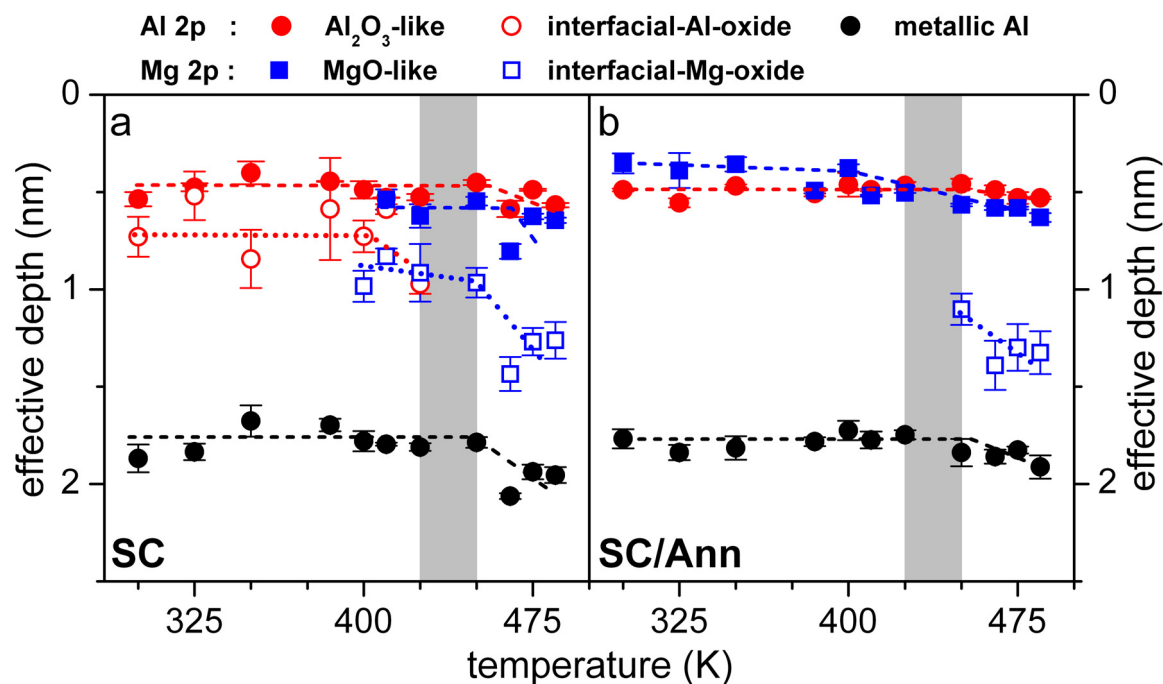

Fig. 4.7: Effective depths [25] of the resolved metallic and oxidic Al 2p and Mg 2p chemical species below the oxide surface (as determined by AR-XPS) as function of the oxidation temperature for the oxidized (**a**) SC and (**b**) SC/Ann Al - 1.1 at.% Mg substrates (oxidized for 6×10^3 s and $pO_2 = 1 \times 10^{-4}$ Pa). The transition temperature range of $425 \text{ K} \leq T \leq 450 \text{ K}$, beyond which an effect of the surface pre-treatment on the depth-resolved oxide-film constitution is no longer apparent, has been indicated by the grey area. The dashed and dotted lines have been drawn to guide the eye.

B.   Chemical constitution of the oxide films

Spectral reconstructions of the Al 2p and Mg 2p AR-XPS spectra, as recorded from the SC and SC/Ann Al - 1.1 at.% Mg substrate after oxidations for 6×10^3 s at 300 K, 400 K and 475 K (and at $pO_2 = 1 \times 10^{-4}$ Pa), are presented in Figs. 4.2 – 4.4, respectively. The calculated effective depths of the resolved metallic and oxidic Al 2p and Mg 2p species below the oxide-film surface (as obtained from the variations of their resolved PZL intensities with photoelectron detection angle; see Sec. 4.3.1) have been plotted versus

oxidation temperature for the oxidized SC and SC/Ann alloy substrates in Figs. 4.7a and b, respectively.[5] Furthermore, the overall Al-to-Mg cation ratio, as well as the overall anion-to-cation ratio (i.e. the O/(Al+Mg) atomic ratio), of the grown oxide films (as also determined by AR-XPS; see Sec. 4.3.1) are shown as function of the oxidation temperature in Figs. 4.8a and b, respectively.
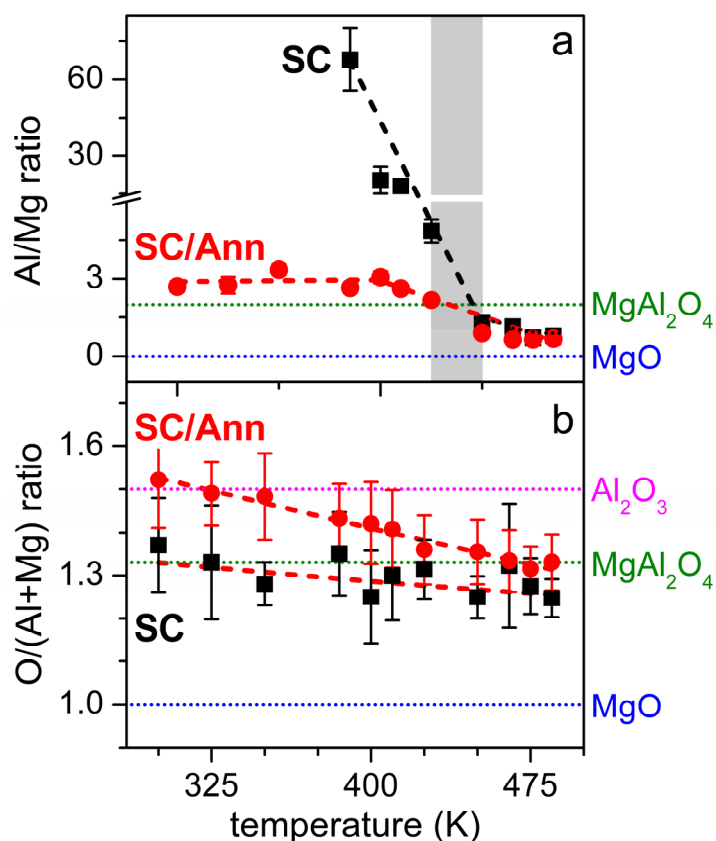
Fig. 4.8: (**a**) Overall Al-to-Mg cation ratio and (**b**) overall anion-to-cation ratio (i.e. the O/(Al+Mg) ratio) of the grown oxide films as function of the oxidation temperature for the oxidized SC and SC/Ann Al - 1.1 at.% Mg substrates (oxidized for 6×10^3 s and $pO_2 = 1 \times 10^{-4}$ Pa), as determined by AR-XPS (see Sec. 4.3.1). The corresponding atomic ratios for $MgAl_2O_4$, MgO and Al_2O_3 have been indicated by the dotted, horizontal lines. The transition temperature range of 425 K $\leq T \leq$ 450 K, beyond which an effect of the surface pre-treatment on the Al-to-Mg-ratio of the oxide film is no longer apparent, has been indicated by the grey area in (a). The dashed lines have been drawn to guide the eye.

---

[5] The resolved O 1s LBE, MBE and HBE components (cf. Table 4.1) are concentrated at the oxide surface, in the interior of the oxide film and at the alloy/oxide interface [21]. As verified in the present study, their relative effective depths are independent of the surface pre-treatment.

It follows that oxidation of the (Mg-depleted) SC substrates at relatively low temperatures $T \leq 385$ K results in the formation of an (amorphous [33,34]) Al-oxide film of near-limiting thickness, whereas a mixed (Al,Mg)-oxide film of near-limiting thickness develops on the (Mg-enriched) SC/Ann substrate (cf. Figs. 4.2, 4.5, 4.6 and 4.8). This indicates that, for $T \leq 385$ K, the thermal diffusion of Mg in the alloy substrate is too slow to enable (in the SC substrates) the Gibbsian segregation of Mg from the alloy's interior to the Mg-depleted alloy surface during oxidation up to the near-limiting thickness (see Sec. 4.4.2.A and Fig. 4.5). As a result, no Mg gets incorporated into the oxide films grown on the SC surfaces at $T \leq 385$ K, whereas both Al solvent atoms and segregated (during the pre-annealing step) Mg atoms at the alloy surface are incorporated in the developing oxide film on the SC/Ann surface.

For the oxidation of the **SC substrates at $T \leq 385$ K**, two different local chemical states were identified for the Al cations in the grown Al-oxide films (see Table 4.1, Figs. 4.2(a,b) and 4.7a): (*i*) an 'Al$_2$O$_3$-like' Al 2p main peak at the higher BE side of the oxidic Al 2p peak envelop, which originates from Al^{3+} cations in the interior of the oxide film and (*ii*) an 'interfacial-Al-oxide' main peak at the lower BE side of the oxidic Al 2p peak envelop, which can be attributed to a deficient coordination of Al cations by nearest-neighbour O anions *at* the alloy/oxide interface (associated with a valence state, Al$^{\delta+}$ with $\delta < 3$) [29].[6] The average anion-to-cation ratio of the Al-oxide films grown on the SC substrates at $T \leq 385$ K equals $1.3^{\pm 0.1}$ (Fig. 4.8b). Using the calculation method of Ref. [21] it is found that, the anion-to-cation ratio of $1.3^{\pm 0.1}$ is mainly due to a small deficiency of oxygen anions with respect to the composition Al$_2$O$_3$ (whereas the average cation molar density resembles that of γ-Al$_2$O$_3$).

For the oxidation of the **SC/Ann substrates at $T \leq 385$ K**, on the other hand, the local chemical states identified for Al and Mg in the oxide film, resemble Al$_2$O$_3$-like (similar as for the SC substrates) and MgO-like chemical states pertaining to the corresponding 'bulk' oxide phases (see Table 4.1, Figs. 4.2(c,d)). Note that, the Mg in the oxide layer originates from the segregated Mg at the SC/Ann surface before oxidation (see Sec. 4.4.1). For $T \leq 385$ K, the Al$_2$O$_3$-like and MgO-like states for the Al cations and Mg cations, respectively, are concentrated at the alloy/oxide interface and near the surface,

---

[6] The interfacial Al-oxide detected by AR-XPS can be directly associated with the interfacial EMA layer (of submonolayer thickness) in the ellipsometric model description (see Sec. 4.3.2).

respectively (in agreement with recent model predictions on the basis of interface thermodynamics [36]). The average Al/Mg and O/(Al+Mg) ratios of these mixed (Al,Mg)-oxide films grown on the SC/Ann substrates at $T \leq 385$ K are $2.9^{\pm 0.2}$ and $1.5^{\pm 0.1}$, respectively (see Figs. 4.8a and b). Using the calculation method of Ref. [21], it follows that the corresponding anion and combined cation molar densities are similar to that of γ-Al$_2$O$_3$.

For the oxidations of the **SC and SC/Ann substrates at $T \geq 400$ K**, the thermally activated segregation of Mg from the interior of the alloy to the interface between the Al-Mg alloy substrate and the oxide overgrowth (driven by a lowering of the interfacial energy [36]) becomes distinct. This interfacial segregation of Mg at $T \geq 400$ K is characterized by the emergence of an 'interfacial-Mg-oxide' local chemical state in the measured AR-XPS spectra of the oxidized SC (see Table 4.1 and Figs. 4.3b and 4.7a). This 'interfacial-Mg-oxide' species is ascribed to the presence of Mg cations with a lower valence state (as compared to Mg^{2+}) at the alloy/oxide interface (as a result of the deficient coordination of Mg cations by nearest-neighbour O anions at the alloy/oxide interface). For the SC substrates, the emergence of the 'interfacial-Mg-oxide' component is accompanied with the gradual disappearance of the interfacial-Al-oxide component (see Figs. 4.4(a,b) and 4.7a). Also for the SC/Ann surfaces, the 'interfacial-Mg-oxide' component arises for the oxidations at $T \geq 450$ K (see Table 4.1, Figs. 4.4d and 4.7b).

The segregating Mg ions *at* the alloy/oxide interface at $T > 400$ K are preferentially oxidized during the second, slow (but continuous) growth stage. Consequently, eventually (i.e. $T > 450$ K; see Fig. 4.7) identical chemical states develop for the Al and Mg cations in the oxide overgrowths on both the SC and SC/Ann surfaces: i.e. an 'Al$_2$O$_3$-like', an 'interfacial-Mg-oxide' and a 'MgO-like' chemical state (see Figs. 4.4 and 4.7). As a result, for the initially Mg-depleted SC substrates, no longer only Al, but also Mg, gets incorporated in the oxide overgrowths (cf. Figs. 4.3b, 4.4b and 4.8a), while for the SC/Ann surfaces, the Mg content of the oxide films further increases (cf. Figs. 4.3d, 4.4d and 4.8a). This leads to a decrease of the overall Al-to-Mg-ratio of the grown oxide films on the SC and SC/Ann surfaces with increasing temperature (and thus with increasing oxide-film thickness) until it reaches an approximately constant value of about $0.8^{\pm 0.1}$ at $T \geq 450$ K, independent of the surface pre-treatment (Fig. 4.8a); the corresponding O/(Al+Mg) atomic ratio of the oxide films then equals $1.30^{\pm 0.07}$ (with anion and cation molar densities close to those of c-MgO and γ-Al$_2$O$_3$).

As evidenced by HR-TEM analysis in this project [34], a gradual development of long range order sets in for the thickening (initially amorphous) oxide films of relatively high Mg content grown at $T \geq 475$ K, which eventually results in local nucleation of a crystalline MgO-type oxide phase, which is the thermodynamically preferred *bulk* oxide phase for the thermal oxidation of Al-Mg alloy surfaces [6]. The preferential oxidation of segregated Mg *at* the alloy/oxide interface explains the observed inversion of the effective depth (distributions) of the Al and Mg cations in the thickening oxide films grown on the SC/Ann surfaces at $T \geq 410$ K: i.e. the effective depths of oxidized Al and oxidized Mg move towards the oxide surface and the alloy/oxide interface, respectively (Fig. 4.7b).

4.5. Conclusions

In-vacuo sputter-cleaning treatments of Al-based Al-Mg alloy result in a Mg-depleted alloy surface (further designated as SC surface), due to preferential sputtering of Mg. Subsequent in-vacuo annealing of such a sputter-cleaned alloy surface produces a Mg-enriched alloy surface (further designated as SC/Ann surface) due to the thermally-activated segregation of Mg to the alloy surface.

The oxidation kinetics of the SC and SC/Ann surfaces are characterized by an initial regime of very fast oxide-film growth, which is succeeded by a second oxidation stage in which the oxide-film growth rate becomes very small. Approximately constant, near-limiting oxide-film thicknesses of $0.64^{\pm 0.09}$ nm and $0.72^{\pm 0.09}$ nm are observed for the oxidation of the SC and SC/Ann surfaces, respectively, for 6000 s at $T \leq 425$ K ($pO_2 = 1 \times 10^{-4}$ Pa). The near-limiting oxide-film thicknesses are about 0.1 nm lower for the oxidized SC surfaces than for the corresponding oxidized SC/Ann surfaces, which is due to the faster formation of a laterally closed oxide film on the SC surfaces during the initial, fast oxidation regime.

The faster formation of a laterally closed oxide film on the SC surface as compared to the SC/Ann surface is due to the relatively higher surface energy of the substrate, lower surface energy of the oxide-film and lower interface energy of the SC-substrate/oxide-film system in combination with a larger Pilling Bedworth ratio for the oxide overgrowth.

The oxide-film growth rate in the second, slow oxidation stage increases with increasing temperature for $T > 425$ K. This is due to the enhanced thermal diffusion of the

ions in the developing oxide film in combination with an increasing contribution to electron transport by thermionic emission.

For the oxidation of the **SC surface at $T \leq 385$ K**, the thermal diffusion of Mg in the alloy substrate is too slow to bring about significant chemical segregation of Mg from the alloy's interior to the Mg-depleted alloy surface during oxidation. As a result, no Mg is incorporated into the oxide films grown on the SC surfaces at $T \leq 385$ K, whereas both Al solvent atoms and segregated Mg atoms at the alloy surface (as segregated during the pre-annealing step) are incorporated into the oxide film grown on the SC/Ann surface.

For the oxidation of the **SC surfaces at $T \leq 385$ K**, two different local chemical states occur for the Al cations in the grown Al-oxide films: (*i*) an 'Al$_2$O$_3$-like' state associated with Al^{3+} cations in the interior of the oxide film and (*ii*) an 'interfacial-Al-oxide' due to a deficient coordination of Al cations by nearest-neighbour O anions *at* the alloy/oxide interface. These Al-oxide films have an average anion-to-cation ratio of $1.3^{\pm 0.1}$ (due to an O deficiency with respect to that of γ-Al$_2$O$_3$).

For the oxide films grown on the **SC/Ann surfaces at $T \leq 385$ K**, the Al and Mg cations are concentrated at the alloy/oxide interface and near the surface, respectively, and resemble Al$_2$O$_3$-like and MgO-like local chemical states as in the corresponding 'bulk' oxide phases. These oxide films have average Al/Mg and O/(Al+Mg) ratios of $2.9^{\pm 0.2}$ and $1.5^{\pm 0.1}$, respectively (with corresponding anion and cation molar densities similar to that of γ-Al$_2$O$_3$).

Due to the thermally-activated interfacial segregation of Mg at $T \geq 400$ K, the oxide films on the **SC and SC/Ann surfaces at $T \geq 400$ K** contain both Mg as well as Al. The interfacial segregation of Mg produces Mg cations with a lower valence state (as compared to Mg^{2+}) at the alloy/oxide interface. The interfacially segregated Mg ions are preferentially oxidized during the oxidation at $T > 410$ K, which results in an overall decrease of the Al/Mg-ratio of the grown oxide films on the SC and SC/Ann surfaces to about $0.8^{\pm 0.1}$ (and a corresponding O/(Al+Mg) atomic ratio of $1.30^{\pm 0.07}$), independent of the surface pre-treatment. As a result of the preferential oxidation of interfacially segregated Mg, the effective depths of Al and Mg in the oxide film move towards the oxide surface and the alloy/oxide interface, respectively.

References

[1]   T. J. Nijdam, G. H. Marijnissen, E. Vergeldt, A. B. Kloosterman and W. G. Sloof, Ox. Metals **66** (2006) 269.

[2]   T. J. Nijdam, C. Kwakernaak and W. G. Sloof , Metall. Mater. Trans. A **37** (2006) 683.

[3]   T. J. Nijdam, L. P. H. Jeurgens, J. H. Chen and W. G. Sloof, Ox Metals **64** (2005) 355.

[4]   P. Nolte, A. Stierle, N. Y. Jin-Phillipp, N. Kasper, T. U. Schulli, H. Dosch, Science **321** (2008) 1654.

[5]   A. Lyapin, L. P. H. Jeurgens, P. C. J. Graat, E. J. Mittemeijer, J. Appl. Phys. **96** (2004) 7126.

[6]   L. P. H. Jeurgens, M. S. Vinodh, and E. J. Mittemeijer, Acta Mat. **56** (2008) 4621.

[7]   A. Pasquarello and A. M. Stoneham, J. Physics: Condensed Matter **17** (2005) V1.

[8]   M. Tsuchiya, S. K. R. S. Sankaranarayanan and S. Ramanathan, Prog. Mat. Sc. **54** (2009) 981.

[9]   J. G. Li, Mater. Chem. Phys. **47** (1997) 126.

[10]   C. T. Campbell, Surf. Sci. Rep. **27** (1997) 1.

[11]   F. S. Ohuchi and M. Kohyama, J. Am. Ceram. Soc. **74** (1991) 1163.

[12]   S. B. Sinnott and E. C. Dickey, Mater. Sci. Eng. R **43** (2003) 1.

[13]   E. Pagounis, M. Talvitie and V. K. Lindroos, Comp. Sci. and Tech. **56** (1996) 1329.

[14]   V. Da Costa, C. Tiusan, T. Dimopoulos and K. Ounadjela, Phy. Rev. Lett. **85** (2000) 876.

[15]   G. Hu and Y. Suzuki, Phy. Rev. Lett. **89** (2002) 4.

[16]   A. Atkinson, Rev. Mod. Phys. **57** (1985) 437.

[17]   E. Comini, G. Faglia, G. Sberveglieri, Z. W. Pan and Z. L. Wang, Appl. Phys. Lett. **81** (2002) 1869.

[18]   Z. R. Dai, Z. W. Pan and Z. L. Wang, Adv. Funct. Mat. **13** (2003) 9.

[19]   J. Gustafson, R. Westerstroem, A. Mikkelsen, X. Torrelles, O. Balmes, N. Bovet, J. N. Andersen, C. J. Baddeley and E. Lundgren, Phys. Rev. B **78** (2008) 6.

[20]   C. R. Henry, Surf. Sci. Rep. **31** (1998) 235.

[21]   E. Panda, L. P. H Jeurgens and E. J. Mittemeijer, *submitted to J. Appl. Phys.*

[22]   M. Kurth, P. C. J. Graat, H. D. Carstanjen, E. J. Mittemeijer, Surf. Interface Anal. **38** (2006) 931.

[23]   M. S. Vinodh and L. P. H. Jeurgens, Surf. Interface Anal. **36** (2004) 1629.

[24]   L. P. H. Jeurgens, W. G. Sloof, F. D. Tichelaar, C. G. Borsboom and E. J. Mittemeijer, Appl. Surf. Sci. **161** (2000) 139.

[25]   L. P. H. Jeurgens, M. S. Vinodh, and E. J. Mittemeijer, Appl. Surf. Sci. **253** (2006) 627.

[26]   A. Oliva, R. Kelly and G. Falcone, Nucl. Instr. And Meth. **B19/20** (1987) 101.

[27]   F. Reichel, L. P. H Jeurgens and E. J. Mittemeijer, Phys. Rev. B **73** (2006) 024103.

[28]   T. J. Nijdam, L. P. H. Jeurgens, W. G. Sloof, Acta Mater. **51** (2003) 5295.

[29]   F. Reichel, L. P. H. Jeurgens and E. J. Mittemeijer, Acta Mat. **56** (2008) 2897.

[30]   A. Lyapin, L. P. H. Jeurgens, E. J. Mittemeijer, Acta Mat. **53** (2005) 2925.

[31]   L. P. H. Jeurgens, W. G. Sloof, F. D. Tichelaar, and E. J. Mittemeijer, J. Appl. Phys. **92** (2002) 1649.

[32]   L. P. H. Jeurgens, W. G. Sloof, F. D. Tichelaar and E. J. Mittemeijer, PRB. **62** (2000) 4707.

[33]   F. Reichel, L. P. H Jeurgens, G. Richter and E. J. Mittemeijer, J. Appl. Phys. **103** (2008) 093515.

[34]   E. Panda, L. P. H. Jeurgens, G. Richter and E. J. Mittemeijer, *submitted to J. Mat. Res*.

[35]   F. Reichel, L. P. H Jeurgens and E. J. Mittemeijer, Acta Mat **56** (2008) 659.

[36]   E. Panda, L.P. H Jeurgens and E. J. Mittemeijer, *submitted to Acta Materialia*.

[37]   P. C. J. Graat, M. A. J. Somers and E. J. Mittemeijer, Z. Metallkd. **93** (2002) 532.

5.   Growth kinetics and mechanism of the initial oxidation of Al-based Al-Mg alloys

E. Panda, L. P. H. Jeurgens, E. J. Mittemeijer

Abstract

The relationship between the oxide-film growth kinetics and the depth-resolved local chemical states of Al, Mg and O ions in ultrathin (< 3 nm) oxide films, as grown on sputter-cleaned Al-based Al-Mg substrates in the temperature and partial oxygen pressure ranges of $T = 300 - 610$ K and $pO_2 = 1 \times 10^{-2}$ - 1×10^{-4} Pa, respectively, was established by real-time in-situ spectroscopic ellipsometry (RISE) and in-situ angle-resolved X-ray photoelectron spectroscopy (AR-XPS). An initial regime of first oxide-film growth is succeeded by a second, slow oxidation stage; an oxide-film of near-limiting thickness (~ 1 nm) is observed at $T < 475$ K. Oxidation at $T \leq 385$ K leads to the formation of an Al-oxide film exhibiting both interfacial and bulk 'Al$_2$O$_3$'-like local chemical states of the oxidized Al cations. At $T > 385$ K, an 'interfacial-Mg-oxide' state appears due to the thermally-activated interfacial segregation of Mg from the alloy's interior to the alloy/oxide interface. Continued oxide-film growth at $T > 385$ K is then realized by the preferential oxidation of interfacially segregated Mg, as evidenced by the appearance of a bulk 'MgO'-like state for the Mg cations.

5.1. Introduction

The microstructure of an ultra-thin (thickness < 3 nm) oxide film present on the surface of an elemental metal or metallic alloy substrate decides many of the physical and chemical properties of a metallic component applied in practice, such as its corrosion resistance, adhesion, friction, electrical and thermal conductivity, dielectric capacity and optical appearance. Therefore, optimization and control of the structure - property relationships of such oxide films and the associated metal/oxide interfaces are of crucial importance for a vast array of technological applications, such as pertaining to novel structural materials based on metal/ceramic composites, metal/oxide seals in medical implant construction,

metal/oxide contacts in microelectronics and photovoltaic devices, corrosion-resistant coatings, gas-sensors and oxide-supported transition metal catalysts [1-12].

Functionalization and optimization of such ultrathin-oxide-film-based technologies demand fundamental investigation of the microstructural evolution of the oxide films as function of the growth conditions and the type of metallic substrate. Only very recently [13-16] important thermodynamic and kinetic parameters of the growth of ultra-thin *single-phase* oxide overgrowth on bare elemental metal substrates, such as the amorphous-to-crystalline transition beyond a critical oxide-film thickness and the governing driving forces and mechanism(s) for the oxide-film growth have been exposed in great detail by using a combinatorial experimental approach of real-time in-situ spectroscopic ellipsometry (RISE), Angle-resolved X-ray photoelectron spectroscopy (AR-XPS), low energy electron diffraction (LEED) and/or high-resolution transmission electron microscopy (HR-TEM). Such detailed combinatorial experimental studies on the microstructural evolution of *ultra-thin*, *multiple-metal* oxide films on *alloy* substrates have not been conducted up to date (for a few of such studies, see Refs. [3,17-19]). Until now, investigations on the thermal oxidation of metallic alloys have been performed mainly at *high* temperatures (i.e. $T > 800$ K) and *high* pressures (i.e. $0.1 < p < 10^5$ Pa), where, relatively thick (in the micrometer range) oxide scales, composed of multiple, *crystalline* oxide phases, develop on the alloy surface by preferential oxidation of the alloy constituents [20-23]. The thermal oxidation of metallic alloys at *low* temperatures (say, $T < 600$ K), has been investigated only scarcely up to date. At these temperatures, thermally activated diffusion of reactants through the developing oxide-film is negligibly small, which typically results in the formation of a thin oxide film of near-limiting thickness (< 5 nm) that is constituted of metastable, *multiple-metal* oxide phase(s). The detailed microstructure (i.e. oxide-phase constitution, chemical composition, morphology) and the thickness of such ultrathin, multiple-metal oxide films, as function of the oxidation conditions, are still unknown.

Evidently, microstructural characterization of multiple-metal oxide films is much more challenging than the analysis of single-metal oxide films, because more than one substrate constituent can be incorporated into the developing oxide film (e.g. a multiple-element (e.g. spinel) and/or multi-phase oxide film can be formed), which is associated with compositional changes occurring in the alloy subsurface during oxide growth [3,17,18,24-28]. In particular if *more than one* of the alloy constituents has a strong

affinity towards oxygen, like in the Al-Mg system (in contrast to binary alloy systems such as Au-Cu, Ag-Cu or Pt-Al, where one constituent is relatively nobler than the other), the interrelationships of the microstructural evolution of the growing oxide film, the oxidation-induced compositional changes in the parent alloy substrate and the oxidation conditions can be rather complicated [3].

The alloy constituents Al and Mg, fall in the category of lights metals and Al-based Al-Mg alloys therefore find manifold technological application in areas where weight reduction is a major concern (i.e., in automotive and aerospace industries). Commercially used Al-based Al-Mg alloys generally have a nominal Mg alloying content in the range of 0.5 to 12 at.%. A relatively low Mg content enhances the alloy's formability, which is important for use in exterior and interior trim parts of the automobiles, automobile gas and oil lines. A relatively high Mg content generally leads to an improvement of the castability, strength and wet-corrosion resistance, which is important for application in food handling, cooking utensils, fittings for chemical and sewage use, pressure vessels and marine uses) [29-31].

Earlier works on the oxidation of AlMg alloy surfaces were mostly conducted at relatively high oxidation temperatures and at atmospheric conditions in the presence of a native Al-oxide film on the alloy surface at the onset of oxidation (cf. Refs. [20-23]). In only a few investigations, the oxide films were grown under controlled conditions at room temperature in an ultra high vacuum environment (as studied by e.g. Auger electron spectroscopy [32,33]), but without presenting any detailed analysis of the developing oxide-film microstructure.

The current paper comprises a detailed experimental investigation by RISE and AR-XPS analyses of the growth kinetics and the developing microstructure of ultrathin (< 3 nm) (Al,Mg)-oxide films grown on sputter-cleaned, bare (i.e., without a native oxide) Al-based AlMg alloy substrates by (dry) thermal oxidation in the temperature range of T = 300 - 610 K and at partial oxygen pressures of $pO_2 = 1\times10^{-4}$ Pa and $pO_2 = 1\times10^{-2}$ Pa.

5.2. Experimental: Alloy preparation and oxidation, Analysis and Quantification

Disc-shaped specimens (10 mm diameter; 1 mm thickness) of a single-phase, polycrystalline Al-based AlMg solid-solution alloy with an average grain size in the range of 50 - 100 μm and a homogeneous Mg content of either 0.8 at.% or 1.12 at.% Mg

(henceforth referred to as Al – 0.8% Mg alloy or Al – 1.1% Mg alloy, respectively) were prepared by successive melting, casting and annealing procedures, as described in Ref. [25]. The prepared alloys have the following impurity concentrations (ppm in mass; as determined by Inductive Coupled Plasma–Optical Emission Spectrometry): Zn = 70, Mn = 40, Na = 30, C = 72 ± 8, and [Fe, Ca, Cu, Cr, Ti, Y, O] < 10.

The specimens were introduced into a combined UHV system (base pressure < 3×10^{-8} Pa) for in-vacuo specimen cleaning, annealing, controlled oxidation and in-situ analysis by e.g. AR-XPS and RISE. Prior to each oxidation experiment, the (native) oxide and other contaminants (generally only adventitious carbon) on the specimen surface were removed by sputter-cleaning (SC) at room temperature with a 1 kV Ar^+ beam (rastering the entire sample surface and employing sample rotation at a speed of about 6 °/s) until no other elements than the pure alloy constituents (i.e. Al and/or Mg) were detected in a measured XPS survey spectrum recorded over the binding energy (BE) range from 0 to 1200 eV (for instrumental details, see Ref. [25]). The AlMg specimens as obtained after the described SC treatment are further designated as *sputter-cleaned (SC)* substrates.

Next, ultra-thin (thickness < 3 nm; see Sec. 5.3.1) oxide films were grown in-situ by exposure of the SC substrates for 21 – 21600 s to pure oxygen gas (i.e. ≥ 99.99990 vol.% with a specified residual gas content of H_2O ≤ 0.5 vpm, N_2 / Ar ≤ 2.0 vpm, C_nH_m ≤ 0.1 vpm and CO_2 ≤ 0.1 vpm) in the temperature (T) range of 300 - 610 K at a constant partial oxygen pressure (pO_2) of 1×10^{-4} Pa or 1×10^{-2} Pa (for details, see Ref. [25]).

In-situ AR-XPS analysis of the SC and oxidized alloy substrates was performed with a Thermo VG Thetaprobe system operating in so-called parallel data acquisition mode, while employing monochromatic Al Kα radiation. The average thickness, overall composition, as well as the depth-resolved elemental constitution of the grown oxide films were calculated from the Al 2p, Mg 2p and O 1s primary zero loss (PZL) photoelectron intensities, as resolved from the measured AR-XPS spectra of the oxidized alloy (for various photoelectron detection angle sets), as described in detail in Refs. [17,25]. The average binding energy (BE) values (and corresponding standard deviations) of the different Al 2p, Mg 2p and O 1s main peaks, as resolved from the recorded AR-XPS spectra of the SC and oxidized alloy substrates, have been gathered in Table 5.1.

Table 5.1. Average binding energy (BE) values (and corresponding standard deviations) of the metallic and oxidic Al 2p and Mg 2p main peaks, as well as of the O 1s main peaks, as resolved from the measured AR-XPS spectra of the oxidized SC Al – 0.8% Mg and Al – 1.1% Mg substrates within the oxidation temperature range 300 – 610 K. The thickness range in which each spectral component is discernable in the measured spectra of the oxidized alloy has been indicated. Since the 'MgO-like' oxidic Mg 2p main peak shifts to lower BE values with increasing oxidation temperature, a corresponding BE range (instead of the averaged BE-value) has been given.

Main peak	Designation	BE (eV)	*d*-range (nm)
metallic Al 2p		72.71 ± 0.005	0.3 – 3.0
metallic Mg 2p		49.59	
oxidic Mg 2p	MgO-like	$(51.83 - 51.3) \pm 0.1$	0.3 – 3.0
	interfacial-Mg-oxide	50.60 ± 0.1	0.3 – 1.4
oxidic Al 2p	Al_2O_3-like	75.60 ± 0.1	0.3 – 3.0
	interfacial-Al-oxide	73.92 ± 0.1	0.3 – 1.24
O 1s	LBE	532.06 ± 0.2	0.3 – 3.0
	MBE	533.24 ± 0.4	0.3 – 3.0
	HBE	534.3 ± 0.21	0.3 – 1.26

RISE measurements of the SC substrates during in-vacuo heating up, annealing and subsequent oxidation were carried out employing a J. A. Woollam Co., Inc. rotating compensator ellipsometer (RCE) M-2000L, equipped with a Xe light source (800 wavelengths, λ, in the range of $\lambda = 245$ - 900 nm, in intervals of ~0.8 nm), which is mounted directly on the flanges of the UHV RC (with angles of incidence and reflection of 70° with respect to the sample surface normal). Spectra of the ellipsometric phase-shift and amplitude-ratio dependent parameters Δ and ψ versus λ were simultaneously recorded over the wavelength range of $\lambda = 350$-850 nm (in intervals of ~0.8 nm) from the bare and oxidizing alloy surface as a function of oxidation time (with a time step of $\Delta t = 1.4$ s and an ellipse-shaped analysis area of 2×8 mm^2). The oxide-film growth kinetics of the

developing oxide-film were determined by fitting model descriptions of $\psi(\lambda, t)$ and $\Delta(\lambda, t)$ to the corresponding measured data of $\psi(\lambda, t)$ and $\Delta(\lambda, t)$. To this end, a (physically) realistic model for the optical response of the studied alloy-substrate/oxide-film system was constructed, further designated as the *'alloy|EMA|Cauchy'* model, which considers the overgrowth of a transparent oxide film of uniform thickness, L^{ox}, on top of the bare alloy substrate in combination with an intermediate suboxidic layer of submonolayer thickness, $L^{int} \leq 0.05$ nm (as required to account for the characteristic ellipsometric absorption at the alloy/oxide interface). For details of the RISE evaluation procedure, see Ref. [25,34].
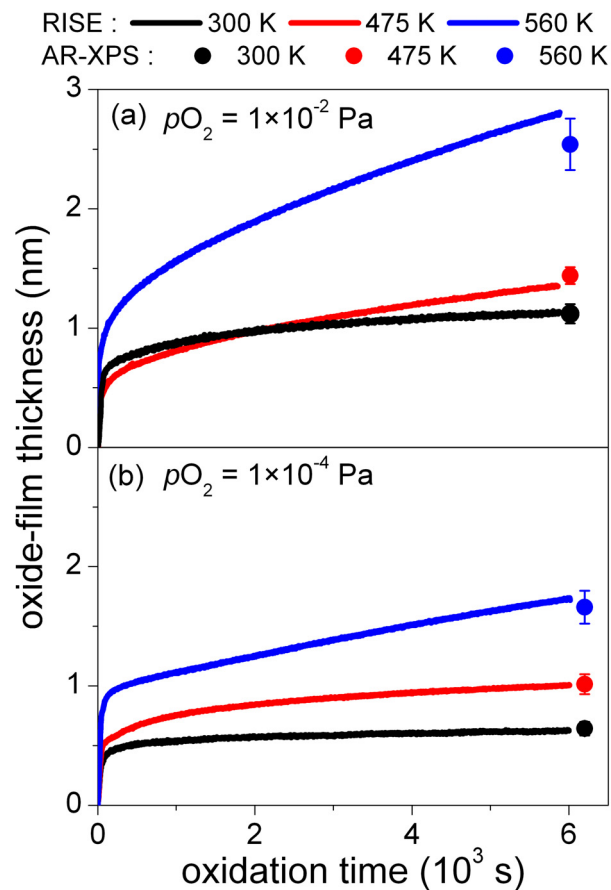

Fig. 5.1: Experimental oxide-film growth curves, as obtained by in situ RISE, pertaining to the oxidation of the bare SC Al - 0.8 at.% Mg substrate for 6×10^3 s at $T = 300$ K, 475 K and 560 K and at a constant partial oxygen pressure of **(a)** $pO_2 = 1\times10^{-4}$ Pa and **(b)** $pO_2 = 1\times10^{-2}$ Pa. The corresponding total oxide-film thicknesses of the oxide films grown after 6×10^3 s, as determined by in situ AR-XPS, have also been plotted.
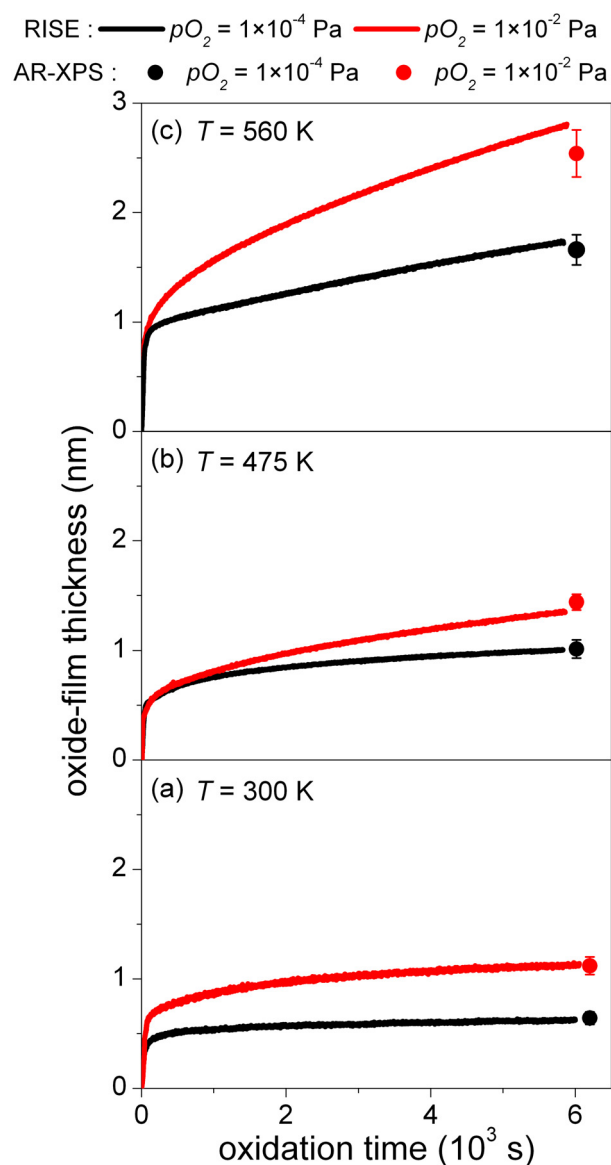
Fig. 5.2: Experimental oxide-film growth curves, as determined by in situ RISE, pertaining to the oxidation of the SC Al - 0.8 at.% Mg substrate for 6×10^3 s at $pO_2 = 1 \times 10^{-4}$ Pa or $pO_2 = 1 \times 10^{-2}$ Pa and **(a)** $T = 300$ K, **(b)** $T = 475$ K and **(c)** $T = 560$ K. The corresponding total oxide-film thicknesses of the oxide films grown after 6×10^3 s, as determined by in situ AR-XPS, have also been plotted.

5.3. Results and discussion

5.3.1   Oxide-film growth kinetics

Oxide-film growth curves, as obtained by RISE (Sec. 5.2), for the oxidation of the SC Al – 0.8% Mg substrates at a $pO_2 = 1 \times 10^{-4}$ Pa or $pO_2 = 1 \times 10^{-2}$ Pa and at various temperatures in the range of $300 - 560$ K are shown in Figs. 5.1 and 5.2. The growth

curves correspond to the sum of the thickness, $L^{ox}(t)$, of the transparent oxide top layer and the thickness, $L^{int}(t)$, of the non-stoichiometric suboxidic layer (of submonolayer thickness) at the alloy/oxide interface, as considered in the model description of $\Delta(\lambda, t)$ and $\Psi(\lambda, t)$ for the evolving substrate/film system (Sec. 5.2): i.e. $L(t) = L^{ox}(t) + L^{int}(t)$. The corresponding oxide-film thicknesses, as determined by AR-XPS, at the end of each oxidation experiment (i.e. after 6×10^3 s), have been plotted versus temperature in Fig. 5.3; these thickness values are also shown in Figs. 5.1 and 5.2 for comparison with the RISE data (at 6×10^3 s).
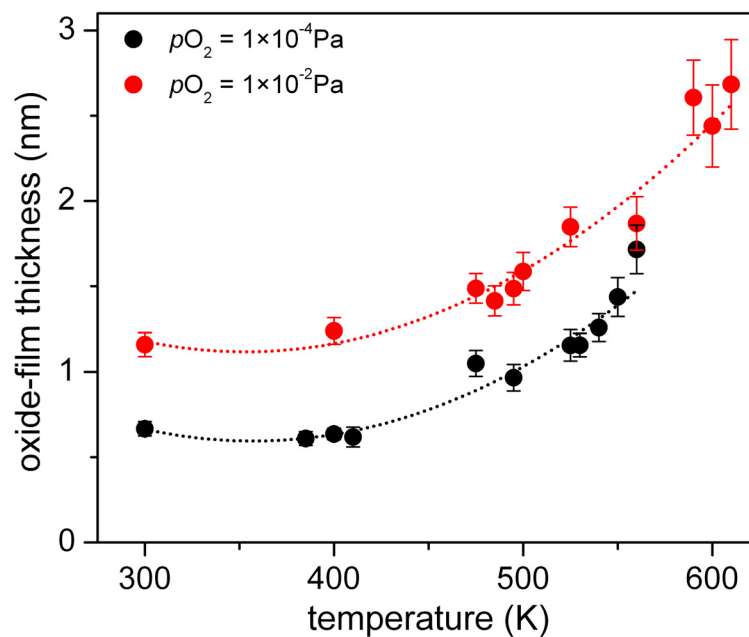

Fig. 5.3: Oxide-film thickness values, as determined by AR-XPS, versus oxidation temperature for the oxidation of the SC Al – 0.8 at.% Mg substrates for 6×10^3 s and at $pO_2 = 1 \times 10^{-4}$ Pa or $pO_2 = 1 \times 10^{-2}$ Pa. The dotted lines have been drawn to guide the eye.

It follows that oxidation of the SC Al – 0.8% Mg substrates for $t = 6 \times 10^3$ s in the temperature and pO_2 ranges of $T = 300 - 560$ K and $10^{-4} - 10^{-2}$ Pa, respectively, produces oxide films with thicknesses in the range of 0.5 to 3 nm. The oxide-film thickness attained after $t = 6 \times 10^3$ s increases with both increasing T (Figs. 5.1 and 5.3) and increasing pO_2 (Figs. 5.2 and 5.3).

The oxide-growth kinetics are characterized by an initial regime of very fast film growth, which is succeeded by a second oxidation stage in which the film growth rate becomes much smaller. This passivation behavior is typical for the oxidation of metals

and alloys at low temperatures, where the rate of thermal diffusion of cations and/or anions through the developing oxide film under influence of the chemical potential (i.e. concentration) gradient is negligibly small [13,35]. As a result [35], a near-limiting oxide-film thickness, L_{lim}, is attained for the oxidations performed at $T < 475$ K (compare Figs. 5.1-5.3).

The oxide-film thickness as reached after $t = 6 \times 10^3$ s increases exponentially (see Fig. 5.3) with increasing T (at constant $p\text{O}_2$) from 0.67 ± 0.04 nm at $T = 300$ K to about 1.72 ± 0.14 nm at $T = 560$ K for $p\text{O}_2 = 1 \times 10^{-4}$ Pa and from 1.16 ± 0.07 nm at $T = 300$ K to about 2.7 ± 0.26 nm at 610 K for $p\text{O}_2 = 1 \times 10^{-2}$ Pa. The exponential increase of the thickness value attained after $t = 6 \times 10^3$ s with increasing temperature can be attributed to the thermally-activated diffusion of ions (i.e. Al cations, Mg cations and/or O anions; see Sec. 5.3.4) in the oxide film, in combination with an increased contribution to electron transport by thermionic emission (at $T \geq 410$ K) [13,35,36]. The increase of the thickness value attained after $t = 6 \times 10^3$ s with increasing $p\text{O}_2$ can be attributed to an increase of the surface charge field strength across the growing oxide film due to the higher density of (negatively charged) chemisorbed oxygen species at the oxide surface at higher $p\text{O}_2$ [13,35].

5.3.2 Composition of the SC alloy surfaces

Due to the in-vacuo sputter treatment performed to clean the AlMg substrates prior to oxidation (i.e. to remove the native oxide; see Sec. 5.2), the alloy subsurface region becomes fully depleted of Mg, as also follows from an analysis of the concurrent processes of preferential sputtering (removal) of Mg and bombardment-enhanced segregation of Mg towards the ion-bombarded alloy surface (for an incident Ar^+ energy of 1 kV (as employed for the SC step in the present study; see Sec. 5.2), the depletion of Mg extends to a depth of approximately 2 to 3 nm below the ion-bombarded alloy surface; see Ref. [37] for details): no Mg 2p signal intensities were detected in the measured AR-XPS spectra of the SC alloy substrates (also see Ref. [28]).

As a result of the depletion of Mg in the subsurface region of the SC alloy substrates, no effect of the bulk Mg alloying content (i.e., 0.8% Mg and 1.1% Mg for the Al-based Al-Mg alloys investigated here) on the developing oxide-film microstructure was observed over the studied temperature (i.e. $T = 300 - 610$ K), time ($t = 21 - 21600$ s) and $p\text{O}_2$ ($p\text{O}_2 = 10^{-4} - 10^{-2}$ Pa) ranges (see Sec. 5.3.3).
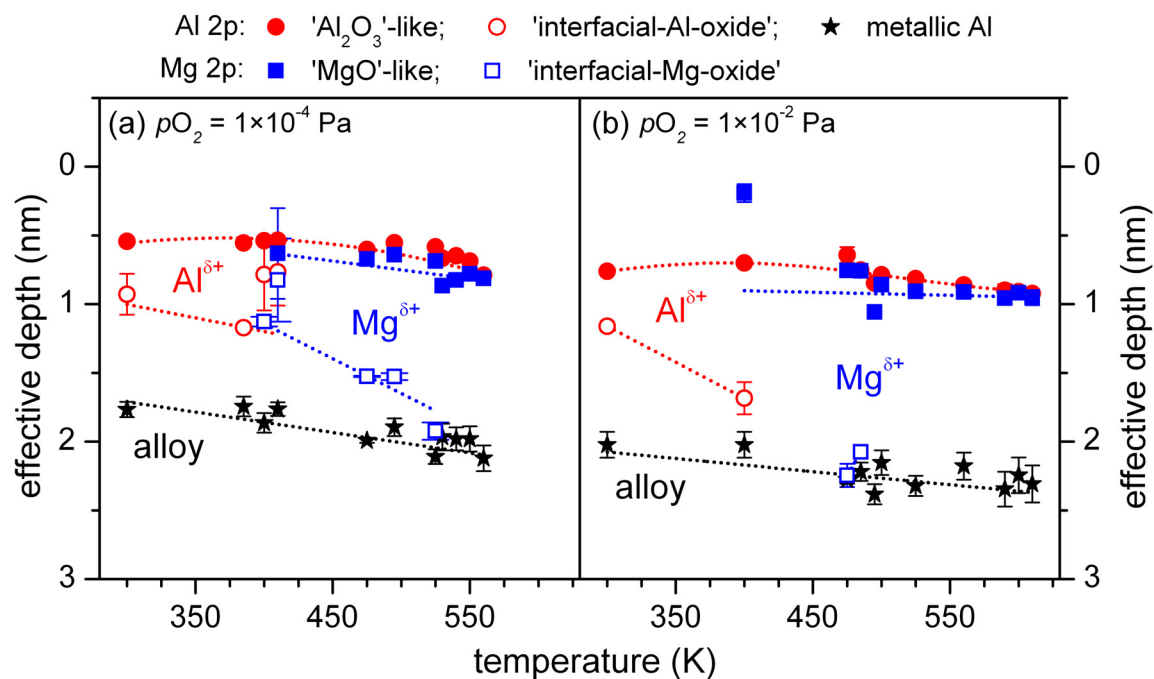
Fig. 5.4: Calculated effective depths (for definition, see Ref. [25]) of the different chemical states of Mg and Al below the oxide surface (as identified by AR-XPS) versus oxidation temperature for the oxidation of the bare SC Al – 0.8 at.% Mg substrates for 6×10^3 s at (**a**) $pO_2 = 1\times10^{-4}$ Pa and (**b**) $pO_2 = 1\times10^{-2}$ Pa, in the temperature range 300 - 610 K. The dotted lines have been drawn to guide the eye.

5.3.3   *Chemical constitution of the grown oxide films*

The spectral reconstructions of the measured Al 2p, Mg 2p and O 1s AR-XPS spectra of the oxidized AlMg substrate (performed in this project according to Ref. [25], where examples of such spectral reconstructions are presented), revealed, depending on oxidation conditions, different local chemical states (i.e. environments) for the Al and/or Mg cations and the O anions in the grown oxide films: see Table 5.1. The corresponding effective depths of the resolved metallic and oxidic Al 2p and Mg 2p species below the oxide-film surface (as calculated from the variations of their resolved PZL intensities with photoelectron detection angle (procedure described in Ref. [25])) have been plotted versus oxidation temperature, for the oxidations for $t = 6\times10^3$ s at $pO_2 = 1\times10^{-4}$ Pa and $pO_2 = 1\times10^{-2}$ Pa, in Figs. 5.4a and b, respectively. Analogously, the corresponding effective depths of the resolved O 1s species have been plotted versus temperature in Figs. 5.5a and b.
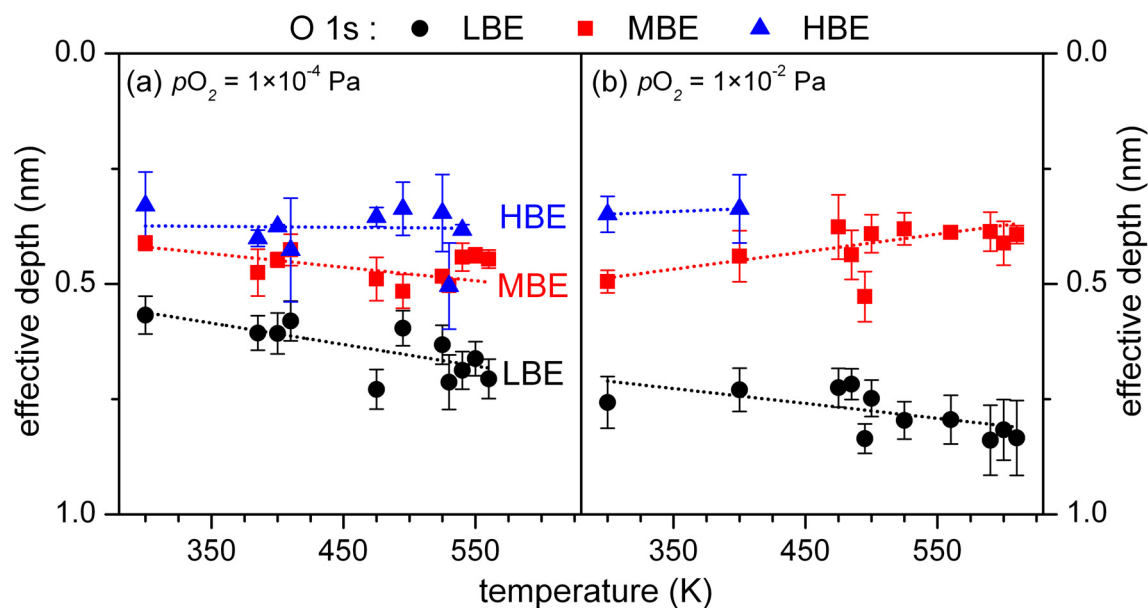
Fig. 5.5: Calculated effective depths (for definition, see Ref. [25]) of the different chemical states of O below the oxide surface (as identified by AR-XPS) versus oxidation temperature for the oxidation of the bare SC Al – 0.8 at.% Mg substrates for 6×10^3 s at (**a**) $pO_2 = 1 \times 10^{-4}$ Pa and (**b**) $pO_2 = 1 \times 10^{-2}$ Pa in the temperature range $T = 300 - 610$ K. The dotted lines have been drawn to guide the eye.

It follows that the oxidations of the *Mg-depleted* (see Sec. 5.3.2) SC alloy surfaces at $T \leq 385$ **K** lead to the formation of ultrathin Al-oxide (Fig. 5.4) films of limiting thickness (Fig. 5.1): i.e. no Mg is taken up in the oxide films grown on the SC substrates at $T \leq 385$ K. In this case, two different local chemical states of Al are identified in the grown oxide films by the AR-XPS analysis (Fig. 5.4 and Table 5.1):

(*i*) a predominant 'Al$_2$O$_3$-like' Al 2p main peak is observed, which originates from Al cations in the interior of the oxide film with a local chemical state similar to that of Al cations in 'bulk' amorphous Al$_2$O$_3$ and crystalline γ-Al$_2$O$_3$;

(*ii*) a much weaker 'interfacial-Al-oxide' Al 2p main peak is observed as well (at a larger effective depth below the oxide surface; see Figs. 5.4(a,b)), which can be attributed to a deficient coordination of Al cations by nearest-neighboring O anions *at* the alloy/oxide interface (associated with a valence state, Al$^{\delta+}$ with $\delta < 3$; cf. Ref. [14]).

It is concluded that, for oxidation at $T \leq 385$ K, the thermally-activated diffusion in the alloy is too slow to promote the Gibbsian segregation of Mg from the alloy's interior to the Mg-depleted alloy substrate region adjacent to the oxide film, as driven by a lowering of the interfacial energy [26].

With increasing temperature, i.e. for **$T > 385$ K**, the thermally activated interfacial segregation of Mg from the alloy's interior to the alloy/oxide interface becomes significant, as evidenced by the appearance of an 'interfacial-Mg-oxide' Mg 2p state in the measured AR-XPS spectra of the oxidized alloy (Figs. 5.4(a,b)). As for the interfacial Al cations, the interfacial Mg cations have a lower valence state (as compared to Mg^{2+}) due to their deficient coordination by nearest-neighboring O anions *at* the alloy/oxide interface. The appearance of the 'interfacial-Mg-oxide' component is accompanied by the disappearance of the interfacial-Al-oxide component upon continued growth of the oxide film at $T > 400$ K (Fig. 5.4).

It was experimentally verified (see Sec. 5.3.4) that, these interfacially segregated Mg cations are incorporated into the thickening oxide film in particular during the second, slow oxidation stage (see Figs. 5.1, 5.2 and discussion in Sec. 5.3.1) at $T > 400$ K. Thus, an additional chemical state of Mg arises in the measured Mg 2p AR-XPS spectra of the oxidized alloy substrate at $T > 400$ K (Fig. 5.4) associated with Mg cations incorporated in the interior of the oxide film (resembling the chemical state of Mg cations in 'bulk' MgO; cf. Table 5.1 and Ref. [3]). If the rate of Mg interfacial segregation is larger than the rate of Mg incorporation in the growing oxide film, the 'interfacial-Mg-oxide' component remains visible in the measured Mg 2p AR-XPS spectra. On the other hand, if the rate of Mg incorporation in the growing oxide film exceeds the rate of Mg interfacial segregation, then the 'interfacial-Mg-oxide' gradually disappears (or is not at all observed) and only the 'MgO'-like component remains. The relative rates of Mg interfacial segregation and Mg incorporation, depend on T, t and pO_2 (see also Fig. 5.4). In association with the increase of oxide-film growth rate during the second growth stage upon increase of pO_2 (see Sec. 5.3.1), the disappearance of the 'interfacial-Mg-oxide' component occurs already at lower temperature for oxidation at higher pO_2: the 'interfacial-Mg-oxide' is absent for the oxidation at $T > 525$ K and $T > 485$ K for $t = 6 \times 10^3$ s at $pO_2 = 1 \times 10^{-4}$ Pa and $pO_2 = 1 \times 10^{-2}$ Pa, respectively (compare Figs. 5.4a and 5.4b).

Because the oxide-film growth rate decreases with time, one would expect, at elevated temperatures where interfacial segregation of Mg occurs, the (re)emergence of the 'interfacial-Mg-oxide' component in the measured Mg 2p AR-XPS spectra. This is not observed (see Fig. 5.4). The reason may be that the 'interfacial-Mg-oxide' component cannot be distinguished from the MgO-like component due to now crystallized 'MgO'

present in the oxide film at the substrate/film interface, under the constraint of the epitaxial orientation relationship $(001)_{AlMg} \parallel (001)_{MgO}$; $[001]_{AlMg} \parallel [001]_{MgO}$ [27].
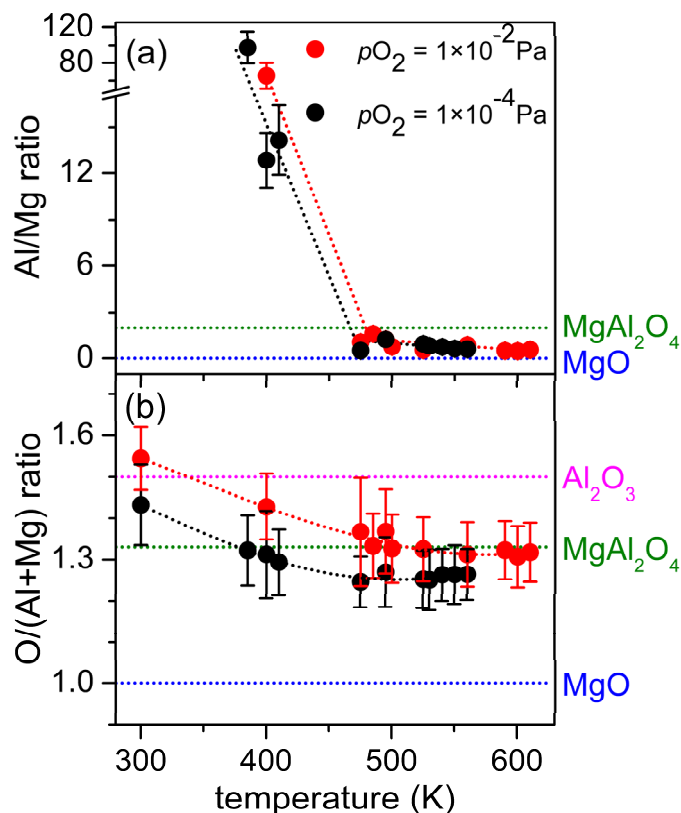

Fig. 5.6: (a) The overall Al-to-Mg atomic ratio and (b) the overall O/(Al+Mg) atomic ratio of the grown oxide films as a function of oxidation temperature (data as obtained by evaluation of the AR-XPS spectra) for the oxidation of the SC Al – 0.8 % Mg substrates for 6×10^3 s at $pO_2 = 10^{-4}$ Pa. The corresponding atomic ratios for stoichiometric MgO, MgAl$_2$O$_4$ and Al$_2$O$_3$ have been indicated by the dotted lines. The dotted lines through the data points have been drawn to guide the eye.

The preferential oxidation of interfacially segregated Mg at $T \geq 400$ K (as compared to oxidation of Al from the alloy substrate) is reflected by a strong decrease of the overall Al-to-Mg atomic ratio in the grown oxide films with increasing T above 400 K, approaching an approximately constant Al/Mg ratio of 0.6 ± 0.1 after $t = 6 \times 10^3$ s at $T = 560$ K (see Fig. 5.6a). The corresponding overall oxide-film composition, expressed as the overall anion-to-cation ratio (i.e. the O/(Al+Mg) atomic ratio) of the grown oxide films, decreases with increasing temperature from values close to the stoichiometric ratio

of 1.5 for Al_2O_3 (i.e. 1.4 ± 0.1 and 1.5 ± 0.1 at 300 K for $pO_2 = 1 \times 10^{-4}$ Pa at $pO_2 = 1 \times 10^{-2}$ Pa, respectively) to an O/(Al+Mg) atomic ratio of about 1.3 ± 0.1 at $T = 485$ K (Fig. 5.6b).

The measured O 1s spectra of the oxidized SC alloy substrates were constituted of up to three O 1s main peaks: one at the lower-BE-side, one in the centre and one at the higher-BE side of the O 1s envelop, further designated as lower-BE (LBE), middle-BE (MBE) and higher-BE components (see Table 5.1 and Figs. 5.5(a,b)). The O 1s effective depth plots in Figs. 5.5(a,b) show that the LBE, MBE and HBE O 1s components are associated with oxygen anions at the alloy/oxide interface, in the interior of the oxide film and at the outer oxide surface, respectively. The surface-adjacent O 1s HBE has disappeared for the oxide films grown at elevated T and higher pO_2. This may be understood as follows. The O1s HBE component is associated to the defect oxide structure adjacent to the oxide-film surface [3]. It may thus be suggested that the defect oxide structure is removed upon the occurrence of crystallization of the oxide film [27].

5.3.4   *Oxide-film growth mechanism*

To reveal the growth mechanisms of the ultrathin oxide films grown on the bare SC Al-based AlMg substrate during the second slow oxidation stage (i.e. after the formation of a closed oxide film on the alloy surface; see Sec. 5.3.1 and Ref. [28]), a bare SC Al-1.1% Mg substrate was first oxidized for $t = 6 \times 10^3$ s at $T = 300$ K and at $pO_2 = 1 \times 10^{-4}$ Pa (further designated as *Stage-I*). After *in-situ* AR-XPS analysis, the thus-obtained oxide film was *either* subjected to (*i*) a post-oxidation step at a more elevated temperature of 475 K and at the same $pO_2 = 1 \times 10^{-4}$ Pa for $t = 6 \times 10^3$ s (further designated as *Stage-IIA*), or (*ii*) a post-annealing step at $T = 475$ K for $t = 6 \times 10^3$ s under ultra-high vacuum conditions (i.e. at a base pressure $< 3 \times 10^{-8}$ Pa) (further designated as *Stage-IIB*). Spectral reconstructions of the corresponding, measured Al 2p, Mg 2p and O 1s AR-XPS spectra of the oxide films, as obtained after stages *I*, *IIA*, and *IIB* are shown in Figs. 5.7 and 5.8. The corresponding total oxide-film thicknesses, overall Al/Mg- and O/(Al+Mg)-atomic ratios and effective depths of the identified Al 2p, Mg 2p and O 1s species (as calculated from the AR-XPS data following the procedure described in Ref. [25]) have been listed in Table 5.2.
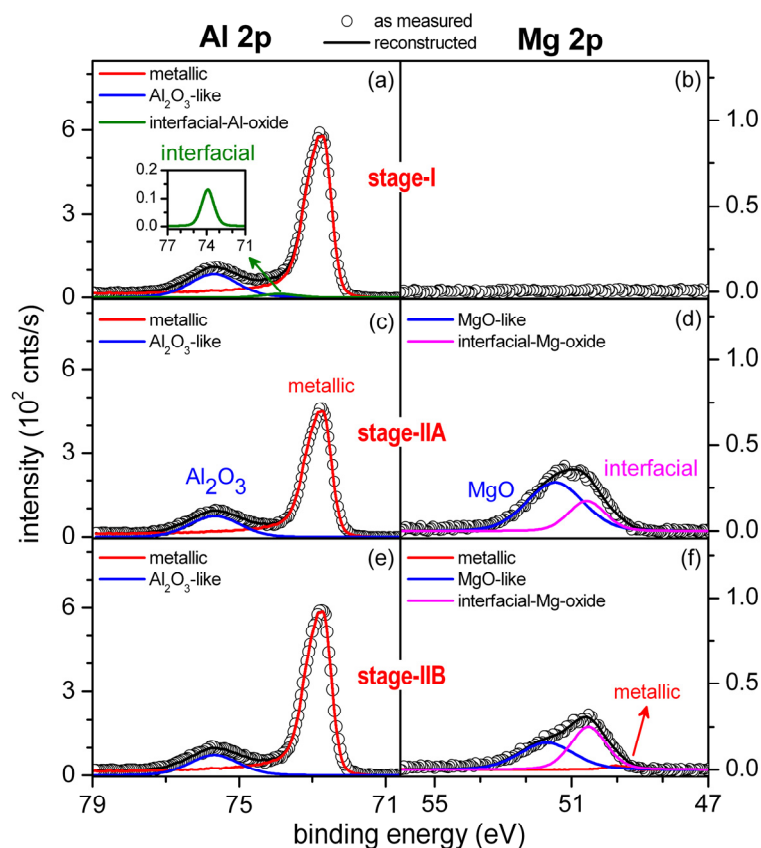
Fig 5.7: Spectral reconstructions of the Al 2p and Mg 2p spectra, as measured at a detection angle set of $(\alpha, \phi) = (38°, 54.75°)$ from the Al - 1.1 at.% Mg substrate after various processing steps: (a,b) after oxidation of the SC alloy substrate at 300 K for 6×10^3 s (*Stage-I*) (c,d) after post-oxidation at 475K for 6×10^3 s at $pO_2 = 1 \times 10^{-4}$ Pa of the oxide film, as obtained after Stage-I (*Stage-IIA*) (e,f) after post-annealing for 6×10^3 s at 475 K under UHV conditions of the oxide film, as obtained after Stage-I (*Stage-IIB*).

The 0.68 ± 0.15 nm thick oxide film, as obtained after the first oxidation step at 300 K (*Stage I*), contains only Al cations in 'Al$_2$O$_3$-like' and 'interfacial-Al-oxide' local chemical environments (see Figs. 5.7(a,b) and Table 5.2), in accordance with our previous findings as discussed in Secs. 5.3.1 and 5.3.3.

Exposure of this Al-oxide film to a post-oxidation step at a more elevated temperature of $T = 475$ K (*Stage-IIA*), results in the incorporation of Mg in the grown oxide film, made possible by the interfacial segregation of Mg from the alloy's interior to the alloy/oxide interface and its subsequent preferential oxidation (see Sec. 5.3.3). Consequently, the local chemical state due to the 'interfacial-Al-oxide' disappears, while additional 'MgO-like' and 'interfacial-Mg-oxide' local chemical states arise in the measured AR-XPS spectra of the oxidized metal (cf. Figs. 5.7(a,b) and Figs. 5.7(c,d) and see Table 5.2). The preferential oxidation of Mg during the post-oxidation step not only

results in an increase of the oxide-film thickness to 1.0 ± 0.16 nm, but also in a considerable decrease of the Al-to-Mg ratio of the oxide film (to 1.1 ± 0.2; see Table 5.2) and a considerable relative increase of the O 1s LBE main peak (cf. Figs. 5.8a and 5.8b). This indicates that the relative increase of the interface-adjacent O 1s LBE main peak is associated with (Mg-rich) oxide formation during the slow growth stage.[1]
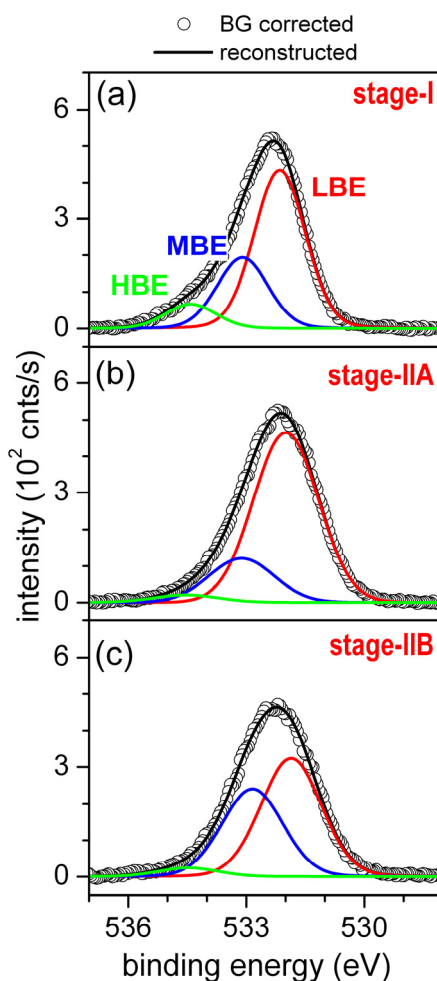

Fig 5.8: Spectral reconstructions of the O 1s spectra, as measured at a detection angle set of $(\alpha, \phi) = (38°, 54.75°)$ from the Al - 1.1 at.% Mg substrate after various processing steps: (a) after oxidation of the SC alloy substrate at 300 K for 6×10^3 s (*Stage-I*) (b) after post-oxidation at 475K for 6×10^3 s at $pO_2 = 1 \times 10^{-4}$ Pa of the oxide film, as obtained after Stage-I (*Stage-IIA*) (c) after post-annealing for 6×10^3 s at 475 K under UHV conditions of the oxide film, as obtained after Stage-I (*Stage-IIB*).

---

[1] Oxidations for different oxidation times at constant T (≤ 475 K) and pO_2 also evidence a relative increase of the LBE O 1s component upon thickening of the oxide films during the slow growth stage.

Table 5.2. Total oxide-film thickness, overall Al-to-Mg ratio and effective depths of the identified Al and Mg cationic species in the oxide film, as obtained after processing stages I, IIA and IIB. See Figs. 5.7(a-f) and 5.8(a-c) and Sec. 5.3.4 for further details and discussion.

	Stage-I	Stage-IIA	Stage-IIB
processing step	oxidation at 300 K	post-oxidation at 475 K	in-vacuo annealing at 475 K
See Figure	5.7(a,b), 5.8a	5.7(c,d), 5.8b	5.7(e,f), 5.8c
thickness (nm)	0.68 ± 0.15	1.0 ± 0.16	0.71 ± 0.10
Al/Mg-ratio	∞	1.1 ± 0.2	1.34 ± 0.2
O/(Al+Mg)-ratio	1.42 ± 0.08	1.3 ± 0.07	1.21 ± 0.05
effective depth (nm)			
Al_2O_3-like	0.5 ± 0.01	0.5 ± 0.03	0.54 ± 0.02
interfacial-Al-oxide	0.72 ± 0.2	-	-
MgO-like	-	0.72 ± 0.02	0.65 ± 0.02
interfacial-Mg-oxide	-	1.58 ± 0.1	1.05 ± 0.03
O1s-HBE	0.34 ± 0.1	0.35 ± 0.17	0.38 ± 0.1
O1s-MBE	0.36 ± 0.05	0.42 ± 0.06	0.46 ± 0.06
O1s-LBE	0.53 ± 0.02	0.58 ± 0.03	0.6 ± 0.03

Exposure of the Al-oxide film, as obtained after Stage I, to a prolonged post-annealing step under UHV conditions (*Stage-IIB*), also results in the disappearance of the 'interfacial-Al-oxide' local chemical state in conjunction with the emergence of 'MgO-like' and 'interfacial-Mg-oxide' local chemical states (cf. Figs. 5.7(a,b) and 5.7(e,f)); in association with a considerable decrease of the Al-to-Mg atomic ratio of the oxide-film to 1.34 ± 0.2 (see Table 5.2). This implies that, even in the absence of a surface-charge field due to chemisorbed oxygen species at the oxide-film surface (which is built up during the oxidation process [13,35]), a strong thermodynamic driving force exists for the uptake of

the interfacially segregating Mg in the oxide-film. Since the oxide-film growth rate by the incorporation of interfacially segregated Mg into the oxide film is obviously very small during the post-*annealing* step of Stage-IIB (i.e., in the absence of an oxygen containing atmosphere), the resulting Mg 2p 'MgO-like' and O 1s LBE main peaks (associated with (Mg-rich) oxide formation; see above) are relatively less pronounced (as compared to the post-oxidation step; compare Figs. 5.7d and 5.7f and Figs. 5.8b and 5.8c). Also, note that the atomic ratio O/(Al+Mg) is smaller after post-annealing than after post-oxidation. Furthermore, a small metallic Mg 2p peak is detected by AR-XPS (Fig. 5.7f) due to the pile-up of metallic Mg in the in the sputter-induced Mg-depletion zone of the alloy substrate (Sec. 5.3.2) below the alloy/oxide interface alloy adjacent to the alloy/oxide interface. (see Fig. 5.7f).

Thus, the above experiments clearly evidence that continued oxide-film growth (after formation of a closed oxide film) is realized by the preferential oxidation of interfacially segregating Mg. The associated oxide-film growth may then be realized by one or a combination of the following mechanisms:

(*i*) the inward diffusion of oxygen through the developing oxide film to react with segregated Mg at the alloy/oxide interface.

(*ii*) the surface-charge-field-enhanced outward 'hopping' of interfacial segregated Mg atoms (thereby becoming $Mg^{\delta+}$ ions), into, and interstitial Mg^{2+} cations and interstitial Al^{3+} cations through, interstices of the "randomly close packed" O-ion arrangement of the predominantly amorphous [40] oxide film.

In oxides with a cubic close packing of the O anions, the formation of oxygen vacancies and interstitials is energetically unfavourable in comparison with the formation of cation defects and, consequently, oxygen volume diffusion is much slower than cation volume diffusion [38]. The observed occurrence of bulk-like Al_2O_3 and MgO local chemical states for the Al and Mg cations incorporated in the oxide films (see above and Sec. 5.3.3) suggests that, the oxygen-anion arrangement of the amorphous oxide films resembles a distorted close-packed oxygen sublattice with the Mg cations preferentially occupying the "octahedral" interstices (like in MgO) and the Al cations concentrated in the "octahedral" and/or "tetrahedral" interstices (like in Al_2O_3). This implies that, also for the amorphous oxide films grown in this study, oxygen-anion diffusion is much slower than metal-cation diffusion. It is therefore suggested that, in the amorphous oxide-film regime (for $T < 475$ K [27]), continued oxide-film growth by preferential oxidation of

interfacially-segregated Mg is predominantly realized by outward 'hopping' of interfacial segregated Mg atoms, etc. (mechanism (*ii*) above) (under influence of the chemical potential gradients and the surface charge field [13,35]). The observed development of a Mg-rich oxide phase at the interface (cf. Fig. 5.7 and Table 5.2) can thus be interpreted as that interstices of the dense close packed O arrangement of the oxide films in the vicinity of the alloy/oxide interface, emptied by outward moving Al cations, are (subsequently) occupied by Mg cations originating from the interfacially-segregated Mg atoms.

Upon crystallization of the thickening films, at elevated temperatures, the oxide growth rate presumably becomes controlled by inward (chemical) diffusion of oxygen along grain boundaries in the crystallized oxide film as well [39].

5.4. Conclusions

The kinetics of oxide-film growth on sputter cleaned Al-based AlMg alloys is characterized by an initial regime of very fast film growth, which is succeeded by a second, slow oxidation stage. A near-limiting oxide-film thickness is attained for the oxidations at $T < 475$ K.

The in-vacuo sputter treatment performed to clean the Al–Mg substrates prior to oxidation, leads to an alloy surface region fully depleted of Mg.

Oxidation at $T \leq 385$ K leads to the formation of Mg-free, ultrathin Al-oxide films of limiting thickness, with two different local chemical states of the oxidized Al cations: (*i*) Al cations in the interior of the oxide film having a local chemical state similar to that of Al cations in 'bulk' Al_2O_3 and (*ii*) Al cations *at* the alloy/oxide interface having a deficient coordination by nearest-neighboring O anions.

Oxidation at $T > 385$ K, induces interfacial segregation of Mg from the alloy's interior to the alloy/oxide interface. These interfacially-segregated Mg cations are preferentially incorporated into the oxide films grown at $T > 400$ K, which gives rise to the occurrence of MgO-like local chemical state of the Mg^{2+} cations in the interior of the developing oxide film.

If the rate of Mg interfacial segregation is larger than the rate of Mg incorporation into the growing oxide film (this holds for not too high T and not too high pO_2), an 'interfacial-Mg-oxide' chemical state is observed in addition to the MgO-like chemical state.

As long as the grown oxide films are predominantly amorphous (i.e. for $T < 475$ K), continued oxide-film growth is realized by the surface-charge-field enhanced outward 'hopping' of interfacial segregated Mg atoms, becoming $Mg^{\delta+}$ cations, into, and interstitial Mg^{2+} cations and interstitial Al^{3+} cations through, interstices of the "randomly-dense-packed" O arrangement of the amorphous oxide film. After crystallization of the thickening films at elevated temperatures, the oxide growth rate presumably becomes also controlled by inward (chemical) diffusion of oxygen along grain boundaries in the crystallized oxide film.

References

[1]   P. Nolte, A. Stierle, N. Y. Jin-Phillipp, N. Kasper, T. U. Schulli and H. Dosch, Science **321** (2008) 1654.

[2]   M. Tsuchiya, S. K. R. S. Sankaranarayanan and S. Ramanathan, Prog. Mat. Sc. **54** (2009) 981.

[3]   L. P. H. Jeurgens, M. S. Vinodh, and E. J. Mittemeijer, Acta Mat. **56** (2008) 4621.

[4]   A. Pasquarello and A. M. Stoneham, J. Physics: Condensed Matter **17** (2005) V1.

[5]   J. G. Li, Mater. Chem. Phys. **47** (1997) 126.

[6]   C. T. Campbell, Surf. Sci. Rep. **27** (1997) 1.

[7]   F. S. Ohuchi and M. Kohyama, J. Am. Ceram. Soc. **74** (1991) 1163.

[8]   S. B. Sinnott and E. C. Dickey, Mater. Sci. Eng. R **43** (2003) 1.

[9]   E. Pagounis, M. Talvitie and V. K. Lindroos, Comp. Sci. and Tech. **56** (1996) 1329.

[10] V. Da Costa, C. Tiusan, T. Dimopoulos and K. Ounadjela, Phy. Rev. Lett. **85** (2000) 876.

[11] J. Gustafson, R. Westerstroem, A. Mikkelsen, X. Torrelles, O. Balmes, N. Bovet, J. N. Andersen, C. J. Baddeley and E. Lundgren, Phys. Rev. B **78** (2008) 6.

[12] C. R. Henry, Surf. Sci. Rep. **31** (1998) 235.

[13] F. Reichel, L. P. H Jeurgens and E. J. Mittemeijer, Acta Mat. **56** (2008) 2897.

[14] F. Reichel, L. P. H Jeurgens, G. Richter and E. J. Mittemeijer, J. Appl. Phys. **103** (2008) 093515.

[15] F. Reichel, L. P. H Jeurgens, G. Richter, P. A. van Aken and E. J. Mittemeijer, Acta Mater. **55** (2007) 6027.

[16] A. Lyapin, L. P. H. Jeurgens and E. J. Mittemeijer, Acta Mat. **53** (2005) 2925.

[17] L. P. H. Jeurgens, M. S. Vinodh, and E. J. Mittemeijer, Appl. Surf. Sci. **253** (2006) 627.

[18] M. S. Vinodh, L. P. H. Jeurgens and E. J. Mittemeijer, J. Appl. Phys. **100** (2006) 044903.

[19] G. −W. Zhou, J. A. Eastman, R. C. Birtcher, P. M. Baldo, J. E. Pearson, L. J. Thompson, L. Wang and J. C. Yang, J. Appl. Phys. **101** (2007) 033521.

[20] G. R.Wakefield and R. M. Sharp, Appl. Surf. Sci. **51** (1991) 95.

[21] D. H. Kim, E. P. Yoon and J. S. Kim, J. Mat. Sc. Lett. **15** (1996) 1429.

[22] K. Shimizu, G. M. Brown, K. Kobayashi, P. Skeldon, G. E. Thompson and G. C. Wood, Corr. Sci. **40** (1998) 557.

[23] K. J. Holub and L. J. Matienzo, Appl. Surf. Sci. **9** (1981) 22.

[24] T. J. Nijdam, L. P. H. Jeurgens and W. G. Sloof, Acta Mater. **51** (2003) 5295.

[25] E. Panda, L. P. H. Jeurgens and E. J. Mittemeijer, *submitted to J. Appl.Phys.*

[26] E. Panda, L. P. H. Jeurgens and E. J. Mittemeijer, *submitted to Acta Mat.*

[27] E. Panda, L. P. H. Jeurgens, G. Richter and E. J. Mittemeijer, *submitted to J. Mat. Res.*

[28] E. Panda, L. P. H. Jeurgens and E. J. Mittemeijer, *submitted to Surf. Sci.*

[29] L. F. Mondolfo, Aluminum Alloys: Structure and Properties, (Butterworths, London 1976).

[30] E. Brillas, P. L. Cabot, F. Centellas, J. A. Garrido, E. Perez and R. M. Rodriguez, Electrochimica Acta **43** (1998) 799.

[31] Metals Handbook. Properties and Selection of Metals, 8th edn., Americal Society for Metals, Ohio (1961) 1.

[32] F. J. Esposto, C. S. Zhang, P. R. Norton and R. S. Timsit, Surf. Sci. **302** (1994) 109.

[33] J. Bloch, D. J. Bottomley, J. G. Mihaychuk, H. M. van Driel and R. S. Timsit, Surf. Sci. **322** (1995) 168.

[34] A. Lyapin, L. P. H. Jeurgens, P. C. J. Graat and E. J. Mittemeijer, J. Appl. Phys. **96** (2004) 7126.

[35] L. P. H. Jeurgens, A. Lyapin and E. J. Mittemeijer, Act. Mater. **53** (2005) 4871.

[36] P. C. J. Graat, M. A. J. Somers and E. J. Mittemeijer, Z. Metallkd. **93** (2002) 532.

[37] F. Reichel, L. P. H Jeurgens and E. J. Mittemeijer, Phys. Rev. B **73** (2006) 024103.

[38] P. Heitjans and J. Kärger, Diffusion in condensed matter, Springer (2005) p. 212.

[39] L. P. H. Jeurgens, W. G. Sloof, F. D. Tichelaar and E. J. Mittemeijer, J. Appl. Phys. **92** (2002) 1649.

[40] P. C. Snijders, L. P. H. Jeurgens and W. G. Sloof, Surf. Sci. **589** (2005) 98.

6. The amorphous to crystalline transition of ultrathin (Al,Mg)-oxide films grown by thermal oxidation of AlMg alloys; an HR-TEM investigation

E. Panda, L. P. H. Jeurgens, G. Richter and E. J. Mittemeijer

Abstract

The microstructural evolution of ultrathin (< 3 nm) oxide films grown on bare Al-based AlMg alloy substrates, by thermal oxidation in the temperature range of 300 - 610 K and at partial oxygen pressures in the range 10^{-4} - 10^{-2} Pa, was investigated by high-resolution transmission electron microscopy. Angle-resolved X-ray Photoelectron Spectroscopy was applied to establish the chemical constitution of the analysed oxide films (i.e. the overall Al/Mg cationic ratio, as well as the relative depth distributions of Al and Mg in the grown oxide films). The ~0.8-nm-thick (Al,Mg)-oxide film grown at 300 K is fully amorphous. A gradual development of long range order in the oxide film sets in for thickening (Al,Mg)-oxide films of relatively high Mg content at $T \geq 475$ K. The amorphous-to-crystalline transition proceeds by a phase separation: still predominantly amorphous oxide regions next to crystallized oxide regions constituted of an MgO-type of oxide phase with a fcc oxygen sublattice and an average lattice parameter of $4.146^{\pm 0.1}$ Å.

6.1.   Introduction

Tuning the functionality of ultrathin (< 3 nm) oxide films applied in nano-technologies, as tunnel junctions, gas sensors, model catalysts and (thin) diffusion barriers for corrosion-resistance, relies on comprehensive characterization of the oxide-film microstructure as function of the surface pretreatment and the growth conditions (e.g. oxidation time, temperature and partial oxygen pressure) [1-9]. Such experimental characterization is a highly challenging endeavour, especially because the microstructure of ultrathin oxide films often differs drastically from what is known and is predicted by bulk thermodynamics. This is consequence of predomination of the contributions of surface

and interface energies to the total Gibbs energy of such low-dimensional systems (see review in Ref. [10]).

In very recent work by our group, the delicate interrelationships between the oxidation conditions and, in particular, the oxide-film morphology, the oxide-film growth kinetics and the depth-resolved chemical state of the ions in the developing oxide film, have been revealed for ultra-thin, *single-metal* oxide overgrowths on surfaces of the same *metal* by using a combinatorial experimental approach of angle-resolved X-ray photoelectron spectroscopy (AR-XPS), real-time in-situ spectroscopic ellipsometry (RISE), low energy electron diffraction (LEED) and high-resolution transmission electron microscopy (HR-TEM) [11-13]. Similar studies on the microstructural evolution of ultra-thin, *multiple-metal* oxide films on *alloy* substrates are rare and especially great need exists for a detailed analysis of the oxide-film microstructure and the interface with the parent alloy substrate on the atomic scale by e.g. HR-TEM. Thus, for many alloy systems, it is unknown if the initial multiple-metal oxide film grown on its alloy surface is single-phase amorphous, single-phase crystalline (e.g. a spinel phase or a crystalline solid solution) or constituted of several mixed crystalline and/or amorphous oxide phases. In particular, if more than one of the alloy constituents has a strong affinity towards oxygen, like in the Al-Mg system (in contrast to binary alloy systems such as Au-Cu, Ag-Cu or Pt-Al, where one constituent is only moderately nobler than the other), the interrelationships between the microstructural evolution of the growing oxide film, the oxidation-induced compositional changes in the parent alloy substrate and the oxidation conditions can be highly complicated [3].

In the present study, the microstructural development of ultra-thin, (Al,Mg)-oxide overgrowths on bare *Al-based* AlMg alloy surfaces is revealed by cross-sectional HR-TEM analysis as function of the oxidation temperature, *T*, (in the range of 300 - 610 K), the oxide film thickness (in the range of 0.7 - 2.7 nm) and the overall Al/Mg atomic ratio in the oxide film (in the range of 2.7 to 0.5). The HR-TEM results are discussed in combination with data from AR-XPS investigations of the studied oxide films obtained in the same project [14,15].

6.2. Experimental

Single-phase, polycrystalline Al-based AlMg solid-solution alloys with a homogeneous Mg content of 0.8 and 1.1 at.% and an average grain size in the range of 50 - 100 μm (henceforth referred to as Al − 0.8% Mg, Al − 1.1% Mg) were prepared by successive melting, casting and annealing procedures, as described in Ref. [14]. The prepared alloys have the following impurity concentrations (ppm in mass; as determined by Inductive Coupled Plasma–Optical Emission Spectrometry): Zn = 70, Mn = 40, Na = 30, C = 72 ± 8, and [Fe, Ca, Cu, Cr, Ti, Y, O] < 10.

The disc-shaped alloy specimens (10 mm diameter; 1 mm thickness; single-side polished down to 0.05 μm) were introduced into a combined UHV system for specimen processing and in-situ analysis (base pressure < $3{\times}10^{-8}$ Pa). Next, the (native) oxide and other contaminants (generally only adventitious carbon) on the alloy surface were removed by sputter-cleaning (SC) at room temperature with a 1 kV Ar^+ beam (rastering the entire sample surface and employing sample rotation at a speed of about 6 °/s) until no other elements than the pure alloy constituents (i.e. Al and Mg) were detected in a measured XPS survey spectrum recorded over the binding energy (BE) range from 0 to 1200 eV [14]. The AlMg specimens as obtained after the described SC treatment are further designated as the *sputter-cleaned (SC)* substrates. As an alternative surface pre-treatment, some of the sputter-cleaned alloy surfaces were subsequently in-vacuo annealed for 1200 s at *T* = 460 K, further referred to as *sputter-cleaned/annealed (SC/Ann)* substrates.

Ultra-thin oxide films (thickness < 3 nm; as determined by in-situ AR-XPS and RISE; see Ref. [14]) were grown by in-situ exposure of the SC or SC/Ann alloy surfaces for $6{\times}10^3$ s to pure oxygen gas (i.e. ≥ 99.99990 vol.% with a specified residual gas content of H_2O ≤ 0.5 vpm, N_2 / Ar ≤ 2.0 vpm, C_nH_m ≤ 0.1 vpm and CO_2 ≤ 0.1 vpm) at a partial oxygen pressure (*pO₂*) of either $1{\times}10^{-4}$ Pa or $1{\times}10^{-2}$ Pa in the temperature range of *T* = 300 - 610 K. The oxidations were carried out in an especially-designed UHV system for specimen processing and analysis, which consists of several interconnected UHV side-chambers (all with a base pressure < $3{\times}10^{-8}$ Pa). The UHV system is equipped with various in-situ surface-sensitive analytical techniques, such as AR-XPS and real-time in-situ spectroscopic ellipsometry (RISE; for details, see Refs. [11,12]), as well as to a UHV side-chamber for thin-film deposition by Molecular Beam Epitaxy (MBE).

Table 6.1. Oxidation conditions and their resulting oxide-film constitutions of the conducted HR-TEM specimens (see Sec. 6.2).

Bulk alloy composition	Surface pre-treatment	Oxidation temperature	Partial oxygen pressure	Oxidation duration	Al/Mg ratio in the oxide film
Al – 1.1% Mg	*SC/Ann*	$T = 300$ K	$pO_2 = 1 \times 10^{-4}$ Pa	$t = 6 \times 10^3$ s	2.7±0.20
Al – 1.1% Mg	*SC/Ann*	$T = 475$ K	$pO_2 = 1 \times 10^{-4}$ Pa	$t = 6 \times 10^3$ s	0.65±0.06
Al – 0.8% Mg	*SC*	$T = 600$ K	$pO_2 = 1 \times 10^{-2}$ Pa	$t = 6 \times 10^3$ s	0.47±0.01

After thermal oxidation and cooling down to room temperature, the grown oxide films were investigated by in-situ AR-XPS. Next, the grown oxide films, as investigated by HR-TEM in the present study (see Table 6.1), were sealed *in-situ* by deposition of a dense ~150 nm thick Al capping layer in the UHV MBE side-chamber. During the MBE deposition step, the specimen (holder) was cooled with liquid nitrogen to prevent any microstructural changes of the oxide film by a local heating up of the oxidized sample surface by heat irradiation from the evaporation source, as well as to minimize the chemical interaction of the Al capping layer with the oxide-film surface. Next, the oxidized specimen with capping layer was removed from the UHV system and, subsequently, a TEM-lamella was cut from the specimen using a dual Focused Ion Beam (FIB Nova Nanolab 600 from FEI company) with Ga[+] ions accelerated at 30 keV and employing an ion current that increased from 7 nA to 30 pA with increasing operation time. Prior to the FIB cutting procedure, the specimen surface was protected with a Pt capping layer deposited on top of the Al capping layer. The thus obtained lamella has a size of 3 μm × 4 μm and a thickness of about 80 nm to 100 nm. An overview of the obtained cross-sectional TEM lamella is shown in the bright-field TEM micrograph of Fig. 6.1.

The HR-TEM analysis was carried out on selected grains of the substrate|oxide-film|Al-seal TEM cross-section using a JEOL JEM-ARM1250 electron microscope with an acceleration voltage of 1250 kV and a point-to-point resolution with the side entry lens of 0.12 nm. Due to the *polycrystalline* nature of the AlMg substrates, the in-vacuo sputter-cleaning treatment prior to the oxidation step produced a large-scale roughness of

the alloy surface (with respect to the thickness of the subsequently grown oxide films), although the metal/oxide interface still appears very flat in the bright-field TEM micrograph of the cross-sectional lamellae in Fig. 6.1. Such a large-scale roughness of the specimen surface was not observed for correspondingly prepared (i.e. by sputter-cleaning and thermal oxidation) *single-crystalline* Al metal surfaces [13]. A number of HR-TEM lamellae could be prepared allowing successful cross-sectional HR-TEM imaging of the ultrathin (< 3 nm) oxide films at atomic-scale resolution.
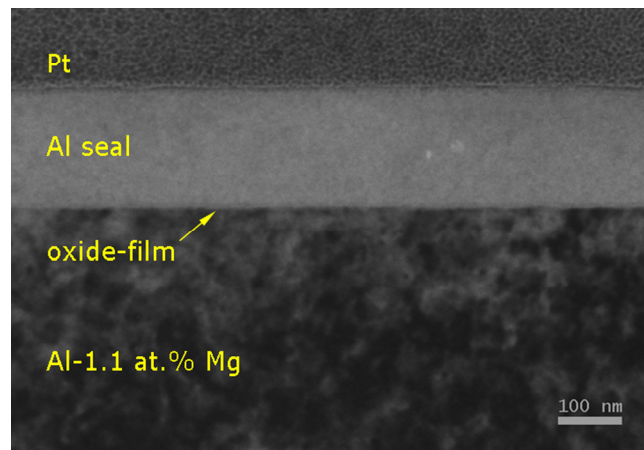
Fig. 6.1. Bright-field transmission electron micrograph of the cross-sectional TEM lamella obtained from the oxidized SC/Ann Al - 1.1% Mg substrate after oxidation for $t = 6 \times 10^3$ s at $T = 300$ K and $pO_2 = 1 \times 10^{-4}$ Pa (and subsequent in-situ deposition of a MBE-grown Al seal; see Sec. 6.2).

To retard any possible microstructural changes in the irradiated area of specimen, as inflicted by the high-energy electron beam, the lamellae were cooled with liquid nitrogen during the HR-TEM analysis. By this precaution the amorphous (Al,Mg)-oxide films grown on the AlMg alloys in this study did not show any noticeable microstructural changes (as induced by the electron irradiation) during prolonged HR-TEM analysis at a single position. This contrasts with analogous HR-TEM analysis of ultra-thin amorphous Al_2O_3 films on Al single crystal surfaces, which gradually crystallize and subsequently dissociate under influence of the electron beam [13]. Apparently, the microstructural stability of ultrathin Al-oxide films under intense electron-beam irradiation is effectively enhanced by the additional incorporation of Mg. Nevertheless, the TEM micrographs as presented in this work (see Sec. 6.3) were only recorded from freshly exposed cross-sectional areas of the TEM lamellae. The negatives of the recorded micrographs were digitized using a CCD camera for further quantitative evaluation using Digital

Micrograph software. The length scale of each investigated micrograph was internally calibrated employing the known lattice parameter of the bulk alloy (i.e. 0.40547 nm and 0.40537 nm for the Al-1.1% Mg alloy or Al-0.8% Mg alloy, as determined by XRD in the present work [16]).

Table 6.2. The oxide-film thicknesses as determined by AR-XPS, RISE and HR-TEM (see Sec. 6.2).

Oxidation temperature	Partial oxygen pressure	Oxide-film thicknesses (nm) as measured by		
		AR-XPS	RISE	HR-TEM
$T = 300$ K	$pO_2 = 1 \times 10^{-4}$ Pa	0.72±0.05	0.76±0.1	1.0±0.2
$T = 475$ K	$pO_2 = 1 \times 10^{-4}$ Pa	0.9±0.10	0.9±0.04	1.4±0.16
$T = 600$ K	$pO_2 = 1 \times 10^{-2}$ Pa	2.44±0.24	2.74±0.45	2.45±0.8

6.3. Results and discussion

Oxidation of the SC and SC/Ann alloy substrates for 6×10^3 s in the temperature range of 300 - 610 K (at $pO_2 = 1 \times 10^{-4}$ Pa or $pO_2 = 1 \times 10^{-2}$ Pa; see Sec. 6.2) resulted in ultrathin oxide films with thicknesses in the range of 0.6 – 3 nm (see Table 6.2). Due to the large-scale roughness of the prepared alloy/oxide cross-sections (Sec. 6.2), the (averaged) thickness values, as obtained from the cross-sectional HR-TEM analysis, generally represent an overestimate of the oxide-film thickness (i.e. more reliable values are obtained from the XPS and RISE analysis; see Ref. [14]). Nonetheless, the thickness values, as determined independently by AR-XPS, RISE and HR-TEM, are in good agreement (Table 6.2).

As evidenced by in-situ AR-XPS, both Al and Mg have been incorporated into the grown oxide films; the values for the overall Al-to-Mg atomic ratio of the oxide films, as

investigated by HR-TEM, have been listed in Table 6.1.[1] It follows that the studied oxide films are all enriched in Mg with respect to the Mg fraction in the bulk of the alloy. Furthermore, the relative Mg content increases (i.e. the Al-to-Mg atomic ratio decreases) pronouncedly with increasing thickness of the grown oxide film (compare Tables 6.1 and 6.2).
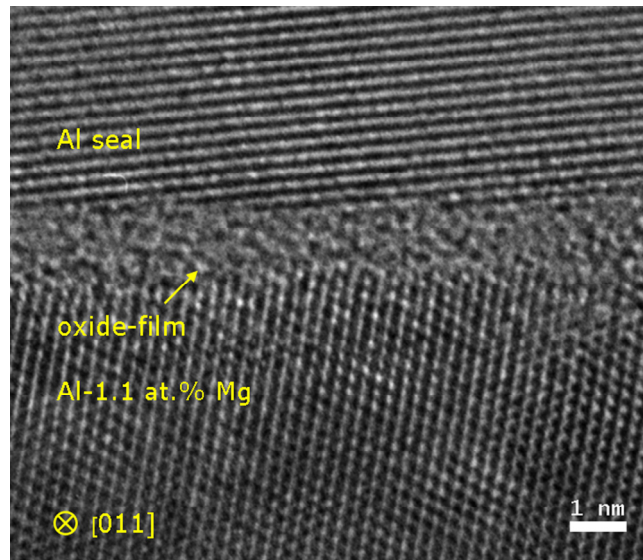

Fig. 6.2. HR-TEM micrograph of the amorphous oxide film formed on the bare SC/Ann Al - 1.1% Mg substrate after oxidation for $t = 6 \times 10^3$ s at $T = 300$ K and $pO_2 = 1 \times 10^{-4}$ Pa. The direction of the primary electron beam was along the zone axis [011] of the investigated grain of the polycrystalline alloy substrate.

The 0.8-nm thick oxide film grown on the SC/Ann AlMg alloy substrate at 300 K is fully amorphous, as shown by HR-TEM (see Fig. 6.2). As evidenced by chemical state analysis of the grown oxide films by AR-XPS in the same project [14,15], the Al and Mg atoms incorporated in these ultrathin amorphous oxide films exhibit Al_2O_3-like and MgO-

---

[1] As shown in Ref. [15], the chemical constitution of the oxide films grown on the Al-based AlMg alloy surfaces (i.e. as revealed by the relative depth distribution of Al and Mg in the grown oxide films, as well as by the overall Al-to-Mg atomic ratio) only depends on the surface pretreatment (i.e. SC versus SC/Ann substrate) for oxidations carried out at temperatures ≤ 450K.

like local chemical states as in the corresponding 'bulk' oxide phases.[2] This suggests that the oxygen anion arrangement of these amorphous (Al,Mg)-oxide films resembles a distorted close-packed oxygen sublattice with the Mg cations preferentially occupying the octahedral(-like) interstices (as in MgO) and the Al cations preferentially concentrated in the tetrahedral(-like) interstices (as in amorphous Al_2O_3 [17]). As evidenced by the depth-resolved analysis of the oxide-film constitution by AR-XPS, as long as the oxide film is still predominantly amorphous, the Al_2O_3-like and MgO-like local chemical states of the Al and Mg cations are concentrated at the alloy/oxide interface and near the surface, respectively (in agreement with recent model predictions on the basis of interface thermodynamics [16]).

As compared to the discussed oxide film grown at 300 K, the (Al,Mg)-oxide film grown on the SC/Ann AlMg alloy substrate at 475 K is slightly thicker (about 0.9 nm thick), has a considerably higher Mg content (see Tables 6.1 and 6.2) and is no longer fully amorphous, as shown by HR-TEM (see Fig. 6.3a). Although the oxide film grown at 475 K is still largely disordered (i.e. predominantly amorphous), first indications of local development of long-range order can be discerned along certain directions in the oxide film (see Fig. 6.3a). Diffraction patterns as obtained by Fourier transformation from regions of the digitized HR-TEM micrographs are shown in Figs. 6.3b and 6.3c for a representative region in the underlying alloy substrate (i.e. corresponding to the square area (*i*) in Fig. 6.3a), as well as for a selected region that encloses both the alloy substrate and the oxide film (i.e. corresponding to the square area (*ii*) in Fig. 6.3a), respectively; an analysis of the diffraction pattern of area (*ii*) is provided by Figs. 6.4a and 6.4b.

---

[2] Only for the SC/Ann alloy substrate oxidized at 475 K (see Table 6.2), two different local chemical environments were resolved for the Mg cations in the grown oxide film: a major bulk 'MgO-like' component (Mg 2p main peak), which originates from Mg cations in the interior of the oxide film, and a minor 'interfacial-Mg-oxide' component due to segregated Mg atoms in the alloy *at* the alloy/oxide interface. For details, see Refs. [3,18].
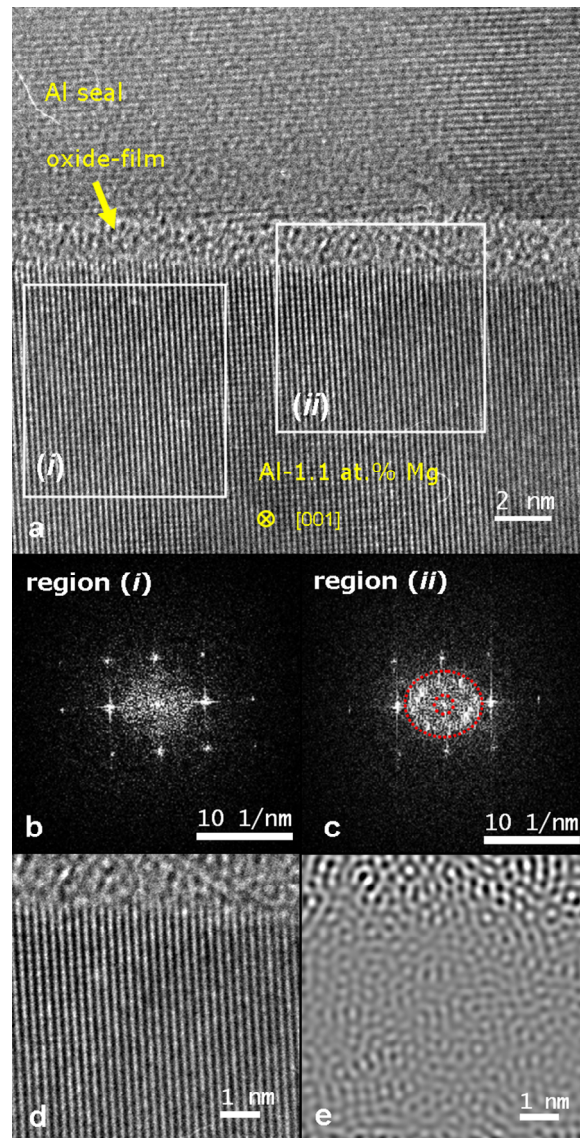
Fig. 6.3. (a) HR-TEM micrograph of the oxide film formed on the bare SC/Ann Al - 1.1% Mg substrate after oxidation for $t = 6\times10^3$ s at $T = 475$ K and $pO_2 = 1\times10^{-4}$ Pa. The direction of the primary electron beam was along the zone axis [001] of the investigated grain of the polycrystalline alloy substrate. **(b, c)** Fourier transformations of the areas (*i*) (comprising only substrate) and (*ii*) (comprising both substrate and oxide) as indicated in (a), respectively. **(d)** Enlargement of area (*ii*) in the micrograph of (a). **(e)** Inverse Fourier transformation from the filtered Fourier image of (c) (pertaining to area (*ii*) in (a), as enlarged in (d)), as obtained after application of a mask, which removes the primary beam and the dominant reflections from the alloy substrate (and thus selects the very diffuse 'forbidden' reflections from the weakly ordered regions of the oxide film). The (at the location of the alloy substrate) superimposed disordered pattern in (e) is produced by the native amorphous oxide formed during preparation on top of the alloy substrate part of the HR-TEM cross-section.
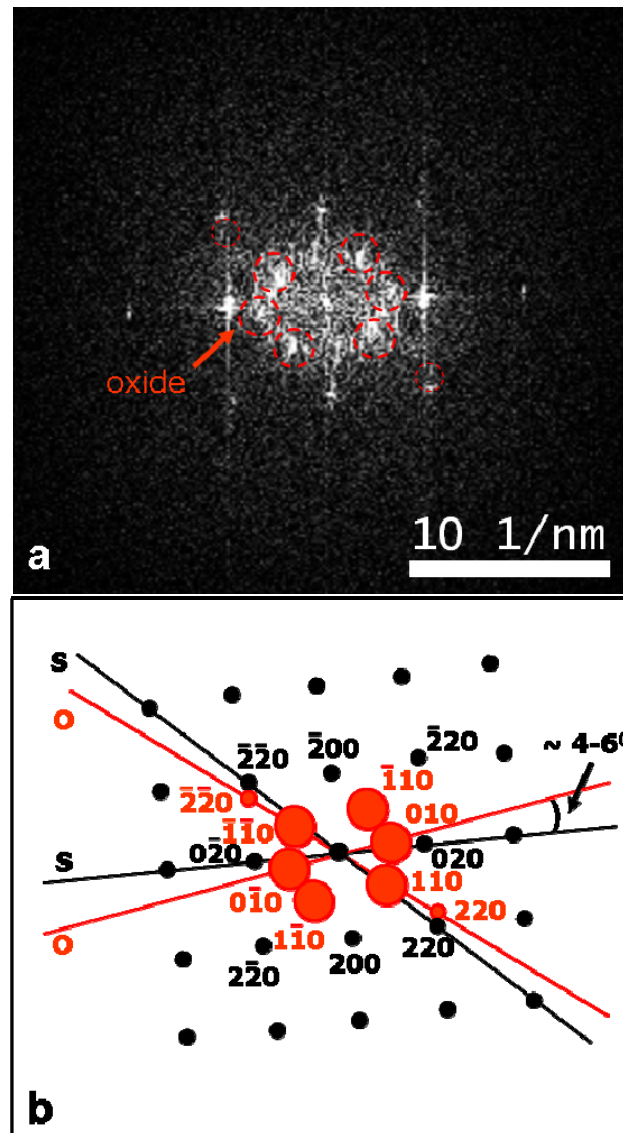
Fig. 6.4. (**a**) Fourier transformation ('diffraction pattern') from the 'partially ordered' regions of the oxide film developed on bare Al-based AlMg alloy substrate after oxidation for $t = 6 \times 10^3$ s at $T = 475$ K and $pO_2 = 1 \times 10^{-4}$ Pa (enlarged Fig. 6.3c). (**b**) Schematic presentation of the diffraction pattern of (a) indicating the positions and identification of the very diffuse reflections from the partially-ordered oxide region (along with those of the substrate reflections). Electron-beam direction: $[001]_{AlMg} \parallel [001]_{MgO}$. It follows that the crystallographic orientation relationship between the oxide overgrowth and the Al-based AlMg alloy substrate deviates 4 to 6 ° from the epitaxial crystallographic orientation relationship $(001)_{AlMg} \parallel (001)_{MgO}$; $[001]_{AlMg} \parallel [001]_{MgO}$.

It follows that some weak intensity maxima from the partially ordered oxide region show up as a diffuse ring / reflections between the central spot due to the primary electron beam and the second order reflections from the Al-based alloy substrate in the diffraction pattern of area (*ii*). Recognizing the structure of the crystalline oxide phase

developing at a more advanced stage of the amorphous-to-crystalline transition (see below), these very diffuse reflections can be interpreted as 'forbidden' (010) and (110) reflections of a partially ordered oxide phase with a fcc-type O sublattice with a lattice-parameter value in between those of the fcc-type O sublattices of crystalline γ-Al_2O_3 and crystalline MgO phases (with lattice-parameter values of 3.9500 Å and 4.2112 Å, respectively). The (at this stage still) irregular distribution of the interstitially dissolved cations is responsible for the occurrence of the "forbidden" reflections. The pattern of 'forbidden' oxide reflections is rotated around the electron beam axis by roughly 4° to 6° with respect to the perfect epitaxial crystallographic orientation relationship (COR) with the Al-based AlMg substrate $(001)_{AlMg} \parallel (001)_{MgO}$; $[001]_{AlMg} \parallel [001]_{MgO}$.

The inverse of the Fourier transform of Fig. 6.3c (see also Figs. 6.4(a,b)) after 'filtering' by application of a mask to remove the primary electron beam and the reflections from the substrate (and thus selecting the very diffuse 'forbidden' reflections from the weakly ordered oxide regions) is shown in Fig. 6.3e. Evidently, these diffuse 'forbidden' reflections originate from the partially ordered regions of the oxide film. It is thus concluded that a gradual development of long-range order in the ultrathin (Al,Mg)-oxide overgrowths on the SC/Ann Al-based AlMg alloy substrates has already commenced for the 0.9-nm thick film grown at 475 K. This oxide-film thickness (i.e. 0.9 nm) exceeds the critical oxide film thickness of about $0.7^{\pm0.1}$ nm, beyond which the crystalline modification of pure Al_2O_3 overgrowth on single-crystalline Al{111} is stable at $T \geq 475$ K [12]. The 'forbidden' oxide reflections, which originate from the partially ordered oxide regions in the still predominantly amorphous oxide-film matrix, disappear in a more advanced stage of the crystallization process (see what follows).
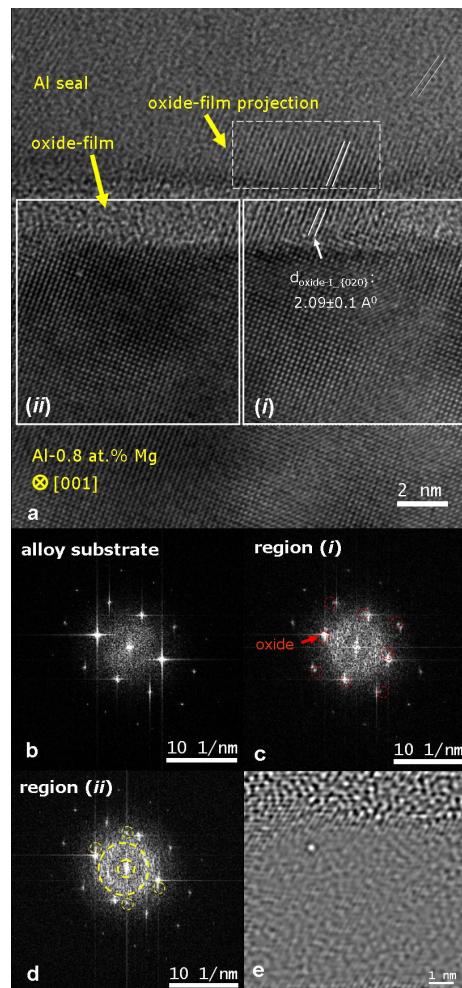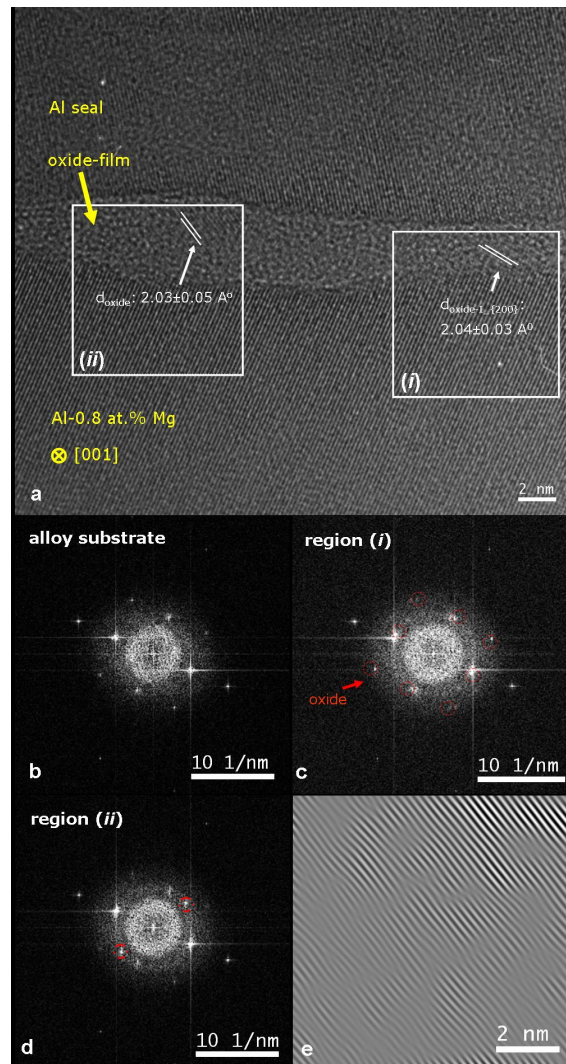
Fig. 6.5. (a) HR-TEM micrograph of the oxide film formed on the bare SC Al – 0.8% Mg substrate after oxidation for $t = 6 \times 10^3$ s at $T = 600$ K and $pO_2 = 1 \times 10^{-2}$ Pa. The direction of the primary electron beam was along the zone axis [001] of the investigated grain of the polycrystalline alloy substrate. (**b, c**, **d**) Fourier transformations of a region in the alloy substrate, as well as of the selected areas (*i*) and (*ii*) (comprising both substrate and oxide) as indicated in (a), respectively. The reflections from oxide-I, as indicated in (c), are about $(4.3\pm0.36)^o$ in-plane rotated with respect to the corresponding (020) reflections from the fcc alloy substrate. (**e**) Inverse Fourier transformation from the filtered Fourier image of (d) (pertaining to area (*ii*) in (a)), as obtained after application of a mask, which removes the primary beam and the reflections from the alloy substrate in area (*ii*) and thus selects the diffracted intensities from the oxide film. The lattice spacing, $d = 2.1^{\pm0.1}$ nm, as determined for the crystalline region of the oxide film within area (*i*), has been indicated in (a). Due to the intrinsic roughness of the specimen surface (see Sec. 2) in combination with the less-uniform thickness of the thicker oxide films grown at elevated temperatures, the lattice fringes from the oxide, the substrate and / or the seal can partially overlap locally (see e.g. the square area as indicated in the Al seal shown in (a) above (*i*)).

Fig. 6.6. (a) HR-TEM micrograph of the oxide film formed on the bare SC Al – 0.8% Mg substrate after oxidation for $t = 6 \times 10^3$ s at $T = 600$ K and $pO_2 = 1 \times 10^{-2}$ Pa. The direction of the primary electron beam was along the zone axis [001] of the investigated grain of the polycrystalline alloy substrate. (**b, c**, **d**) Fourier transformations of a region in the alloy substrate, as well as of the selected areas (*i*) and (*ii*) (comprising both substrate and oxide) as indicated in (a), respectively. The reflections from oxide-I, as encircled in (c), are about $6.4^{\pm 0.3}$ degree, in-plane rotated with respect to the corresponding substrate reflections. (**e**) Inverse Fourier transformation from the filtered Fourier image of (d), as obtained after application of a mask, which exclusively selects the main reflections from the crystalline region of the oxide film (and thus effectively removes the primary beam and the dominant reflections from the alloy substrate, as well as diffuse intensity from the amorphous oxide regions). The lattice spacings $d = 2.04^{\pm 0.03}$ nm and $d = 2.03^{\pm 0.05}$ nm, as determined for the crystalline regions of the oxide film within areas (*i*) and (*ii*), respectively, have been indicated in (a).

Results of the HR-TEM analysis of the (Al,Mg)-oxide film grown on the SC substrate at 600 K (the thickest film with the highest Mg content; see Tables 6.1 and 6.2)

are shown in Figs. 6.5 and 6.6. As compared to the corresponding partially ordered ~0.9 nm thick oxide film grown at 475 K (see above and Figs. 6.3(a-e)), the ~2.6 nm-thick oxide film is less uniform in thickness and the phase separation between weakly-ordered (further designated as predominantly amorphous) and clearly crystalline regions, parallel to the alloy/oxide interface, is advanced. Ultrathin *am*-Al_2O_3 thin films are more stable than ultrathin *am*-MgO thin films (because the surface and interface energies are lower for *am*-Al_2O_3, and because the bulk Gibbs energy difference between the amorphous and crystalline states is considerably smaller for Al_2O_3[18]). This suggests that the predominantly amorphous and crystalline regions in the oxide film grown at 600 K are locally enriched in Al and Mg, respectively.[3]

Diffraction patterns, as obtained by Fourier transformation of selected regions of the digitized HR-TEM micrographs (which comprise areas of the alloy substrate and/or the partially crystallized oxide film), are shown in Figs. 6.5(b-d) and 6.6(b-d); an analysis of the diffraction pattern of area (*i*) in Fig. 6.5 is provided by Fig. 6.7. In contrast with the less-ordered oxide film grown at 475 K (see Figs. 6.3(a-e) and 6.4), the reflections from the crystalline oxide region are no longer positioned *in between* the central primary beam spot and the first order reflections from the substrate (i.e. the 'forbidden' reflections have disappeared: compare Figs. 6.4 and 6.7), which implies that the degree of crystallinity of these crystalline oxide regions has increased. As for the less-ordered oxide film grown at 475 K, the crystalline oxide reflections are rotated around the electron-beam axis by 4º to 6º with respect to the perfect epitaxial COR with the Al-based AlMg substrates (see Figs. 6.4 and 6.7). The positions and corresponding lattice spacings (as calculated from the positions of the reflections in the diffraction patterns of the crystalline oxide regions) are compatible with the interpretation that the oxide domains possess an fcc-type oxygen sublattice with an average lattice parameter of $4.146^{\pm0.1}$ Å. This lattice parameter value (i.e. $4.146^{\pm0.1}$ Å) is closer to that of MgO (4.2112 Å) than to that of γ-Al_2O_3 (3.9500 Å), which is compatible with the above mentioned thermodynamic prediction that MgO is less stable in the amorphous state than Al_2O_3. In less-ordered regions of the same oxide

---

[3] HR-TEM provides no direct information on the Al and Mg cation distributions in the oxide phase. Direct experimental confirmation of the spatial distribution of Al and Mg in the alloy/oxide cross-sections by energy-filtered TEM was attempted in this study, but failed due to the lack of spatial resolution and a too large overlap of peaks in the energy loss spectra of Al and Mg (i.e. a lack of energy resolution).

film, some 'forbidden' oxide reflections, as discussed with respect to Fig. 6.4, can still be observed (see Fig. 6.5d).
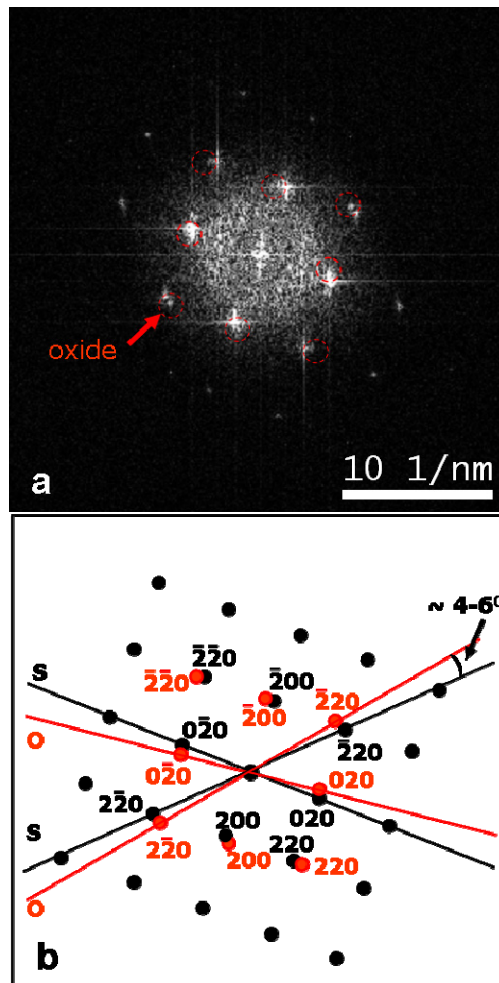

Fig. 6.7. (**a**) Fourier transformation ('diffraction pattern') from the "crystalline" region of the oxide film developed on bare Al-based AlMg alloy substrate after oxidation for $t = 6 \times 10^3$ s at $T = 600$ K and $pO_2 = 1 \times 10^{-2}$ Pa (enlarged Fig. 6.5c). (**b**) Schematic presentation of the diffraction pattern of (a) indicating the reflections from the oxide and their identification (along with those of the substrate reflections). Electron-beam direction: $[001]_{AlMg}$ ∥ $[001]_{MgO}$. Note that, the 'forbidden' reflections as observed for the partially ordered oxide in Figs. 6.3(c) and 6.4(a,b) (as positioned in between the reflections of the primary beam and the second order substrate reflections) do not occur for the crystalline oxide. It follows that the crystallographic orientation relationship between the oxide overgrowth and the Al-based AlMg alloy substrate deviates 4 to 6 ° from the epitaxial crystallographic orientation relationship $(001)_{AlMg}$ ∥ $(001)_{MgO}$; $[001]_{AlMg}$ ∥ $[001]_{MgO}$.

Possible growth strain in the crystalline oxide-film regions, due to the lattice mismatch between the alloy substrate and the crystalline oxide, can be relaxed by the

formation of defects at the metal-oxide interface (presumably misfit dislocations [18]). The present HR-TEM analysis, suggests that strain relaxation has (also) occurred by slight rotations of the crystalline oxide domains (by about ± 4-6º) with respect to the perfect COR relationship with the alloy substrate; a similar observation has very recently been reported for ultrathin γ-Al$_2$O$_3$ overgrowths on Al(100) substrates [13].

Depth-resolved AR-XPS analysis revealed an inversion of the relative depth distributions of Al and Mg in the crystallizing oxide film at $T > 475$ K. Whereas for the fully amorphous oxide film grown at 300 K, the Mg cations are concentrated near the surface and the Al cations are concentrated near the interface with the substrate (see above), for the partially crystallized oxide film grown at $T > 475$ K, the Mg cations are concentrated near the interface with the substrate. This is caused by the thermally-activated interfacial segregation of Mg from the alloy's interior *at* the alloy/oxide interface and the concurrent preferential oxidation of the interfacially segregated Mg [14,15]. Therefore it can be tentatively concluded that the preferential oxidation of interfacially segregated Mg at $T > 475$ K results in the initiation of crystallization of Mg-rich oxide regions (preferentially) adjacent to the alloy/oxide interface. Upon continuation of the crystallization process of Mg-rich oxide this leads to the observed reversal of the Al and Mg effective depth distributions.

6.4.   Conclusions

The oxide films developing upon Al-0.8% Mg and Al-1.1% Mg alloy substrates reveal an amorphous to crystalline transition, which is primarily governed by the oxide-film thickness and likely dependent on the Mg content of the oxide film.

The 0.8-nm thick oxide film grown on the SC/Ann AlMg alloy substrate at 300 K is fully amorphous; the incorporated Al and Mg cations exhibit Al$_2$O$_3$-like and MgO-like local chemical states as in the corresponding 'bulk' oxide phases, respectively.

A gradual development of long-range order is observed for the 0.9-nm-thick oxide film of higher Mg content grown at 475 K, which is accompanied by the local nucleation of an oxide phase with an fcc-type O sublattice.

Further thickening of the (Al,Mg)-oxide films in the range of 475 K $\leq T \leq$ 610 K leads to phase separation between still predominantly amorphous (or weakly-ordered) oxide regions and crystallized oxide regions. The crystalline oxide regions are richer in

Mg than the still predominantly amorphous oxide regions, in agreement with thermodynamic prediction.

Strain relaxation in the crystallized oxide regions is realized by slight rotations of the crystalline oxide domains (by about ± 4-6º) with respect to the perfect epitaxial crystallographic orientation relationship with the alloy substrate.

Acknowledgements

References

[1] P. Nolte, A. Stierle, N. Y. Jin-Phillipp, N. Kasper, T. U. Schulli and H. Dosch, Science **321** (2008) 1654.

[2] A. Lyapin, L. P. H. Jeurgens, P.C. J. Graat and E. J. Mittemeijer, J. Appl. Phys. **96** (2004) 7126.

[3] L. P. H. Jeurgens, M. S. Vinodh, and E. J. Mittemeijer, Acta Mat. **56** (2008) 4621.

[4] A. Pasquarello and A. M. Stoneham, J. Physics: Condensed Matter **17** (2005) V1.

[5] H.-J. Freund Surf. Sci. **601** (2007) 1438.

[6] M. Koyama, Y. Kamimuta, M. Koike, M. Suzuki and A. Nishiyama, Jap. J. Appl. Phys. **43** (2004) 1788.

[7] Z. R. Dai, Z. W. Pan and Z. L. Wang, Adv. Funct. Mater. **13** (2003) 9.

[8] E. Comini, G. Faglia, G. Sberveglieri, Z. Pan and Z. L. Wang, Appl. Phys. Lett. **81** (2002) 1869.

[9] A. Gupta, X. W. Li and G. Xiao, Appl. Phys. Lett. **78** (2001) 1894.

[10] L. P. H. Jeurgens, Z. M. Wang and E. J. Mittemeijer, Int. J. Mater. Research (2009), accepted.

[11] F. Reichel, L. P. H Jeurgens and E. J. Mittemeijer, Acta Mat. **56** (2008) 2897.

[12] F. Reichel, L. P. H Jeurgens, G. Richter and E. J. Mittemeijer, J. Appl. Phys. **103** (2008) 093515.

[13] F. Reichel, L. P. H Jeurgens, G. Richter, P. A. van Aken and E. J. Mittemeijer, Acta Mater. **55** (2007) 6027.

[14] E. Panda, L. P. H Jeurgens and E. J. Mittemeijer, *Submitted to J. Appl. Phys.*

[15] E. Panda, L. P.H Jeurgens and E. J. Mittemeijer, *Manuscript in preparation.*

[16] E. Panda, L. P. H Jeurgens and E. J. Mittemeijer, *Submitted to Acta Mater.*

[17] P. C. Snijders, L. P. H. Jeurgens and W. G. Sloof, Surf. Sci. **98** (2005) 589.

[18] F. Reichel, L. P. H Jeurgens and E. J. Mittemeijer, Acta Mat. **56** (2008) 659.

7.   Summary

The oxide film present on an alloy surface influences many of its physical and chemical properties, such as corrosion resistance, adhesion, electrical and thermal conductivity, friction and wear resistance. The technological demand to control and optimize these properties by tailoring both the alloy-substrate and oxide-film microstructure has led to a large interest for the thermal oxidation behavior of metallic alloys in the last decades. However, up to date, investigations on the oxidation of metallic alloys have been performed mainly at relatively high temperatures (i.e. $T > 800$ K) and high pressures (i.e. $0.1 < p < 10^5$ Pa). At these high temperatures, relatively *thick* (i.e. in the µm-range) oxide scales, composed of multiple, *crystalline* oxide phases, develop on the alloy surface by sequential, preferential oxidation of the alloy constituents. The oxidation of metallic alloys at low temperatures (i.e. $T < 600$ K), on the other hand, has been investigated only very scarcely up to date. At these low temperatures, thermally activated diffusion of reactants through the developing oxide-film is negligibly small and, consequently, *ultra-thin* (< 3 nm) oxide films of near-limiting thicknesses are formed, which are generally constituted of a *metastable* (often amorphous), multi-metal oxide phase. However, the detailed microstructures (i.e. thickness, morphology, crystallographic structure, chemical composition and constitution) of these initial oxide films as a function of the alloy microstructure (e.g. alloying content, surface orientation), the surface pretreatment (e.g. with or without a native oxide) and the growth conditions (e.g. temperature, time and partial oxygen pressure) are often unknown.

This PhD thesis addresses the initial stages of dry, thermal oxidation of bare (i.e. without a native oxide) Al-based Al-Mg alloy surfaces as a function of the oxidation conditions (*here:* oxidation temperature, time and partial oxygen pressure) and for different pre-treatments of the bare alloy surface prior to oxidation. To this end, a state-of-the-art combinatorial experimental approach by real-time in-situ spectroscopic ellipsometry (RISE), angle-resolved X-ray Photoelectron Spectroscopy (AR-XPS) and high resolution-Transmission Electron Microscopy (HR-TEM) was applied to investigate the interrelationships between the oxide growth kinetics, the microstructural evolution of the oxide film, the oxidation-induced compositional changes in the alloy subsurface and the surface pretreatment and oxidation conditions of the bare alloy surface. Such

comprehensive knowledge on the initial, low-temperature oxidation of AlMg alloy surfaces is of increasing technological interest for applications where a low-density, corrosion-resistant alloy is required (e.g. aerospace, automotive industries, marine applications, handling and fitting of food, chemicals and sewage). Earlier works on the oxidation of AlMg alloy surfaces were mostly conducted in the presence of a native Al-oxide film on the alloy surface at the onset of oxidation and without providing a comprehensive characterization of the developing oxide-film microstructure. Moreover, a fundamental investigation on the initial oxidation of AlMg alloy surfaces presents a scientific challenge, because both alloy constituents (i.e. Al and Mg) have a strong affinity for oxygen (in contrast with binary alloy systems such as Cu-Au or Pt-Al, where one constituent is nobler than the other) and, consequently, the aforementioned interrelationships between the developing alloy and oxide microstructures and the oxidation conditions can be very complicated.

First, a **thermodynamic model**, which accounts for the crucial role of surface and interface energetics in such ultra-thin oxide-film systems, was developed to predict the initial, amorphous oxide overgrowth (i.e. am-Al_2O_3, am-MgO and/or am-$MgAl_2O_4$) developing on a bare AlMg alloy substrate as a function of the growth temperature, the Mg alloying content at the alloy/oxide interface and the oxide-film thickness (≤ 5 nm). To this end, experimental or empirically-estimated values for the surface energies of the competing *amorphous* oxide phases of am-Al_2O_3, am-MgO or am-$MgAl_2O_4$ (further denoted as $\{Al_2O_3\}$, $\{MgO\}$ and $\{MgAl_2O_4\}$) as a function of the growth temperature were employed. Required values for the interface energy between the alloy substrate and the competing *amorphous* oxide phases as a function of the temperature and the Mg alloying content at the alloy/oxide interface, were estimated from corresponding expressions, as derived on the basis of the macroscopic atom approach.

It follows that, in particular, the $\langle AlMg \rangle - \{Al_2O_3\}$ interface of the am-Al_2O_3 overgrowth is considerably more stable than the corresponding interfaces of the $\{MgAl_2O_4\}$ and $\{MgO\}$ overgrowths (see Fig. 7.1). For the formation of a multi-component oxide film on the $\langle AlMg \rangle$ substrate that consists of a mixture of $\{Al_2O_3\}$, $\{MgO\}$ and/or $\{MgAl_2O_4\}$, interface thermodynamics will therefore favor the distribution of the $\{Al_2O_3\}$ and $\{MgO\}$ oxide phases at the interface and surface, respectively, in accordance with experimental observations (see Chapters 4 and 5). The

relatively low energy of the $\langle AlMg \rangle - \{Al_2O_3\}$ interface is predominantly due to a relatively high density of oxygen-metal bonds across the $\langle AlMg \rangle - \{Al_2O_3\}$ interface and hence a more negative chemical interaction contribution to the interface energy per unit area, $\gamma_{\langle AlMg \rangle - \{Al_2O_3\}}$. Furthermore, due to the relatively strong Mg-O chemical bond strength (as compared to the Al-O bond strength), the interaction contribution to the interface energies decreases with increasing Mg alloying content, x_{Mg}^i, at the $\langle AlMg \rangle - \{oxide\}$ interface. This implies the existence of a strong driving force for the chemical segregation of Mg from the interior of the $\langle AlMg \rangle$ substrate to the $\langle AlMg \rangle - \{oxide\}$ interface, which also complies well with experiment (see Chapters 4 and 5).
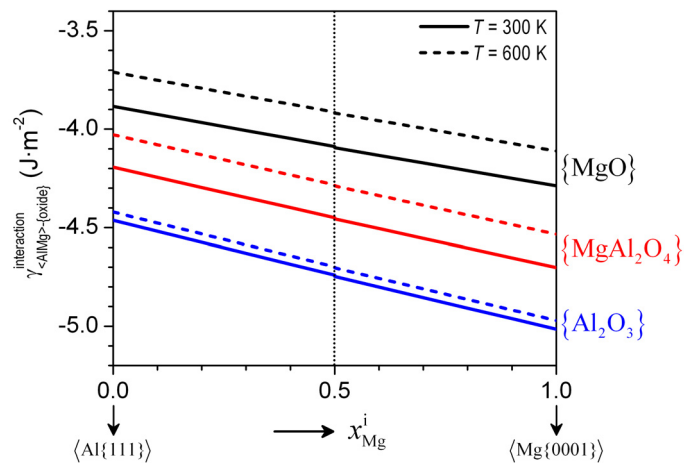
Fig. 7.1. Interface energies $\gamma_{\langle AlMg \rangle - \{MgO\}}$, $\gamma_{\langle AlMg \rangle - \{Al_2O_3\}}$ and $\gamma_{\langle AlMg \rangle - \{MgAl_2O_4\}}$ for the amorphous oxide overgrowths (i.e., $\{MgO\}$, $\{Al_2O_3\}$ and $\{MgAl_2O_4\}$) on the most densely packed surface of the $\langle AlMg \rangle$ substrate (see Chapter 2) as a function of the Mg alloying content at the alloy/oxide interface (x_{Mg}^i) at a growth temperature of $T = 300$ K and 600 K. The interface energies were calculated from Eqs. (2.8), (2.9) and (2.10) in Chapter 2, respectively. For further details, see chapter 2.

Thus, accounting for the individual bulk Gibbs free energies, interface energies and surface energies of the various amorphous oxide overgrowths on the AlMg alloy substrates as a function of oxide growth conditions (see Chapter 2), it follows that the formation of amorphous Al_2O_3 is thermodynamically preferred. This model prediction is consistent with the experimentally observed (by AR-XPS) native amorphous Al_2O_3 film

that forms on an Al-0.8% Mg substrate under atmospheric conditions at room temperature, as well as with the microstructural evolution of ultrathin oxide films grown by controlled oxidation of bare Al-based and Mg-based AlMg alloy substrates in a combined UHV system in this study (see what follows).

Chapters 3 to 6 are devoted to a comprehensive **experimental investigation** of the interrelationships between the oxide growth kinetics, the microstructural evolutions in the oxide overgrowth and the alloy subsurface and the oxidation conditions. To this end, polycrystalline AlMg alloy specimens with nominal Mg alloying contents of 0.8 and 1.1 at. % were thermally oxidized in a dedicated UHV system (base pressure $< 3 \times 10^{-8}$ Pa) for specimen processing (i.e. cleaning, annealing and oxidation) and in-situ analysis. After introduction of the polished alloy sample surface in the UHV system, first the native oxide on the alloy surface was removed by sputter cleaning with a focussed 1 keV Ar^+ ion beam rastering the entire alloy surface (of 7×7 mm^2). The thus obtained sputter-cleaned (as verified by in-situ AR-XPS) alloy surfaces will be further designated as *SC-substrate*. These SC-substrates were subsequently in-situ exposed to pure O_2 gas in the partial oxygen pressure range of $pO_2 = 10^{-4}$ - 10^{-2} Pa for durations varying from 15 s up to 6 hrs and for various temperatures in the range of $T = 300 - 610$ K. As an additional surface pretreatment, some *SC-substrates* were in-vacuo annealed for 1200 s at $T = 460$ K prior to the oxidation. The thus obtained sputter-cleaned, annealed alloy surfaces will be further designated as *SC/Ann-substrate*. RISE was applied to establish the oxide-film growth kinetics. The thicknesses, compositions and chemical constitutions of the grown films were determined by in-situ AR-XPS. Furthermore, the microstructures of some of the grown oxide films were analysed on an atomic scale by cross-sectional HR-TEM.

In Chapter 3, generally applicable procedures were developed for the **depth-resolved quantitative analysis** by RISE and AR-XPS of ultrathin (< 3 nm), multiple-metal or multi-phase oxide overgrowths on binary alloy surfaces. The proposed methods for data evaluation and quantification were applied to the initial, thermal oxidation of sputter-cleaned Al - 1.1 at.% Mg alloy surfaces in the temperature range of $T = 300$ - 485 K (at $pO_2 = 1 \times 10^{-4}$ Pa). Thereby, detailed knowledge was obtained on depth-resolved microstructural evolution of the developing amorphous (Al,Mg)-oxide film, as well as on the accompanied oxidation-induced compositional changes in the parent alloy substrate, as a function of the oxidation temperature (see below).

Typical as measured and reconstructed spectra of the Al 2p and Mg 2p core-level photoelectron lines, as recorded from the oxidized Al-based AlMg alloy surfaces by AR-XPS, are shown in Figs. 7.2a and b, respectively. As evidenced from the depth-dependent AR-XPS analysis, depending on the surface pre-treatment and the oxidation conditions, only Al or both Al and Mg were incorporated into the grown oxide films. Furthermore, a single or a combination of different local chemical states can occur for the Al and Mg cations in the oxide film, some of which resemble corresponding local chemical states in stiochiometric Al_2O_3 or MgO 'bulk' phases (see Figs. 7.2(a,b)). The thicknesses, elemental depth-distributions, chemical constitutions and compositions of the grown oxide films were calculated from the resolved Al 2p, Mg 2p and O1s total PZL intensities of the oxidized metal (for various detection angle sets), according to the calculation scheme presented in Chapter 3.

Quantitative RISE analysis was performed by fitting an optical model description of the magnitude- and phase-dependent ellipsometric parameters $\psi(\lambda, t)$ and $\Delta(\lambda, t)$ for the evolving substrate/film system to the corresponding measured courses of $\psi(\lambda, t)$ and $\Delta(\lambda, t)$. The developed model description considers the overgrowth of an oxide film of uniform thickness on top of the bare AlMg substrate in combination with an intermediate layer of submonolayer thickness to account for the characteristic ellipsometric absorption at the metal/oxide interfacial region (further details are provided in Chapter 3). Several exemplary total oxide-film growth curves, as obtained by the quantitative RISE analysis, are presented in Figs. 7.3(a,b).
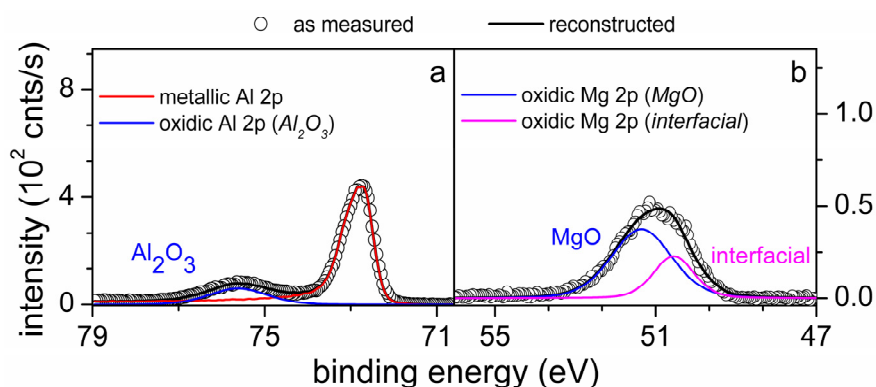
Fig. 7.2: As measured and reconstructed (a) Al 2p and (b) Mg 2p spectra, as recorded at a detection angle set of $(\alpha, \phi) = (38°, 54.75°)$ from the oxidized Al-1.1 at.% Mg substrate. Oxidation was performed by exposure of the sputter-cleaned Al-1.1 at.% Mg substrate to pure oxygen gas for 6×10^3 s ($pO_2 = 1 \times 10^{-4}$ Pa) at a constant substrate temperature of 475 K. For further details, see Chapter 3.
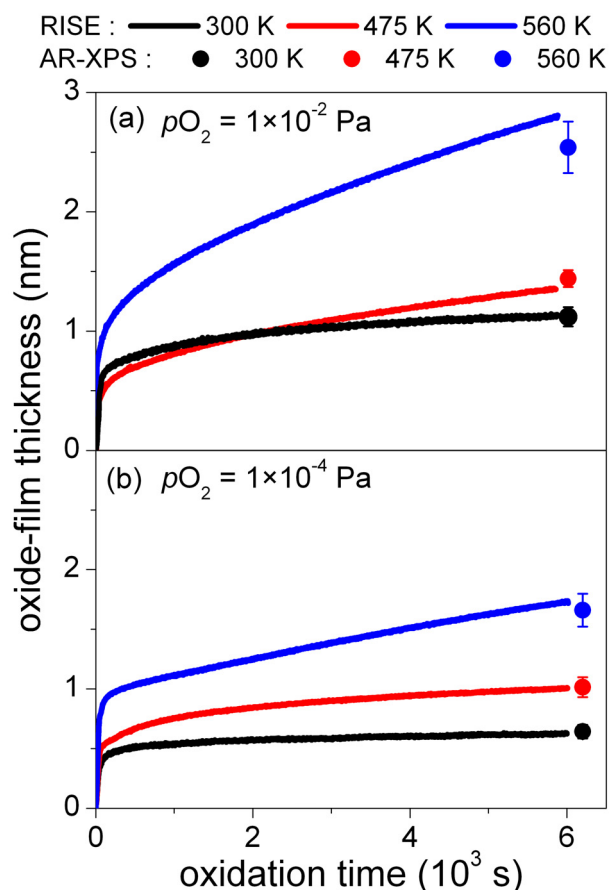
Fig. 7.3: Total oxide-film growth curves, as obtained by real-time in-situ spectroscopic ellipsometry (RISE), for the oxidation of the bare *SC* Al - 0.8 at.% Mg substrate for 6×10^3 s at (**a**) $pO_2 = 1 \times 10^{-4}$ Pa and (**b**) $pO_2 = 1 \times 10^{-2}$ Pa and at various temperatures in the range of 300 K - 560 K.

Chapter 4 addresses the effect of the **surface pretreatment** (i.e. SC-substrate versus SC/Ann-substrate, see above) on the oxide-film growth kinetics and the depth-resolve compositional changes in the alloy subsurface and the oxide film. It follows that during the in-vacuo sputter treatment, as performed to clean the AlMg substrates prior to oxidation, the alloy subsurface region becomes fully depleted of Mg due to the concurrent processes of preferential sputtering (removal) of Mg and bombardment-enhanced segregation of Mg towards the ion-bombarded alloy surface. Since chemical segregation of Mg to the alloy surface is kinetically impeded at $T \leq 385$ K, subsequent oxidation of the **SC** Al-based AlMg substrates at $\boldsymbol{T \leq 385 \text{ K}}$ then results in the formation of ultra-thin oxide films of limiting thicknesses in the range of $0.66 - 0.62$ nm, which consists of only Al_2O_3 (see Fig. 7.4a). Two different local chemical environments exist for the Al cations in these oxide films grown on SC AlMg substrates at $T \leq 385$ K: (*i*) a 'bulk-Al_2O_3-like' Al 2p main peak, which originates from Al cations in the interior of the oxide film and (*ii*) an

'interfacial-Al-oxide' component due to a deficient coordination of Al by nearest-neighbour O anions *at* the alloy/oxide interface. The interfacial Al-oxide detected by AR-XPS is identified with the interfacial EMA layer (of submonolayer thickness) as adopted in the ellipsometric model description (see above). For the oxidation of the **SC** Al-based AlMg substrates at more elevated temperatures, $T > 385$ **K**, the interfacial segregation of Mg from the interior of the alloy to the alloy/oxide interface becomes thermally activated, as evidenced by the appearance of an 'interfacial-Mg-oxide' component (due to a deficient coordination of Mg by nearest-neighbour O anions *at* the alloy/oxide interface) in the measured AR-XPS oxide films grown on SC AlMg substrates at $T > 385$ K (see Figs. 7.2b and 7.4a). These experimental observations are in excellent agreement with the model-predicted driving force for the chemical segregation of Mg from the interior of the AlMg substrate to the alloy/oxide interface (see Fig. 7.1).

For the oxidation of the *SC/Ann* substrates, Mg has chemically segregated onto the bare *SC/Ann* alloy surface as a result of the preannealing step carried out prior to oxidation. Consequently, both Al and Mg are incorporated into the oxide films during the initial, fast oxidation regime for the oxidation of the SC/Ann substrates. For oxidation of the **SC/Ann** Al-based AlMg substrates at $T < 410$ **K**, the Al_2O_3-like and MgO-like local chemical states cations are then concentrated in the amorphous oxide films at the alloy/oxide interface and near the surface, respectively, which complies well with the theoretical prediction (see Figs. 7.1, 7.4b and Chapter 2).

As confirmed by **HR-TEM** (see Fig. 7.5 and Chapter 6), the oxide-films grown on bare AlMg substrates at $T < 450$ K are amorphous. The chemical state analysis by AR-XPS suggests that the oxygen anion arrangement of the grown oxide films resembles a distorted close-packed oxygen sublattice with the Mg cations preferentially occupying the tetrahedral interstices (like in MgO) and the Al cations concentrated in the octahedral and/or tetrahedral interstices adjacent to the alloy/oxide interface.
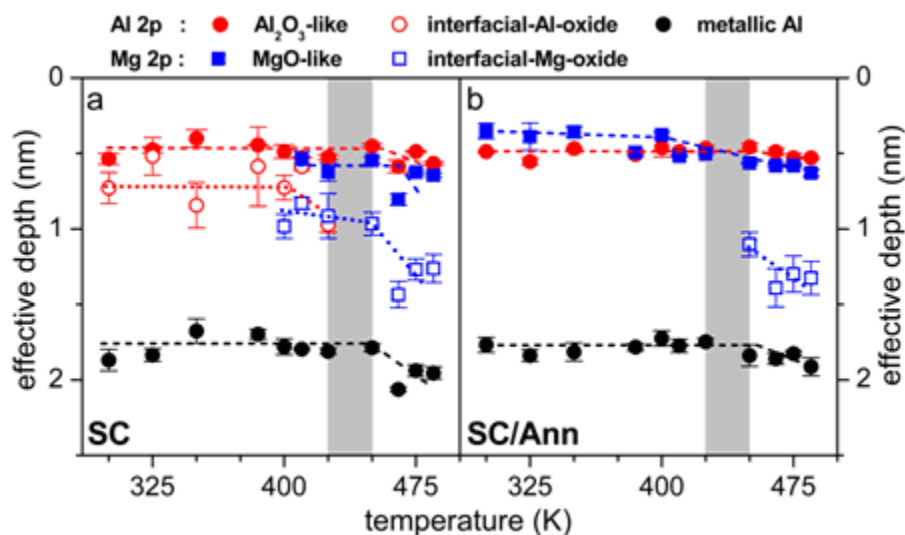
Fig. 7.4: Effective depths of Al and Mg cations in ultra-thin (i.e., 0.6 to 1 nm thick) oxide films grown on (a) *SC* and (b) *SC/Ann* Al-based Al – 1.1% Mg substrates by dry, thermal oxidation for 6×10^3 s at $pO_2 = 1 \times 10^{-4}$ Pa within the temperature range of $T = 300\text{-}485$ K (as determined by AR-XPS). The dotted lines are drawn to guide the eye. The shaded area represent a 'transition zone' beyond which an effect of surface pre-treatment on the resulting oxide-film constitution after 6000 s of oxidation is no longer observed.

At more elevated temperatures $T > 425$ K, the segregation of Mg from the interior of the alloy towards the reacting alloy/oxide interface becomes thermally activated, as evidenced by the appearance of an additional local chemical state for Mg *at* the reacting alloy/oxide interface (see Fig. 7.4b). Continued oxide-film growth then proceeds by the selective oxidation of Mg, which has segregated *at* the AlMg alloy subsurface. This results in a strong decrease of the Al/Mg atomic ratio in the developing oxide film (see Fig. 7.6) with the total anion-to-cation ratio approaching the overall stoichiometry of MgO. As evidenced by HR-TEM (see Chapter 6), the thickening oxide film at $T > 425$ K is already partially transformed into bulk-thermodynamically preferred *crystalline* MgO; the determined lattice parameter of the corresponding crystalline-MgO-like oxide phase equals $4.15^{\pm 0.1}$ Å. Furthermore, the effective depth (distributions) of the Al$_2$O$_3$-like and MgO-like local chemical states become reversed for thicker, already partially crystalline, oxide films grown at $T > 425$ K. The grey area (i.e., the region 425 K $\leq T \leq 450$ K), as indicated in Figs. 7.4(a,b) and 7.6 denotes the transition stage beyond which the development of the oxide-film constitution is no longer governed by the surface pretreatment at the onset of oxidation due to the thermally-activated interfacial segregation of Mg from the interior of the alloy towards the alloy/oxide interface.

The **oxide-film growth kinetics** for the thermal oxidation of the SC and SC/Ann Al-based AlMg substrates in the temperature range of $T = 300 - 560$ K for $pO_2 = 1 \times 10^{-4}$ Pa, as well as in the range of $T = 300 - 525$ K for $pO_2 = 1 \times 10^{-2}$ Pa (see Figs. 7.3(a,b)), as determined by RISE, are characterized by an initial regime of very fast film growth, which is succeeded by a second oxidation stage in which the film growth rate becomes very small: i.e. a near-limiting oxide-film thickness is attained. This passivation behavior is typical for the oxidation of metals and alloys at low temperatures, where the rate of thermal diffusion of cations and/or anions through the developing oxide film under influence of the chemical potential (i.e. concentration) gradient is negligibly small (for more details, see Chapter 5). For oxidations at $pO_2 = 1 \times 10^{-2}$ Pa and $T \geq 560$ K, a separation between an initial, fast and a second, slow oxidation stage can no longer be made. Instead, the first stage of very fast growth kinetics decreases much more gradually with increasing oxidation time without approaching a near-limiting thickness (see Fig. 7.3b). This is attributed to the enhanced thermal diffusion of ionic species under the influence of the concentrations gradients, as well as the enhanced rate of electron transport by thermionic emission, across the developing oxide film at these elevated temperatures $T \geq 560$ K.
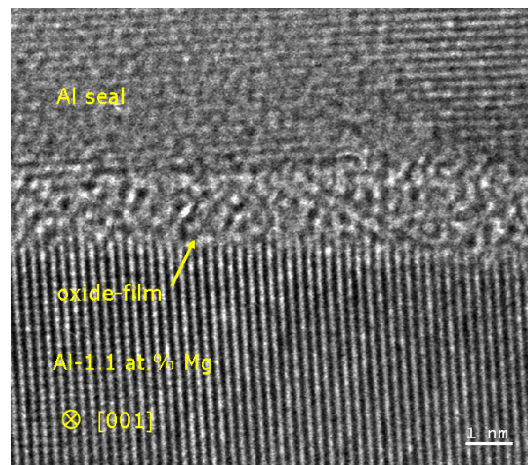
Fig. 7.5. Cross-sectional high resolution transmission electron micrograph of an oxide film grown on the SC/Ann Al-1.1 at% Mg substrate after oxidation for $t = 6 \times 10^3$ s at $T = 475$ K and $pO_2 = 1 \times 10^{-4}$ Pa (and subsequent in-situ deposition of a MBE-grown Al seal). The direction of the primary electron beam was along the zone axis [001] of the Al-1.1 at% Mg substrate. The oxide film contains both Al and Mg (as evidenced by AR-XPS).
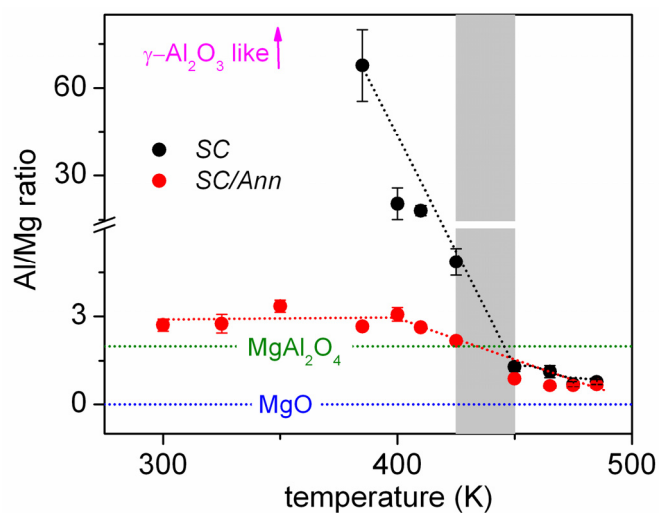
Fig. 7.6: Calculated, overall Al-to-Mg cation ratio within the grown oxide films, as determined by AR-XPS (see Chapter 3), versus oxidation temperature (K) for the oxidation of the bare *SC* and *SC/Ann* Al – 1.1 at.% Mg substrates for 6×10^3 s at $pO_2 = 1 \times 10^{-4}$ Pa. The Al/Mg cation ratio for stoichiometric $MgAl_2O_4$ and MgO are represented by the corresponding dotted lines. The shaded area represent a 'transition zone' beyond which an effect of surface pre-treatment on the resulting oxide-film constitution after 6000 s of oxidation is no longer observed.

8. Zusammenfassung

Die Oxidschicht auf der Oberfläche einer Legierung beeinflusst viele ihrer physikalischen und chemischen Eigenschaften, wie beispielsweise die Korrosionsbeständigkeit, Haftung, elektrische und thermische Leitfähigkeit, Reibung und Verschleißfestigkeit. Technologische Anwendungen erfordern die Kontrolle und Optimierung dieser Eigenschaften durch die gezielte Einstellung der Mikrostruktur sowohl der Legierung als auch der Oxidschicht, was zu einem großen Interesse an dem thermischen Oxidationsverhalten von metallischen Legierungen in den letzten Jahrzehnten geführt hat. Dennoch wurden bislang Untersuchungen der Oxidation von metallischen Legierungen überwiegend bei relativ hohen Temperaturen (d.h. $T > 800$ K) und hohen Sauerstoffdrücken (d.h. $0,1 < p < 10^5$ Pa) durchgeführt. Bei diesen hohen Temperaturen bilden sich auf der Legierung durch stufenweise, bevorzugte Oxidation der Legierungs-Bestandteile relativ *dicke* Oxidschichten (d.h. in der Größenordnung von Mikrometern), bestehend aus vielfältigen, *kristallinen* Oxidphasen. Demgegenüber wurde die Oxidation von metallischen Legierungen bei niedrigen Temperaturen (d.h. $T < 600$ K) bisher nur sehr spärlich untersucht. Bei diesen niedrigen Temperaturen ist die thermisch aktivierte Diffusion der Edukte durch die wachsende Oxidschicht vernachlässigbar gering und folglich bilden sich *sehr dünne* (< 3 nm) Oxidschichten mit nahezu limitierenden Dicken, die im Allgemeinen aus einer *metastabilen* (oft amorphen), metallischen mischoxid-Phase bestehen. Dennoch sind die genauen Mikrostrukturen (d.h. Dicke, Morphologie, kristallographische Struktur, chemische Zusammensetzung und Struktur) dieser anfänglichen Oxidschichten in Abhängigkeit der Mikrostruktur der Legierung (z.B. Legierungsgehalt, Oberflächenorientierung), der Vorbehandlung der Oberfläche (z.B. mit oder ohne natürliche Oxidschicht) und der Wachstumsbedingungen (z.B. Temperatur, Zeit und Sauerstoff-Partialdruck) häufig unbekannt.

Diese Doktorarbeit widmet sich den anfänglichen Stadien der trockenen, thermischen Oxidation von reinen (d.h. ohne natürliche Oxidschicht) Al-basierten AlMg-Legierungsoberflächen abhängig von den Oxidationsbedingungen (*hier:* Oxidationstemperatur, Zeit und Sauerstoff-Partialdruck), und dem Einfluss von verschiedenen Vorbehandlungen der reinen Oberfläche vor der Oxidation. Zu diesem Zweck wurde ein experimenteller Ansatz gewählt, der die, dem aktuellen Stand der

Technik entsprechenden, experimentellen Verfahren spektroskopische in-situ Echtzeitellipsometrie (RISE), winkelaufgelöste Röntgen-Photoelektronen-Spektroskopie (AR-XPS) und Hochauflösungs-Transmissionselektronenmikroskopie (HR-TEM) kombiniert. Dieser ermöglicht, die Zusammenhänge zwischen der Wachstumskinetik, der mikrostrukturellen Entwicklung der Oxidschicht, der durch die Oxidation induzierten, oberflächlichen Zusammensetzungsänderungen der Legierung, und der Vorbehandlung der reinen Oberfläche und ihrer Oxidationsbedingungen zu untersuchen. Diese umfassende Kenntnis der anfänglichen Oxidation von AlMg-Legierungen bei niedrigen Temperaturen ist von wachsendem technologischen Interesse für Anwendungen, die korrosionsbeständige Leichtmetalllegierungen erfordern (z.B. Luft- und Raumfahrt, Automobilindustrie, marine Anwendungen, Handhabung von Nahrungsmitteln, Chemikalien und Abwässern). Bisherige Arbeiten über die Oxidation von AlMg-Legierungen wurden meist unter Anwesenheit einer natürlichen Al-Oxidschicht zu Beginn der Oxidation durchgeführt, und ohne die Mikrostruktur der entstehenden Oxidschicht umfassend zu charakterisieren. Überdies stellt eine grundlegende Untersuchung der anfänglichen Oxidation von AlMg-Legierungen eine wissenschaftliche Herausforderung dar, da beide Legierungsbestandteile (d.h. Al und Mg) eine starke Affinität zu Sauerstoff besitzen (im Gegensatz zu binären Legierungssystemen wie Cu-Au oder Pt-Al, bei denen ein Bestandteil edler ist als der andere) und folglich die bereits genannten Zusammenhänge zwischen den entstehenden Mikrostrukturen der Legierung und des Oxids und den Oxidationsbedingungen sehr kompliziert sein können.

Zunächst wurde ein **thermodynamisches Modell**, welches die bestimmende Rolle von Oberflächen- und Grenzflächenenergien in diesen sehr dünnen Oxidschicht-Systemen berücksichtigt, entwickelt, um das Wachstum einer anfänglichen, amorphen Oxidschicht (d.h. *am*-Al_2O_3, *am*-MgO und/oder *am*-$MgAl_2O_4$) auf einer reinen AlMg-Legierung abhängig von der Wachstumstemperatur, des oberflächlichen Legierungsgehalts und der Oxidschichtdicke (≤ 5 nm) vorherzusagen. Dazu wurden experimentelle oder empirisch abgeschätzte, temperaturabhängige Werte der Oberflächenenergien der konkurrierenden *amorphen* Oxidphasen *am*-Al_2O_3, *am*-MgO oder *am*-$MgAl_2O_4$ (im Folgenden als $\{Al_2O_3\}$, $\{MgO\}$ und $\{MgAl_2O_4\}$ bezeichnet) verwendet. Benötigte Werte der Grenzflächenenergie zwischen der Legierung und der konkurrierenden *amorphen* Oxidphasen in Abhängigkeit der Temperatur und des

oberflächlichen Mg-Legierungsgehalts wurden durch geeignete Gleichungen abgeschätzt, abgeleitet auf der Basis des Ansatzes des „makroskopischen Atoms".

Daraus folgt, dass im Besonderen die $\langle AlMg \rangle - \{Al_2O_3\}$ -Grenzfläche deutlich stabiler ist als die entsprechende Grenzfläche von $\{MgAl_2O_4\}$ und $\{MgO\}$ (siehe Abb. 8.1). Durch Grenzflächen-Thermodynamik wird damit für die Bildung einer mehrkomponentigen Oxidschicht, bestehend aus $\{Al_2O_3\}$, $\{MgO\}$ und/oder $\{MgAl_2O_4\}$, die Verteilung der $\{Al_2O_3\}$- beziehungsweise $\{MgO\}$-Oxidphase an der Grenzfläche beziehungsweise Oberfläche bevorzugt, in Übereinstimmung mit experimentellen Beobachtungen (siehe Kapitel 4 und 5). Die vergleichsweise niedrige Energie der $\langle AlMg \rangle - \{Al_2O_3\}$ -Grenzfläche beruht vorwiegend auf einer relativ hohen Dichte von Sauerstoff-Metall-Bindungen und dem damit stärker negativen chemischen Wechselwirkungsbeitrag zur Grenzflächenenergie pro Einheitsfläche $\gamma_{\langle AlMg \rangle - \{Al_2O_3\}}$. Des Weiteren nimmt der Wechselwirkungsbeitrag zur Grenzflächenenergie mit zunehmendem Mg-Legierungsgehalt x_{Mg}^i durch die relativ starke chemische Bindung von Mg-O (im Vergleich zu Al-O) betragsmäßig zu. Dies beinhaltet die Existenz einer starken Triebkraft für die chemische Segregation von Mg aus dem Inneren des $\langle AlMg \rangle$ -Substrats zur $\langle AlMg \rangle - \{Oxid\}$ -Grenzfläche, was ebenfalls gut mit Experimenten übereinstimmt (siehe Kapitel 4 und 5).

Unter Berücksichtigung der Gibbs-Energien der entsprechenden Bulk-Materialien und der Grenzflächen- und Oberflächenenergien der verschiedenen amorphen Oxidschichten in Abhängigkeit der Wachstumsbedingungen der Oxide (siehe Kapitel 2) folgt hieraus, dass die Bildung von amorphem Al_2O_3 thermodynamisch bevorzugt ist. Diese Vorhersage des Modells steht im Einklang sowohl zur experimentell (mit AR-XPS) beobachteten natürlichen amorphen Al_2O_3-Schicht, die sich auf einem Al-0,8 At.-% Mg-Substrat unter atmosphärischen Bedingungen bei Raumtemperatur bildet, als auch zur mikrostrukturellen Entwicklung von sehr dünnen Oxidschichten, die sich bei der kontrollierten Oxidation von reinen Al- und Mg-basierten AlMg-Legierungssubstraten in einem kombinierten UHV-System in dieser Untersuchung bildeten (siehe unten).
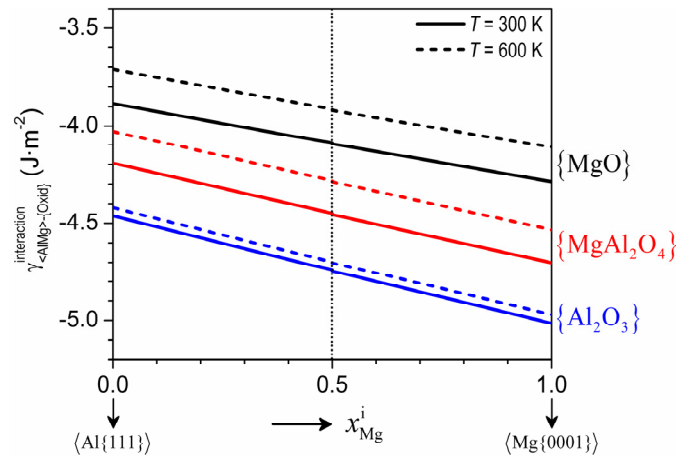
Abb. 8.1. Grenzflächenenergien $\gamma_{\langle AlMg\rangle-\{MgO\}}$, $\gamma_{\langle AlMg\rangle-\{Al_2O_3\}}$ und $\gamma_{\langle AlMg\rangle-\{MgAl_2O_4\}}$ für die amorphen Oxidschichten (d.h. $\{MgO\}$, $\{Al_2O_3\}$ und $\{MgAl_2O_4\}$) der dichtgepacktesten Oberfläche des $\langle AlMg\rangle$-Substrats (siehe Kapitel 2) als Funktion des Mg-Legierungsgehalts an der Grenzfläche von Legierung und Oxid (x_{Mg}^i) bei Wachstumstemperaturen von $T = 300$ K und 600 K. Die Grenzflächenenergien wurden mit Hilfe der Gleichungen (2.8), (2.9) beziehungsweise (2.10) in Kapitel 2 berechnet. Weitere Einzelzeiten siehe Kapitel 2.

Kapitel 3 bis 6 widmen sich einer umfassenden **experimentellen Untersuchung** der Zusammenhänge zwischen der Wachstumskinetik der Oxide, den mikrostrukturellen Entwicklungen in den Oxidschichten und der Legierung und der Oxidationsbedingungen. Zu diesem Zweck wurden polykristalline AlMg-Proben mit einem nominellen Mg-Legierungsgehalt von 0,8 und 1,1 At.-% in einem für die Probenbearbeitung (d.h. Reinigung, Auslagerung und Oxidation) und in-situ-Analyse ausgestatteten UHV-System (Basisdruck < 3×10^{-8} Pa) thermisch oxidiert. Nachdem die polierten Legierungsoberflächen in das UHV-System gebracht worden sind, wurde zuerst das natürliche Oxid durch Sputter-Reinigung entfernt, wofür ein fokussierter 1 keV Ar$^+$-Ionenstrahl über die gesamte Oberfläche (von 7×7 mm^2) gerastert wurde. Die so erhaltenen, sputter-gereinigten Legierungsoberflächen (mit in-situ AR-XPS überprüft) werden im Folgenden als *SC-Substrate* bezeichnet. Diese SC-Substrate wurden anschließend in-situ reinem O$_2$-Gas ($pO_2 = 10^{-4}$ - 10^{-2} Pa) für Zeiträume von 15 s bis zu 6 h bei verschiedenen Temperaturen von $T = 300 – 610$ K ausgesetzt. Als zusätzliche Vorbehandlung der Oberfläche wurden einige *SC-Substrate* vor der Oxidation 1200 s bei $T = 460$ K im Vakuum ausgelagert. Die so erhaltenen, sputter-gereinigten, ausgelagerten Legierungsoberflächen werden im Folgenden als *SC/Ann-Substrate* bezeichnet. RISE wurde angewandt, um die Wachstumskinetik der Oxidschicht aufzuklären. Die Dicken,

Zusammensetzungen und chemischen Strukturen der gewachsenen Schichten wurden mit in-situ AR-XPS bestimmt. Zudem wurden die Mikrostrukturen einiger der gewachsenen Oxidschichten mit Querschnitts-HR-TEM atomar analysiert.

Im dritten Kapitel wurden allgemein anwendbare Vorgehensweisen für die **tiefenaufgelöste quantitative Analyse** von sehr dünnen (< 3 nm), gemischt-metallischen oder mehrphasigen Oxidschichten auf binären Legierungen mit RISE und AR-XPS entwickelt. Die vorgeschlagenen Methoden der Datenauswertung und Quantifizierung wurden auf die anfängliche, thermische Oxidation von sputter-gereinigten Al – 1,1 At.-% Mg-Legierungsoberflächen bei T = 300 - 485 K (pO_2 = 1×10^{-4} Pa) angewandt. Dadurch wurde ein detailliertes Verständnis sowohl der tiefenabhängigen mikrostrukturellen Entwicklung der amorphen (Al,Mg)-Oxidschicht als auch der damit einhergehenden Zusammensetzungsänderungen in der Legierung abhängig von der Oxidationstemperatur erhalten (siehe unten).

Typische gemessene und berechnete AR-XPS-Spektren der Photoelektronen-Linien der Al 2p und Mg 2p Kern-Niveaus sind in Abb. 8.2a beziehungsweise 8.2b gezeigt. Mit der tiefenaufgelösten AR-XPS-Analyse wurde nachgewiesen, dass, abhängig von der Vorbehandlung der Oberfläche und den Oxidationsbedingungen, lediglich Al oder Al und Mg in die wachsenden Oxidschichten eingebaut wurden. Zudem kann ein einzelner lokaler chemischer Zustand oder eine Kombination davon für die Al- und Mg-Kationen in der Oxidschicht auftreten. Manche dieser Zustände gleichen entsprechenden lokalen chemischen Zuständen in stöchiometrischen Al_2O_3- oder MgO-"Bulk"-Phasen (siehe Abb. 8.2(a,b)). Die Dicken, Tiefenverteilungen der Elemente, chemische Strukturen und Zusammensetzungen der gewachsenen Oxidschichten wurden aus den aufgetrennten Al 2p, Mg 2p und O1s PZL-Gesamtintensitäten des oxidierten Metalls (bei verschiedenen Detektionswinkeln) berechnet, gemäß dem in Kapitel 3 gezeigten Berechnungsschema.

Quantitative RISE-Analyse wurde durchgeführt, indem eine optische Modellbeschreibung für die Ellipsometrieparameter $\psi(\lambda, t)$ und $\Delta(\lambda, t)$ für das entstehende Substrat/Schicht-System an die entsprechenden gemessenen Verläufe angepasst wurde. Das Modell berücksichtigt eine wachsende Oxidschicht einheitlicher Dicke auf einem reinen AlMg-Substrat zusammen mit einer Zwischenschicht mit einer Dicke von weniger als einer Monolage, um die charakteristische ellipsometrische Absorption im Bereich der Metall/Oxid-Grenzfläche zu berücksichtigen (weitere Einzelheiten siehe Kapitel 3).

Einige exemplarische Wachstumskurven der gesamten Oxidschicht sind in Abb. 8.3(a,b) gezeigt.
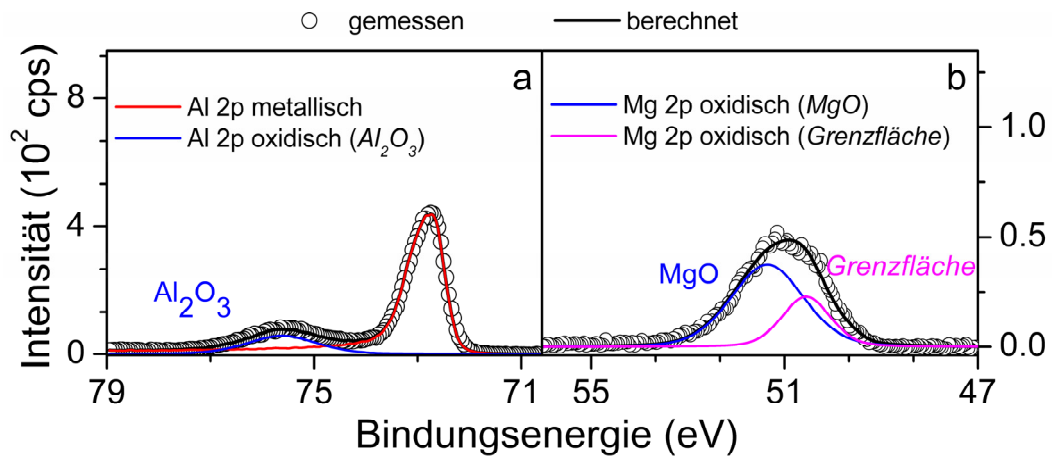

Abb. 8.2: Gemessene und berechnete (a) Al 2p and (b) Mg 2p Spektren, aufgenommen bei einem Detektionswinkelpaar von $(\alpha, \phi) = (38°, 54, 75°)$ vom oxidierten Al-1,1 At.-% Mg-Substrat. Zur Oxidation wurde das sputter-gereinigte Substrat bei einer konstanten Substrattemperatur von 475 K 6×10^3 s lang reinem Sauerstoffgas (pO$_2$ = 1×10^{-4} Pa) ausgesetzt. Weitere Einzelheiten siehe Kapitel 3.
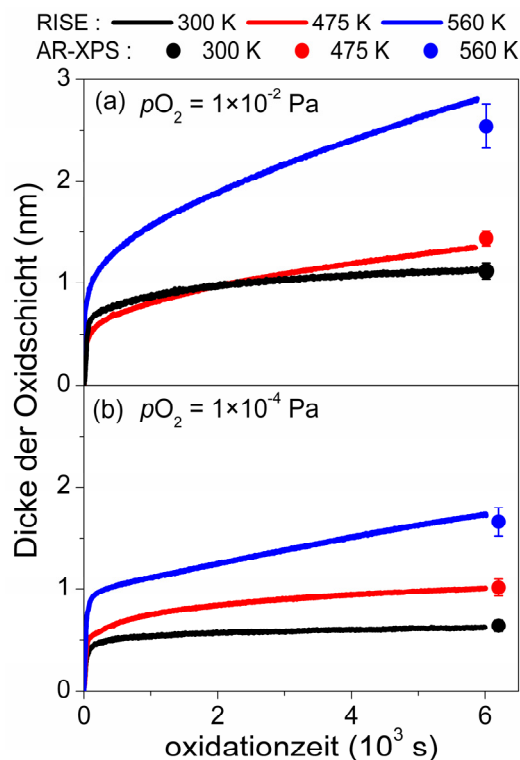
Abb. 8.3: Wachstumskurven der gesamten Oxidschicht, durch spektroskopische in-situ Echtzeitellipsometrie (RISE) für die Oxidation des reinen *SC* Al – 0,8 At.-% Mg-Substrats für 6×10^3 s bei (**a**) pO$_2$ = 1×10^{-4} Pa und (**b**) pO$_2$ = 1×10^{-2} Pa und bei Temperaturen von 300 K bis 560 K erhalten.

Kapitel 4 befasst sich mit der Auswirkung der **Vorbehandlung der Oberfläche** (d.h. SC-Substrat versus SC/Ann-Substrat, siehe oben) auf die Wachstumskinetik der Oxidschicht und die tiefenabhängigen Zusammensetzungsänderungen in der Legierung und der Oxidschicht. Demnach verarmt während der Sputter-Behandlung im Vakuum, wie sie zur Reinigung der AlMg-Substrate vor der Oxidation durchgeführt wurde, der oberflächliche Bereich der Legierung vollständig an Mg wegen der gleichzeitig ablaufenden Prozesse bevorzugtes Sputtern (Entfernen) von Mg und durch Beschuss erhöhte Segregation von Mg in Richtung der mit Ionen beschossenen Oberfläche. Da die chemische Segregation von Mg bei $T \leq 385$ K kinetisch gehemmt ist, führt die nachfolgende Oxidation der **SC** Al-basierten AlMg-Substrate bei **$T \leq 385$ K** dann zur Bildung von sehr dünnen Oxidschichten mit begrenzten Dicken im Bereich von 0,66 – 0,62 nm, die ausschließlich aus Al_2O_3 bestehen (siehe Abb. 8.4a). In diesen Oxidschichten gibt es für die Al-Kationen zwei verschiedene lokale chemische Umgebungen: (*i*) ein "Bulk-Al_2O_3-artiger" Al 2p-Hauptpeak, der von Al Kationen im Inneren der Oxidschicht stammt und (*ii*) eine "Grenzflächen-Al-Oxid"-Komponente wegen einer unvollständigen Koordination von Al durch O-Anionen *an* der Grenzfläche. Das durch AR-XPS nachgewiesene Grenzflächen-Al-Oxid entspricht der EMA-Schicht (mit einer Dicke von weniger als einer Monolage), die in der Modellbeschreibung für die Ellipsometrie angenommen wurde (siehe oben). Die Segregation von Mg aus dem Inneren der Legierung zur Grenzfläche von Legierung und Oxid wird für die Oxidation der **SC** Al-basierten AlMg-Substrate bei höheren Temperaturen **$T > 385$ K** thermisch aktiviert. Dies wurde durch das Auftauchen einer „Grenzflächen-Mg-Oxid"-Komponente (wegen einer unvollständigen Koordination von Mg durch O-Anionen *an* der Grenzfläche) mit AR-XPS nachgewiesen (siehe Abb. 8.2b und 8.4a). Diese experimentellen Beobachtungen stimmen mit der vom Modell vorhergesagten Triebkraft für die chemische Grenzflächensegregation von Mg hervorragend überein (siehe Abb. 8.1).

An der reinen Oberfläche der *SC/Ann*-Substrate ist, als Folge des der Oxidation vorausgehenden Auslagerungsschritts, Mg bereits chemisch segregiert. Folglich werden sowohl Al als auch Mg während der anfänglichen, schnellen Oxidation der SC/Ann-Substrate in die Oxidschicht eingebaut. Für die Oxidation der **SC/Ann**-Substrate bei **$T < 410$ K** sind die Kationen mit Al_2O_3- beziehungsweise MgO-ähnlichen lokalen chemischen Zuständen dann in den amorphen Oxidschichten an der Grenzfläche

beziehungsweise nahe der Oberfläche angereichert, was gut mit den theoretischen Vorhersagen übereinstimmt (siehe Abb. 8.1, 8.4b und Kapitel 2).

Wie durch **HR-TEM** (siehe Abb. 8.5 und Kapitel 6), betätigt wurde, sind die auf reinen AlMg-Substraten bei $T < 450$ K gewachsenen Oxidschichten amorph. Die Analyse der chemischen Zustände mit AR-XPS legt nahe, dass die Anordnung der Sauerstoffanionen der gewachsenen Oxidschichten einem gestörten dichtgepackten Sauerstoff-Untergitter ähnelt, wobei die Mg-Kationen vorwiegend die Tetraederlücken besetzen (wie in MgO) und die Al-Kationen in den Oktaeder- und/oder Tetraederlücken in der Nähe der Grenzfläche von Legierung und Oxid angereichert sind.
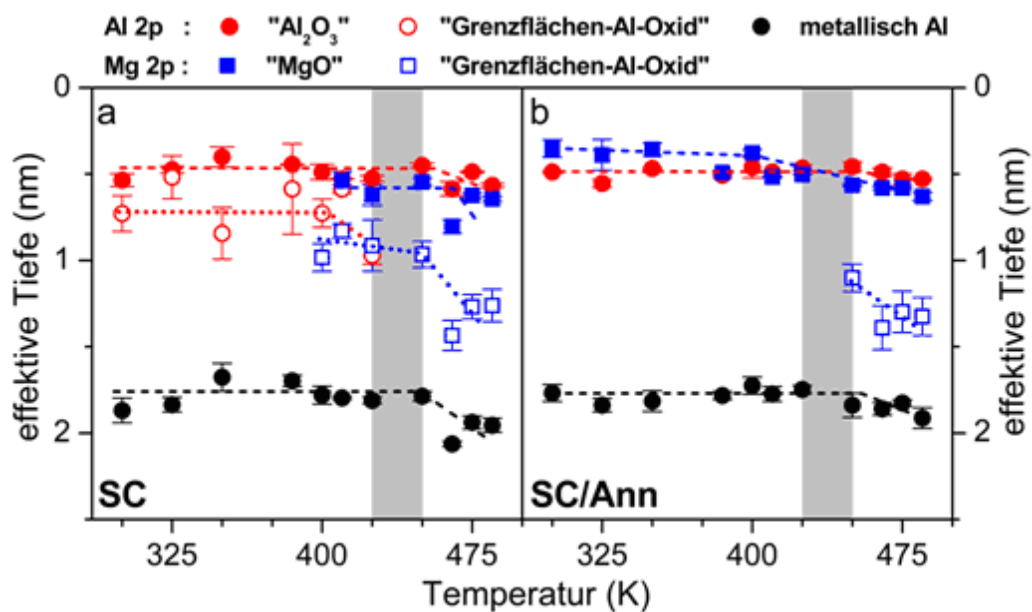
Abb. 8.4: Effektive Tiefen der Al- und Mg-Kationen in sehr dünnen (d.h. 0.6 bis 1 nm dicken) Oxidschichten, auf (a) *SC* und (b) *SC/Ann* Al-basierten Al − 1.1% Mg-Substraten durch trockene, thermische Oxidation für 6×10^3 s bei $pO_2 = 1\times10^{-4}$ Pa innerhalb des Temperaturbereichs von $T = 300\text{-}485$ K gewachsen (bestimmt mit AR-XPS). Die gepunkteten Linien sind zur leichteren Erkennbarkeit eingezeichnet. Die schattierte Fläche stellt einen "Übergangsbereich" dar, jenseits dessen eine Auswirkung der Vorbehandlung der Oberfläche auf die entstehende Struktur der Oxidschicht nach 6000 s Oxidation nicht mehr beobachtet wird.

Bei höheren Temperaturen $T > 425$ K wird die Segregation von Mg aus dem Inneren der Legierung in Richtung der Grenzfläche, wo die Reaktion stattfindet, thermisch aktiviert, wie durch das Auftauchen eines zusätzlichen chemischen Zustand für Mg *an* der Grenzfläche von Legierung und Oxid (siehe Abb. 8.4b) gezeigt wurde. Das Wachstum der Oxidschicht schreitet dann durch die selektive Oxidation von Mg, das *an* die Grenzfläche segregiert ist, fort. Die führt zu einer starken Abnahme des Al/Mg-

Atomverhältnisses in der entstehenden Oxidschicht (siehe Abb. 8.6), wobei das gesamte Anionen-zu-Kationen-Verhältnis sich der allgemeinen Stöchiometrie von MgO annähert. Wie durch HR-TEM (siehe Kapitel 6) nachgewiesen wurde, ist die dicker werdende Oxidschicht bei $T > 425$ K bereits teilweise in von Bulk-Thermodynamik bevorzugtes *kristallines* MgO umgewandelt; der Gitterparameter der zugehörigen, kristallinem MgO-ähnlichen Oxidphase wurde zu (4,15±0,1) Å bestimmt. Außerdem dreht sich die effektive Tiefe (Verteilung) der Al_2O_3- und MgO-artigen lokalen chemischen Zustände für dickere, bereits teilweise kristalline Oxidschichten um. Die in Abb. 8.4(a,b) und 8.6 eingezeichnete graue Flächen (d.h. der Bereich 425 K $\leq T \leq$ 450 K) kennzeichnen den Übergangsbereich jenseits dessen die strukturelle Entwicklung der Oxidschicht nicht mehr durch die Vorbehandlung der Oberfläche bestimmt wird. Dies wird verursacht durch die thermisch aktivierte Segregation von Mg aus dem Inneren der Legierung an die Grenzfläche.

Die mit RISE bestimmte **Wachstumskinetik der Oxidschichten** für die thermische Oxidation der SC und SC/Ann Al-basierten AlMg-Substrate im Temperaturbereich von sowohl $T = 300 – 560$ K für $pO_2 = 1×10^{-4}$ Pa als auch im Bereich von $T = 300 – 525$ K für $pO_2 = 1×10^{-2}$ Pa (siehe Abb. 8.3(a,b)) ist durch ein Anfangsstadium sehr schnellen Schichtwachstums gekennzeichnet, dem ein zweites Oxidationsstadium folgt, in dem die Wachstumsrate der Schicht sehr klein wird: d.h. eine nahezu limitierende Dicke der Oxidschicht wird erreicht. Dieses Passivierungverhalten ist typisch für die Oxidation von Metallen und Legierungen bei niedrigen Temperaturen, wo die Geschwindigkeit der thermischen Diffusion von Kationen und/oder Anionen unter dem Einfluss des Gradienten des chemischen Potentials (d.h. der Konzentration) durch die sich bildende Oxidschicht vernachlässigbar gering ist (weitere Einzelheiten siehe Kapitel 5). Für Oxidationen bei $pO_2 = 1×10^{-2}$ Pa und $T \geq 560$ K kann nicht mehr zwischen einem anfänglichen, schnellen, und einem zweiten, langsamen Oxidationsstadium unterschieden werden. Stattdessen nimmt während des ersten Stadiums die sehr schnelle Wachstumskinetik mit zunehmender Oxidationszeit viel langsamer ab, ohne sich einer nahezu limitierenden Dicke anzunähern (siehe Abb. 8.3b). Dies wird bei diesen erhöhten Temperaturen $T \geq 560$ K sowohl der verstärken thermischen Diffusion der ionischen Spezies unter dem Einfluss der Konzentrationsgradienten als auch der erhöhten Geschwindigkeit des Elektronentransports durch thermionische Emission durch die entstehende Oxidschicht hindurch zugeschrieben.
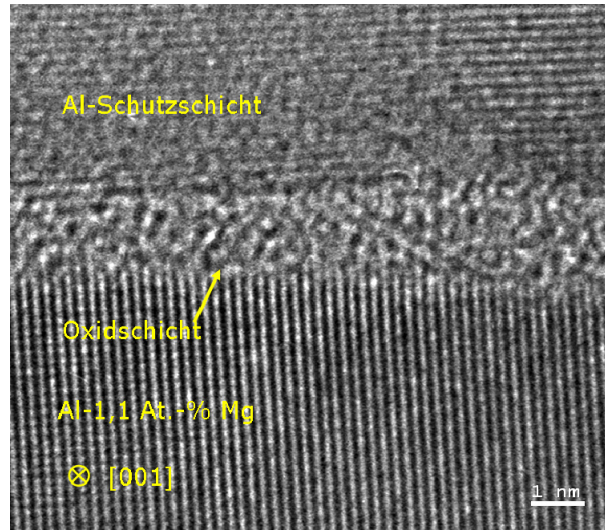
Abb. 8.5. Höchauflösungs-transmissionselektronenmikroskopische Querschnittsaufnahme einer Oxid-schicht, gewachsen auf einem SC/Ann Al-1.1 At.-% Mg-Substrat nach $t = 6 \times 10^3$ s Oxidation bei $T = 475$ K und $pO_2 = 1 \times 10^{-4}$ Pa (und anschließender Abscheidung einer Al-Schutzschicht in-situ mittels MBE). Die Richtung des Primärelektronenstrahls liegt entlang der [001]-Zonenachse des Al-1,1 At.-% Mg-Substrats. Die Oxidschicht enthält sowohl Al als auch Mg (mit AR-XPS nachgewiesen).
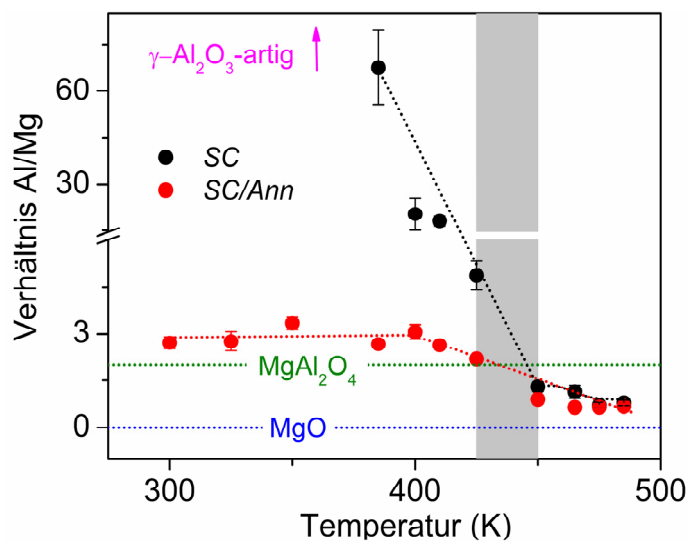

Abb. 8.6: Berechnetes, gesamtes Al-zu-Mg-Kationenverhältnis innerhalb der gewachsenen Oxidschichten, bestimmt mit AR-XPS (siehe Kapitel 3), aufgetragen gegen die Oxidationstemperatur in K für die Oxidation der reinen *SC* und *SC/Ann* Al – 1,1 At.-% Mg-Substrate für 6×10^3 s bei $pO_2 = 1 \times 10^{-4}$ Pa. Das Al/Mg-Kationenverhältnis für stöchiometrisches $MgAl_2O_4$ und MgO sind durch die entsprechenden gepunkteten Linien dargestellt. Die schattierte Fläche stellt einen "Übergangsbereich" dar, jenseits dessen eine Auswirkung der Vorbehandlung der Oberfläche auf die entstehende Struktur der Oxidschicht nach 6000 s Oxidation nicht mehr beobachtet wird.

List of publications

1. E. Panda, P.K. Sahoo, S.K. Singh, S. Bhattacharjee, P.K. Mishra and R.K. Galgali, *Preparation of titania slag by plasma smelting of ilmenite*, Proceedings of 39th National Metallurgists' Day & 55th Annual Technical Meeting of The Indian Institute of Metals (2001) p. 38.

2. E. Panda, Dipak Mazumdar and S.P.Mehrotra, *Mathematical Modelling of Particle Segregation during Centrifugal Casting of Metal Matrix Composites*, Metallurgical and materials Transactions A 37A (2006) 1675.

3. E. Panda, L.P.H. Jeurgens and E.J. Mittemeijer, *Effect of surface pre-treatment on the initial, thermal oxidation of Al-1.12 at% Mg surfaces*, Proceedings of 14th International Conference on Thin Films & Reactive Sputter Deposition 2008 (2008) p. 49.

4. E. Panda, L.P.H. Jeurgens, G. Richter and E.J. Mittemeijer, *Microstructural evolution of ultra-thin oxide films grown on Al-Mg alloys at low temperatures*, Proceedings of 13th European Conference on Applications of Surface and Interface Analysis (2009) p. 182.

5. E. Panda, L.P.H. Jeurgens and E.J. Mittemeijer, *Interface thermodynamics of ultrathin, amorphous oxide overgrowths on AlMg alloys*, (in press) Acta Mater. (Chapter 2 of the thesis).

6. E. Panda, L.P.H. Jeurgens and E.J. Mittemeijer, *The initial oxidation of Al-Mg alloys: Depth-resolved quantitative analysis by angle-resolved XPS and real-time in-situ ellipsometry*, (in press) J. Appl. Phys. (Chapter 3 of the thesis).

7. E. Panda, L.P.H. Jeurgens and E.J. Mittemeijer, *Effect of in-vacuo surface pretreatment on the microstructure and growth kinetics of the ultra-thin oxide films grown on Al-Mg alloy substrates*, (in press) Surf. Sci. (Chapter 4 of the thesis).

8. E. Panda, L.P.H. Jeurgens, E.J. Mittemeijer, *Kinetics and thermodynamics of the Initial oxidation of AlMg alloys*, submitted. (Chapter 5 of the thesis).

9. E. Panda, L.P.H. Jeurgens, G. Richter and E.J. Mittemeijer, *The amorphous to crystalline transition of ultrathin (Al,Mg)-oxide films grown by thermal oxidation of AlMg alloys; an HR-TEM investigation*, accepted in J. Mat. Res. (Chapter 6 of the thesis).

Acknowledgements

Curriculum Vitae

Personal Data

Name	Emila Panda
Date and Place of Birth	07.04.1979, Bhubaneswar, India
Marital Status	Married
Nationality	Indian

Schooling

1983 - 1994	University High School, Bhubaneswar, India
1994 - 1996	B. J. B. College, Bhubaneswar, India

Higher education

Aug. 1996 – May 2000	Bachelor of Engineering (Metallurgy)
	Regional Engineering College, Rourkela, India
Jan. 2002 – Aug. 2003	Master of Technology (Materials and Metallurgical Engg.)
	Indian Institute of Technology, Kanpur, India

Research experience

Nov. 2000 – Dec. 2001	Junior Research Fellow
	Regional Research Laboratory (RRL), Bhubaneswar, India
Jun. 2004 – Feb. 2006	Scientist
	National Metallurgical Laboratory (NML), Jamshedpur, India

Production experience

Sept. 2003 – May 2004	Assistant Manager
	Kalyani Carpenters Special Steels Ltd., Pune, India.

Dissertation

Apr. 2006 - Present	Ph. D. at the Max-Planck-Institut für Metallforschung and
	Universität Stuttgart
	Title: "The Initial Oxidation of AlMg alloys"